Technische Universität München
Lehrstuhl für Hochfrequenztechnik

Metamaterials in Arbitrary Waveguiding Structures

Yvonne Weitsch

Vollständiger Abdruck der von der Fakultät für Elektrotechnik und Informationstechnik der Technischen Universität München zur Erlangung des akademischen Grades eines

– *Doktor-Ingenieurs* –

genehmigten Dissertation.

Vorsitzender: Univ.-Prof. Paolo Lugli, Ph.D.

Prüfer der Dissertation:

1. Univ.-Prof. Dr.-Ing. Thomas Eibert
2. Univ.-Prof. Dr.-Ing. Volkert Hansen (i.R.)
   Bergische Universität Wuppertal

Die Dissertation wurde am 19.04.2011 bei der Technischen Universität München eingereicht und durch die Fakultät für Elektrotechnik und Informationstechnik am 12.07.2011 angenommen.

Contents

Symbols and Acronyms

a	inward normalised complex power wave amplitude
A	complex amplitude
$\boldsymbol{A}$	magnetic vector potential
$ABCD$-matrix	transmission matrix with respect to voltage and current
b	outward normalised complex power wave amplitude
$\boldsymbol{B}$	magnetic flux density
C	capacitance
C'	per-unit-length capacitance
C_L	left-handed capacitance
C_R	right-handed capacitance
x^*	conjugate complex of a number x
C_s	series capacitance
C_{sh}	shunt capacitance
c_0	$= 2.998 \cdot 10^8$ m/s, velocity of light
CRLH	composite right/left-handed
CST MWS	computer simulation technology microwave studio
$\boldsymbol{D}$	electric flux density,
	diagonal matrix
dB	decibel
$\det(\boldsymbol{X})$	determinant of a matrix $\boldsymbol{X}$
$\operatorname{diag}(\boldsymbol{X})$	diagonal of a matrix $\boldsymbol{X}$
$\dim(\boldsymbol{X})$	dimension of a matrix $\boldsymbol{X}$
$\boldsymbol{E}$	electric field strength
EQC	equivalent circuit
EVD	eigenvalue decomposition
f	frequency
$\boldsymbol{F}$	electric vector potential
f_c	cut-off frequency
FD	finite difference
FDTD	finite difference time domain
FE	finite element
FIT	finite integration technique
$f(k_z(k_x))$	amplitude function
G	Green's function
$\boldsymbol{X}^H$	conjugate transpose of a matrix $\boldsymbol{X}$, Hermitian
$\boldsymbol{H}$	magnetic field strength
HFSS	high frequency structure simulator
I	electric current
I_f	amplitude of forward travelling current wave

$\boldsymbol{I}$	identity matrix
$\bar{\boldsymbol{I}}$	identity dyad
Im	imaginary part
$\boldsymbol{J}$	electric current density
$\boldsymbol{J}_A$	electric surface current density
$\boldsymbol{j}_F$	electric surface current density (instantaneous quantity)
$k_{x,y,z}$	Cartesian components of the wave vector, wavenumbers
l	length
L	free-moving window length for the matrix pencil method, inductance
L'	per-unit-length inductance
L_L	left-handed inductance
L_R	right-handed inductance
L_p	inductance in parallel
L_s	series inductance
L_{sh}	shunt inductance
LH	left-handed
LWA	leaky-wave antenna
M	number of waves, modes
$\boldsymbol{M}$	magnetic current density
$\boldsymbol{M}_A$	magnetic surface current density
MP	matrix pencil method
MWEs	Maxwell's Equations
n	noise, refractive index
$\boldsymbol{n}$	unit normal vector
p	period or periodical length, dimension
$\boldsymbol{p}$	generalised eigenvector
P	power
PC	photonic crystals
PCB	printed circuit board
PEC	perfectly electric conducting
PMC	perfectly magnetic conducting
PML	perfectly matched layer
q_E	eigenvalue of E mode depending on transversal geometry
q_H	eigenvalue of H mode depending on transversal geometry
Re	real part
r_B	reflection coefficient related to the Bloch impedance
$\boldsymbol{r}$	position vector
$\boldsymbol{r'}$	vector of source location
RH	right-handed
$\boldsymbol{S}$	Poynting vector
S_{ij}	scattering parameter, relation between ingoing wave at port j to outgoing wave at port i
$\boldsymbol{S}$-matrix	scattering matrix

SIW	substrate integrated waveguide
SMA	scattering matrix approach
SRR	split-ring resonator
SVD	singular value decomposition
$\boldsymbol{X}^T$	transpose of a matrix $\boldsymbol{X}$
t	time
$\tan\delta$	loss factor
TE	transverse electric
TEM	transverse electromagnetic
TL	transmission line
TM	transverse magnetic
$\boldsymbol{T}$-matrix	transfer matrix
U	voltage
U_f	amplitude of forward travelling voltage wave
V	mode voltage
$\boldsymbol{v}$	(eigen)vector
v_g	group velocity
v_{ph}	phase velocity
w	width
y	representation of a signal
Y	admittance
z	$= \mathrm{e}^{\gamma t}$, complex pole, eigenvalue of a matrix $\boldsymbol{Z}$
$\boldsymbol{z}$	eigenvector of a matrix $\boldsymbol{Z}$
Z	impedance
Z_B	Bloch impedance
Z_c	characteristic impedance
Z_{F0}	$= 120\pi\ \Omega$, field impedance of free space
Z_{FE}	characteristic impedance of E mode
Z_{FH}	characteristic impedance of H mode
Z_L	transmission line impedance
$Z_i(k_u)$	impedance function for mode i dependent on wavenumber in u-direction

α	attenuation constant
β	phase constant
δ	Dirac impulse,
	delta function distribution
Δ	differential length
$\delta_{m,n}$	Kronecker symbol
ε_0	$= 8.854 \cdot 10^{-12}$ As/(Vm), permittivity of free space
ε_{eff}	effective permittivity
ε_m	Neumann factor
ε_r	relative permittivity
η	efficiency
φ	coordinate in the cylindrical coordinate system
ϕ	electric scalar potential,
	phase
γ	propagation constant
Γ	eigenvalue
κ	sample distance
λ	wavelength
λ_g	guided wavelength
λ_0	wavelength in free space
λ_{HPW}	wavelength of a homogeneous plane wave
μ_0	$4\pi \cdot 10^{-7}$ Vs/(Am), permeability of free space
μ_r	relative permeability
ϑ	coordinate in the spherical coordinate system
ρ	coordinate in the cylindrical coordinate system,
	electric charge density
ρ_A	electric surface charge density
ρ_{mA}	magnetic surface charge density
ρ_m	magnetic charge density
σ	electric conductivity
τ	singular value
ω	angular frequency
ω_0	balanced frequency
ω_{pe}	electric plasma frequency
ω_s	series resonant frequency
ω_{sh}	shunt resonant frequency
Ω	Ohm
ψ	magnetic scalar potential
ψ_E	z-component of magnetic vector potential
ψ_H	z-component of electric vector potential
∇	Nabla operator, gradient
$\nabla\cdot$	divergence operator
$\nabla\times$	curl operator
$\Delta = \nabla^2$	Laplace operator

1 Abstract

One of the main goals of this work is to extend the concept of metamaterials to arbitrary waveguiding structures. Starting at the transmission line equations for composite right/left-handed transmission lines (CRLH TL) it is shown that a pure description by voltage and current restricts to a certain type of wave, normally the TEM mode, which is not sufficient for a characterisation of arbitrary waveguiding structures. Hence, the solution of waveguides in general is derived by a formulation in terms of fields. By introducing inhomogeneities to cylindrical waveguides, novel characteristics can be triggered which cannot be attained with conventional materials. To highlight the contributions of metamaterials to electromagnetic devices, the performance of conventional applications is presented, in particular of leaky-wave antennas where the effect of metamaterials is especially obvious. Typically, with the purpose to simplify production and analysis, these modifications are realised in a periodical manner. Therefore, the Bloch-Floquet theorem is employed facilitating the analysis of fields in periodic configurations such that the field solution of the entire periodic cell continuation can be derived by the field solution of one unit cell.

The second key contribution of this work is to obtain the eigensolutions of inhomogeneous periodic eigenproblems derived from the cylindrical waveguides, which are modified in inhomogeneous manner. The eigensolutions are needed for characterisation reasons and to promote an efficient design procedure. A modal series expansion is formulated to express the field solutions of periodically loaded waveguides where purely analytical and numerical computation procedures for solving eigenproblems encounter difficulties. In this way, the field solution in cross sections of the waveguide transversal to the propagation direction are achieved where a pair of transversal planes, also called port planes, define a periodic unit cell. The eigensolutions for the electric and the magnetic field, respectively, of the background waveguide supply the basis functions in the series expansion. For simple host waveguides, these eigensolutions can even be given analytically. If more complicated configurations are concerned the 2D eigensolutions for the host waveguides can be gained numerically by employing a computer simulation tool such as CST Microwave Studio (CST MWS). The weighting coefficients in the series expansion are constituted by the amplitudes of the modes in the port planes, which are obtained by considering the coupling of the modes in the unit cell. The relation can be described by the transfer or T-matrix. The T-matrix is chosen because it can be utilised to formulate a linear eigenvalue equation. Another advantage of the T-matrix is that it is related to the scattering or S-matrix, which is a common quantity to describe the physical properties of electromagnetic devices by waves. The S-matrix is conveniently obtained by measurements or in any numerical computation. Therefore, the field solution of the 3D unit cell is computed in a driven full-wave simulation and in this way the cumbersome computation by a numerical eigensolver is circumvented. Another decisive factor is that the excitation by few modes suffices to gain the field solution for closed waveguiding structures which are

mostly operated in the fundamental mode to ensure stable working. Thereby, the final eigenproblem is reduced tremendously and can be solved by conventional means without any difficulties.

Since the eigensolutions of the cylindrical host waveguides serve as basis functions they are derived from Maxwell's equations and are studied in particular because basis functions must fulfill requirements of completeness and orthogonality. Eigenproblems which allow separation of variables with the product ansatz result in 1D coupled scalar eigenproblems, which are of Sturm-Liouville type. The solutions of Sturm-Liouville problems feature the desired properties of orthogonality and completeness. Moreover, the orthogonality principle is generally regarded for vector quantities which is for ubiquitous application. With view to the subsequent realisations, the field solutions for the E and H modes in rectangular hollow waveguides and in the grounded dielectric slab as well as a shielded three-layer structure are derived in particular.

By the introduced inhomogeneities, wave propagation is enabled even in the former evanescent wave regime. For this reason, real energy transfer of evanescent modes is examined required to apply a modal series expansion in the evanescent frequency domain.

Given that arbitrary waveguiding structures also include open region problems, the needed comprehensive integral formulation is presented. With the aim to evade such an integral evaluation, a tricky conversion is introduced by which the open field problem is restored to a closed equivalence while maintaining the behaviour of the open configuration. This is reached by placing an absorption layer in front of a closing metal shield. An alternative absorption layer is conceived which replaces the desirable perfectly matched layer (PML) to avoid corresponding numerical problems. The influence and the performance of the alternative absorbing layer is studied before it is applied to compute the modal field solution of the grounded dielectric slab.

Having provided the theoretical background, practical realisations are inspected. First, corrugated waveguides found in literature are evaluated by the modal series expansion. With the purpose to relieve sophisticated hollow waveguide design, a CRLH waveguide is implemented by substrate integrated waveguide technology. Its fundament is the H_{10} hollow rectangular waveguide mode which strongly resembles the equivalent circuit (EQC) of the CRLH TL. By special but simple modifications a considerable value of the missing series capacitance is achieved. This procedure is especially beneficial in many aspects in contrast to microstrip realisations which make up the majority of metamaterial realisations. Another important aspect in metamaterial terms is perfectly manageable by the H_{10} hollow waveguide mode design. It is the balanced state. Since the shunt resonance frequency is already determined by the transverse geometry it remains to adjust the series resonance by the longitudinal dimensions to result in identical resonance frequencies. The crucial point is that the two parameters are decoupled from each other.

Based on similar concepts, two leaky-wave antennas are developed which feature broadside radiation by operation in the fundamental mode not achievable by conventional means. To complement the family of arbitrary waveguiding structures, periodicities are introduced in the grounded dielectric slab which is the prototype of the open waveguide kind. This is however operated on higher space harmonics but by subsampling, the wavenumbers can be reverted to the fast wave region in the visible range ascribable to the left-handed range. Radiation in the entire upper hemisphere is proven for the metal-backed dielectric slab as well, broadside radiation inclusive. Evaluation by the modal series expansion delivers the corresponding dispersion behaviour and the modal field solution.

2 Introduction

In 1967, Victor Veselago [Ves68] theoretically speculated on the existence of "substances with simultaneously negative ε and μ", which is generally classified as left-handed (LH) effect, and which is the origin of all research on metamaterials. Not until 2000, Smith et al. [SPV$^+$00] succeeded in demonstrating experimentally a structure exhibiting negative ε and μ at the same time for a certain frequency range. Since the negative values result from resonance effects in this structure they only appear close to the resonance frequency. Moreover, the designed composition is lossy. An engineering approach to metamaterials is attained by extending the well-known lumped-element equivalent circuit model used for the analysis of transmission lines to the case of metamaterials. Since a realisation of purely LH configurations is not possible due to natural right-handed (RH) physical effects the desired properties of metamaterials are tried to emulate by employing lumped or distributed circuit elements to set up the equivalent circuit (EQC) of a composite right/left-handed transmission line (CRLH TL) [EIK02],[Oli02],[CI02]. Equally, short-circuited or open transmission lines can also function as the required inductors and capacitors [SMIN06]. The majority of up-to-date conceived CRLH TL configurations are based on microstrip design and are therefore open.

Contrary to the designs based on microstrip technology, which are mainly restricted to TEM-wave operation, the goal of this work is to expand the concept of metamaterials to arbitrary waveguiding structures. By introducing inhomogeneities to homogeneous waveguiding structures, characteristics can be generated which are unprecedented. By observing the EQC of the H_{10} rectangular hollow waveguide mode [ZB65], it is obvious that the EQC strongly resembles the EQC of the CRLH TL apart from the missing series capacitance. By only small modifications, the series capacitance can be introduced achieving the aimed CRLH configuration. The EQC is well established and the physical nature of the H_{10} mode is inherent unlike microstrip compositions which only mimic the behaviour of the CRLH TL. Further, by the unavoidable inhomogeneities in microstrip configurations, part of the energy leaks into air. In antenna applications, this is even aspired but not if the purpose is energy transfer, then leakage must be prevented. Hollow waveguides offer here attractive solutions as they transport energy with little losses and they are closed by themselves. Another important benefit of in particular an H_{10} mode waveguide realisation is that operation in the fundamental mode can be ensured being stable and predictable. One possible implementation, which exhibits the H_{10} waveguide mode, is a rectangular hollow waveguide with corrugated walls as analysed in [EK06]. However, such a conventional hollow waveguide design is expensive and elaborate to fabricate and due to the deep corrugations by no means a compact solution.

The design presented in [YCN$^+$07] does also not seem to cater for a simple fabrication procedure. The closed CRLH TL is derived from a stripline configuration and in order to suppress radiation it is closed in a box-like manner. Hollow waveguide modes may arise in the box-like construction. To avoid them the sidewalls must be placed as close as possible

to the inner conductor leading overall to a structure of complicated shape.

In [DW05], substrate integrated waveguide (SIW) technology is demonstrated facilitating hollow waveguide design in which the vertical side walls are replaced by lateral rows of vias leading to light weight. The entire structure results as a miniaturisation of possibly bulky hollow waveguides. Potential integration into microwave devices becomes easy. With the aim to circumvent the complex fabrication of a hollow waveguide and being economical, SIW technology is adopted and an SIW operating in the H_{10} rectangular hollow waveguide mode is presented in chapter 7.2. Spurious radiation, as it is the case for similar designs based on microstrip technology [YCN^{+}07], does not occur due to the closed configuration. The architecture in chapter 7.2 features periodic unit cells which can easily be manufactured by multi-layer printed circuit technology [WE08b],[WE09a]. By the special design a sufficient serial capacitance is achieved resulting in unit sections of remarkably short lengths compared to wavelength complying well with the homogeneity criterion of metamaterials. Consequently, refractive effects dominate diffraction of which the effects are more difficult to handle. In the macroscopic view, the SIW architecture shows a homogeneous overall behaviour.

Another issue in metamaterials, especially in those based on the CRLH TL theory, is to attain the balanced state [CI06]. This means that the series resonant circuit and the shunt resonant circuit are adjusted in a way that they reveal the same resonant frequency. A design based on the H_{10} hollow waveguide mode is advantageous in this respect, too. The shunt resonant frequency is prescribed by the transverse dimension of the geometry and the series resonant frequency can be tuned mainly by finding the appropriate longitudinal length of the unit cell in propagation direction. The balancing process is thus handy to manage. The CRLH SIW exhibits broadband matching in the balanced state. The attenuation rate is well comparable to similar designs, despite low-cost dielectric substrate, which is not particularly of low loss.

The balanced state can be characterised as a 0th order resonance where the wavelength appears to be infinitely long leading to a homogeneous field distribution within the SIW. A homogeneous illumination of the waveguiding structure by the field is especially advantageous with regard to antennas because a large aperture results in a high directivity. For a periodically constituted closed SIW structure as described above, leakage would be an undesired side effect. Nonetheless, it can also be implemented as open configuration and can thus function as leaky-wave antenna. Leaky-wave antennas are not only attractive as conformal antennas which makes them adequate for integration in radar applications or in communication devices predominantly working in the microwave regime. Having a low profile, they achieve a relatively high gain. Leaky-wave antennas belong to the travelling wave type of antennas where the wave while propagating along the structure radiates a certain part of the energy more or less in a continuous manner. The beam direction can be shifted by merely sweeping the frequency. Hence, neither additional phase shifters nor other complex feeding mechanisms are required. The scan direction of conventional RH leaky-wave antennas is yet restricted to forward direction related to the propagation direction of the wave. Only with metamaterial based leaky-wave antennas the scan range can easily be extended while operation takes place in a single mode. Now, radiation is feasible from close to backfire to nearly endfire including the broadside direction. The latter is achieved if the antenna structure is balanced. Two leaky-wave antennas of this kind are realised, one by multi-layer printed circuit design *cf.* section 8.1 and another one

by single-layer printed circuit technology facilitating even more simple manufacturing *cf.* section 8.2. The concept of the second leaky-wave antenna has been adopted by [DI09] but the design of the slots does not account exactly enough for the currents flowing in the upper metallisation. As a result, the bandwidth is narrower and the radiation performance is worse.

Additionally to the SIW based leaky-wave antennas, another antenna is conceived which is based on a grounded dielectric waveguide *cf.* section 8.3. Conversely to the other realisations, this kind of antenna is an inherently open configuration. It is supposed to represent an arbitrary type of waveguides extending the limited range of modes exhibited by SIWs derived from the H_{10} rectangular hollow waveguide mode. It also belongs to the travelling wave kind of antennas. A grounded dielectric waveguide features a TM wave with zero cut-off frequency as well as higher TE and TM modes, synonymic for H and E modes, respectively. In order to compare the dielectric slab antenna with the other designs implemented in this work, TE wave operation is ensured. By introducing periodically repeated corrugations onto the dielectric slab, the radiation can be expanded until backfire proving LH wave operation. Broadside radiation is also observed.

All realisations in this work favor H modes. The concept could also have been conceived for TM guiding structures by analogous designs. However, to ensure stable operation in electromagnetic devices operation in the fundamental mode is preferred. In a rectangular hollow waveguide, the first electric mode is the E_{11} mode of which the cut-off frequency is yet higher than of the magnetic fundamental mode H_{10} and is therefore of less technical importance. Instead, the E_{01} mode could have been considered in a waveguide with circular cross section. However, the magnetic fundamental mode H_{11} possesses a lower cut-off frequency in a circular hollow waveguide and its propagation must be suppressed [MG92]. For these difficulties with respect to electric mode types, magnetic mode types are chosen for the configurations particularly the H_{10} mode. By selecting the first TE mode, the dielectric slab was not operated in its fundamental mode. However, this structure was basically investigated in order to demonstrate the advanced simulation method realised in this work. Equally, cross coupling to the fundamental TM mode is not an issue for this kind of structure.

The accomplished waveguiding structures demonstrate different metamaterial-based properties. They are implemented in a closed fashion to exhibit wave propagation conversely to the direction of energy transfer or show waves at certain frequency with an infinite wavelength. The open SIWs working as leaky-wave antennas radiate in the entire upper hemisphere by just scanning the frequency. Moreover, they perform broadside radiation often not achievable by conventional leaky-wave antennas. Yet to theoretically predict the performance of developed structures and to promote a straightforward design procedure, an analysis is necessary yielding in particular the eigenvalues and eigensolutions of the structures. A good tool of giving immediate insight into the physical meaning of the eigenvalues is obtained by illustrating the eigenvalues in a so-called dispersion diagram. It distinguishes guided waves from leaky waves and also the attenuation rate of the wave can be added. Therefore, the solution of the dispersion eigenproblems is of main scientific interest in this work.

The eigenvalues and the corresponding eigenmodes reveal the inherent traits of a structure and of any system without any kind of excitation. Once the eigenvalues and eigensolutions are known the determination of the response of a linear system to every arbitrary excitation can be reduced to the projection of the excitation onto the eigensolutions, what is more or less trivial. This solution procedure is yet not often pursued in the field of numerical electromagnetics since the numerical determination of eigensolutions and eigenvalues is often of great computational expense. Instead, the direct solution of the problem with the relevant excitation is mostly more efficient. In particular, since many eigensolutions are needed for a sufficiently accurate description of complicated field problems.

The situation changes if a linear system is operated in a frequency range in which only few eigensolutions are relevant, ideally just one. Resonators for instance mostly work on their lowest resonance and waveguides transfer electromagnetic signals usually in the fundamental mode, for which single operation can be ensured in a certain frequency range. This is for example the TE_{10} (transversal electric) or H_{10} wave for rectangular waveguides or the TEM (transversal electromagnetic) waves or quasi-TEM waves for multi-conductor waveguides. Then, it is necessary to characterise the essential behaviour of the operating mode but also of the neighbouring modes. For resonators, the eigenvalues are the resonance frequencies and the eigensolutions are the corresponding field distributions within the resonator. They need to be known for characterising the resonator with respect to field strength, loss etc. For waveguides, the eigenvalues are pairs of frequencies and propagation constant, e.g. ω and γ, and their relation for a waveguide mode is known as the dispersion relation of the mode. This means that for waveguide problems many eigenvalues and eigensolutions need to be determined namely the complete dispersion relations of all relevant modes in the frequency range of interest.

Waveguiding problems in general require to revert to numerical field computation methods. Nearly every numerical method can possibly be employed for solving eigenproblems. Essential is that the basic discretised operator is regarded without any form of excitation while describing the field problem and by taking into account the boundary conditions. The eigensolutions are hence obtained as null space of the operator. Eigensolutions normally exist only for definite discrete frequencies or discrete pairs of frequency and propagation constant. In another interpretation, eigensolutions are such functions which are not changed except for a multiplicative constant, the eigenvalue, if the corresponding operator is applied to them. In this work, eigensolutions can be regarded in the first form, that is the elements of a null space for an operator which depends on one or two parameters (propagation constant, frequency) or either in the second way because the eigenvector containing the field quantities on one side of a periodic unit cell is mapped by a factor, the phase difference or the transfer matrix, onto the field quantities on the opposite side.

For solving waveguiding or rather dispersion problems, a 2D formulation is used in which an exponential field dependence with a complex propagation constant along the waveguide is assumed. This is exactly the mentioned eigenproblem with an operator, which depends on the two parameters frequency and propagation constant. Examples for numerically solving eigenproblems of the waveguide type are to find in [MZ89],[DP02],[SGG02]. In [MZ89],[DP02], integral solver solutions are pursued whereas in [SGG02], the method of finite elements (FE) is employed. Basic information for solving waveguide problems with the FE method are also contained in [Jin02].

2D formulations of cylindrical waveguides, where material and geometry do not change along the waveguide longitudinal axis, require rather few discretisation unknowns and are relatively easy to solve. The problems become explicitly more difficult to solve if inhomogeneous waveguides are treated. Here, only such waveguides are considered which are composed of cylindrical host waveguides with periodical perturbations. The periodical modifications are used to alter the dispersion behaviour of the waveguide and generate a truly new performance. Such a dispersion engineering is particularly employed in the area of metamaterials [CI06],[EZ06]. The periodic configuration enables a formulation of the corresponding eigenproblem based on the Bloch-Floquet theorem [Col91] that factorises the field solution in a periodic and a non-periodic field part. Wave propagation of the desired eigenmode is expressed by the non-periodic part and is implemented in form of periodic boundary conditions. Numerical solutions of such problems demand the discretisation of an elementary cell, where a 3D problem follows to solve. The numerical description of such problems can fast lead to a great number of unknowns especially in case of metamaterials, which mostly exhibit elaborate material and geometry variation within small dimensions. All numerical eigenproblem solvers, which represent the operator equation in form of a linear equation system, require to solve such a linear equation system. Thus, a problem of linear algebra results. Nowadays, a variety of diverse and potent algebraic procedures already exist but in many cases nevertheless this potential is not enough. Very efficient program packages for the solution of algebraic eigenproblems are indeed even freely available [LSY98]. The most efficient algebraic eigenproblem solvers are the so-called Krylov subspace methods [Saa92], which start with an error vector and continue with building a Krylov subspace by subsequent matrix-vector products. The eigenproblem is formulated as such in the subspace and finally solved. A comprehensive description of the topic is to find in [Saa92]. For many problems, it is often still impossible to find reasonable solutions and then, it is simultaneously not possible even to determine the cause of the failure. This is especially the case for eigenproblems where the dependencies of eigenvalue and frequency are not linear. Then the algebraic solution is not at all satisfying and very tedious. Non-linear dependencies of the parameters are however unavoidable in case of integral equation formulations or other open problems and local numerical procedures with perfectly matched layer (PML) boundary conditions.

In [BSS10], the authors try to sort out the unphysical modes caused by the PML already during the solution process by using a-priori knowledge of the field pattern with the purpose to improve the iterative Jacobi-Davidson algorithm, that is used e.g. in the numerical eigensolver in CST MWS [CST11]. The method seems promising but the studied structures are still simple. They do not contain any metal and are dielectric substrates with air holes.

For these reasons, purely algebraic eigenproblem strategies are not pursued further in this work. Instead procedures are searched which result in a simplification of the algebraic eigenproblem or rather which completely circumvent the solution of an algebraic eigenproblem.

A simplification of the algebraic eigenproblem can be achieved by diminishing the number of needed unknowns. Nevertheless, it is to be kept in mind that the structure of the equation system, namely dense or sparse, plays an important factor with view to the solution behaviour of the eigenproblem. In general, integral equation formulations need

notedly less unknowns than local procedures like finite elements (FE) [Jin02], finite difference (FD) or finite integration technique (FIT), employed in the computer simulation program CST MWS [WTM08],[CST11], but lead to fully populated equation systems.

Other methods, related to integral equation formulations in a certain sense, are Trefftz methods [KW93],[Li07], which construct the solutions of the eigenproblem with particular solutions of the corresponding differential operator in the infinite homogeneous space. In this manner, the description of the problem can be reduced to the boundary and continuity conditions on material and solution domain boundaries, similar to surface integral equations. If one succeeds in formulating the field solution with very few particular solutions an eigenproblem results with very few unknowns. A special form of the Trefftz method is the method of fundamental solutions or method of auxiliary sources, where the particular solutions are created as solutions of sources outside of the solution domain [Kar01]. This procedure is also known from the generalised multipole technique or multiple multipole method [Haf90]. The difficulty of this procedure is yet the "right" choice of fundamental solutions for general problems.

A very efficient formulation of inhomogeneous periodic eigenproblems can be achieved if one arrives at constructing the searched eigensolutions with the eigensolutions of the homogeneous background eigenproblem, the cylindrical waveguide. These are the eigensolutions of the host waveguide in case of periodically modified waveguides as considered in this work. For many cylindrical waveguides such as hollow waveguides and layered structures, the eigensolutions can be given analytically. The concept ideally applies to the periodically loaded substrate integrated waveguides studied in this work. For more complicated background structures, the eigensolutions can be computed by solving 2D eigenproblems numerically. If the periodic boundary conditions of the inhomogeneous problem can be placed in the homogeneous parts of the underlying structure it is possible to develop the fields in the periodic boundaries by the eigensolutions of the homogeneous case. The coupling of the fields at the boundaries can be computed by an adequate numerical field computation method. The algebraic eigenproblem to be solved then just comprises the expansion coefficients for the fields at the boundaries and it is mostly so small that its solution is not a problem at all anymore. The main computation effort is the determination of the coupling coefficients in form of a series of excitation problems, where one homogeneous mode is excited at a time and the coupling onto all other modes is to observe. This procedure is known as scattering (SMA) or transfer matrix approach and is also used in [LBSW09]. In [LBSW09], however, two pairs of perfectly magnetic (PMC) and perfectly electric conducting (PEC) boundary conditions are defined in order to gain a closed parallel-plate configuration with the TEM mode as fundamental mode. Higher order modes are also considered. In this way, a 3D periodic configuration with plane wave incidence is approximated. In [GRB00] a similar procedure is chosen but the homogeneous modes are not only applied at the outer boundaries but also at sectional boundaries within the solution domain. This method becomes critical if no suitable homogeneous waveguide sections can be used or if a great number of homogeneous modes are needed for describing the field problem.

For the closed waveguide problems treated in this work, the solution set is finite and the computation method is very well suited. Only few modes suffice for an accurate solution of eigenvalues because the waveguides are particularly operated in a single mode,

the fundamental mode, to ensure stable working. However, for field problems with open boundaries, an expansion of the fields in modes is difficult because the series expansion is generally to be extended to an integral formulation, i.e. a continuous spectrum of modes, what would be very cumbersome in a numerical implementation.

Nevertheless, the modal series expansion delivers approximate but good results compared to reference data for hollow waveguide based leaky-wave antennas as in section 8.2 [WE10a] because the energy is mainly guided in the waveguide and only a minor part leaks into the surroundings. However, the approximate computation can be improved by a more advanced computation procedure, which will be a core contribution of this work.

The systematic analysis of open dielectric waveguides started with an increasing interest in integrated circuits operated in the millimeter wavelength regime in the 1970ties. The pure analytical solution of the eigenproblem requires comprehensive integral procedures. Marcatili [Mar69] and McLevige et al. [MIM75] analyse dielectric image lines by the effective dielectric constant method which supplies approximate eigenvalues but no complete field distributions. Solbach et al. [SW77] instead present an exact formulation, where the problem is embedded in a closed waveguide. The conversion from the open region problem into a closed problem type has the decisive advantage of being treatable by known means and no demanding integration techniques are required. The problem is further subdivided into subregions and the analytical solution is to derive for each subregion. A successive matching of the boundaries finally delivers the desired results. Since dielectric image lines are considered the guided waves are hardly disturbed by the PEC top shield set in an appropriate distance. Mittra et al. [MHJ80] also transform the original open region problem into an equivalent closed configuration. The fields are expanded into the eigenfunctions of each subregion and the eigenvalues are obtained by mode-matching and further improved by a variational method.

Derudder et al. [DdZO98],[DOdZvdB01] place a perfectly matched layer (PML) in front of the PEC boundary in order to diminish its reflection properties. They get the eigenvalue solution of the host waveguide analytically and employ the mode-matching technique to solve inhomogeneous waveguide problems. The accuracy is enhanced compared to [SW77],[MHJ80] while less modes are needed in the expansion. Bérenger developed the concept of the PML [Ber94] to truncate finite-difference time-domain lattices in 1994. Later, the finite-element technique adopts the PML [WKLL02] and shows that it can be interpreted as an anisotropic simultaneously lossy and active layer. In [DdZO98],[DOdZvdB01], the original open waveguide is treated as closed configuration but by preserving the properties of the original open waveguide. The continuous eigenspectrum of the open region is transformed into a discrete set of substrate, evanescent and so-called PML modes of the equivalent closed waveguide and can be handled by a series expansion instead of a complicated integral procedure. The drawback of this procedure is that it requires to find the analytical field solutions of every subregion and it is therefore constrained in its application range. A purely numerical approach to find the eigenmodes of the host waveguides would be plagued by the strange material composition of the PML, active and anisotropic.

In this work, the idea from [DdZO98],[DOdZvdB01] is adopted and upgraded that it becomes more practical. The open problem is closed by a PEC shield but an isotropic lossy absorber is employed to suppress the reflections of the shield. The cylindrical background waveguide modes used for the series expansion can thus be easily computed and

the series expansion concept with background waveguide modes can be used as discussed
before but now for open problems [WE11]. The result is a very reduced eigenproblem
which is easily solvable. The solution procedure perfectly functions for waveguide prob-
lems but would be inefficient for problems tackled in [LBSW09] or [SLW05]. For field
problems where no homogeneous waveguide regions can be found or if a large number
of waveguide modes is required to describe the field problem, the expansion in modes
becomes difficult. Then, a direct frequency-dependent excitation is to prefer, where the
reaction of the system to the excitation is observed. From the course of the response
of the system, the resonance frequency can be determined. This procedure is pursued
in [EW10],[EWC11] employing the FEBI technique [EW06], where analogies to electric
circuits, resonators and to measurement techniques are utilised and which aims to solve
periodic problems in two or three dimensions. The eigenvalues and eigensolutions are de-
rived from the reaction of the system to the response. Similar approaches are pursued in
[Reu07],[Reu08],[Reu09],[Reu10], where problems from mechanics [Reu07], homogeneous
waveguide problems [Reu08], Laplace problems [Reu09], [FYC09], and general Sturm-
Liouville problems [Reu10] are treated. The technique is yet not further explained in this
work since this work focuses on waveguiding architectures, where the modal expansion is
well suited.

The work is structured as follows: Chapter 3 provides the knowledge about state-of-the-
art metamaterials and reports about the performance of conventional leaky-wave antennas
to understand the benefits of metamaterial-based leaky-wave antennas as realised later.
Chapter 4 explains the modal series expansion procedure which is conceived to compute
the class of periodically composed metamaterial waveguides. The basis functions in the
modal series expansion are supplied by the eigensolutions of the cylindrical host waveg-
uides which are derived from Maxwell's equations in chapter 5. The left-handed properties
created by the periodicities in the waveguides often refer to the frequency domain where
formerly no wave propagation has taken place. Therefore, as the series expansion is based
on effective wave contributions in form of energy, it is proven that the proposed computa-
tion concept is valid even in the evanescent frequency domain. Not only closed waveguides
are treated but equally open ones. Chapter 6 explains the difficulties in evaluating open
region problems. Section 6.2 presents a strategy to circumvent the complex computation
procedure. By a tricky conversion, the actual integral-demanding open problems can
fully and accurately be computed by a modal series expansion. The following chapters
concentrate on metamaterial realisations and evaluation of the modal series expansion
technique. It is tested on a waveguide found in literature [EKYG05],[EK06] in section 7.1
and on a realised closed waveguide implemented in SIW technology in section 7.2 but the
fabrication process is simplified tremendously by planar printed circuit technology. Fur-
thermore, leaky-wave antennas are computed being implemented by double-layer printed
circuit technology in section 8.1 and even simpler by single-layer printed circuit technol-
ogy in section 8.2. The last realised travelling wave antenna in section 8.3 is based on
a grounded dielectric slab, which represents the inherently open kind of waveguide and
there, the modal series expansion method computes efficiently the problem which actually
requires complicated integration. In the appendix 9, the singular value decomposition is
likened to the eigenvalue decomposition of matrices and the term pseudoinverse is ex-
plained. The matrix pencil method is also explained which provides reference data for
the computed eigenvalues.

3 Metamaterials

3.1 Maxwell's Equations and Material Properties

The fundamental differential equations of electromagnetic theory are Maxwell's equations (MWEs) and were formulated by Maxwell in 1865 [Max92]:

$$\nabla \times \boldsymbol{H}\left(\boldsymbol{r}\right) = \mathrm{j}\omega\boldsymbol{D}\left(\boldsymbol{r}\right) + \boldsymbol{J}\left(\boldsymbol{r}\right), \tag{3.1}$$

$$\nabla \times \boldsymbol{E}\left(\boldsymbol{r}\right) = -\mathrm{j}\omega\boldsymbol{B}\left(\boldsymbol{r}\right) - \boldsymbol{M}\left(\boldsymbol{r}\right), \tag{3.2}$$

$$\nabla \cdot \boldsymbol{D}\left(\boldsymbol{r}\right) = \rho\left(\boldsymbol{r}\right), \tag{3.3}$$

$$\nabla \cdot \boldsymbol{B}\left(\boldsymbol{r}\right) = \rho_m\left(\boldsymbol{r}\right). \tag{3.4}$$

They completely describe the generation of electric and magnetic fields in a closed form by charges and currents as well as the interaction between the two fields. All field quantities are assumed to vary in time according to the complex exponential function $\mathrm{e}^{\mathrm{j}\omega t}$ and are location-dependent, i.e. $\boldsymbol{E} = \boldsymbol{E}\left(\boldsymbol{r}\right)$. Maxwell's equations only are not sufficient. They need to be complemented by the material relations which are in an isotropic linear medium

$$\boldsymbol{D}\left(\boldsymbol{r}\right) = \varepsilon\boldsymbol{E}\left(\boldsymbol{r}\right) = \varepsilon_r\varepsilon_0\boldsymbol{E}\left(\boldsymbol{r}\right), \tag{3.5}$$

$$\boldsymbol{J}\left(\boldsymbol{r}\right) = \sigma\boldsymbol{E}\left(\boldsymbol{r}\right) + \boldsymbol{J}_{\mathrm{exc}}\left(\boldsymbol{r}\right), \tag{3.6}$$

$$\boldsymbol{B}\left(\boldsymbol{r}\right) = \mu\boldsymbol{H}\left(\boldsymbol{r}\right) = \mu_r\mu_0\boldsymbol{H}\left(\boldsymbol{r}\right), \tag{3.7}$$

where $\boldsymbol{J}_{\mathrm{exc}}\left(\boldsymbol{r}\right)$ is assumed as impressed. The material parameters ε_r and μ_r are direction-independent since isotropic media are assumed but they may depend on location. In the anisotropic case, the material parameters would be tensors instead of scalar quantities. The material parameters can also become complex to account for losses in materials. The conductivity of a material can be described by the imaginary part of ε_r according to

$$\mathrm{j}\omega\varepsilon_r\varepsilon_0\boldsymbol{E}\left(\boldsymbol{r}\right) + \kappa\boldsymbol{E}\left(\boldsymbol{r}\right) = \mathrm{j}\omega\varepsilon_0 \underbrace{\left(\varepsilon_r - \mathrm{j}\frac{\sigma}{\omega\varepsilon_0}\right)}_{\varepsilon_r' - \mathrm{j}\varepsilon_r''}\boldsymbol{E}\left(\boldsymbol{r}\right). \tag{3.8}$$

Common natural materials have $\varepsilon_r' > 1$, $\mu_r' > 1$ and $\varepsilon_r'' > 0$, $\mu_r'' > 0$. $\varepsilon_r'' < 0$ or $\mu_r'' < 0$ denote active materials. For classification, media can be sorted in a diagram such as in Fig. 3.1, in which only the real part is considered. Media with a negative ε_r' are to find as electric plasma or as metals at optical frequencies. A negative μ_r' is exhibited by ferrimagnetic materials. In both cases, waves cannot propagate. To date, no combination of negative ε_r' and negative μ_r' is known to exist in nature. The properties of the material parameters are yet to expand since in 1967, a material with negative refractive index has been derived theoretically by Victor Veselago [Ves68]. The history of metamaterials began. A simultaneous negative permeability and negative permittivity demand to revise physical laws. The characteristics of metamaterials are demonstrated with MWEs in
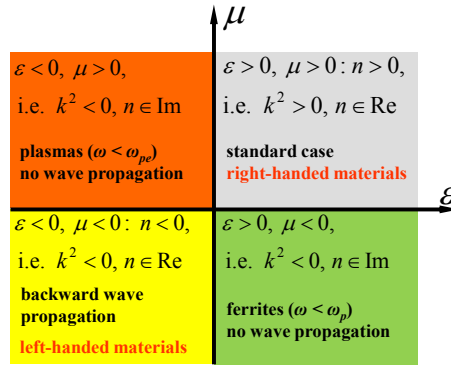
Figure 3.1: The diagram of permittivity-permeability combinations.

simplified form, considered for plane waves $\mathrm{e}^{-\mathrm{j}(\boldsymbol{k}\cdot\boldsymbol{r}-\omega t)}$ without sources, since any other wave can be expressed by a superposition of plane waves. Inserting $\boldsymbol{E} = \boldsymbol{E}_0\mathrm{e}^{-\mathrm{j}(\boldsymbol{k}\cdot\boldsymbol{r}-\omega t)}$ and $\boldsymbol{H} = \boldsymbol{H}_0\mathrm{e}^{-\mathrm{j}(\boldsymbol{k}\cdot\boldsymbol{r}-\omega t)}$ into Eqs. (3.1)-(3.7) without excitation, results in (μ_r, ε_r assumed to be real)

<table>
<tr><td align="center">RH case</td><td align="center">LH case</td></tr>
</table>

$$-\mathrm{j}\boldsymbol{k} \times \boldsymbol{E}\left(\boldsymbol{r}\right) = -\omega\mu_0|\mu_r|\boldsymbol{H}\left(\boldsymbol{r}\right) \quad (3.9) \qquad -\mathrm{j}\boldsymbol{k} \times \boldsymbol{E}\left(\boldsymbol{r}\right) = \omega\mu_0|\mu_r|\boldsymbol{H}\left(\boldsymbol{r}\right) \quad (3.11)$$

$$-\mathrm{j}\boldsymbol{k} \times \boldsymbol{H}\left(\boldsymbol{r}\right) = \omega\varepsilon_0|\varepsilon_r|\boldsymbol{E}\left(\boldsymbol{r}\right) \quad (3.10) \qquad -\mathrm{j}\boldsymbol{k} \times \boldsymbol{H}\left(\boldsymbol{r}\right) = -\omega\varepsilon_0|\varepsilon_r|\boldsymbol{E}\left(\boldsymbol{r}\right). \quad (3.12)$$

By comparing the RH case with the LH case we observe that $-\mathrm{j}\boldsymbol{k} \times \boldsymbol{E}\left(\boldsymbol{r}\right)$ and $-\mathrm{j}\boldsymbol{k} \times \boldsymbol{H}\left(\boldsymbol{r}\right)$ point in opposing directions in the LH event. The Poynting vector, however, maintains its direction. The wavenumber k in a LH medium is negative such that phase and group velocities become anti-parallel. Since $k < 0$, the refractive index is negative in a LH medium. In the RH case, the electric field, the magnetic field and the wave vector compose a right-handed triad, which is anticlockwise or left-oriented in the LH case. To build the triad, one now needs the left hand, which also reasons the origin of the name. Consequently, physical laws as e.g. Snellius law are to upgrade. The speciality of LH refractive behaviour was later theoretically utilised in a perfect lens by Pendry [Pen00]. Due to the LH mechanism, originally evanescent waves are reinforced and waves are reconstructed at the location of the focus. Thus, the traditional resolution limit can theoretically be broken.

In theory, the LH material has already been deduced in 1967 whereas a practical implementation was difficult and required a long time to be accomplished. The breakthrough of man-made realisation was achieved by Smith et al. [SPV$^+$00] in 2000. The group of physicists implemented an artificial effectively homogeneous structure consisting of a particularly designed microstructure, where the wave does not resolve the constituents. The material is composed of split-ring resonators (SRRs) and metal wires, as pictured in Fig. 3.2. The behaviour of the structure can be described in terms of an equivalent electric circuit. The electric field of an incident wave is parallel to the wire grid generating a current in the wires such that the magnetic field encircles the wires and a shunt left-handed inductance L_L is caused. The inductance may lead to an effective negative permittivity. The SRRs can be modeled by a series capacitance C_L and an inductor L_p in
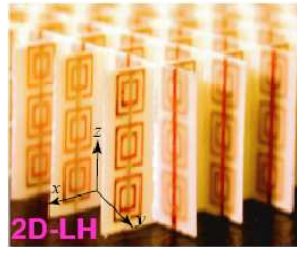
Figure 3.2: Split-ring resonators and metal wires [SPV+00].

parallel to C_L. The magnetic field of the incident wave stands perpendicular on the SRR plane and interacts with the resonator such that it changes the permeability. The free space in between can be described by the natural right-handed elements L_R in series and C_R in shunt. The corresponding simplified equivalent circuit is shown in Fig. 3.3. The left-handed effect of equally negative permittivity and permeability can also be described by a combined Lorentz/Drude dispersion model [Lor16] and [Dru00] in physical terms. The negative permeability only occurs if the SRRs are near to resonance and therefore merely for a small bandwidth. The combination of both negative quantities may lead to a negative refractive index with $n = -\sqrt{\varepsilon_r \mu_r}$. The SRR composition performs a magnetic response despite no magnetically conducting material is included. The fact contributes to the definition of metamaterials which are the materials after (=meta in Greek) the materials. They represent distinguished properties other than the materials they are composed of. The SRRs work on resonances and are therefore strongly dependent on frequency. Yet, they can be regarded as effectively homogeneous meaning the dimensions p of their constituents are $p << \lambda_g$, with λ_g as the wavelength of the guided wave in the structure. Therefore the electromagnetic wave only "feels" the macroscopic nature of the structure and not the characteristics of the constituents. Atoms of a material are comparable, which are not visible either.

Another realisation of metamaterials is offered by photonic crystals (PCs), of which the mechanism is demonstrated in Fig. 3.4. They are operated in the frequency range where the lattice period p is about a multiple of half a guided wavelength λ_g, $p \approx \lambda_g/2$. This is in the Bragg regime where interferences take place. The wave notices the lattice and a periodic setup is substantial. In contrast, effectively homogeneous compositions dominate the long wave domain and no interference effects appear. The internal architecture does not require periodicity for working. Here, periodicity is mainly employed to facilitate anal-
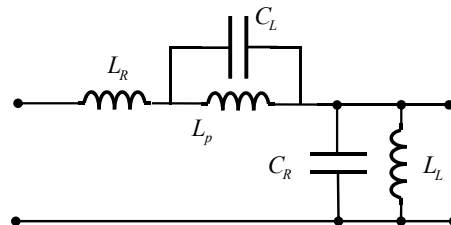
Figure 3.3: The equivalent circuit represents the left-handed effects due to the SRRs and the metal wires.
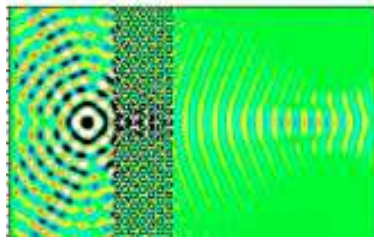
Figure 3.4: Photonic crystals mimic a negative refractive index and a flat lens enables focusing [GAA$^+$04].

ysis and fabrication. Effectively homogeneous materials exhibit refraction whereas PCs feature scattering and diffraction. Nevertheless, it has been achieved to realise negative refractive effects with photonic crystals [GAA$^+$04] and [Not00].

In microwave engineering, according to the size of the components lumped components with maximum $p < \lambda_g/4$, quasi-lumped in the order of $(\lambda_g/4 < p < \lambda_g/2)$ and distributed components $(p > \lambda_g/2)$ are to distinguish. The difference is whether the phase variation of the signal from the input to the output of the component is negligible or not. In the distributed case, the wave character must be considered.

A rough overview has been given in this section to imagine a metamaterial and its implementational possibilities. Literature, e.g. [CI06], provides further details. Many realisations include microstrip technology and others which guide and function with TEM waves. In this work, the aim is not to restrict to a special guiding type but to expand the scope of transmission lines. The novel functionalities enabled by metamaterials can furthermore reform electromagnetic devices such as antennas. This becomes especially obvious with view to the leaky-wave type, which is focused on in this work. To understand the benefits of metamaterial based leaky-wave antennas, the class of conventional leaky-wave antennas and their performance is presented in section 3.4. First, the characteristics of metamaterials are explained by means of transmission-line theory.

3.2 Combined Right/Left-Handed Transmission Lines

Resonant-type LH architectures like SRRs have the drawback of being bandwidth-limited and lossy. By analogy of backward waves and LH waves, a transmission line (TL) approach was published in 2002 by three goups: Eleftheriades et al. [IE02],[GE02], Oliner [Oli02] and Caloz et al. [CI02],[COII02] almost at the same time. The advantage of metamaterial TLs is that they can be engineered in planar configurations integrable in microwave integrated circuits and planar printed circuit boards (PCBs). The TL theory is well-established and promotes an efficient design of microwave applications. Yet, as a pure realisation of left-handedness is not possible the combined RH-/LH TL forges ahead, which is visualised in Fig. 3.5. The RH elements represent the natural physical effects caused by currents flowing in the metallisations inducing magnetic flux proportional to the inductance $L'_R \Delta z$ and by voltage gradients between upper and lower metallisations contributing to the shunt capacitance $C'_R \Delta z$. The EQC of the RH TL is pictured in Fig. 3.6a. At low frequencies, the RH elements with the inductance in series and the capacitance in shunt tend to be short and open, respectively, so that the EQC is reduced to the LH elements $(1/C_L)' \Delta z$ and $(1/L_L)' \Delta z$ in Fig. 3.6b. They are dual to the RH elements. In the LH band, backward wave propagation occurs, while the energy still maintains its transfer direction like in the RH case. Phase and group velocities are therefore anti-parallel. At high frequencies, the CRLH EQC is dominated by the RH components as in Fig. 3.6a. It is the conventional and known RH TL, where the wave propagates in the same direction as the energy does.
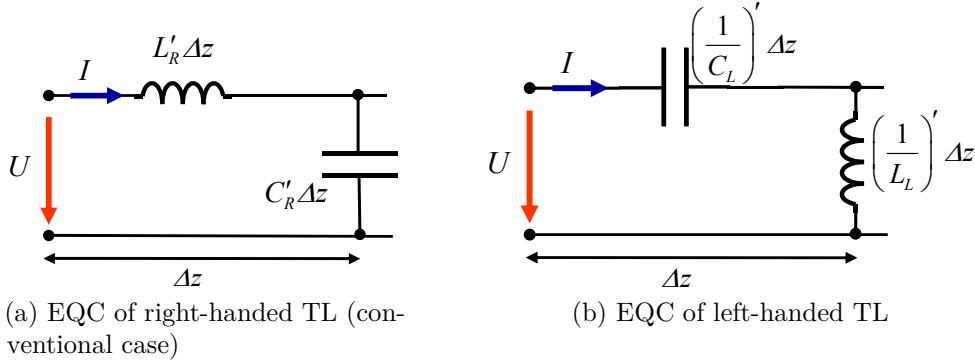
The transmission-line equations for the RH case are well-known. For the CRLH TL the EQC of the RH TL in Fig. 3.6a and the EQC of the LH TL in Fig. 3.6b are to combine and the result is depicted in Fig. 3.5. A transmission line is assumed to consist of a cascade of sections with length Δz. For vanishing Δz, the line is uniform with per-unit-length impedance $Z' = \mathrm{j}\omega L'_R - \frac{\mathrm{j}}{\omega C'_L}$ and per-unit-length admittance $Y' = \mathrm{j}\omega C'_R - \frac{\mathrm{j}}{\omega L'_L}$. In order to simplify notation, for instance $\left(\frac{1}{C_L}\right)'$ is written in short $\left(\frac{1}{C_L}\right)$. Losses are not considered. Applying Kirchoff's current and voltage laws [Har01] for vanishing $\Delta z \to 0$, the transmission line differential equations

$$\frac{-dU}{dz} = \left(\mathrm{j}\omega L'_R - \frac{\mathrm{j}}{\omega C'_L} \right) I, \tag{3.13}$$

$$\frac{-dI}{dz} = \left(\mathrm{j}\omega C'_R - \frac{\mathrm{j}}{\omega L'_L} \right) U \tag{3.14}$$
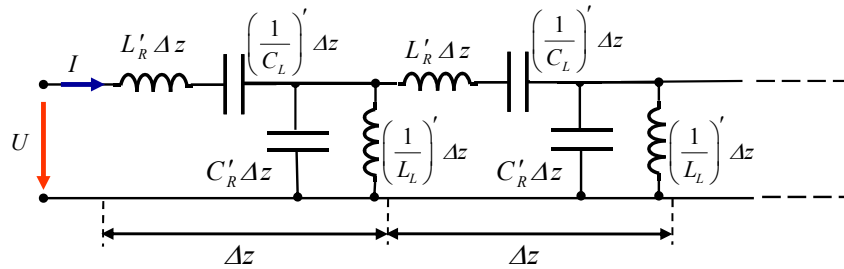
Figure 3.5: The equivalent circuit of a CRLH transmission line.

(a) EQC of right-handed TL (conventional case)

(b) EQC of left-handed TL

Figure 3.6: Lumped-circuit model of the RH TL and the LH TL respectively.

are obtained. Decoupling both equations yields

$$\gamma^2 U - Z'Y'U = 0, \tag{3.15}$$

by considering forward wave progress with $U = U_f e^{-\gamma z}$ in z-direction. The equivalent gives the equation for the current

$$\gamma^2 I - Z'Y'I = 0 \tag{3.16}$$

with $I = I_f e^{-\gamma z}$. Eqs. (3.15) and (3.16) correspond to one-dimensional Helmholtz equations. From both equations, the complex propagation constant γ can be determined as

$$\gamma = \alpha + \mathrm{j}\beta = \sqrt{Z'Y'}. \tag{3.17}$$

The phase constant is the imaginary part of γ given as

$$\beta = \sqrt{\left(\omega L'_R - \frac{1}{\omega C'_L}\right)\left(\omega C'_R - \frac{1}{\omega L'_L}\right)} \tag{3.18}$$

and becomes real for $\left(\omega L'_R - \frac{1}{\omega C'_L}\right)\left(\omega C'_R - \frac{1}{\omega L'_L}\right) > 0$. α is in this case zero but a radicand smaller than zero would yield $\alpha \neq 0$ and $\beta = 0$. The complex propagation constant is the characteristic quantity of the solution mode denoted as eigenvalue. It depends on the angular frequency ω and on the transmission line quantities. In Figs. 3.7a and 3.7b the dispersion relation for β is plotted revealing where pairs of ω and β yield a solution set to the eigenvalue problem. The phase constant in Eq. (3.18) can be purely real and a passband emerges for the frequency range since $\gamma = \mathrm{j}\beta$. For the frequencies for which β is purely imaginary, it can be treated as $\gamma = \alpha$ and a stop band arises, where no wave propagation occurs. The sign is to maintain according to the reference wave direction. Only the CRLH TL shows a stop band but not the pure RH or LH TL. No energy is transported in the so-called bandgap that is illustrated in Fig. 3.7a. In contrast in Fig. 3.7b, the dispersion graph of a so-called balanced structure [CI06] is not interrupted. Precondition is the relation $L'_R C'_L = C'_R L'_L$ resulting in an identical resonant frequency of the shunt ω_{sh} and the series circuit ω_s

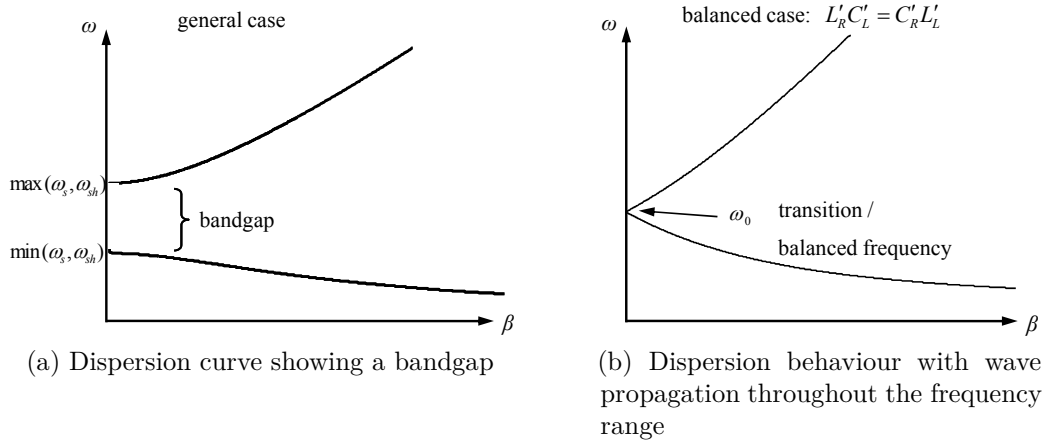$$\omega_s = \omega_{sh}. \tag{3.19}$$

The balanced frequency follows with

$$\omega_0 = \sqrt[4]{\frac{1}{C_R' L_R' C_L' L_L'}} = \sqrt{\omega_{sh}\omega_s} \tag{3.20}$$

meaning a smooth transition from the LH frequency band to the RH band corresponding to continuous wave propagation. With (3.19), the expression for the phase constant simplifies to

$$\beta = \omega\sqrt{C_R' L_R'} - \frac{1}{\omega\sqrt{L_L' C_L'}}. \tag{3.21}$$

It becomes evident that the first part described by the RH elements dominates the higher frequency range and the second part composed of the LH elements governs the lower frequency range.

At the transition point, the set ω_0, $\beta = 0$ induces particular performance for electromagnetic devices. For a leaky-wave antenna, radiation in broadside direction occurs, which is not easily achievable by conventional LWAs *cf.* section 3.4. In addition, it follows from $\beta = 0$ the wavelength as $\lambda = \frac{2\pi}{\beta} \to \infty$, such that the field is evenly distributed along the structure, whereas the group velocity is $v_g = (\frac{d\beta}{d\omega})^{-1} \neq 0$.

(a) Dispersion curve showing a bandgap

(b) Dispersion behaviour with wave propagation throughout the frequency range

Figure 3.7: The phase constant visualised in a dispersion diagram.

By dividing the differential equations Eqs. (3.13) and (3.14) and substituting γ, the characteristic impedance of the transmission line

$$Z_c = \sqrt{\frac{Z'}{Y'}} \tag{3.22}$$

is determined. With the terms above and the impedance due to the LH elements $Z_L = \sqrt{\frac{L_L'}{C_L'}}$ it is

$$Z_c = Z_L \sqrt{\frac{\left(\frac{\omega}{\omega_s}\right)^2 - 1}{\left(\frac{\omega}{\omega_{sh}}\right)^2 - 1}}. \tag{3.23}$$

The homogeneous CRLH TL with $\Delta z \to 0$ does not exist in nature, but CRLH TL with finite Δz can often be assumed to be effectively homogeneous in certain frequency ranges. The electromagnetic wave does not "see" a perturbed structure what happens in the frequency range where the wavelength is much larger than the inhomogeneities. The model in Fig. 3.5 has an infinitesimal physical length Δz [m] $\to 0$ whereas in Fig. 3.8, the phase along the unit cell in symmetric realisation is represented in terms of its electrical length $\beta p = \Delta\phi$ [rad]. A physical length p is eventually ascribed to a practical implementation. In particular, p refers to the length of one period in a periodical arrangement. In the limit $p = \Delta z \to 0$, the unit cell of Fig. 3.8 is identical with the continuous model. In practice, the LC-based CRLH TL is regarded as effectively homogeneous for waves if the dimension of the unit cell is considerably smaller than the guided wavelength, $p < \lambda_g/4$ at least and the electrical length of the unit cell is smaller than $\pi/2$.

The structures considered within this work are periodically constructed architectures. For their analysis, periodic boundary conditions can be applied to one cell of the periodic network, and it suffices to find the solution for one preferably symmetric unit cell of the CRLH TL depicted in Fig. 3.8 in reference to the Bloch-Floquet theorem *cf.* section 3.3. V_n and I_n are the total voltage and current amplitudes, i.e. the sum of the contributions from the incident and reflected waves at the terminal plane n. The voltage and current at the $(n+1)^{\text{th}}$ terminal plane are identical with the voltage and current at the previous terminal apart from a propagation factor. The system in between the two terminals or ports can be represented by an $ABCD$-matrix, hence it is

$$\begin{pmatrix} V_n \\ I_n \end{pmatrix} = e^{\gamma p} \begin{pmatrix} V_{n+1} \\ I_{n+1} \end{pmatrix} = \begin{pmatrix} A & B \\ C & D \end{pmatrix} \begin{pmatrix} V_{n+1} \\ I_{n+1} \end{pmatrix} \tag{3.24}$$

or

$$\begin{pmatrix} A - e^{\gamma p} & B \\ C & D - e^{\gamma p} \end{pmatrix} \begin{pmatrix} V_{n+1} \\ I_{n+1} \end{pmatrix} = 0, \tag{3.25}$$

from which an matrix eigenvalue equation arises for γ. For the symmetric unit cell of the CRLH TL the $ABCD$-matrix is

$$\begin{pmatrix} A & B \\ C & D \end{pmatrix} = \begin{pmatrix} 1 + \frac{ZY}{2} & Z\left(1 + \frac{ZY}{2}\right) \\ Y & 1 + \frac{ZY}{2} \end{pmatrix}, \tag{3.26}$$

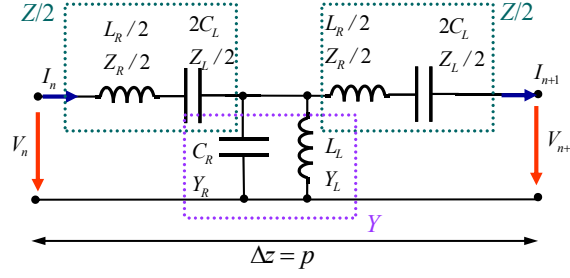and it renders the phase constant as imaginary part of γ

$$\beta = \frac{1}{p}\cos^{-1}\left(1 + \frac{ZY}{2}\right) \tag{3.27}$$

as nontrivial solution from the zero determinant. The procedure is well described in [Col00] and [CI06] for instance. Eq. (3.27) simplifies to

$$\cos(\beta p) \approx 1 - \frac{(\beta p)^2}{2} = 1 + \frac{ZY}{2} \tag{3.28}$$

by using a Taylor series approximation, which is permissible for an electrically small length $|\beta p| = |\Delta\phi| << 1$. In the general case, β is then

$$\beta = \sqrt{\left(\omega L_R - \frac{1}{\omega C_L}\right)\left(\omega C_R - \frac{1}{\omega L_L}\right)}, \tag{3.29}$$

Figure 3.8: The CRLH transmission line and its immitances.

which is identical to Eq. (3.18).

The waves, which progress in periodic compositions, are called Bloch waves. Together with γ or β, the Bloch impedance Z_B is referred to as characteristic quantity of them. Like any other impedance quantity, Z_B is defined by a voltage-current relationship, which is at the terminal plane $(n+1)$ given as

$$Z_B^{f,b} = \frac{V_{n+1}^{f,b}}{I_{n+1}^{f,b}} = \frac{2B}{D - A \pm \sqrt{(A+D)^2 - 4}}, \tag{3.30}$$

derived from Eq. (3.25) and by the exploitation of further relations [Col00]. The upper and the lower signs refer to wave propagation in forward and backward direction, respectively, provided that only one forward or one backward wave is regarded. The voltage-current ratio is constant at the terminals of any unit cell in the TL. In case of the unit cell $(Z/2 - Y - Z/2)$, the Bloch impedance takes the form

$$Z_B = \frac{\sqrt{(ZY/2)^2 + ZY}}{Y}. \tag{3.31}$$

In general, the Bloch impedance is a complex quantity. Since the real part of Z_B corresponds to real power flow Z_B is commonly defined according to power flow considerations. As the direction of power transfer is identical in the conventional right-handed case as well as in the novel left-handed event, the sign of the real part of Z_B is therefore equal as well. In the bandgap, reactive power is present and Z_B appears as imaginary number. If power is complex, Z_B also arises as complex number.

The Bloch impedance is identical within a terminal plane in periodic repetition. The location of a terminal plane can be set arbitrarily within one period and the Bloch impedance varies within the period. The characteristic impedance of a homogeneous waveguide may differ from the characteristic impedance of a periodically composed waveguide. In the homogeneity limit $p \to 0$, $Z, Y \to 0$ and the Bloch impedance in Eq. (3.31) for the periodical network reduces to the characteristic impedance Z_c of the homogeneous guide [CI06]:

$$\lim_{p \to 0} Z_B = \lim_{p \to 0} \sqrt{\frac{Z}{Y}} = \sqrt{\frac{Z'}{Y'}} = Z_c. \tag{3.32}$$

Similarly, it is $Z_B = Z_c$ for the balanced case, where $Z_L = \sqrt{\frac{L'_L}{C'_L}} = Z_R = \sqrt{\frac{L'_R}{C'_R}}$, since $\omega_{se} = \omega_s$ (cf. Eq. (3.23)) suppressing resonance effects and the characteristic impedance

becomes a frequency-independent quantity [CI06] providing matching over a wide bandwidth.

With the practical realisation and a finite electrical length, a stop band emerges which limits the LH band with highpass character in the lower frequency range and the lowpass-like RH band at higher frequencies *cf.* Fig. 3.9. The combination eventually features bandpass behaviour with ω_L as lower limiting frequency and with ω_R as upper bound to the consecutive stop band because $|\cos(\beta p)| \leq 1$. These frequencies deliver estimate values for practical designs. Although having spoken of a filter-like behaviour metamaterials rather influence the phase than the magnitude of signals. However, an approach to design a balanced CRLH TL from a Chebyshev filter due to their similarity is suggested in [LM07].
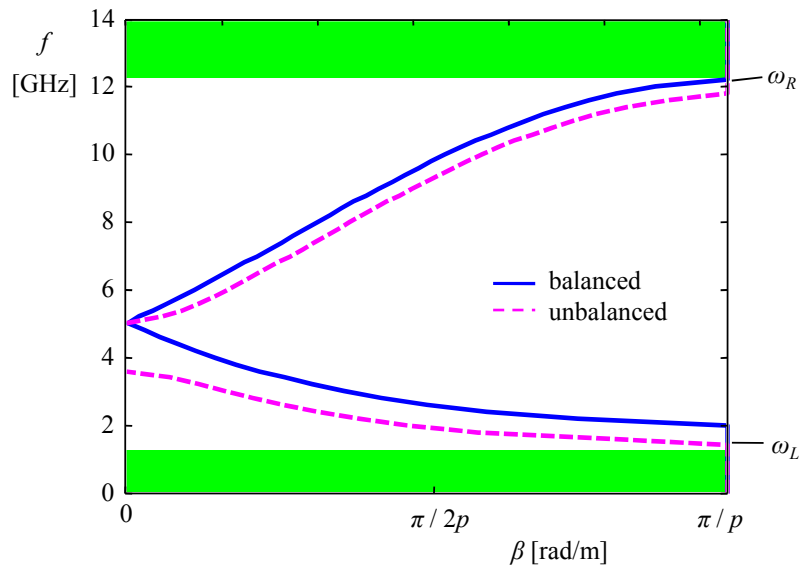
Figure 3.9: Dispersion diagram for the balanced and unbalanced CRLH TL for a finite length. Balanced: $L_R = L_L = 1$ nH, $C_R = C_L = 1$ pF; unbalanced: $C_L = 2$ pF.

In this section, the waves on a transmission line have been explained, namely first for continuous TLs with an infinitesimal unit cell and secondly for TLs with finite length unit cells in view of practical implementations. LC-based unit cells can be restored to the homogeneous state in the limit. The consecutive simplifications deliver conveniently good first approximations. The transmission line model is always described via voltage and current. The transmission line is typically realised in form of a TEM waveguide, if this one is operated in its fundamental mode, the TEM wave with zero cut-off. On a TEM waveguide, higher-order modes may also exist. On non-TEM waveguides like rectangular hollow waveguides or dielectric waveguides, the lowest mode often exhibits a nonzero cut-off frequency. For determining the characteristic quantities of arbitrary waveguides, it is necessary to turn to a formulation by fields. For this purpose, various guiding architectures and the associated waves are investigated, let it be RH waves, LH waves and also several modes on one guide. The procedure is the following. For understanding waveguides in general, the knowledge of modes on a homogeneous background material is provided first

cf. chapter 5. The well-known waveguide theory is treated for hollow waveguides in especially to cover the case of a closed region with a finite set of propagating modes and an infinite series of evanescent waves. Thereafter, discontinuities are introduced and the behaviour of the resulting modes is examined. LH waves are generated in this fashion. By this strategy, leaky-wave antennas are analysed and constructed as well. The modelling gives a good approximation of the performance. As open waveguiding prototype, the dielectric slab is studied on which again a finite set of propagating modes is promoted as well as an infinite set of evanescent modes.

Contrary to the closed cross section, these modes are, however, not sufficient to describe the waves on the corresponding periodically loaded metamaterial waveguides. In order to achieve a complete representation of the fields, an integral over the continuous spectrum of waves which are not bound to the homogeneous waveguide must be added.

3.3 Bloch-Floquet Theorem

Since a formulation by fields is recommended, an adequate suitable analysis method is shown for fields in periodic configurations. Metamaterials are usually implemented periodically. Periodic structures, meaning periodic along the propagation direction e.g. along z in a Cartesian coordinate system, allow the application of Bloch-Floquet's theorem [Col91] stating that the field solution is the product of a periodic function and a non-periodic term, the propagation term, according to

$$\begin{Bmatrix} \boldsymbol{E}(z) \\ \boldsymbol{H}(z) \end{Bmatrix} = \begin{Bmatrix} \boldsymbol{E}_p(z) \\ \boldsymbol{H}_p(z) \end{Bmatrix} \mathrm{e}^{-\gamma z}, \ \begin{Bmatrix} \boldsymbol{E}_p(z) \\ \boldsymbol{H}_p(z) \end{Bmatrix} = \begin{Bmatrix} \boldsymbol{E}_p(z+p) \\ \boldsymbol{H}_p(z+p) \end{Bmatrix}, \tag{3.33}$$

in which p denotes the length of a period and γ the complex propagation constant. Thus, by knowing the solution at one plane at z_0 in the structure, the solution at any plane in the periodic array can be derived. With the periodic loading the traits are repeated periodically as well.

Although the analysis of the periodic cell array can be broken down to only one unit cell the analytical solution of a complex unit cell is often complicated till impossible to compute. This truly applies to metamaterials, where material and geometry compositions vary fast within small dimensions. The complexity and the extent of the analysis are described in chapter 4.

3.4 Leaky-Wave Antennas

In the last section of this chapter, which presents the state-of-the-art related to this work, leaky-wave antennas are examined. They represent an important antenna type, which is supposed to demonstrate the peculiarities of metamaterials. The class of leaky-wave antennas can further be subdivided into subtypes as uniform and periodic. A good overview of leaky-wave antenna classes is provided in [OJ07] and [GTRQP+06]. In fact, metamaterials do not need to be periodic but are nevertheless mostly constructed periodically for simplification reasons. Since they operate in the sub wavelength regime they can be

regarded as homogeneous in the macroscopic view. Yet before turning to leaky-wave antennas based on metamaterials, the knowledge of the working and the performance of traditional leaky-wave antennas is to convey not only to understand the improvements enabled by metamaterials.

A leaky-wave antenna belongs to the travelling wave type of antennas and guides a wave along its structure while permitting the wave to radiate power into the surroundings. Due to the leakage, the propagation constant γ is complex with an imaginary part as phase constant β and a real part, the attenuation constant α. A large α means that the power leaked away per unit length is big, which ends up in a short effective aperture length and a large beamwidth. A small value of α leads to a large effective aperture provided the physical length is sufficiently long. A long effective aperture in turn is known for a high gain and a narrow beam. The fixed aperture primarily decides about the beamwidth whereas the value of α strongly affects the efficiency of radiation. 90 percent of the power should be leaked away while the mode propagates along the structure in order to yield a proper radiation efficiency. A larger leakage rate would result in a strongly increased α at the end of the antenna in order to have useful radiation contributions from these parts of the aperture. The remaining power at the end should be absorbed by a matched load to avoid the appearance of backlobes. Generally, the beam direction varies with frequency like the phase constant such that scanning is acquired by changing the frequency. Thus, no additional phase shifters are required. Leaky-wave antennas are mainly conformal with a low profile that makes them easy to integrate into other devices or applications. The early leaky-wave antennas are based on closed waveguides, which are "opened" by a cut to let radiation take place. They were followed by already open waveguides operating in the millimeter wave range, some of them are dielectric waveguides, groove guides, microstrip lines etc. Nevertheless, the fundamental modes on the open waveguides are typically bound meaning that no radiation occurs not even by inserting a slot. Instead, introducing asymmetry or modifying the geometry are examples of measures to achieve radiation.

3.4.1 Overview of Leaky-Wave Antenna Types

The uniform type of leaky-wave antennas reveals a uniform geometry along the length of the guiding architecture. Its operation mode is fast and therefore radiates. However, radiation is limited to the forward quadrant. If the antenna is strictly uniform the side lobe level is considerably high. The drawback can be improved by tapering the geometry which controls the amplitude of the aperture distribution. The difficult task is to modify α slightly while keeping β constant along the antenna length to maintain constructive interference in the desired radiation direction. This fact also applies to the periodic type.

The uniform type can be further subdivided as reported in [OJ07] dependent on whether it is air-filled or partially dielectric filled. For the two-material leaky-wave antenna, the transition between the slow and the fast wave range is rapid, which occurs at endfire, and thus, the beam directs very closely to endfire. The scan range is in general broader. The single-medium antenna stays 10°-15° away from broadside and endfire and the frequency sensitivity is rather inert. Its main advantage is that the beamwidth remains constant while scanning [OJ07]. The radiation directions are illustrated with Fig. 3.10.

The periodic type of LWAs exhibits a slow dominant mode with $\beta_0 > k_0$, which does not show radiation even though the structure is open. Only the introduction of a periodic array produces an infinity of space harmonics with β_n for each of them. They are related to each other by

$$\beta_n = \beta_0 + \frac{2n\pi}{d} \tag{3.34}$$

with d the period and β_0 of the fundamental space harmonic of the waveguide. The fast ones of them radiate. With view to Eq. (3.34), β_n can adopt various values, the mode n can be fast or slow, forward or backward. For being fast in nature, $|\beta_n/k_0| < 1$ is required, but $|\beta_0/k_0| > 1$. With

$$\frac{\beta_n}{k_0} = \frac{\beta_0}{k_0} + \frac{n\lambda_0}{d} \tag{3.35}$$

it is evident that $|\beta_n/k_0| < 1$ can result with $n < 0$ and adequate λ_0/d. Since a stable operation is demanded the design is to alter such that preferably merely the first harmonic radiates, so $n = -1$ is chosen. The scan behaviour ranges from the backward quadrant into some part of the forward quadrant, leaving an open stop band at broadside as explained in [OJ07]. The range in the forward quadrant is limited by the emergence of the $n = -2$ mode from backfire, endfire or the next waveguide mode emerging above the cut-off frequency. The periodic discontinuities along the structure appear as small loadings. If they are nonresonant a smooth antenna results and it seems to be quasi-continuous. In contrast, the functional principle of slots in a slot array is based on resonance and they are to be considered individually with mutual coupling effects. Their operation is very dependent on frequency. A slot array is nevertheless good for rapid scanning but the scan range of such an antenna is narrow.
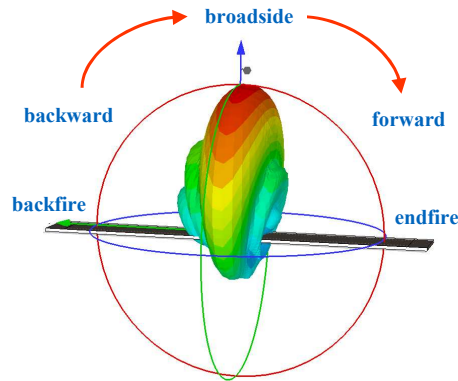
Figure 3.10: Beam steering enabled by tuning the operation frequency.

A surface-wave antenna is an open waveguide with a dominant mode purely bound. Surface-wave antenna are just endfire antennas as radiation is generated only at discontinuities such as the end [OJ07].

Open waveguides, though they are already open, usually furnish a dominant mode that is purely bound, no matter if their realisation is accomplished via a uniform or a periodic design. As well as based on open waveguides is a group of travelling-wave antennas which is formed by employing microstrip lines. The interest in leaky-wave antennas based on microstrip lines arose in the 70ties along with the interest to work in the millimeter wave domain and even higher frequencies. Well-known publications analysing modes in microstrip lines are [Men78] and [Erm78]. New types of antennas were sought because of the increase in losses with higher frequencies. Small dimensions often mean a limit in fabrication so that novel manufacturing techniques are demanded. The connection to a feed might cause spurious radiation and is therefore problematic.

The other category of leaky-wave antennas is constructed with closed waveguides. They support a fast wave and operate on the $n = 0$ space harmonic but physical opening is needed. One method to open them is to cut a long slit along their length, but the disadvantage is that it disrupts the current lines promptly with the consequence of a wide beam instead of a narrow one. An alternative is to use a series of closely spaced holes instead, such that the current can just flow around them. Moreover, due to the close distance between the holes the structure appears as quasi-uniform. Since the closed waveguides are simple in the cross section and easy to analyse, accurate expressions of the complex wavenumber are easy to obtain. The feed junction produces only little spurious radiation. The result is a remarkably good agreement between theory and practice [OJ07].

To sum up the most important traits of the different basic waveguides, open waveguides feature a slow wave and need periodic modulations causing radiation. Yet their beam may swing from the backward quadrant to some part of the forward quadrant. Closed waveguides with introduced closely spaced holes provide a fast wave and seem quasi-uniform with only the $n = 0$ space harmonic leaking. However, they reveal the disadvantage of radiating only in the forward quadrant.

In conclusion, closed waveguides appear as good means to supply the basic concept for metamaterials since they already provide useful prerequisites. The integration of metamaterials in waveguides could diminish their drawbacks and together they might even lead to unprecedented devices with novel functionalities.

3.4.2 Bound or Leaky Wave - Slow or Fast Wave

Whether the wave is just guided or additionally radiating while propagating along the architecture depends on the mathematical nature of the wavenumber pointing perpendicular to the antenna aperture. A representation by the wavenumber k is preferred for this purpose, which is related to the propagation constant by $\gamma = \mathrm{j}k$. For illustration of the radiation mechanism, a scalar plane wave representation is considered according to

$$\psi(x, z) = \psi_0 e^{-\mathrm{j}k_x x} e^{-\mathrm{j}k_z z}. \tag{3.36}$$

The relationship of the wavenumbers is visualised in Fig. 3.11. The functional dependence of the scalar wave potential is held generally and serves mainly for the demonstration of the principle. The wavenumbers k_z longitudinal and k_y transverse to the structure,
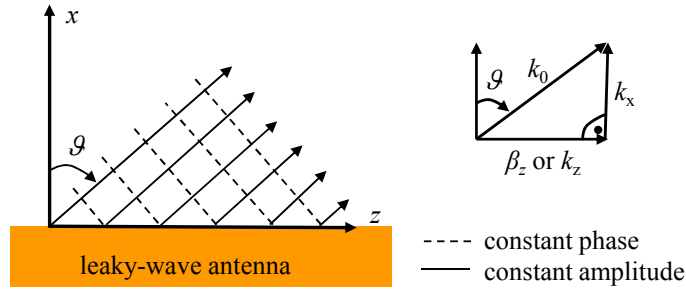
Figure 3.11: Radiated wave front with corresponding wavenumber components.

the wavenumber k_x pointing into the space and the wavenumber of free space, which furthermore denotes the light line with $k_0 = \pm\omega\sqrt{\varepsilon\mu}$, fulfill the separation equation

$$k_x^2 + k_y^2 + k_z^2 = k_0^2. \tag{3.37}$$

Assuming a laterally constant field distribution in y-direction, $k_y = 0$ is obtained (*cf.* section 5.7) and Eq. (3.37) reduces to the two-dimensional case, the propagation constant in x can be ascertained. Whether propagation or attenuation takes place two cases are to distinguish, namely

if $|k_z| < k_0$, it is   if $|k_z| > k_0$, it is

$$k_x = \pm\sqrt{k_0^2 - k_z^2} \tag{3.38}$$ $$k_x = \pm\sqrt{k_0^2 - k_z^2} \tag{3.39}$$

with $k_x \in \mathrm{Re}$.   with $k_x \in \mathrm{j\,Im}$.

Fig. 3.12 depicts the relation. If an imaginary k_x results the corresponding exponent in (3.36) becomes real and no wave propagation in x-direction occurs. Since $k_x = \beta_x - \mathrm{j}\alpha_x$, a positive $\alpha_x > 0$ leads to wave attenuation with $\mathrm{e}^{-\alpha_x x}$ and a negative α_x to an exponential increase of energy for $x \to \infty$. As this is only acceptable within short distances but physically not reasonable for $x \to \infty$, the wave is called improper. This topic is referred to in detail in section 6.1.

From the radiation condition Eq. (3.38),

$$k_0 > k_z \to \frac{k_z}{k_0} = \sqrt{\varepsilon_{r,\mathrm{eff}}} < 1 \tag{3.40}$$

results. For higher order modes k_z must still be of lower value to satisfy condition (3.40). Above $\sqrt{\varepsilon_{r,\mathrm{eff}}} = 1$ all energy remains confined within the structure. Other combinations are conceivable since $k_z = \beta_z - \mathrm{j}\alpha_z$ and $k_x = \beta_x - \mathrm{j}\alpha_x$ but the combinations are here limited to the case $\beta_z > 0$. Tab. 3.1, like the table in [Ish90], usefully summarises the relations where the exponential functional dependence is added as compared to [Ish90].
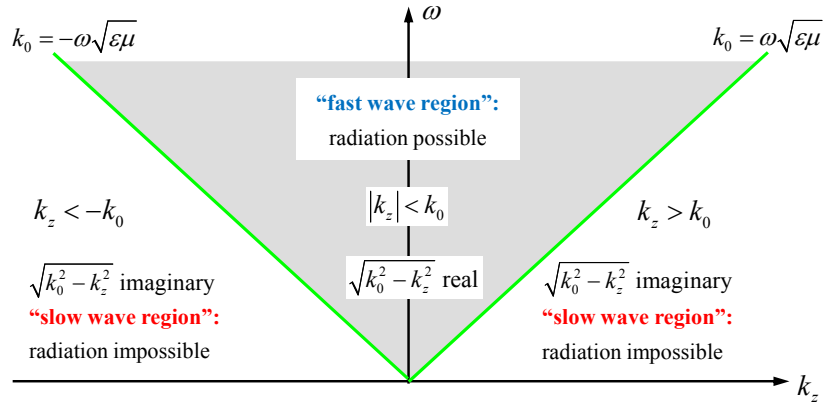
Figure 3.12: The light line separates the slow and the fast wave regions, deciding about pure guiding or the capability of radiation.

Beam Direction, Radiation Efficiency

The beam direction follows directly with regard to Fig. 3.11 as

$$\sin \vartheta_m \approx \frac{\beta_z}{k_0}, \tag{3.41}$$

with ϑ_m as the angle of the maximum of the beam. The length of the leaky-wave antenna is L and the beamwidth $\Delta\vartheta$, which is [OJ07]

$$\Delta\vartheta \approx \frac{1}{L/\lambda_0 \cos \vartheta_m}. \tag{3.42}$$

With the knowledge of the complex wavenumber k_z or β_z and α_z, a proper design can be proceeded effectively. The beam direction, radiation efficiency, beam-steering with frequency and the handling of the side lobe level can be controlled efficiently.

| Case:	β_z	α_z	β_x	α_x	Propagation Term	Meaning
	+	0	+	0	$e^{-j|\beta_z|z-j|\beta_x|x}$	fast wave
	+	−	+	+	$e^{-j|\beta_z|z+|\alpha_z|z-j|\beta_x|x-|\alpha_x|x}$	backward leaky
	+	0	0	+	$e^{-j|\beta_z|z-|\alpha_x|x}$	trapped surface wave
	+	+	−	+	$e^{-j|\beta_z|z-|\alpha_z|z+j|\beta_x|x-|\alpha_x|x}$	Zenneck wave
	+	0	−	0	$e^{-j|\beta_z|z+j|\beta_x|x}$	plane wave incidence
	+	−	−	−	$e^{-j|\beta_z|z+|\alpha_z|z+j|\beta_x|x+|\alpha_x|x}$	
	+	0	0	−	$e^{-j|\beta_z|z+|\alpha_x|x}$	untrapped surface wave
	+	+	+	−	$e^{-j|\beta_z|z-|\alpha_z|z-j|\beta_x|x+|\alpha_x|x}$	forward leaky wave

Table 3.1: Classification of wave types.

3.4.3 Working Principles: Conventional Versus Novel Functionalities with Metamaterials

A LWA devised by metamaterials does not need to be periodic in order to yield radiation as it is sufficient to operate it in the fundamental mode, which is typically fast in nature. Nevertheless, normally they reveal a periodic constitution but with the purpose to ease manufacturing and analysis. In contrast, usual LWAs need periodicities in order to generate leaky space harmonics. Actually, since the period in metamaterial LWAs is much smaller than the operating wavelength $p << \lambda_g$ the entity can be seen as uniform. With reference to the scan range of customary uniform LWAs described in section 3.4.1, the broad scanning range of the metamaterial LWAs is a crucial benefit.

Due to the operation at the $n = 0$ space harmonic, the feeding mechanism can be kept simple and efficient meaning small and broadband by just employing a feed line in comparison to a traditional LWA, where e.g. a balun is needed to excite the odd, the fast mode [QCI+99].

With view to the dispersion diagram in Fig. 3.13 of CRLH TL structures in general, it becomes apparent that an open CRLH structure can radiate since the dispersion curve indicates $|\frac{\beta}{k_0}| < 1$ in certain frequency regions, where β refers to the longitudinal phase constant which was β_z in section 3.4.2. In contrast to conventional LWAs, CRLH structures present backfire to endfire scanning capability including broadside radiation if the structural elements are balanced. At the frequency where $\beta = 0$, radiation perpendicular to the antenna plane occurs and the wavelength as well as the phase velocity is infinite. These specialities can be exploited for promising new gadgets.
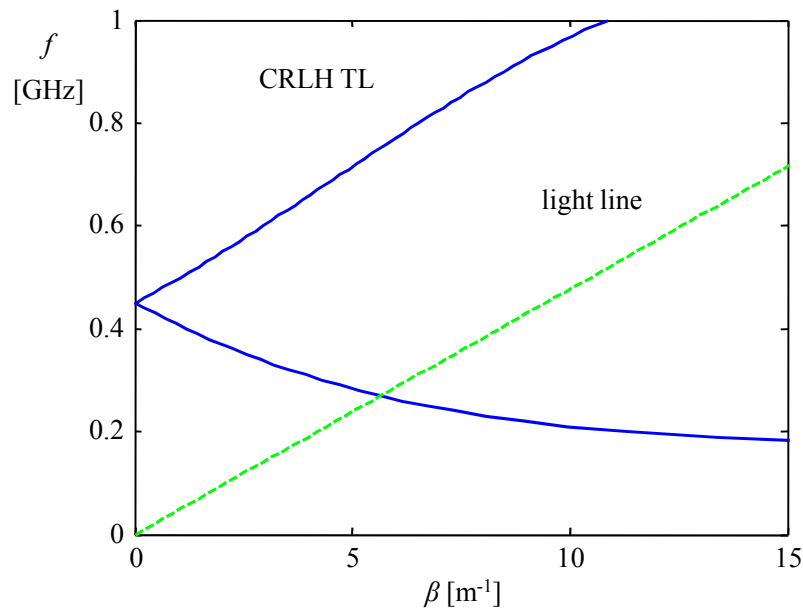

Figure 3.13: The light line (dashed green line) distinguishes the radiation region from the purely guided wave range. Exemplary dispersion curve of CRLH TL (blue solid line).

4 Modal Series Expansion of Periodically Loaded Waveguides

The concept here is to generate the eigensolutions of inhomogeneous periodic eigenproblems, as sketched in Fig. 4.1, in a series expansion employing the eigensolutions of the underlying background waveguides as basis functions. These eigensolutions are best suited
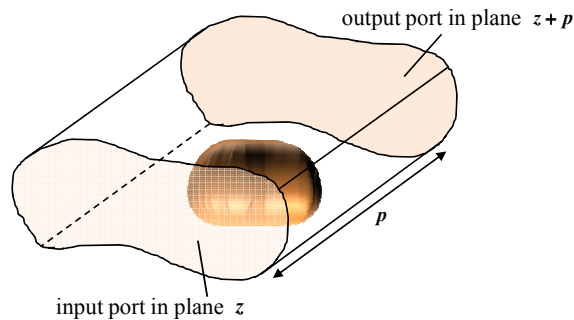
Figure 4.1: Unit cell with periodic loading.

since they comply with the preconditions of orthonormality and completeness. To ensure stable working, a waveguide is typically operated in the fundamental mode and only one mode up to a finite number of propagating modes exist in the frequency range of interest. Hence, the expansion with only very few modes (propagating and some evanescent) may suffice to provide an accurate solution. For many cylindrical waveguides, the eigensolutions can be given analytically. In case the background structure is more complicated the eigensolutions can be computed by numerically solving 2D eigenproblems, e.g. with CST MWS [CST11]. The studied periodically constructed waveguides allow the Bloch-Floquet theorem to be applied, *cf.* section 3.3, meaning that the solution of an entire periodic waveguide is obtained by considering the solution of one unit cell, for which the boundaries are defined as periodic. The periodic boundaries can be placed arbitrarily. However, by positioning them in the undistorted regions of the background waveguide transversal to the propagation direction, here the z-direction, it is possible to formulate the fields depending on x, y in the input periodic boundary according to

$$\boldsymbol{E}_{port,in}\left(x,y\right) = \sum_{m=1}^{M}\left[a_m\boldsymbol{e}_{m,port}\left(x,y\right) + b_m\boldsymbol{e}_{m,port}\left(x,y\right)\right] \tag{4.1}$$

$$\boldsymbol{H}_{port,in}\left(x,y\right) = \sum_{m=1}^{M}\left[a_m\boldsymbol{h}_{m,port}\left(x,y\right) - b_m\boldsymbol{h}_{m,port}\left(x,y\right)\right] \tag{4.2}$$

by the eigensolutions $\boldsymbol{e}_{m,port}$ and $\boldsymbol{h}_{m,port}$ for the electric and for the magnetic field, respectively, of the background waveguide as basis functions. The wave coefficients a_m indicate

inward waves, whereas the wave coefficients b_m denote outward waves. The term with the outward wave coefficient b_m is to subtract in case of the magnetic field in order to maintain an orientation in the right-hand sense. The waveguide cross section is identical with the port planes in a full-wave simulation of the unit cell, from where the M feeding modes directly excite the structure. One mode after the other may excite the unit cell and the couplings onto all the other modes can be recorded. The two port planes (*in* and *out*) limit a unit cell constituting the whole periodic waveguide by periodic repetition in longitudinal, i.e. z-direction. By inserting the modal expansion, Eqs. (4.1) and (4.2), into the Bloch-Floquet theorem, section 3.3, the field solution in the output port plane

$$\boldsymbol{E}_{port,out}\left(x,y\right) = \boldsymbol{E}_{port,in}\left(x,y\right)\mathrm{e}^{-\gamma p} \tag{4.3}$$

$$\boldsymbol{H}_{port,out}\left(x,y\right) = \boldsymbol{H}_{port,in}\left(x,y\right)\mathrm{e}^{-\gamma p} \tag{4.4}$$

is obtained, where

$$\boldsymbol{E}_{port,out}\left(x,y\right) = \sum_{m=1}^{M}\left[b_m'\boldsymbol{e}_{m,port}\left(x,y\right) + a_m'\boldsymbol{e}_{m,port}\left(x,y\right)\right] \tag{4.5}$$

$$\boldsymbol{H}_{port,out}\left(x,y\right) = \sum_{m=1}^{M}\left[b_m'\boldsymbol{h}_{m,port}\left(x,y\right) - a_m'\boldsymbol{h}_{m,port}\left(x,y\right)\right], \tag{4.6}$$

and likewise the field solution in the port planes of the entire waveguide. The length of the periodic unit cell and thus of one period is p, and γ denotes the complex eigenvalue $\gamma = \alpha + \mathrm{j}\beta$, composed of the phase constant β and the attenuation constant α. Actually the eigenvalue is $\Gamma = \mathrm{e}^{\gamma p}$ and it is a scalar quantity, which belongs to a nonzero eigenvector $\boldsymbol{v}$ as defined below. For wave problems, γ specifies the nature of the wave. The incident modes a_m in the input port plane are related to the outgoing primed modes b_m' in the output port plane by the propagation factor according to

$$a_m = b_m'\mathrm{e}^{\gamma p} \tag{4.7}$$

and vice versa

$$b_m = a_m'\mathrm{e}^{\gamma p}. \tag{4.8}$$

4.1 Eigenproblem and Transfer Matrix Representation

Eqs. (4.7) and (4.8) relate the amplitudes of individual modes to each other under the assumption that they belong to an eigensolution. However, the relative amplitudes of the individual modes are not yet defined. They are obtained by considering the couplings of the modes according to

$$
\begin{pmatrix} b_1 \\ \vdots \\ b_M \\ a_1 \\ \vdots \\ a_M \end{pmatrix} = \begin{pmatrix} T_{11}^{11} & \dots & T_{11}^{1M} & T_{12}^{11} & \dots & T_{12}^{1M} \\ \vdots & \ddots & \vdots & \vdots & \ddots & \vdots \\ T_{11}^{M1} & \dots & T_{11}^{MM} & T_{12}^{M1} & \dots & T_{12}^{MM} \\ T_{21}^{11} & \dots & T_{21}^{1M} & T_{22}^{11} & \dots & T_{22}^{1M} \\ \vdots & \ddots & \vdots & \vdots & \ddots & \vdots \\ T_{21}^{M1} & \dots & T_{21}^{MM} & T_{22}^{M1} & \dots & T_{22}^{MM} \end{pmatrix} \begin{pmatrix} a_1' \\ \vdots \\ a_M' \\ b_1' \\ \vdots \\ b_M' \end{pmatrix}. \tag{4.9}
$$

The complex wave amplitudes of the modes in the output port plane can be grouped in the vector $\boldsymbol{v} = (\ldots, a'_m, \ldots, b'_m, \ldots)$. The transfer matrix $\boldsymbol{T}$ thus describes the couplings of the modes at the input port to the modes at the output port, pictured in Fig. 4.2 for the kth unit cell. The superscripts of the T-parameters in Eq. (4.9) are introduced to distinguish the contribution of the mth mode at the input port, indicated by the first superscript, from the contribution of the mth mode at the output port indicated by the second superscript. The subscripts are just for localisation reasons in the matrix and have no physical meaning. The $\boldsymbol{T}$-matrix is usually full, unsymmetric and complex. At each port, M modes are observed leading to a $\boldsymbol{T}$-matrix with dimension $2M \times 2M$ because to each mode belongs an inward wave a and an outward wave b. In a periodic network, the outward wave b' at the output port of the kth unit cell is the inward wave a at the input port of the subsequent $(k+1)^{\text{th}}$ unit cell. The behaviour of the wave quantities of the total series network of K subsystems can easily be obtained by matrix multiplication

$$\boldsymbol{T}_{\text{total}} = \prod_{k=1}^{K} \boldsymbol{T}_k, \tag{4.10}$$

where the order in the product has to be respected. With the goal to classify periodic architectures, the $\boldsymbol{T}$-matrix is the ideal form of description.

The function of the $\boldsymbol{T}$-matrix can be interpreted as a mapping from the modes at the output port onto the modes at the input port. The same mapping is described by the propagation term $\mathrm{e}^{\gamma p}$. The equality can be subsumed in the linear eigenvalue equation

$$\begin{aligned} \mathrm{e}^{\gamma p} \boldsymbol{v} &= \boldsymbol{T}_k \boldsymbol{v} \quad \text{or} \\ (\boldsymbol{T}_k - \mathrm{e}^{\gamma p} \boldsymbol{I}) \boldsymbol{v} &= 0, \end{aligned} \tag{4.11}$$

with the identity matrix $\boldsymbol{I}$.

According to the relation stated with Eq. (4.11), the matrix $\boldsymbol{T}$ has to be decomposed into its eigenvalues. In general, an eigenvalue decomposition analyses a matrix when it represents a mapping from a vector space into itself. The eigenvectors of the square $\boldsymbol{T}$-matrix are multiplied by the matrix and remain proportional to the original vector. They only change in magnitude by a factor which is the eigenvalue, which is here in form of the propagation factor $\mathrm{e}^{\gamma p}$. In contrast, a singular value decomposition serves for analysing a mapping from one vector space into another one with potentially different dimensions. Ideally, $\boldsymbol{T}$ is to diagonalise and the relation reads

$$\boldsymbol{T}\boldsymbol{V} = \boldsymbol{V}\boldsymbol{D}. \tag{4.12}$$

The diagonal matrix $\boldsymbol{D}$ presents the eigenvalues on its diagonal and its ith entry corresponds to the ith column vector $\boldsymbol{v}_i$ of $\boldsymbol{V}$. If $\boldsymbol{V}$ is nonsingular the eigenvalue decomposition
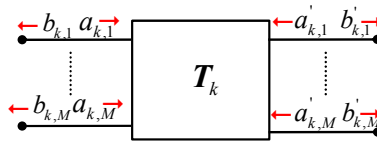
Figure 4.2: The $\boldsymbol{T}$-matrix characterising the kth unit cell.

can be posed as

$$\boldsymbol{T} = \boldsymbol{V}\boldsymbol{D}\boldsymbol{V}^{-1}. \tag{4.13}$$

Is $\boldsymbol{T}$ not to diagonalise an eigenvalue decomposition is not possible. To different eigenvalues $\Gamma_i \neq \Gamma_j$ the eigenvectors $\boldsymbol{v}_i \neq \boldsymbol{v}_j$ correspond, which are orthogonal to each other, therefore it is

$$\boldsymbol{v}_i^{T*}\boldsymbol{v}_j = 0, \tag{4.14}$$

where $\boldsymbol{v}_i^{T*}$ denotes the complex conjugate transpose to $\boldsymbol{v}_i$. Orthogonalilty or rather orthonormality of the vectors is the precondition to express any vector $\boldsymbol{x}$ in terms of a system of orthogonal unit vectors in the form

$$\boldsymbol{x} = c_1\boldsymbol{v}_1 + \cdots c_{2M}\boldsymbol{v}_{2M}, \tag{4.15}$$

where the coefficients c_i are found by multiplying (4.15) by each of the vectors $\boldsymbol{v}_i^*$ [CH53]; they are

$$c_i = \boldsymbol{x}\boldsymbol{v}_i^*. \tag{4.16}$$

The eigenvectors establish a solution space of which the dimension is determined by the number of linearly independent eigenvectors, equally specified by the rank of the matrix. For j modes or eigenvectors j eigenvalues follow if not degenerated. An indication of degeneracy is if the multiplicity of the eigenvalues is bigger than the dimension of the eigenspace spanned by the eigenvectors. In case an eigenvalue exists n-times

$$\Gamma = \Gamma_1 = \Gamma_2 = \ldots = \Gamma_n \tag{4.17}$$

but n linearly independent eigenvectors exist, thus $\dim(\boldsymbol{v_\Gamma}) = n$ and not $\dim(\boldsymbol{v_\Gamma}) < n$, then the matrix $\boldsymbol{T}$ is diagonalisable. If two eigenvectors possess one and the same eigenvalue a degeneracy results. But the eigenvectors $\boldsymbol{v}_i$ and $\boldsymbol{v}_j$ can be combined in the way that $\overline{\boldsymbol{v}_i} = \boldsymbol{v}_i$ and $\overline{\boldsymbol{v}_j} = \boldsymbol{v}_i + C\boldsymbol{v}_j$ such that they end up as orthogonal. The new eigenvectors are indeed orthogonal but have one eigenvalue in common.

The concept of expressing any vector in terms of a system of orthogonal unit vectors stated in Eq. (4.15) is analogous. It can be transferred to express any piecewise continuous function in a solution domain by a set of orthonormal functions. The proof in terms of functions is given in section 5.4. Here, the application is demonstrated by expanding field solutions in port planes by the orthonormal set of eigensolutions $\boldsymbol{e}_{m,port}$ and $\boldsymbol{h}_{m,port}$ as in Eqs. (4.1) and (4.2). The expansion coefficients for the basis functions supply the components of the eigenvectors $\boldsymbol{v} = (\ldots, a'_m, \ldots, b'_m, \ldots)$. They are found by Eq. (4.12) and construct the matrix $\boldsymbol{V}$ while each eigenvector corresponds to an eigenvalue on the diagonal in matrix $\boldsymbol{D}$. The jth column vector belongs to the jth eigenvalue as jj^{th} entry on the diagonal of $\boldsymbol{D}$. The relation is illustrated in Fig. 4.3 for an example of two considered port modes. The first component a'_{j1} corresponds to the first inward wave of the background waveguide. The $(M+1)^{\text{th}}$ component b'_{j1} is the corresponding outward wave. The quotient b'_1/a'_1 can be interpreted as a kind of reflection coefficient for the first port mode at the second port. The second component of $\boldsymbol{v}_j$ belongs to the second port
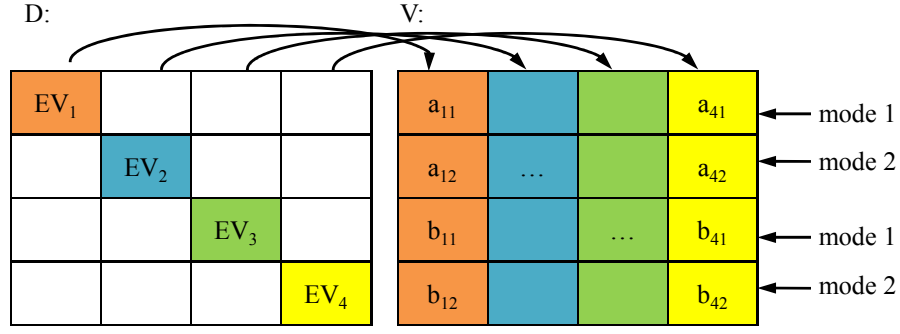
Figure 4.3: Correspondence between eigenvalue j in $\boldsymbol{D}$, eigenvector j in $\boldsymbol{V}$ and exciting modes.

mode and so on. The vector $\boldsymbol{v}_j$ is of dimension $2M$ because of M considered port modes. From eigenvalue j corresponding to eigenvector $\boldsymbol{v}_j$, the propagation and attenuation constant can be deduced. If studying closed waveguides, the eigenvalue of the propagating fundamental mode can be selected according to the criterion

$$|\mathrm{e}^{\gamma p}| \cong 1, \tag{4.18}$$

if no or only little losses are present. Evanescent modes reveal $|\mathrm{e}^{\gamma p}| \neq 1$. From the determined eigenvalue, the propagation and the attenuation constant can be retrieved by

$$\beta = -\angle(\mathrm{e}^{-\gamma p})/p \tag{4.19}$$

$$\alpha = \ln(|\mathrm{e}^{-\gamma p}|)/p \tag{4.20}$$

for the forward wave. The attenuation and the propagation constant can be depicted in a dispersion diagram giving immediately insight in the physical properties of the complex mathematical solution of the wave which may be guided, attenuated, leaky or combinations of it.

4.2 Scattering Matrix and Numerical Implementation

The T-parameters (Eq. (4.9)) are not directly accessible because they have no physical meaning. Instead, the scattering parameters in the $\boldsymbol{S}$-matrix express the physical properties of an electromagnetic system such as a unit cell with respect to accessible ports. While the $\boldsymbol{T}$-matrix relates the wave quantities at the input port to the wave quantities at the output port, the $\boldsymbol{S}$-matrix describes the relation of the outward waves b to the inward waves a at one port or from one port to the other one under the condition that the remaining ports are matched, i.e.

$$S_{ij} = \left.\frac{b_i}{a_j}\right|_{a_n=0,\ a_j\neq0} \tag{4.21}$$

and they represent the degree of cross-coupling from one mode to the others caused by the inhomogeneity contained in the examined unit cell. The coupling of the fields at the boundaries can then be solved via an appropriate numerical field computation program
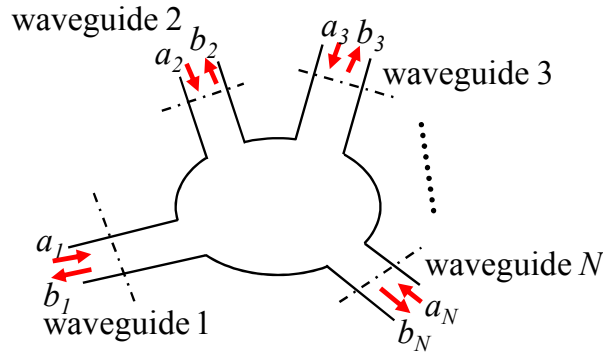
Figure 4.4: N waveguides terminate in a common junction.

like CST MWS [CST11], in which an exact formulation of the problem description is numerically implemented. So, the main computational effort is to determine the couplings but it is just a series of M excitation problems, where the periodic boundary conditions are yet not to consider. The solution procedure is known as the scattering matrix approach (SMA), e.g. [SLW05].

Usually, N waveguides may terminate in a common region which may contain active and/or passive elements as sketched in Fig. 4.4. The system is accordingly attributed to as an N-port. Then, one mode is commonly assumed to exist in each waveguide. On the other hand, only one waveguide may be present while furnishing M modes and the system can be addressed to as an M-port. For this work, waveguide systems are concerned carrying M modes. It is an MN-port and the number of ingoing and outgoing waves at each port is the same. In Fig. 4.4, the dotted line marks the reference location for the waves to be registered. Measuring the wave in a distance away from the reference terminal would generate an additional phase shift and possibly amplitude change. Here, a multimode wise excitation is performed on unit cells of a periodically constituted waveguide with an input port and an output port. The ports are thereby directly placed on one unit cell without additional feeding lines. To clarify the notation, the number of waveguides is referred to with $N = 2$ and the modes are denoted as M modes that excite the two-port system. In total, the matrix of the system is of size $2M \times 2M$ due to an inward and an outward wave of every mode as to see with view to the $\boldsymbol{S}$-matrix reading

$$
\begin{pmatrix} b_1 \\ \vdots \\ b_M \\ b_1^{'} \\ \vdots \\ b_M^{'} \end{pmatrix} = \begin{pmatrix} \boldsymbol{S}_{11} & \boldsymbol{S}_{12} \\ \boldsymbol{S}_{21} & \boldsymbol{S}_{22} \end{pmatrix} \begin{pmatrix} a_1 \\ \vdots \\ a_M \\ a_1^{'} \\ \vdots \\ a_M^{'} \end{pmatrix} \tag{4.22}
$$

where $\boldsymbol{S}_{11}$, $\boldsymbol{S}_{12}$, $\boldsymbol{S}_{21}$ and $\boldsymbol{S}_{22}$ can be treated as submatrices of dimension $M \times M$ of $\boldsymbol{S}$. The primed quantities again mark the waves at the output port. Here, the S-parameters express the behaviour of modes. Contrary to background waveguides, where waves can travel unimpededly, the amplitudes of reflected waves are determined by the physical properties of waveguide inhomogeneities. Moreover, the inhomogeneities cause a cross
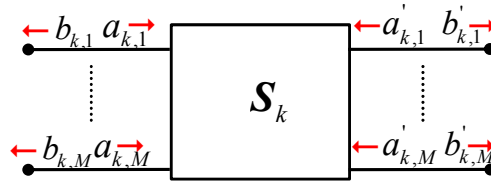
Figure 4.5: The $\boldsymbol{S}$-matrix describes the kth cell with $2M$ modes.

coupling of the modes. The transmission parameter S_{21}^{23} signifies that mode 3 is transmitted from the first to the second port while coupling onto mode 2. The elements on the main diagonal are the reflection parameters, e.g. S_{ii}^{jj} is the reflection coefficient of mode j on port i. Each S-parameter is defined under the precondition that all the other modes are matched. Symmetric unit cells yield symmetric $\boldsymbol{S}$-matrices.

The relation in Eq. (4.22) is illustrated with Fig. 4.5 for the kth unit cell. Since the unit cell is part of a periodic network the description by the $\boldsymbol{T}$-matrix is beneficial. Moreover, the relation to an eigenproblem is needed. Therefore, the $\boldsymbol{S}$-matrix is to convert into the $\boldsymbol{T}$-matrix by the following transformation formulas [Col91]:

$$\boldsymbol{T}_{11} = -\det\{\boldsymbol{S}\}\backslash\boldsymbol{S}_{21} = \boldsymbol{S}_{12} - \boldsymbol{S}_{11}\boldsymbol{S}_{22}\backslash\boldsymbol{S}_{21} \tag{4.23}$$

$$\boldsymbol{T}_{12} = \boldsymbol{S}_{11}\backslash\boldsymbol{S}_{21} \tag{4.24}$$

$$\boldsymbol{T}_{21} = -\boldsymbol{S}_{22}\backslash\boldsymbol{S}_{21} \tag{4.25}$$

$$\boldsymbol{T}_{22} = 1\backslash\boldsymbol{S}_{21}. \tag{4.26}$$

Consequently, the benefits of both matrices can be combined. Since the division of matrices does not exist the symbol "$\backslash$" is introduced representing rather the multiplication by the inverse matrix. This operation must be carried out with caution because small singular values of a matrix may falsify the result, *cf.* 9.3 in the appendix. If a matrix is even singular the inverse does not exist at all and the pseudoinverse must be used instead.

By closer regarding the conversion formulas Eqs. (4.23)-(4.26), it is obvious that the $\boldsymbol{T}$-matrix can not result as symmetric. Furthermore, it is conspicuous that the multiplication with the inverse of the submatrix of the transmission coefficient $\boldsymbol{S}_{21}$ is contained. The inverse of a matrix however does not exist if it is singular creating instability. Such small singular values may occur if modes are included which do not really contribute to the field solutions. These modes now appear among the dominant modes that falsifies the actual behaviour. Therefore and to recover numerical stability, the contributions of these modes must be eliminated beforehand. A singular value decomposition (SVD) *cf.* 9.1 of each submatrix of the $\boldsymbol{S}$-matrix is carried out and a threshold is introduced below which the minor SVs are deleted. As such, a pseudoinverse is generated *cf.* 9.3. The submatrices are rebuilt and the $\boldsymbol{S}$-matrix can be transformed into the $\boldsymbol{T}$-matrix. Consequently, the eigenproblem (4.11) can be solved numerically stable and it is reduced due to only few feeding modes.

The essential trait of this modal series expansion method is that the solution of complex eigenproblems can be reverted to the solution of corresponding and simplified excitation problems or rather to the excitation with a series of single modes. The system matrix

arising from the discretisation of a unit cell and to be solved is greatly reduced compared to the system matrix relevant for the original eigenproblem. The final algebraic eigenproblem only encompasses the coefficients in the expansion for the boundary fields and is of minor computational expense. Driven problems in turn can be computed efficiently with numerical programs. Since the excitation is run with only few M modes a scattering matrix of manageable size $2M \times 2M$ results saving computational complexity and simulation time tremendously. In this manner, the M modal field solutions $\boldsymbol{e}_{m,port}$ and $\boldsymbol{h}_{m,port}$ as field solutions of the port region provide the basis functions. The modal field solutions of the background structure are best suited as basis functions. Their wave nature and their derivation is elucidated in the next chapter. In sections 5.4 and 5.5, it is demonstrated that the waveguide modes fulfill the requirements of proper basis functions like orthonormality and completeness.

   Additionally, a driven simulation seems advantageous offering best boundary flexibility in contrast to a simulation with an eigensolver, where open boundary conditions are often problematic. They are notwithstanding necessary for computing the fields of antenna applications. However, for field problems with open boundary conditions, implying infinite free space, an endless number of modes needs to be considered and the discrete set of modes coalesces into a continuous spectrum signifying that the series expansion is to extend by an integral representation. The solution procedure just described delivered yet approximate and good results in case of leaky-wave antennas presented in chapter 8 compared to reference data because the field modes are mainly concentrated and guided in the waveguides. In section 8.2, the basis functions are the eigensolutions of the actual waveguide without the open space. This approximate approach is improved with the computation strategy presented in chapter 6.2, which extends the modal series expansion with a discrete set of modes to open structures.

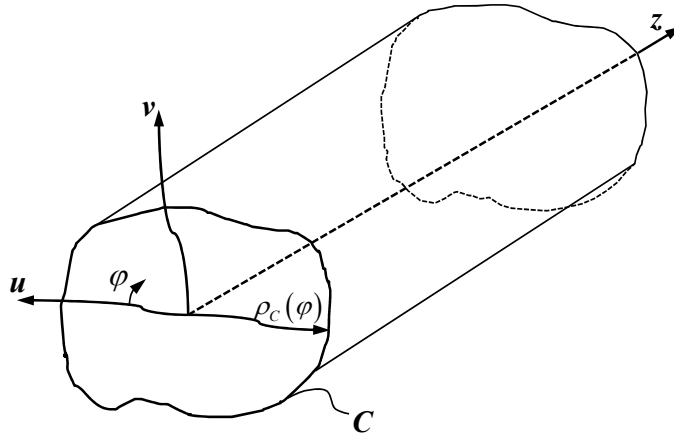# 5 Solutions of Cylindrical Waveguides

In this chapter, modal field solutions are derived for cylindrical waveguides since they provide the background media for periodically repeated inhomogeneities in these waveguides. Cylindrical waveguides are characterised by a transversal cross section which may be inhomogeneous in material and geometry. This cross section is uniform along the longitudinal axis of the waveguide, which is taken as z-axis and which is assumed to extend to infinity. Consequently, the position vector can be decomposed as

$$\boldsymbol{r} = \boldsymbol{\rho} + z\boldsymbol{e}_z. \tag{5.1}$$

The vector $\boldsymbol{\rho}$ in the transversal plane can further be split up in

$$\boldsymbol{\rho} = u\boldsymbol{e}_u + v\boldsymbol{e}_v, \tag{5.2}$$

where u, v denote orthogonal curvilinear coordinates as shown in Fig. 5.1. The waveguides

Figure 5.1: The cylindrical waveguide.

can be closed or open, they are of general kind and the transversal cross section is enclosed by a curve C. The curve C is defined by the radius vector $\boldsymbol{\rho}_C(\varphi)$. If the curve C completely or partly extends to infinity, the waveguides are open.

Typically, waveguides exhibit conventional material parameters and artificial material properties will later be considered when periodic inhomogeneities are placed in the cylindrical waveguides.

The material relations are inserted in Maxwell's equations which consequently read

$$\nabla \times \boldsymbol{H}(\boldsymbol{r}) = \mathrm{j}\omega\varepsilon\boldsymbol{E}(\boldsymbol{r}) + \boldsymbol{J}(\boldsymbol{r}), \tag{5.3}$$

$$\nabla \times \boldsymbol{E}(\boldsymbol{r}) = -\mathrm{j}\omega\mu\boldsymbol{H}(\boldsymbol{r}) - \boldsymbol{M}(\boldsymbol{r}), \tag{5.4}$$

$$\nabla \cdot (\varepsilon\boldsymbol{E})(\boldsymbol{r}) = \rho(\boldsymbol{r}), \tag{5.5}$$

$$\nabla \cdot (\mu\boldsymbol{H}(\boldsymbol{r})) = \rho_m(\boldsymbol{r}). \tag{5.6}$$

For the solution of electromagnetic problems the boundary conditions have to be defined. On the boundary between some adjacent domains 1 and 2 with different material properties, it is to distinguish whether surface currents or surface charges exist or not [Col91]. Thereby, it is assumed that the unit normal vector $\boldsymbol{n}$ points from medium 2 into medium 1. Then, the boundary conditions result in

$$\boldsymbol{n} \times (\boldsymbol{H}_1(\boldsymbol{r}) - \boldsymbol{H}_2(\boldsymbol{r})) = \begin{cases} 0 & : \text{standard} \\ \boldsymbol{J}_A(\boldsymbol{r}) & : \text{surface currents} \end{cases} \tag{5.7}$$

for the magnetic field and for the electric field in

$$\boldsymbol{n} \times (\boldsymbol{E}_1(\boldsymbol{r}) - \boldsymbol{E}_2(\boldsymbol{r})) = \begin{cases} 0 & : \text{standard} \\ -\boldsymbol{M}_A(\boldsymbol{r}) & : \text{surface currents.} \end{cases} \tag{5.8}$$

In the event of charges, the situation for the electric flux density yields

$$\boldsymbol{n} \cdot (\boldsymbol{D}_1(\boldsymbol{r}) - \boldsymbol{D}_2(\boldsymbol{r})) = \begin{cases} 0 & : \text{standard} \\ \rho_A(\boldsymbol{r}) & : \text{surface charges} \end{cases} \tag{5.9}$$

and for the magnetic flux, it is

$$\boldsymbol{n} \cdot (\boldsymbol{B}_1(\boldsymbol{r}) - \boldsymbol{B}_2(\boldsymbol{r})) = \begin{cases} 0 & : \text{standard} \\ \rho_{mA}(\boldsymbol{r}) & : \text{surface charges.} \end{cases} \tag{5.10}$$

In section 5.1, auxiliary potential functions are introduced to solve Maxwell's equations *cf.* [Bal05] and some general considerations are given. In section 5.2, field modes in waveguides are examined first generally while in section 5.3, E and H modes are deduced in the form of five-component fields. Section 5.4 elucidates scalar eigenproblems and the characteristics in general. In section 5.5, a more general vectorial orthogonality principle is derived. Next, special field modes are presented. It starts with the TEM wave in section 5.6, followed by the solutions for a rectangular cross section bounded by perfectly conducting walls in section 5.7. Section 5.8 demonstrates that evanescent modes contribute to real power transfer and section 5.9 is concerned with open dielectric waveguiding structures and in especially with the modal solutions of TE and TM waves on the grounded dielectric slab. In section 5.10, the modal solution is analytically derived for a three-layer composition which is bounded by PEC at the top and the bottom.

5.1 Solutions of Maxwell's Equations by Auxiliary Potential Functions

For simplicity, homogeneous space is implied. In addition, for isotropic and linear media, ε_r and μ_r are scalar and constant. First, MWEs are considered under the excitation of purely electric currents:

$$\nabla \times \boldsymbol{H}(\boldsymbol{r}) = \mathrm{j}\omega\varepsilon\boldsymbol{E}(\boldsymbol{r}) + \boldsymbol{J}(\boldsymbol{r}), \tag{5.11}$$

$$\nabla \times \boldsymbol{E}(\boldsymbol{r}) = -\mathrm{j}\omega\boldsymbol{B}(\boldsymbol{r}), \tag{5.12}$$

$$\nabla \cdot \boldsymbol{B}(\boldsymbol{r}) = 0. \tag{5.13}$$

Eq. (5.13) results from the fact that no magnetic sources exist, hence the divergence of the magnetic field is 0. It is known that any vector field e.g. $\boldsymbol{C}(\boldsymbol{r})$ can be decomposed into a rotational field part and a gradient field part [Ish90]:

$$\boldsymbol{C}(\boldsymbol{r}) = \nabla \times \boldsymbol{A}(\boldsymbol{r}) + \nabla \phi(\boldsymbol{r}). \tag{5.14}$$

The divergence yields

$$\nabla \cdot \boldsymbol{C}(\boldsymbol{r}) = \underbrace{\nabla \cdot (\nabla \times \boldsymbol{A}(\boldsymbol{r}))}_{=0} + \underbrace{\nabla \cdot \nabla \phi(\boldsymbol{r})}_{\neq 0}. \tag{5.15}$$

Since $\nabla \cdot \boldsymbol{B}(\boldsymbol{r}) = 0$ equally vanishes,

$$\boldsymbol{B}(\boldsymbol{r}) = \nabla \times \boldsymbol{A}(\boldsymbol{r}) \qquad\qquad \boldsymbol{A}(\boldsymbol{r}) : \text{magnetic vector potential} \tag{5.16}$$

can be defined. Eq. (5.16) is inserted into (5.12) resulting in

$$\nabla \times (\boldsymbol{E}(\boldsymbol{r}) + \mathrm{j}\omega\boldsymbol{A}(\boldsymbol{r})) = 0, \tag{5.17}$$

where the term in parentheses can be represented by the gradient of a scalar potential. Thus, it is

$$\boldsymbol{E}(\boldsymbol{r}) = -\mathrm{j}\omega\boldsymbol{A}(\boldsymbol{r}) - \nabla\phi(\boldsymbol{r}). \qquad\qquad \phi(\boldsymbol{r}) : \text{electric scalar potential} \tag{5.18}$$

Inserting (5.18) with (5.16) into (5.11) gives

$$\nabla \times \nabla \times \boldsymbol{A}(\boldsymbol{r}) = \omega^2 \mu\varepsilon \boldsymbol{A}(\boldsymbol{r}) - \mathrm{j}\omega\mu\varepsilon\nabla\phi(\boldsymbol{r}) + \mu\boldsymbol{J}(\boldsymbol{r}). \tag{5.19}$$

The relation

$$\nabla \times \nabla \times \boldsymbol{A}(\boldsymbol{r}) = \nabla\nabla \cdot \boldsymbol{A}(\boldsymbol{r}) - \Delta\boldsymbol{A}(\boldsymbol{r}) \tag{5.20}$$

renders

$$\Delta\boldsymbol{A}(\boldsymbol{r}) + \omega^2\mu\varepsilon\boldsymbol{A}(\boldsymbol{r}) = \nabla(\nabla \cdot \boldsymbol{A}(\boldsymbol{r}) + \mathrm{j}\omega\mu\varepsilon\phi(\boldsymbol{r})) - \mu\boldsymbol{J}(\boldsymbol{r}), \tag{5.21}$$

where the wavenumber k can replace $\omega\sqrt{\mu\varepsilon}$.

Alternatively, Eq. (5.14) can be stated such that any vector field consists of a curl-free component $\boldsymbol{A}'$ and a divergence-free component $\boldsymbol{A}''$: $\boldsymbol{A} = \boldsymbol{A}' + \boldsymbol{A}''$ with $\nabla \times \boldsymbol{A}' = 0$ and $\nabla \cdot \boldsymbol{A}'' = 0$. Since $\nabla \times \boldsymbol{A} = \nabla \times \boldsymbol{A}'' = \boldsymbol{B}$ as defined in (5.16), $\nabla \cdot \boldsymbol{A} = \nabla \cdot \boldsymbol{A}'$ is still free to choose and this is accomplished by satisfying the Lorenz gauge

$$\nabla \cdot \boldsymbol{A}(\boldsymbol{r}) + \mathrm{j}\omega\mu\varepsilon\phi(\boldsymbol{r}) = 0. \tag{5.22}$$

Finally, with the Lorenz gauge and from (5.21), the inhomogeneous vector Helmholtz equation

$$\Delta\boldsymbol{A}(\boldsymbol{r}) + k^2\boldsymbol{A}(\boldsymbol{r}) = -\mu\boldsymbol{J}(\boldsymbol{r}) \tag{5.23}$$

follows, which would be a homogeneous eigenvalue problem equation without an electric current excitation $\boldsymbol{J}$. Applying the divergence operator on (5.19), imposing the Lorenz condition and the continuity equation, which is

$$\nabla \cdot \boldsymbol{J}\left(\boldsymbol{r}\right) = -\mathrm{j}\omega\rho\left(\boldsymbol{r}\right),$$ (5.24)

it returns

$$\Delta\phi\left(\boldsymbol{r}\right) + k^2\phi\left(\boldsymbol{r}\right) = \frac{\nabla \cdot \boldsymbol{J}\left(\boldsymbol{r}\right)}{\mathrm{j}\omega\varepsilon} = -\frac{\rho}{\varepsilon}$$ (5.25)

which is the inhomogeneous scalar Helmholtz equation.

Applying (5.22) to (5.18),

$$\boldsymbol{E}\left(\boldsymbol{r}\right) = -\mathrm{j}\omega\left(\boldsymbol{A}\left(\boldsymbol{r}\right) + \frac{1}{k^2}\nabla\nabla \cdot \boldsymbol{A}\left(\boldsymbol{r}\right)\right)$$ (5.26)

is obtained and from (5.11) with (5.16), the electric field can be computed from the magnetic vector potential and the electric currents:

$$\boldsymbol{E}\left(\boldsymbol{r}\right) = \frac{1}{\mathrm{j}\omega\mu\varepsilon}\nabla \times \nabla \times \boldsymbol{A}\left(\boldsymbol{r}\right) - \frac{1}{\mathrm{j}\omega\varepsilon}\boldsymbol{J}\left(\boldsymbol{r}\right).$$ (5.27)

For reasons of completeness, the computation of the magnetic vector potential is given due to sources, since this is the common case although primarily source-free fields are treated in this work. The magnetic vector potential is gained via integrating over either volume source currents as

$$\boldsymbol{A}\left(\boldsymbol{r}\right) = \frac{\mu}{4\pi}\iiint\limits_{V} \frac{e^{-\mathrm{j}k|\boldsymbol{r}-\boldsymbol{r}'|}}{|\boldsymbol{r}-\boldsymbol{r}'|}\boldsymbol{J}(\boldsymbol{r}')dV'$$ (5.28)

or over surface source currents with

$$\boldsymbol{A}\left(\boldsymbol{r}\right) = \frac{\mu}{4\pi}\iint\limits_{A} \frac{e^{-\mathrm{j}k|\boldsymbol{r}-\boldsymbol{r}'|}}{|\boldsymbol{r}-\boldsymbol{r}'|}\boldsymbol{J}_A(\boldsymbol{r}')dA'$$ (5.29)

where the term $\frac{1}{4\pi}\frac{e^{-\mathrm{j}k|\boldsymbol{r}-\boldsymbol{r}'|}}{|\boldsymbol{r}-\boldsymbol{r}'|}$ denotes the Green's function of the scalar Helmholtz equation for the three-dimensional free space. This is the solution of the scalar Helmholtz equation for an excitation with the delta Dirac function. Having computed $\boldsymbol{A}\left(\boldsymbol{r}\right)$, the result can be inserted into (5.26) which finally yields the electric field in form of

$$\boldsymbol{E}\left(\boldsymbol{r}\right) = \frac{-\mathrm{j}\omega\mu}{4\pi}\iiint\limits_{V} \left(\bar{\boldsymbol{I}} + \frac{1}{k^2}\nabla\nabla\right) \frac{e^{-\mathrm{j}k|\boldsymbol{r}-\boldsymbol{r}'|}}{|\boldsymbol{r}-\boldsymbol{r}'|} \cdot \boldsymbol{J}(\boldsymbol{r}')dV'$$ (5.30)

for source currents within a volume and equivalently for source currents within a surface. $\bar{\boldsymbol{I}}$ is here the unit dyad.

By the principle of duality, the fields of magnetic source currents can be computed by means of an electric vector potential, of which the definition is

$$\boldsymbol{E}\left(\boldsymbol{r}\right) = -\frac{1}{\varepsilon}\nabla \times \boldsymbol{F}\left(\boldsymbol{r}\right) \qquad\qquad\qquad \boldsymbol{F}\left(\boldsymbol{r}\right): \text{electric vector potential}$$ (5.31)

because $\nabla \cdot (\varepsilon \boldsymbol{E}(\boldsymbol{r})) = 0$. The resulting field representations by the electric vector potential and the magnetic scalar potential $\psi(\boldsymbol{r})$ involving magnetic current sources $\boldsymbol{M}(\boldsymbol{r})$ are

$$\boldsymbol{H}(\boldsymbol{r}) = -\mathrm{j}\omega \boldsymbol{F}(\boldsymbol{r}) - \nabla\psi(\boldsymbol{r}), \tag{5.32}$$

$$\boldsymbol{H}(\boldsymbol{r}) = -\mathrm{j}\omega \left(\boldsymbol{F}(\boldsymbol{r}) + \frac{1}{k^2}\nabla\nabla\cdot\boldsymbol{F}(\boldsymbol{r}) \right), \tag{5.33}$$

$$\boldsymbol{H}(\boldsymbol{r}) = \frac{1}{\mathrm{j}\omega\mu\varepsilon}\nabla\times\nabla\times\boldsymbol{F}(\boldsymbol{r}) - \frac{1}{\mathrm{j}\omega\mu}\boldsymbol{M}(\boldsymbol{r}). \tag{5.34}$$

The computations of the potentials follow with

$$\Delta\boldsymbol{F}(\boldsymbol{r}) + k^2\boldsymbol{F}(\boldsymbol{r}) = \varepsilon\boldsymbol{M}(\boldsymbol{r}), \tag{5.35}$$

$$\Delta\psi(\boldsymbol{r}) + k^2\psi(\boldsymbol{r}) = -\frac{\rho_m(\boldsymbol{r})}{\mu}, \tag{5.36}$$

$$\boldsymbol{F}(\boldsymbol{r}) = \frac{\varepsilon}{4\pi}\iiint \frac{\mathrm{e}^{-\mathrm{j}k|\boldsymbol{r}-\boldsymbol{r}'|}}{|\boldsymbol{r}-\boldsymbol{r}'|}\boldsymbol{M}(\boldsymbol{r}')dV'. \tag{5.37}$$

After deriving the tools for computing the electromagnetic field solutions they can be used to achieve the field solutions for waveguiding structures.

5.2 Field Modes in Waveguides

The fundamental properties are examined with respect to Maxwell's equations in the subsequent sections. Since the medium parameters do not vary along the z-axis field types can be conveniently computed by separation of location dependence into longitudinal and transversal functional dependencies. The field types feature the form

$$\boldsymbol{E}(u,v,z) = \boldsymbol{E}_0(\boldsymbol{\rho})e^{\pm\gamma z}, \tag{5.38}$$

$$\boldsymbol{H}(u,v,z) = \boldsymbol{H}_0(\boldsymbol{\rho})e^{\pm\gamma z}, \tag{5.39}$$

where the $e^{\pm\gamma z}$-dependence is due to the translation invariance in z. The number of field types or modes with different cross sectional dependence approaches infinity. It is to distinguish between propagating wave types with a purely imaginary propagation constant in the lossfree case

$$\gamma = \mathrm{j}\beta \tag{5.40}$$

and evanescent modes with a real propagation constant

$$\gamma = \alpha. \tag{5.41}$$

Losses or radiation lead to a complex propagation constant. The number of wave types in a cylindrical waveguide is always finite whereas the number of evanescent modes is infinite. Wave types may have a cut-off frequency above which they are able to propagate and to transport energy. Below this very frequency, they are evanescent. One type without a lower cut-off frequency is the transversal electromagnetic (TEM) wave existing in multi-conductor systems. It cannot propagate in a fully closed waveguide without inner conductor since the potential difference on a closed boundary is zero and the solution to

the Laplace equation in the transversal plane is hence also zero. A mode is termed fundamental if it is the only one to propagate in a specific frequency range, which is typically at low frequencies. For instance, a rectangular waveguide has the H_{10} mode as fundamental mode if the vertical dimension b and the horizontal length a show a relation of $0.5 \geq \frac{b}{a}$ and the wavelength of a homogeneous plane wave λ_{HPW} is $1 \leq \frac{\lambda_{HPW}}{a} \leq 2$.

Phase and Group Velocity

In time domain, a wave type travelling in $+z$-direction is

$$\boldsymbol{E}(\boldsymbol{r}, t) = \mathrm{Re}\left\{\boldsymbol{E}_0(\boldsymbol{\rho})e^{\mathrm{j}(\omega t - \beta z)}\right\}. \tag{5.42}$$

Keeping the argument of the exponential constant yields the phase velocity of the wave as

$$c = \frac{\omega}{\beta}. \tag{5.43}$$

An information-carrying wave set can be seen as a superposition of harmonic waves with different frequencies. While integrating over a small band the integral describes the corresponding envelope curve. By keeping the integration result constant [Col91], the group velocity of the envelope curve follows with

$$v_g = \left(\frac{d\beta}{d\omega}\right)^{-1}. \tag{5.44}$$

The group velocity is consequently the velocity with which the information or energy of the electromagnetic wave advances. It is always smaller than the velocity of light whereas the phase velocity may turn out greater than the velocity of light.

5.3 Five-Component Fields for $\boldsymbol{E}$ and $\boldsymbol{H}$ Modes

The vector eigenvalue problem is simplified by a split-up into scalar eigenvalue problems adequate for many cross-sectional domains. This scalarisation is equivalent with a decomposition into E and H modes [FM94]. It is possible to pursue modal expansions of independent transverse fields $\boldsymbol{E}_t$ and $\boldsymbol{H}_t$ and to formulate the dependent longitudinal components thereby. For this reason, it is desirable to eliminate the longitudinal component and to seek field equations for the independent transverse components only. As such, the field is decomposed into a transverse part and a longitudinal component according to

$$\boldsymbol{E}(u, v, z) = \left[\boldsymbol{E}_t(u, v) + \boldsymbol{e}_z E_z\right] e^{-\gamma z}, \tag{5.45}$$
$$\boldsymbol{H}(u, v, z) = \left[\boldsymbol{H}_t(u, v) + \boldsymbol{e}_z H_z\right] e^{-\gamma z} \tag{5.46}$$

for longitudinal z-direction. The operators are separated likewise:

$$\nabla = \nabla_t + \boldsymbol{e}_z \frac{\partial}{\partial z}, \tag{5.47}$$

$$\nabla^2 = \Delta = \nabla_t^2 + \frac{\partial^2}{\partial z^2}. \tag{5.48}$$

A facilitating decomposition into E and H modes results which is appropriate for many configurations. An ansatz is posed for the marked direction of propagation.

For the E-type modes, the ansatz reads

$$\boldsymbol{A} = \boldsymbol{e}_z \psi_E, \qquad \boldsymbol{F} = 0, \tag{5.49}$$

$$\psi_E = \psi_{Et} e^{-\gamma_E z}. \tag{5.50}$$

It results in

$$\boldsymbol{E} = \frac{1}{\mathrm{j}\omega\mu\varepsilon} \nabla \times \nabla \times \boldsymbol{A} = -\frac{\gamma_E}{\mathrm{j}\omega\mu\varepsilon} \nabla_t \psi_E - \boldsymbol{e}_z \frac{\nabla_t^2 \psi_E}{\mathrm{j}\omega\mu\varepsilon}, \tag{5.51}$$

$$\boldsymbol{H} = \frac{1}{\mu} \nabla \times \boldsymbol{A} = -\frac{1}{\mu} \boldsymbol{e}_z \times \nabla_t \psi_E \qquad \text{yielding} \qquad H_z = 0 \tag{5.52}$$

generating the transversal magnetic (TM) modes without an H-component in propagation direction.

Likewise for the H modes or the transversal electric (TE) modes the ansatz is

$$\boldsymbol{F} = \boldsymbol{e}_z \psi_H, \qquad \boldsymbol{A} = 0, \tag{5.53}$$

$$\psi_H = \psi_{Ht} e^{-\gamma_H z}, \tag{5.54}$$

$$\boldsymbol{E} = -\frac{1}{\varepsilon} \nabla \times \boldsymbol{F} = \frac{1}{\varepsilon} \boldsymbol{e}_z \times \nabla_t \psi_H \qquad \text{yielding} \qquad E_z = 0, \tag{5.55}$$

$$\boldsymbol{H} = \frac{1}{\mathrm{j}\omega\mu\varepsilon} \nabla \times \nabla \times \boldsymbol{F} = -\frac{\gamma_H}{\mathrm{j}\omega\mu\varepsilon} \nabla_t \psi_H - \boldsymbol{e}_z \frac{\nabla_t^2 \psi_H}{\mathrm{j}\omega\mu\varepsilon}. \tag{5.56}$$

In both cases, the ansatz just contains one z-component which entails vector field solutions depending only on one scalar quantity. Since they have to fulfill the scalar Helmholtz equation the ansatz is applied to the homogeneous form of (5.25) considering no sources. Without any excitation, the equation represents an eigenvalue problem. For E modes, it is

$$\Delta \psi_E + k^2 \psi_E = 0, \tag{5.57}$$

$$\Delta_t \psi_E + \underbrace{\left(k^2 + \gamma_E^2 \right)}_{q_E^2} \psi_E = 0 \tag{5.58}$$

where

$$q_E = \sqrt{k^2 + \gamma_E^2} \tag{5.59}$$

is the eigenvalue of the E-field modes, and similarly for H-field types one gets

$$\Delta \psi_H + k^2 \psi_H = 0, \tag{5.60}$$

$$\Delta_t \psi_H + \underbrace{\left(k^2 + \gamma_H^2 \right)}_{q_H^2} \psi_H = 0 \tag{5.61}$$

with

$$q_H = \sqrt{k^2 + \gamma_H^2} \tag{5.62}$$

as eigenvalue of the H-field modes.

Eqs. (5.59) and (5.62) constitute the separation equations for the E and the H modes, respectively. Each of the field types is just composed of five components. However, any six-components fields can be generated by superposition of E and H modes because E and H modes together typically form a complete set and an arbitrary field within a closed region can be represented. Consequently, it is sufficient to describe such fields by only two scalar quantities.

Both eigenvalues q_E and q_H result from the field solution and depend on the transversal geometry. The wavenumber $k = \omega\sqrt{\varepsilon\mu}$ characterises the solution medium and contains the frequency for which the eigenvalue equation is to solve. The propagation constant $\gamma = \sqrt{q^2 - k^2}$ specifies whether the field mode is able to propagate or whether it is attenuated.

It yields for a real k

with real eigenvalues $|q| < k$: propagating waves with

$$\gamma = \mathrm{j}\beta, \quad \alpha = 0 \qquad\qquad (5.63)$$

and the wavelength

$$\lambda_g = \frac{2\pi}{\beta} = \frac{2\pi}{\sqrt{k^2 - q^2}} \qquad (5.64)$$

$$\text{with} \quad \lambda_g > \lambda_0 = \frac{2\pi}{k}. \qquad (5.65)$$

with real eigenvalues $|q| > k$: evanescent waves with

$$\gamma = \alpha, \quad \beta = 0, \qquad\qquad (5.66)$$

where λ_g is imaginary.

Every field type with an eigenvalue q possesses a frequency which is called the cut-off frequency since $\omega_c = 2\pi f_c$ with $k = \omega_c\sqrt{\varepsilon\mu} = k_c = q$, with which the propagation constant becomes $\gamma_c = \sqrt{q^2 - k_c^2} = 0$ and $\alpha = 0$ as well as $\beta = 0$. Generally, q and k can become complex quantities. Consequently, γ will be complex, too and a classification of the modes is not that clear anymore.

Besides γ, the other characteristic quantity of a field mode is the field impedance. The modal field impedance is defined with respect to the transverse field components and the corresponding relations are

for E/TM modes: **for H/TE modes:**

$$\boldsymbol{E_t} = -\frac{\gamma_E}{\mathrm{j}\omega\mu\varepsilon}\nabla_t\psi_E \qquad (5.67)$$

$$\boldsymbol{E_t} = \frac{1}{\varepsilon}\boldsymbol{e_z}\times\nabla_t\psi_H \qquad (5.71)$$

$$\boldsymbol{H_t} = -\frac{1}{\mu}\boldsymbol{e_z}\times\nabla_t\psi_E \qquad (5.68)$$

$$\boldsymbol{H_t} = -\frac{\gamma_H}{\mathrm{j}\omega\mu\varepsilon}\nabla_t\psi_H \qquad (5.72)$$

turning to   thus

$$\boldsymbol{e_z}\times\boldsymbol{E_t} = Z_{FE}\boldsymbol{H_t} \qquad (5.69)$$

$$\boldsymbol{e_z}\times\boldsymbol{E_t} = Z_{FH}\boldsymbol{H_t} \qquad (5.73)$$

$$\text{with}\quad Z_{FE} = \frac{\gamma_E}{\mathrm{j}\omega\varepsilon} \qquad (5.70)$$

$$\text{with}\quad Z_{FH} = \frac{\mathrm{j}\omega\mu}{\gamma_H} \qquad (5.74)$$

From the previous equations it becomes obvious that the transversal E- and H-fields are perpendicular to each other and that the field impedances are location-independent for constant ε and μ.

5.4 General One-Dimensional Eigenvalue Problem

The scalar eigenvalue problems are given in (5.58) and (5.61) for E modes and H modes, respectively. If separation of variables is possible with the product ansatz, then, coupled 1D scalar eigenproblems result which are typically of Sturm-Liouville type. The solutions of Sturm-Liouville problems possess the important properties of orthogonality and completeness, what will be discussed in the sequel.

An eigenvalue problem of the Sturm-Liouville type [FM94] is given as

$$\left[\frac{d}{dx}\left(s(x)\frac{d}{dx}\right) - g(x) + \Gamma_m h(x)\right]f_m(x) = 0, \qquad x_1 \leq x \leq x_2 \qquad (5.75)$$

subject to the homogeneous boundary conditions

$$s(x)\frac{df_m(x)}{dx} + c_{1,2}f_m(x) = 0, \qquad x = x_{1,2}, \qquad (5.76)$$

while $s(x), g(x)$ and the weighting function $h(x)$ are supposed to be piecewise continuous functions of x in the domain of focus. The eigenvalues Γ_m are real for real $s(x), g(x), h(x)$ and $c_{1,2}$, marking the Hermitian case, and they belong to a non-dissipative medium. The proof can be found in [FM94]. For the derivation of the orthogonality relation for the Hermitian case, Eq. (5.75) is to multiply by the eigenfunction $f_n^*(x)$ belonging to the eigenvalue $\Gamma_n^* = \Gamma_n$. Furthermore, integration is necessary over the defined x-domain to obtain

$$\int\limits_{x_1}^{x_2} f_n^*(x)\frac{d}{dx}\left(s(x)\frac{df_m(x)}{dx}\right)dx - \int\limits_{x_1}^{x_2} g(x)f_n^*(x)f_m(x)dx + \Gamma_m\int\limits_{x_1}^{x_2} h(x)f_n^*(x)f_m(x)dx = 0. \quad (5.77)$$

Equally, it is to proceed by defining Eq. (5.75) for f_n^* and multiplication with f_m and a subsequent integration. The outcome is Eq. (5.77) but with m and n interchanged.

Subsequently, the second equation is to subtract from the first one and eventually

$$(\Gamma_m - \Gamma_n) \int_{x_1}^{x_2} h f_n^*(x) f_m(x) dx = \left[s \left(f_m(x) \frac{df_n^*(x)}{dx} - f_n^*(x) \frac{df_m(x)}{dx} \right) \right]_{x1}^{x2} \tag{5.78}$$

turns out. The boundary conditions let the right-hand side vanish and lead to the orthogonality property of $f_m(x)$ and $f_n^*(x)$ relative to the weighting factor $h(x)$

$$\int_{x_1}^{x_2} h(x) f_m(x) f_n^*(x) dx = 0, \qquad m \neq n. \tag{5.79}$$

The requirement

$$\int_{x_1}^{x_2} h(x) |f_m(x)|^2 dx = 1 \tag{5.80}$$

states that the eigenfunctions are normalised to unity.

In the special case that $\Gamma_m = \Gamma_n$, it is said that the corresponding modes are degenerate and the proof of orthogonality just given fails [Col91]. However, a suitable linear combination of the degenerate modes can always be formulated such that the subset of modes is orthogonal again [Col91]. For example, letting f_1 and f_2 be two degenerate modes with eigenvalue Γ in common, a new subset of modes could be $f_1' = f_1$, $f_2' = f_2 + c f_1$, in which c is a constant and chosen such that $\iint_S f_1' f_2'^* dS = 0$. Now with $\iint_S f_m f_n^* dS = P_{mn}$ with $m = 1$ and $n = 2$, it is $c = -\frac{P_{12}}{P_{11}}$ and the two modes f_1' and f_2' are orthogonal [Col91]. This is the Gram-Schmidt orthogonalisation procedure.

The set of eigenfunctions $f_m(x)$ constitutes a complete set and it encompasses all possible solutions for Eq. (5.75) [FM94],[CH53]. The set can represent a permissible function $F(x)$ in the x-interval, for which the sum

$$F(x) = \sum_m F_m f_m(x) \tag{5.81}$$

over all eigenfunctions $f_m(x)$ converges. In order to find the coefficients F_m, (5.81) is multiplied by $h(x) f_m^*(x)$ with the purpose to obtain Eqs. (5.79) and (5.80) and make use of the orthogonality property. Subsequently, F_m can be evaluated as

$$F_m = \int_{x_1}^{x_2} h(\xi) F(\xi) f_m^*(\xi) d\xi. \tag{5.82}$$

The completeness of the set of f_m is usually shown by choosing for $F(x)$ the expressive delta function $\delta(x - x')$. With regard to the Fourier transform, the delta function comprises all frequencies. Hence, it is

$$F_m = \int_{x_1}^{x_2} h(\xi) \delta(\xi - x') f_m^* (\xi) \, d\xi = h(x') f_m^*(x'). \tag{5.83}$$

From Eq. (5.81) the completeness relation

$$\frac{\delta(x - x')}{h(x')} = \sum_m f_m(x) f_m^*(x'), \qquad x_1 < x, x' < x_2 \tag{5.84}$$

results. In conclusion, Eq. (5.84) gives the final representation of a permissible function $F(x)$ as in Eq. (5.81). A more detailed explanation on functions which can be expanded in terms of the eigenfunctions into an absolutely and uniformly convergent series implying completeness and orthogonality of the eigenfunctions can be found in [CH53]. The previous deduction has been made since the differential equation (5.75) together with the boundary condition (5.76) constitute a Sturm-Liouville system which reveals important properties being prerequisite for the basis functions in the modal expansion concept employed in chapter 4. The principle characteristics, among others, but which are valuable within this work are:

1. The eigenfunctions form an orthogonal set over the closed interval $x_1 \leq x \leq x_2$, with respect to the weighting function h.

2. The eigenfunctions form a complete set, such that a piecewise-continuous function of x defined over the interval $x_1 \leq x \leq x_2$ may be expanded.

3. An infinite number of eigenfunctions with discrete eigenvalues exists.

Such a Sturm-Liouville system holds e.g. for the special case of a homogeneous rectangular waveguide considered in section 5.7, where separation of the variables is performed in Cartesian coordinates.

5.5 General Orthogonality Principle

A vectorial and more general orthogonality principle can be derived from the Lorentz reciprocity principle as demonstrated in [Col91]. It is required for instance for a waveguide with walls having a finite conductivity where the eigenfunctions no longer satisfy the boundary conditions stated in Eq. (5.76) and where the various E and H modes cross couple. Additionally in inhomogeneously filled waveguides, the propagating modes are usually combinations of E and H modes. Therefore, a more general orthogonality relation is demanded in order to expand any arbitrary field into a series of the very modes. For the derivation, $\boldsymbol{H}_{tn}$, $\boldsymbol{E}_{tn}$ and $\boldsymbol{H}_{tm}$, $\boldsymbol{E}_{tm}$ are designated as transverse fields for two linearly independent solutions of Maxwell's equations [Col91]. For each solution, the curl equation for the electric field gives

$$\nabla \times \boldsymbol{E}_n = -\mathrm{j}\omega \boldsymbol{H}_n \qquad \nabla \times \boldsymbol{E}_m = -\mathrm{j}\omega \boldsymbol{H}_m, \tag{5.85}$$

where $\boldsymbol{H}_n$, $\boldsymbol{E}_n$ and $\boldsymbol{H}_m$, $\boldsymbol{E}_m$ include the axial and the transverse components. The latter equations are scalarly multiplied by $\boldsymbol{H}_m$ and $\boldsymbol{H}_n$, respectively, and subsequent subtraction renders

$$\boldsymbol{H}_m \cdot \nabla \times \boldsymbol{E}_n - \boldsymbol{H}_n \cdot \nabla \times \boldsymbol{E}_m = 0. \tag{5.86}$$

Analogously, the same procedure is applied to the curl equations for the magnetic field yielding an equivalent result but with the roles of $\boldsymbol{E}$ and $\boldsymbol{H}$ interchanged:

$$\boldsymbol{E}_m \cdot \nabla \times \boldsymbol{H}_n - \boldsymbol{E}_n \cdot \nabla \times \boldsymbol{H}_m = 0. \tag{5.87}$$

The addition of these two equations results in

$$\nabla \cdot (\boldsymbol{E}_n \times \boldsymbol{H}_m - \boldsymbol{E}_m \times \boldsymbol{H}_n) = 0. \tag{5.88}$$

Since the fields $\boldsymbol{E}_n$, $\boldsymbol{H}_n$ and $\boldsymbol{E}_m$, $\boldsymbol{H}_m$ depend on the z-coordinate with $\mathrm{e}^{\gamma_n z}$ and $\mathrm{e}^{\gamma_m z}$, respectively, this equation can be expressed as

$$\begin{aligned} \nabla \cdot (\boldsymbol{E}_n \times \boldsymbol{H}_m - \boldsymbol{E}_m \times \boldsymbol{H}_n) &= \nabla_t \cdot (\boldsymbol{E}_n \times \boldsymbol{H}_m - \boldsymbol{E}_m \times \boldsymbol{H}_n) \\ &\quad - (\gamma_n + \gamma_m)\boldsymbol{e}_z \cdot (\boldsymbol{E}_{tn} \times \boldsymbol{H}_{tm} - \boldsymbol{E}_{tm} \times \boldsymbol{H}_{tn}) = 0. \end{aligned} \tag{5.89}$$

By application of the two-dimensional form of the divergence theorem to the waveguide cross section bounded by the contour C one gets

$$\iint\limits_S \nabla_t \cdot (\boldsymbol{E}_n \times \boldsymbol{H}_m - \boldsymbol{E}_m \times \boldsymbol{H}_n)\, dA = \oint\limits_C \boldsymbol{n} \cdot (\boldsymbol{E}_n \times \boldsymbol{H}_m - \boldsymbol{E}_m \times \boldsymbol{H}_n)\, dl. \tag{5.90}$$

The contour integral vanishes because $\boldsymbol{n} \times \boldsymbol{E}_n$ and $\boldsymbol{n} \times \boldsymbol{E}_m$ vanish, that is particularly true for perfectly electric and perfectly magnetic conducting walls and fields at infinity, and the latter expression on the right-hand side of (5.89) remains as

$$(\gamma_n + \gamma_m) \iint\limits_S \boldsymbol{e}_z \cdot (\boldsymbol{E}_{tn} \times \boldsymbol{H}_{tm} - \boldsymbol{E}_{tm} \times \boldsymbol{H}_{tn})\, dA = 0. \tag{5.91}$$

Eq. (5.91) also holds on imperfect conductors by using the impedance boundary condition $\boldsymbol{E}_t = Z_m \boldsymbol{n} \times \boldsymbol{H}$ [Col91] since the integrand is zero on the waveguide contour. By the introduction of transverse fields in the form

$$\boldsymbol{H}_{tn} = \boldsymbol{h}_n(u, v)\mathrm{e}^{-\gamma_n z}, \tag{5.92}$$

$$\boldsymbol{E}_{tn} = \boldsymbol{e}_n(u, v)\mathrm{e}^{-\gamma_n z}, \tag{5.93}$$

with $\boldsymbol{h}_n$ and $\boldsymbol{e}_n$ as transverse vector functions of the transverse coordinates u, v, Eq. (5.91) becomes

$$(\gamma_n + \gamma_m) \iint\limits_S \boldsymbol{e}_z \cdot (\boldsymbol{e}_n \times \boldsymbol{h}_m - \boldsymbol{e}_m \times \boldsymbol{h}_n)\, dA = 0. \tag{5.94}$$

It can be demonstrated that each cross product term disappears separately, which is the desired orthogonality condition. For this purpose, the two solutions $\boldsymbol{E}_n$, $\boldsymbol{H}_n$ and $\boldsymbol{E}'_m$, $\boldsymbol{H}'_m$ are considered where $\boldsymbol{E}'_m$, $\boldsymbol{H}'_m$ is the same mode as before but now oppositely directed in z-direction. The direction of the transverse magnetic field is hence reversed. The equation analogue to Eq. (5.94) is

$$(\gamma_n - \gamma_m) \iint\limits_S \boldsymbol{e}_z \cdot (-\boldsymbol{e}_n \times \boldsymbol{h}_m - \boldsymbol{e}_m \times \boldsymbol{h}_n)\, dA = 0. \tag{5.95}$$

Addition and subtraction of the latter equation in both forms referring to a propagation direction in positive and in negative direction eventually yields

$$\iint\limits_S (\boldsymbol{e}_n \times \boldsymbol{h}_m) \cdot \boldsymbol{e}_z\, dA = 0, \tag{5.96}$$

$$\iint\limits_S (\boldsymbol{e}_m \times \boldsymbol{h}_n) \cdot \boldsymbol{e}_z\, dA = 0. \tag{5.97}$$

In the absence of losses it can moreover be shown that

$$\iint\limits_{S} (\boldsymbol{e}_n \times \boldsymbol{h}_m^*) \cdot \boldsymbol{e}_z dA = 0 \tag{5.98}$$

with $\boldsymbol{h}_m^*$ the complex conjugate of $\boldsymbol{h}_m$. Eq. (5.98) evidences that the power flow in a lossfree guide is the sum of the power transported by each mode individually. The outcome in Eqs. (5.96) and (5.97) is even valid for two degenerate modes which are an E mode and an H mode as considered in [Col91]. Completeness considerations of vector modes are again based on modal representations of the Dirac delta functions and the properties of the integral transforms with the corresponding Green's functions. Further considerations on this topic can be found in [CH53].

5.6 Transverse Electromagnetic Field Type

A wave type with cut-off frequency zero is the transverse electromagnetic field type (TEM) existing in a waveguide with a homogeneous cross section and a multi-conductor configuration as mentioned earlier e.g. *cf.* section 5.2, and it can be deduced from the E and H modes, respectively:

E/TM modes:
For $\gamma_E = \mathrm{j}k$, $q_E = 0$ results and it is

$$\Delta_t \psi_{Et} = 0: \qquad \text{Laplace equation}$$

$$\boldsymbol{E} = \frac{1}{\mathrm{j}\omega\mu\varepsilon} \nabla \times \nabla \times \boldsymbol{A}$$

$$= -\frac{\gamma_E}{\mathrm{j}\omega\mu\varepsilon} \nabla_t \psi_E \rightarrow E_z = 0$$

$$\boldsymbol{H} = \frac{1}{\mu} \nabla \times \boldsymbol{A}$$

$$= -\frac{1}{\mu} \boldsymbol{e_z} \times \nabla_t \psi_E \rightarrow H_z = 0$$

H/TE modes:
For $\gamma_H = \mathrm{j}k$, $q_H = 0$ results and it follows

$$\Delta_t \psi_{Ht} = 0: \qquad \text{Laplace equation}$$

$$\boldsymbol{E} = -\frac{1}{\varepsilon} \nabla \times \boldsymbol{F}$$

$$= \frac{1}{\varepsilon} \boldsymbol{e_z} \times \nabla_t \psi_H \rightarrow E_z = 0$$

$$\boldsymbol{H} = \frac{1}{\mathrm{j}\omega\mu\varepsilon} \nabla \times \nabla \times \boldsymbol{F}$$

$$= -\frac{\gamma_H}{\mathrm{j}\omega\mu\varepsilon} \nabla_t \psi_H \rightarrow H_z = 0$$

In case the Laplace equation is satisfied in the transverse plane, the gradient of suitable scalar functions arises. The name TEM already preludes that both fields do not possess a component in propagation direction. Their E and H fields are perpendicular to each other, that means that the E and H fields are interchanged for both field types. The boundary conditions eventually decide which field type exists in a waveguide. A TEM wave is basically the fundamental mode of propagation on a transmission line exhibiting a potential difference between two separated conductors. Such a TEM wave can never exist on a waveguide, of which the cross section is completely closed by a continuous conductive material and no other electrically insulated conductor exist inside the enclosure. Therefore, no potential difference can develop like in e.g. a coaxial cable.

5.7 Rectangular Hollow Waveguide

In this section, the eigenvalue equations according to (5.58) and (5.61) are solved explicitly [FM94] for the finite rectangular region depicted in Fig. 5.2 with vertical side length b and horizontal side length a. The shape of the waveguide cross section is bounded by perfectly conducting walls. In this case, the transverse Laplace operator is represented by

$$\Delta_t = \nabla_t^2 = \frac{\partial^2}{\partial x^2} + \frac{\partial^2}{\partial y^2}. \tag{5.99}$$

The product ansatz can be formulated as

$$\psi_t = \psi_{t0} \psi_{k_x}(x) \psi_{k_y}(y), \tag{5.100}$$
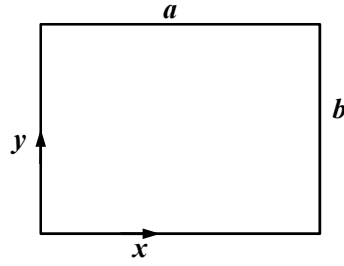
Figure 5.2: Rectangular cross section of a waveguide.

where the factor ψ_{t0} is a constant amplitude factor carrying appropriate physical units. The boundary condition for the E modes reads $\psi_{Et} = 0$, named direct or Dirichlet condition, whereas for the H modes the indirect or Neumann condition $\frac{\partial}{\partial n}\psi_{Ht} = 0$ holds on the metallic walls at $x = 0; a$ and $y = 0; b$. In the following, the solutions for H modes are regarded more in detail being more significant within this work. Since the cross-section is homogeneous the vector eigenvalue equation can be scalarised into two one-dimensional equations

$$\left(\frac{d^2}{dx^2} + k_x{}^2\right)\psi_{Hk_x}(x) = 0, \qquad \frac{\partial}{\partial x}\psi_{Hk_x}(0) = \frac{\partial}{\partial x}\psi_{Hk_x}(a) = 0, \tag{5.101}$$

$$\left(\frac{d^2}{dy^2} + k_y{}^2\right)\psi_{Hk_y}(y) = 0, \qquad \frac{\partial}{\partial y}\psi_{Hk_y}(0) = \frac{\partial}{\partial y}\psi_{Hk_y}(b) = 0, \tag{5.102}$$

in which k_x and k_y are separation constants or eigenvalues and are related to the transverse wavenumber q_H in Eq. (5.62) by

$$q_H^2 = k_x{}^2 + k_y{}^2. \tag{5.103}$$

Similar relations are valid for the E mode functions.
Respecting the boundary conditions, the solutions to the eigenvalue equations (5.101) and (5.102) are found to be

$$\psi_{Hk_x}(x) = \sqrt{\frac{2}{a}}\cos(k_x x), \quad \text{with } k_x = \frac{m\pi}{a}, \ m = 1, 2, 3, \cdots; \quad \psi_{H0}(x) = \frac{1}{\sqrt{a}} \tag{5.104}$$

$$\psi_{Hk_y}(y) = \sqrt{\frac{2}{b}}\cos(k_y y), \quad \text{with } k_y = \frac{n\pi}{b}, \ \ n = 1, 2, 3, \cdots; \quad \psi_{H0}(y) = \frac{1}{\sqrt{b}} \tag{5.105}$$

The multiplicative constants are necessary for normalisation reasons, which is

$$\int_0^a \psi_{Hk_x}^2(x)dx = 1 = \int_0^b \psi_{Hk_y}^2(y)dy. \tag{5.106}$$

The orthogonality property of the eigenfunctions is proven by

$$\int_0^a \cos\left(\frac{m\pi x}{a}\right)\cos\left(\frac{m'\pi x}{a}\right)dx = 0, \quad m \neq m'; \quad m, m' = 0, 1, 2, 3, ..., \tag{5.107}$$

where $\psi_{Hk_y}(y)$ satisfies the property as well. It can be formulated in one single orthonormality relation

$$\int_0^a \boldsymbol{\psi}_{Hk_x}(x)\boldsymbol{\psi}_{Hk_x{}'}(x)dx = \delta_{k_x k_x{}'} = \begin{cases} 1, & k_x = k_x{}' \\ 0, & k_x \neq k_x{}', \end{cases} \tag{5.108}$$

where $\delta_{m,n}$ is the Kronecker delta. The proofs of (5.107) and (5.108) are evident due to the Sturm-Liouville type of (5.101) and (5.102) as well as the boundary conditions. Alike, completeness and orthonormality of the mode set $\psi_{Hk_x}(x)$ is satisfied as in Eq. (5.84) by the delta function:

$$\delta(x - x') = \sum_{m=0}^{\infty} \psi_{Hk_x}(x)\psi_{Hk_y}(x') = \frac{1}{a}\sum_{m=0}^{\infty} \varepsilon_m \cos(k_x x)\cos(k_x x'), \qquad 0 < x, x' < a, \tag{5.109}$$

with the Neumann factor ε_m, which is

$$\varepsilon_m = \begin{cases} 1, & m = 0 \\ 2, & m \neq 0. \end{cases} \tag{5.110}$$

The eigenfuntions for the two-dimensional, rectangular region conclude by multiplication of the two one-dimensional solutions. The two-dimensional delta function can be represented by $\delta(\boldsymbol{\rho} - \boldsymbol{\rho}') = \delta(x - x')\delta(y - y')$ and it is concisely

$$\delta(\boldsymbol{\rho} - \boldsymbol{\rho}') = \frac{1}{ab}\sum_{m=0}^{\infty}\sum_{n=0}^{\infty}\varepsilon_m\varepsilon_n\cos\left(\frac{m\pi x}{a}\right)\cos\left(\frac{n\pi y}{b}\right)\cos\left(\frac{m'\pi x}{a}\right)\cos\left(\frac{n'\pi y}{b}\right), \tag{5.111}$$
$$0 < x, x' < a, \quad 0 < y, y' < b.$$

The orthonormality relation consequently holds for the two-dimensional function set as well as it does for the one-dimensional.

H Mode (TE Mode) Field Components

The H_{mn} waves feature $E_z = 0$. The other components ensue from the two-dimensional transverse scalar potential

$$\psi_{Ht} = \psi_{t0}\sqrt{\frac{\varepsilon_m\varepsilon_n}{ab}}\cos\left(\frac{m\pi}{a}x\right)\cos\left(\frac{n\pi}{b}y\right) \tag{5.112}$$

with respect to Eqs. (5.55)-(5.56) as

$$H_z = \frac{\psi_{t0}}{j\omega\mu}\sqrt{\frac{\varepsilon_m\varepsilon_n}{ab}}\left(k_x^2 + k_y^2\right)\cos(k_x x)\cos(k_y y)e^{-\gamma_H z}, \tag{5.113}$$

$$H_x = \frac{\gamma_H\psi_{t0}}{j\omega\mu}\sqrt{\frac{\varepsilon_m\varepsilon_n}{ab}}k_x\sin(k_x x)\cos(k_y y)e^{-\gamma_H z}, \tag{5.114}$$

$$H_y = \frac{\gamma_H\psi_{t0}}{j\omega\mu}\sqrt{\frac{\varepsilon_m\varepsilon_n}{ab}}k_y\sin(k_y y)\cos(k_x x)e^{-\gamma_H z}, \tag{5.115}$$

$$E_x = H_y Z_{FH}, \tag{5.116}$$

$$E_y = -H_x Z_{FH}, \tag{5.117}$$

fulfilling the features of Fig. 5.2. The wave impedance specific for the H mode is Z_{FH}

$$Z_{FH} = \frac{j\omega\mu}{\gamma_H} = \frac{\lambda_g}{\lambda_{HPW}} Z_F \quad \text{and} \quad Z_F = \sqrt{\frac{\mu}{\varepsilon}} \tag{5.118}$$

with the wavelength in the waveguide

$$\lambda_g = \frac{\lambda_{HPW}}{\sqrt{1 - \left(\frac{\lambda_{HPW}}{\lambda_c}\right)^2}} \tag{5.119}$$

and λ_{HPW} as the wavelength of the homogeneous plane wave let it be in free space or in dielectric substrate if the waveguide is filled with one. The cut-off wavelength λ_c is derived from the separation equation in general as follows:

$$\lambda_c = \frac{1}{\sqrt{\left(\frac{m}{2a}\right)^2 + \left(\frac{n}{2b}\right)^2}} \tag{5.120}$$

The phase constant at cut-off is β_c which is related to the cut-off wavelength as $\beta_c = \frac{2\pi}{\lambda_c}$. At cut-off, it is $q_H^2 = \beta_c^2 = k_x^2 + k_y^2$ analogue to Eq. (5.62). The H_{mn} modes comprise the fundamental mode with $m = 1$, $n = 0$, and (5.112) yields

$$E_y = -\psi_{t0}\sqrt{\frac{2}{ab}} \sin\left(\frac{\pi}{a}x\right) e^{-\gamma_H z}, \tag{5.121}$$

$$H_{-x} = \frac{E_y}{Z_{FH}}, \tag{5.122}$$

$$H_z = \frac{\psi_{t0}}{j\omega\mu}\sqrt{\frac{2}{ab}} \left(k_x^2 + k_y^2\right) \cos\left(\frac{\pi}{a}x\right) e^{-\gamma_H z}. \tag{5.123}$$

From Eq. (5.120), $\lambda_c = 2a$ results with $m = 1$ and $n = 0$. Usually, the various field types are denoted by two indices m, n, which give clue on the number of half waves or extremes in the different coordinate directions of the cross section. The H_{10} mode is particularly beneficial because it has the lowest critical frequency f_c and thus it occupies a certain frequency range, in which only itself is able to propagate. So, no interference with higher order modes is to expect. This fact can be exploited in applications like waveguides or antennas in which single mode operation must be ensured.

E Mode (TM Mode) Field Components

For E modes, the solution functions are to derive in a similar manner taking into account the Dirichlet boundary condition for the sake of which, cosine is to exchange by sine. The E_{mn} waves with $H_z = 0$ arise from the transversal scalar potential for the electric field

$$\psi_{Et} = \frac{2\psi_{t0}}{\sqrt{ab}} \sin\left(\frac{m\pi x}{a}\right) \sin\left(\frac{n\pi y}{b}\right), \tag{5.124}$$

where the prefactor is chosen for normalisation reasons and to account for the appropriate physical units. With respect to Eqs. (5.51) and (5.52), the components result as

$$E_z = \frac{2\psi_{t0}}{j\omega\varepsilon\sqrt{ab}}(k_x^2 + k_y^2)\sin(k_x x)\sin(k_y y)e^{-\gamma_E z}, \tag{5.125}$$

$$E_x = \frac{-2\gamma_E\psi_{t0}}{j\omega\varepsilon\sqrt{ab}}k_x\cos(k_x x)\sin(k_y y)e^{-\gamma_E z}, \tag{5.126}$$

$$E_y = \frac{-2\gamma_E\psi_{t0}}{j\omega\varepsilon\sqrt{ab}}k_y\sin(k_x x)\cos(k_y y)e^{-\gamma_E z}, \tag{5.127}$$

$$H_x = \frac{-E_y}{Z_{FE}}, \tag{5.128}$$

$$H_y = \frac{E_x}{Z_{FE}}. \tag{5.129}$$

Solutions for $m = 0$ or $n = 0$ are not possible without violating the boundary conditions. The wave impedance for the E field is

$$Z_{FE} = \frac{\gamma_E}{j\omega\varepsilon} = \frac{\lambda_{HPW}}{\lambda_g}Z_F. \tag{5.130}$$

Transport of Energy

For H_{mn} modes in general, the transferred complex power in time average is

$$\boldsymbol{S} = \frac{1}{2}\{\boldsymbol{E} \times \boldsymbol{H}^*\} \tag{5.131}$$

$$S_z = \frac{1}{2}\left\{E_x H_y^* - E_y H_x^*\right\} = \frac{1}{2}\left\{\frac{1}{Z_{FH}^*}(|E_x|^2 + |E_y|^2)\right\}, \tag{5.132}$$

$$P = \int_{y=0}^{b}\int_{x=0}^{a} S_z dx dy = \frac{|\psi_{t0}|^2}{2Z_{FH}^*}\left(k_x^2 + k_y^2\right) \tag{5.133}$$

for effective field quantities in the mean time average. From Eq. (5.133), a factor can be deduced in order to normalise the field components thus assuring energy transport of 1 Watt per m^2.

Mode Patterns

The corresponding mode patterns of the instantaneous field distribution are shown in Fig 5.3 and Fig. 5.4. Plots of the electric and magnetic fields are helpful for the illustration of the field distributions of the various modes. One type of pattern visualises the electric and magnetic field strengths on transverse and longitudinal planes within the waveguide. It delivers information about the locations of maximum field strength, power flow etc. The other kind of pattern presents the magnetic field intensity or rather current density on the inner surface of the waveguide walls. The current flow is indicative of dissipation and of coupling by apertures in the waveguide walls. All in all, they provide understanding of the field behaviour. Not only give they hints for the design of equivalent circuit diagrams but also for the appropriate design of electromagnetic structures guiding the modes, what is important. Electric field lines are drawn as solid, while magnetic field lines and electric current lines are dashed lines [ZB65].

(a) Front view   (b) Vertical longitudinal side view
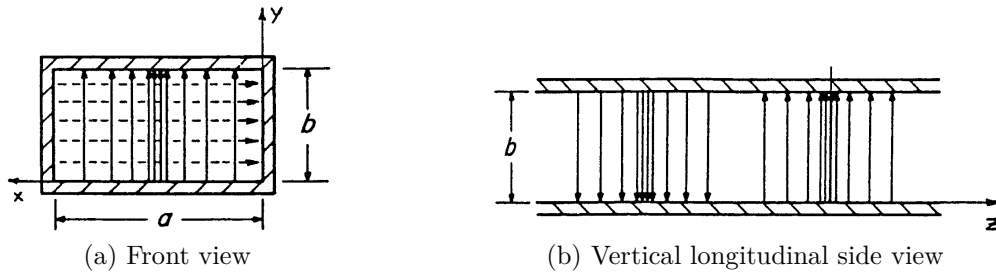
Figure 5.3: Field distributions of the H_{10} mode in the rectangular waveguide. Electric field lines are solid, magnetic field lines are dashes.

Current Circuits

To fulfill the boundary conditions at perfectly conducting waveguide walls, the tangential electric field vanishes and according to (5.7), the electric surface current density ensues with

$$\boldsymbol{J_F} = \boldsymbol{n} \times \boldsymbol{H}(0). \tag{5.134}$$

Hence, the electric surface current density forces the magnetic field to zero. Losses in the waveguide walls are calculated via perturbation computation by assuming a finite conductive layer in which the surface wall currents flow homogeneously distributed and which matches with the exponential current distribution in the lossy conductor ("skin" effect). The power loss is integrated and is summed up over transversal and longitudinal side walls. With increasing frequencies, the longitudinal losses dominate, the transversal losses vanish gradually. Not only the ohmic losses need to be accounted for but also the dielectric losses, because they are frequency-dependent as well. Losses as well as radiation contribute to the attenuation constant α as real part of the propagation constant of a guided mode and the loss considerations are useful for interpreting the value of α.

Again, for illustration of the wall currents, $t = t_0$ is chosen and $\boldsymbol{j_F} = \boldsymbol{f}(x, y, z)$ is drawn in time domain [ZB65]. Fig. 5.5a depicts the electric and magnetic field lines and the corresponding wall currents. They can be divided into longitudinal currents (Fig. 5.5b)

(a) Horizontal longitudinal side view   (b) Surface currents on the walls
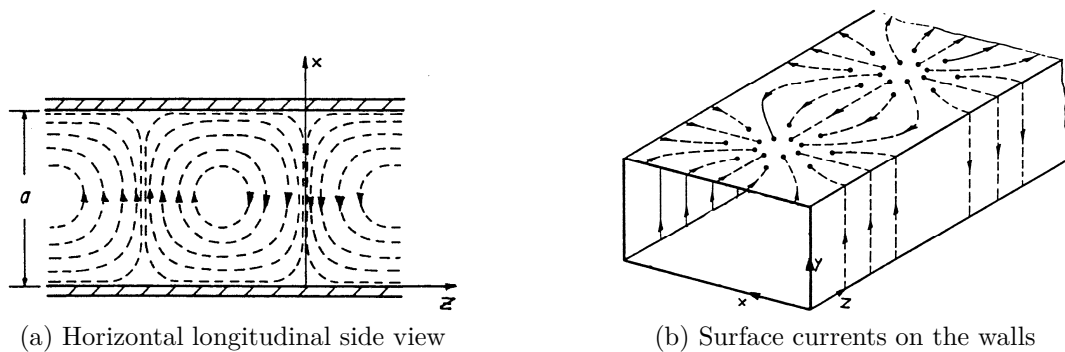
Figure 5.4: Field distributions and surface currents of the H_{10} mode. Electric field lines are solid, magnetic field lines are dashes.

and transversal currents (Fig. 5.5c). Current circuits are closed by displacement currents (Fig. 5.6a and Fig. 5.6b).

(a) Electric and magnetic field lines and surface currents

(b) Longitudinal wall currents

(c) Transverse currents
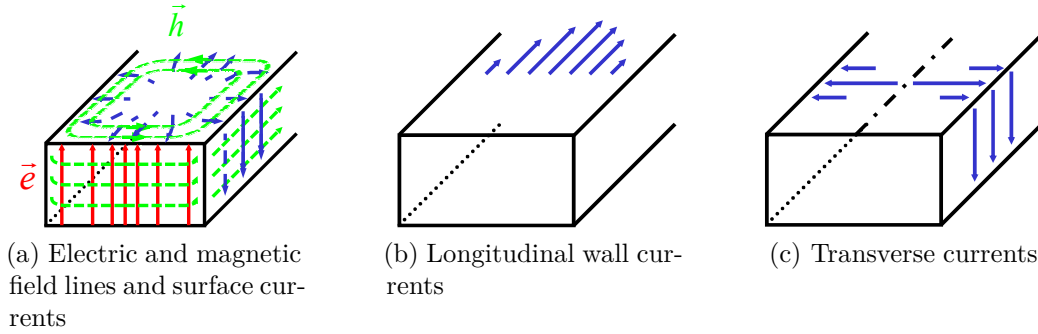
Figure 5.5: Surface wall currents of the H_{10} mode in the rectangular waveguide.

(a) Longitudinal side view

(b) Displacement currents
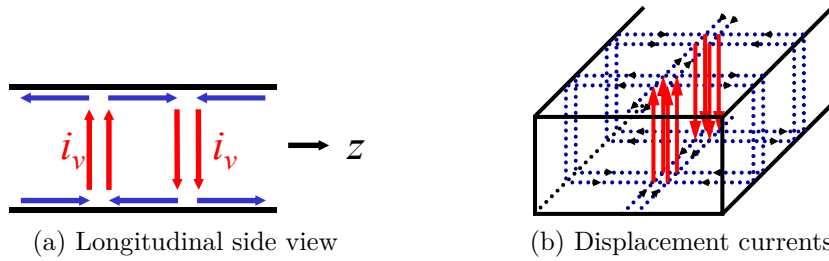
Figure 5.6: Continuation of electric currents by displacement currents.

From the course of the currents and the field distribution, the equivalent circuits (EQCs) can be concluded. With view to the EQC of the TEM transmission line wave, the rectangular hollow waveguide mode H_{10} is represented by lumped circuit elements as well (Fig. 5.7a). As for TEM waves, only short lengths Δz of transmission lines compared to wavelength are embodied by lumped elements (Fig. 5.7b).

Comparing to transmission-line theory, the line impedance for H modes results from the longitudinal and transversal reactive loadings

$$Z_{L(H)} = \sqrt{\frac{X'_{long.}}{B'_{transv.}}} = \sqrt{\frac{L'_s}{C'}} \frac{1}{\sqrt{1 - \left(\frac{\omega_c}{\omega}\right)^2}} \tag{5.135}$$

$$\text{with} \quad \omega_c = \frac{1}{\sqrt{L'_p C'}}. \tag{5.136}$$

The EQC of the H_{10} wave is similar to the EQC of a TEM line but the metal side walls of a waveguide cause transversal currents and hence shunt inductances. The resonant frequency of the shunt resonator is equivalent with f_c of the rectangular waveguide. Higher order H modes reveal a similar EQC with only varied values of the lumped elements.

For completeness, the mode patterns and the EQC of the electric wave type are displayed. By setting $m = 1$ and $n = 1$, the first electric mode is obtained of which the mode patterns are to find in Fig. 5.8a. The EQC of the electric wave types is illustrated

in Fig. 5.8b, which furnishes the dual case to Fig. 5.7 in the sense that the shunt resonant circuit is replaced by a resonant circuit in series and the series inductance is substituted by a shunt capacitance.

(a) Lumped circuit elements represent the H_{10} mode.

(b) Lumped circuit elements for a short length Δz
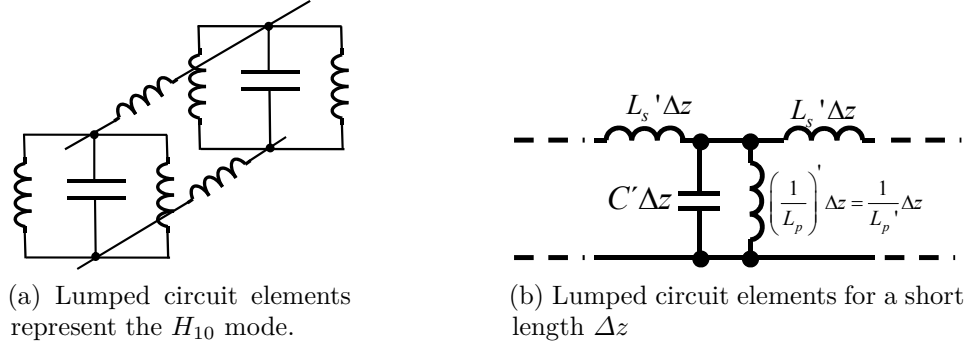
Figure 5.7: EQC of the H_{10} mode.

(a) Field pattern of the E_{11} mode [Mar51]

(b) Equivalent circuit
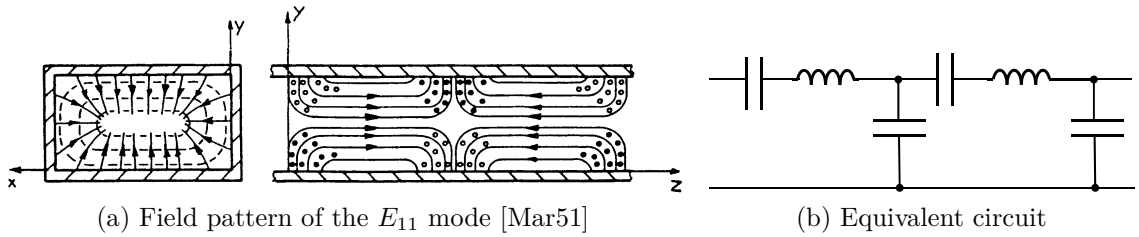
Figure 5.8: Equivalent circuit for E modes.

The transmission line impedance can also be given in terms of field quantities. Since the focus in this work is especially on periodic structures the Bloch impedance Z_B [Col00],[Poz04] is preferably to consider *cf.* 3.3. In particular, the transmission line or Bloch impedance is relevant for matching purposes. Though not unique it is a characteristic quantity for every eigensolution and is the ratio of voltage and current according to the corresponding EQC, where voltage is associated with the electric field and current with the magnetic field according to

$$V = \int_{C_v} \boldsymbol{E} \cdot \boldsymbol{n}_{ground} ds, \tag{5.137}$$

$$I = \int_{C_i} (\boldsymbol{n}_{ground} \times \boldsymbol{H}) \cdot \boldsymbol{n}_{port} ds. \tag{5.138}$$

For the line or Bloch impedance three definitions can consequently be given:

$$Z_{B,VI} = \frac{V}{I}, \tag{5.139}$$

$$Z_{B,PI} = \frac{2P}{|I|^2}, \tag{5.140}$$

$$Z_{B,PV} = \frac{|V|^2}{2P}, \tag{5.141}$$

where the transported power is

$$P = \frac{1}{2} \iint\limits_{S} (\boldsymbol{E} \times \boldsymbol{H}^*) \cdot \boldsymbol{n}_{port} dA. \tag{5.142}$$

The integration paths in the cross section are illustrated in Fig. 5.9. Nevertheless, only for TEM-waveguides the three definitions deliver the same result for the characteristic impedance because the transverse fields are gradient fields. In non-TEM guiding architectures like rectangular waveguides, only the power flow together with the longitudinal component of the surface wall current appear as physically most self-evident. Therefore, a definition of the characteristic impedance according to Eq. (5.140) is preferred. The definition of voltage instead significantly depends on the line of integration. The field distribution of the electric field for the H_{10} mode is given in Eq. (5.121). For definition of (5.139), different equivalent circuit models may be obtained, which describe the same traits of the considered mode, provided they remain consistent within the equivalent circuit.
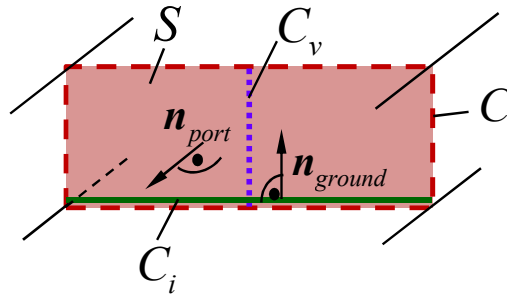
Figure 5.9: Ways of integration in the plane to compute Z_B.

5.8 Energy Transfer of Evanescent Modes

The modal solutions of the periodically loaded waveguides are formulated by series expansion in the eigensolutions of the host waveguides *cf.* chapter 4. The method is well-known [Col91] but as it is also applied to the frequency range where the host waveguides by itself exhibit no wave propagation it is to investigate whether the series expansion is usable in this frequency range, too. The cut-off frequency of the fundamental mode of the background waveguide is the key threshold below which traditionally no wave propagation occurs. By having introduced periodicities, wave propagation in the left-handed sense is yet enabled in the former evanescent frequency domain. If wave propagation is now to observe below the former cut-off frequency a representation by series expansion with evanescent waves must be possible as well.

Real power transfer above cut-off is stated in Eq. (5.133). It follows to demonstrate that evanescent modes can transfer real power as well as shown in [WE10b]. The study reduces to transverse components $\boldsymbol{E}_t$, $\boldsymbol{H}_t$ of TE modes according to Eqs. (5.55), (5.56)

considered in an appropriately chosen orthogonal curvilinear coordinate system:

$$\boldsymbol{e}_z S_z = \frac{1}{2} \operatorname{Re} \left\{ \boldsymbol{E}_t \times \boldsymbol{H}_t^* \right\} \cdot \boldsymbol{e}_z. \tag{5.143}$$

The examination starts with the complex fields of two oppositely directed evanescent modes in any cross-sectional plane in the waveguide where $\gamma_H = \alpha$ and ε, μ are assumed to be real quantities. The index f stands for forward and b for backward directed waves:

$$\boldsymbol{E}_t = \frac{1}{\varepsilon} \left(\psi_{0f} \mathrm{e}^{-\gamma_H z + \mathrm{j}\varphi_f} + \psi_{0b} \mathrm{e}^{\gamma_H z + \mathrm{j}\varphi_b} \right) (\boldsymbol{e}_z \times \nabla_t \psi_{Ht}), \tag{5.144}$$

$$\boldsymbol{H}_t^* = \frac{\gamma_H}{\mathrm{j}\omega\mu\varepsilon} \left(\psi_{0f} \mathrm{e}^{-\gamma_H z - \mathrm{j}\varphi_f} - \psi_{0b} \mathrm{e}^{\gamma_H z - \mathrm{j}\varphi_b} \right) \nabla_t \psi_{Ht}^*, \tag{5.145}$$

which yields

$$\frac{1}{2} \operatorname{Re} \left\{ \boldsymbol{E}_t \times \boldsymbol{H}_t^* \right\} = \frac{1}{2} \operatorname{Re} \Bigg\{ \frac{-\gamma_H}{\mathrm{j}\omega\mu\varepsilon^2} |\nabla_t \psi_{Ht}|^2 \left(\psi_{0f}^2 \mathrm{e}^{-2\gamma_H z} - \psi_{0b}^2 \mathrm{e}^{2\gamma_H z} \right.$$
$$\left. - 2\mathrm{j}\psi_{0f}\psi_{0b} \sin\left(\varphi_f - \varphi_b \right) \right) \Bigg\} \tag{5.146}$$
$$= \frac{\gamma_H}{\omega\mu\varepsilon^2} |\nabla_t \psi_{Ht}|^2 \psi_{0f}\psi_{0b} \sin\left(\varphi_f - \varphi_b \right). \tag{5.147}$$

For evanescent waves, it is $\gamma_H = \alpha$ indicating exponential decay or increase. The result verifies that the Poynting vector possesses a real part, signifying real power transport if the forward and backward wave differ in their phases. It is to imagine as superimposition of the in forward and in backward direction decaying waves.

Lastly, the focus has particularly been on hollow waveguide modes in a rectangular waveguide because the H_{10} hollow waveguide mode provides the starting point for the substrate integrated waveguide designs presented in this work. The SIW structures exhibit modes with a cut-off frequency. However, the goal of this work is to generalise the concept of waveguides and arbitrary waveguiding structures are investigated exhibiting any kind of modes. For this purpose, a grounded dielectric slab is chosen as prototype which features not only modes with a cut-off frequency but also one without, namely the TM_0 mode.

In addition, a grounded dielectric slab waveguide is a representer of open problems which call for a more cleverly devised computation strategy as considered so far, which is addressed in chapter 6.

5.9 *H* Waves and *E* Waves on the Grounded Dielectric Slab

Surface waves can exist in a variety of geometries involving dielectric interfaces. Besides grounded dielectric slabs, surface waveguides furthermore incorporate ungrounded dielectric slabs, dielectric rods, corrugated conductors or dielectric coated conducting rods to name a few. The wave impedance normal to the air-dielectric interface can be shown to be reactive promoting wave guidance along the boundary. Here a coated dielectric slab is considered as a very basic guiding type with a reactive surface. For the typification of surface waves, the field exponentially decays away from the dielectric surface, which is physically reasonable, while the electromagnetic wave travels along the dielectric layer. The field is mostly contained in or near the dielectric and becomes more bound to it with increasing frequencies.

In the sequel, the eigensolutions of the modes on the grounded homogeneous dielectric slab are derived to supply the basis functions in the modal series expansion when applied to the periodically modified grounded dielectric slab waveguide in chapter 8.3.

The analytical eigensolutions of the simple grounded dielectric slab depicted in Fig. 5.10 are also to find in literature, e.g. [Har01],[Poz04],[Ish90]. The solving procedure is the same as for the three-layer structure examined in section 5.10. Further details are hence to find there. The solutions for the TM modes, synonymic for *E* modes, are easily obtained from the TE case by the principle of duality. The solution for the TE mode type, synonymic for *H* modes, is considered as later TE modes are promoted to exist on the slab. Generally, a field ansatz is to apply for every layer and the tangential fields are to match at the interfaces of the layers. To distinguish the wavenumbers of the various layers, the notation of the wavenumber $k_x = k'_x - \mathrm{j}k''_x$ is preferred to $\gamma = \alpha + \mathrm{j}\beta$. The two forms are related in the way $\gamma = \mathrm{j}k$. Together with the separation equations, a set of transcendental equations is derived. The ansatz for the *H* wave type guarantees the tangential electric field to vanish at the conductor referring to the geometry in Fig. 5.10. Therefore, the transverse functional dependence is odd. The ansatz is

$$\psi_{H1} = A\cos(k_{x1}x)\mathrm{e}^{-\mathrm{j}k_z z} \tag{5.148}$$

$$\psi_{H2} = B\mathrm{e}^{-k''_{x2}x}\mathrm{e}^{-\mathrm{j}k_z z} \tag{5.149}$$

for layer 1 and for layer 2, respectively, and denoted by the corresponding subscripts. The
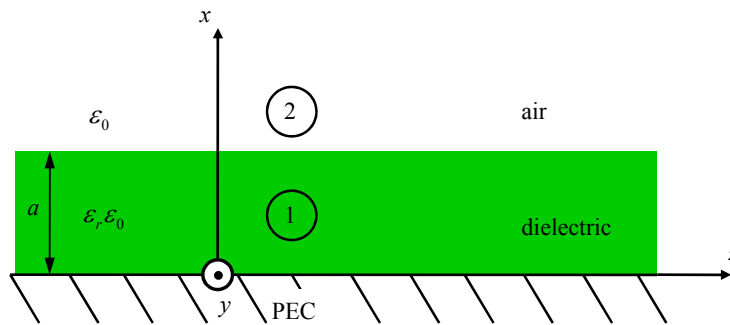
Figure 5.10: Grounded dielectric slab geometry.

wavenumber k_z is identical in both regions since belonging to one wave existing in both layers equally. The transverse wavenumber in medium 1 is k_{x1}. For the air layer, it is $k_{x2} = -\mathrm{j}k''_{x2}$ in order to ensure $\mathrm{e}^{-k''_{x2}x}$ with k''_{x2} real and to provide physically reasonable field solutions. As such, the field decays with increasing distance. The ansatz for both regions has to fulfill the Helmholtz equation in the way

$$\Delta_t \psi_{Ht1,2} + (k_{1,2}^2 - k_z^2)\psi_{Ht1,2} = 0. \tag{5.150}$$

The field components are

$$\begin{aligned} E_{y1} &= \frac{\partial}{\partial x}\psi_{H1} \\ &= -Ak_{x1}\sin(k_{x1}x)\mathrm{e}^{-\mathrm{j}k_z z} \end{aligned} \tag{5.151}$$

$$\begin{aligned} H_{x1} &= \frac{1}{\mathrm{j}\omega\mu_0}\frac{\partial^2}{\partial x\partial z}\psi_{H1} \\ &= A\frac{k_z k_{x1}}{\omega\mu_0}\sin(k_{x1}x)\mathrm{e}^{-\mathrm{j}k_z z} \end{aligned} \tag{5.152}$$

$$\begin{aligned} H_{z1} &= \frac{1}{\mathrm{j}\omega\mu_0}\left(\frac{\partial^2}{\partial z^2} + k^2\right)\psi_{H1} \\ &= A\frac{k_0^2\varepsilon_r - k_z^2}{\mathrm{j}\omega\mu_0}\cos(k_{x1}x)\mathrm{e}^{-\mathrm{j}k_z z} \end{aligned} \tag{5.153}$$

for region 1, and for region 2

$$E_{y2} = \pm Bk''_{x2}\mathrm{e}^{-k''_{x2}x}\mathrm{e}^{-\mathrm{j}k_z z} \tag{5.154}$$

$$H_{x2} = \pm B\frac{k_z k''_{x2}}{\omega\mu_0}\mathrm{e}^{-k''_{x2}x}\mathrm{e}^{-\mathrm{j}k_z z} \tag{5.155}$$

$$H_{z2} = B\frac{k_0^2 k_z^2}{\mathrm{j}\omega\mu_0}\mathrm{e}^{-k''_{x2}x}\mathrm{e}^{-\mathrm{j}k_z z}. \tag{5.156}$$

A and B are constants to be determined in a way that the field continuity conditions are fulfilled. The permeability is $\mu_{1,2} = \mu_0\mu_r$ with $\mu_r = 1$. The permittivity in region 2 is just ε_0 with $\varepsilon_r = 1$, but in region 1, it is $\varepsilon_r \neq 1$. Further, the separation equations for region 1 and for region 2 are

$$k_{x1}^2 + k_z^2 = k_0^2\varepsilon_r \tag{5.157}$$

$$-k_{x2}^{''2} + k_z^2 = k_0^2. \tag{5.158}$$

By fulfilling the continuity condition of the tangential components at the dielectric-air interface and by considering the separation equations, transcendental equations follow as

$$-k''_{x2} = k_{x1}\cot(k_{x1}a) \tag{5.159}$$

$$k''_{x2} = \sqrt{k_0^2(\varepsilon_r - 1) - k_{x1}^2}, \tag{5.160}$$

where a is the height of the dielectric. Equations (5.159) and (5.160) must be solved simultaneously for the variables k_{x1} and k''_{x2} in the real $k_{x1}a, k''_{x2}a$-plane as shown in Fig. 5.11. The found intersections are inserted in Eq. (5.157) or Eq. (5.158) giving the final solutions
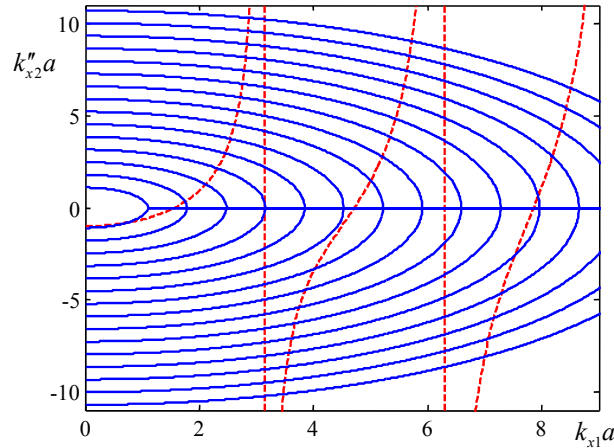
Figure 5.11: Intersections of cotangens with semicircles increasing with frequency deliver solutions.

for propagation constant k_z and frequency as plotted in Fig. 5.12. The second equation (5.160) represents semicircles, of which the radius increases with frequency. Solutions for $k''_{x2} < 0$ are called improper or leaky modes. Since they make physically no sense they are normally excluded from the solution but in [HHMS91], it is pointed out that information about the exact position of such leaky wave poles is valuable for enhancing the computation efficiency of the steepest descent method [FM94]. This method is applied to evaluate improper integrals which arise from solving for the fields in open regions. The first TE mode does not start to propagate as guided wave until the radius of the semicircle becomes greater than $\pi/2$. At cut-off, it is $k_z = k_0$ as the lowest real value of k_z from (5.158) and from (5.157), k_z becomes at most $k_z = k_0\sqrt{\varepsilon_r}$. This makes sense with regard to phase velocity which is faster than that of a plane wave in dielectric $1/\sqrt{\mu_0\varepsilon_0\varepsilon_r}$ but lower than that in free space $1/\sqrt{\mu_0\varepsilon_0}$. In contrast, a TM_0 mode with zero cut-off exists because the tangent function replaces the cotangent function in the transcendental equations for TM mode types as will be seen shortly. The first branch of the tangent function starts at zero. Hence, a TM mode with zero cut-off is present. The cut-off frequencies of the TE_n modes can be determined by

$$f_c = \frac{(2n-1)c}{4a\sqrt{\varepsilon_r - 1}}, \quad \text{for} \quad n = 1, 2, 3, \ldots \tag{5.161}$$

and are obtained if $k''_{x2} = 0$ and $k_z = k_0$. The cut-off frequencies by Eq. (5.161) are depicted as diamond symbols in Fig. 5.12 for an example waveguide and match the transition from the leaky into the guided state obtained by the intersections. The cut-off frequencies for the first to the third mode are: 5.72 GHz, 17.17 GHz and 28.62 GHz. Above these frequencies, the modes hence appear as guided surface waves. The corresponding solution curves are depicted in Fig. 5.12 as continuous lines with crosses. The modes are trapped in the dielectric and are called trapped surface waves. Below cut-off, they show up as leaky waves. The corresponding solutions are marked as single crosses in Fig. 5.12.

Mathematically, leaky and guided waves exist simultaneously because one semicircle representative for one frequency may intersect the cotangent curve in the negative as well as in the positive part. The first branch supports only leaky modes at low frequencies.
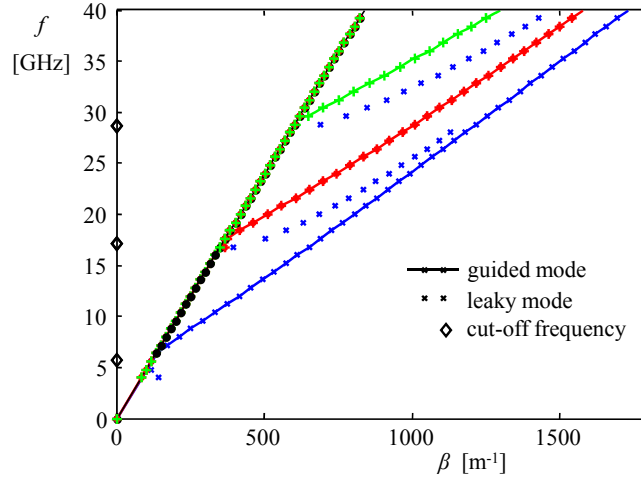
Figure 5.12: Graphical solution of the characteristic equations for a grounded dielectric slab with thickness 7 mm and $\varepsilon_r = 4.5$.

The transversal functional dependence of TM modes in x-direction is even. The ansatz for layer 1 and layer 2 is

$$\psi_{E1} = A\sin(k_{x1}x)\mathrm{e}^{-\mathrm{j}k_z z} \tag{5.162}$$

$$\psi_{E2} = B\mathrm{e}^{-k_{x2}''x}\mathrm{e}^{-\mathrm{j}k_z z}. \tag{5.163}$$

The fields are obtained from the function ψ_E by equations dual to Eqs. (5.151)-(5.156), which are

$$E_{x1} = \frac{-k_z k_{x1}}{\omega\varepsilon_0\varepsilon_r}A\cos(k_{x1}x)\mathrm{e}^{-\mathrm{j}k_z z} \tag{5.164}$$

$$E_{z1} = \frac{A}{\mathrm{j}\omega\varepsilon_0\varepsilon_r}(k_0^2\varepsilon_r - k_z^2)\sin(k_{x1}x)\mathrm{e}^{-\mathrm{j}k_z z} \tag{5.165}$$

$$H_{y1} = -Ak_{x1}\cos(k_{x1}x)\mathrm{e}^{-\mathrm{j}k_z z} \tag{5.166}$$

in the dielectric and in air, they read

$$E_{x2} = \frac{k_z k_{x2}''B}{\omega\varepsilon_0}\mathrm{e}^{-k_{x2}''x}\mathrm{e}^{-\mathrm{j}k_z z} \tag{5.167}$$

$$E_{z2} = \frac{B}{\mathrm{j}\omega\varepsilon_0}(k_0^2 - k_z^2)\mathrm{e}^{-k_{x2}''x}\mathrm{e}^{-\mathrm{j}k_z z} \tag{5.168}$$

$$H_{y2} = k_{x2}''B\mathrm{e}^{-k_{x2}''x}\mathrm{e}^{-\mathrm{j}k_z z}. \tag{5.169}$$

The detailed derivation of the solution for this kind of mode is given in [Ish90]. The transcendental set of equations for the TM wave type results as

$$k_{x2}'' = \frac{k_{x1}}{\varepsilon_r}\tan(k_{x1}a) \tag{5.170}$$

$$k_{x2}'' = \sqrt{k_0^2(\varepsilon_r - 1) - k_{x1}^2}, \tag{5.171}$$

where $k_{x2} = -\mathrm{j}k_{x2}''$ again asserts physically reasonable solutions. The cut-off frequencies of the TM_n modes can be determined by

$$f_c = \frac{(2n-2)c}{4a\sqrt{\varepsilon_r - 1}} \quad \text{for} \quad n = 1, 2, 3, \ldots. \tag{5.172}$$

A and B are again determined by the continuity conditions of the tangential components. Then, the field configurations for the TM modes are achieved together with the obtained solutions for the eigenvalue k_{x1} characteristic of the geometry and the propagation constant k_z for TE modes correspondingly [Ish90].

5.10 Analytical Solution for the Shielded Three-Layer Model

Another homogeneous waveguiding configuration is the shielded three-layer model as displayed in Fig. 5.13, which is bounded at x_{min} and x_{max} by PEC. An infinite extension in the y- and z-directions is assumed. Furthermore, propagation in the positive z-direction is supposed and expressed by a $\mathrm{e}^{-\mathrm{j}k_z z}$ propagation factor, with k_z the wavenumber in z-direction. The invariance in y-direction is considered by $\frac{\partial}{\partial y} = 0$. The dielectric layer is
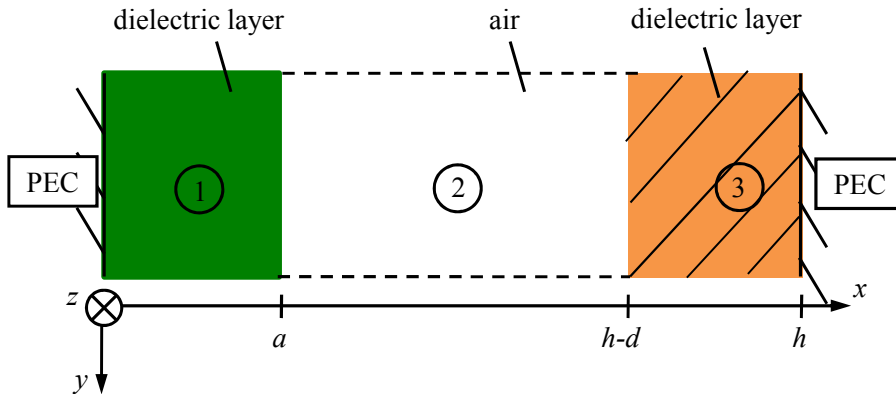
Figure 5.13: A grounded dielectric slab waveguide with air region and PEC terminated dielectric cover layer.

located at $0 \leq x \leq a$, the air region extends from $a < x < h - d$ and another dielectric layer from $h - d \leq x \leq h$. The permittivity and permeability are generally denoted by the appropriate subscript for the regions $1, 2, 3$. Since having three distinct regions, three field solutions must be individually found in the first step. In the second step, the continuity criterion of the tangential fields has to be satisfied at the interfaces. For a simple dielectric slab, the even TM modal solution constitutes the dual solution to the odd TE modal solution and vice versa. For the metal-backed dielectric slab in region 1, only the odd TE mode function supplies a solution and the even TM eigenfunction. Odd and even refers to the transverse fields, i.e. in x-direction. In the following, TE modes are considered but the solution for TM modes can simply be derived by the principle of duality. Consequently for region 1, the ansatz for the TE or H mode reads

$$\psi_{H1} = A\cos(k_{x1}x)\mathrm{e}^{\mathrm{j}k_z z} \tag{5.173}$$

with k_x as wavenumber in x-direction. All wavenumbers are complex numbers. In the sequel, A, B, C, D are arbitrary constants to be determined. The media are characterised by $k_i = \omega\sqrt{\varepsilon_i\mu_i}$ with $i = 1, 2, 3$ and $\varepsilon_i = \varepsilon_0\varepsilon_{ri}$, $\mu_i = \mu_0\mu_{ri}$. The field components follow as

$$H_{x1} = \frac{Ak_{x1}k_z}{\omega\mu_1}\sin\left(k_{x1}x\right)e^{-jk_z z} \tag{5.174}$$

$$H_{y1} = 0 \tag{5.175}$$

$$H_{z1} = \frac{A}{j\omega\mu_1}\left(k_1^2 - k_z^2\right)\cos\left(k_{x1}x\right)e^{-jk_z z} \tag{5.176}$$

and

$$E_{x1} = 0 \tag{5.177}$$

$$E_{y1} = -Ak_{x1}\sin\left(k_{x1}x\right)e^{-jk_z z} \tag{5.178}$$

$$E_{z1} = 0. \tag{5.179}$$

It is evident that the tangential electric field component vanishes at the boundary $x = 0$, which is PEC. For the air region 2, two solution parts exist accounting for a wave propagating in positive direction and one in negative x-direction. Thus, the ansatz is

$$\psi_{H2} = \left(Be^{-jk_{x2}x} + Ce^{jk_{x2}x}\right)e^{-jk_z z}. \tag{5.180}$$

The field components then read

$$H_{x2} = \frac{k_{x2}k_z}{j\omega\mu_2}\left(Ce^{jk_{x2}x} - Be^{-jk_{x2}x}\right)e^{-jk_z z} \tag{5.181}$$

$$H_{y2} = 0 \tag{5.182}$$

$$H_{z2} = \frac{k_2^2 - k_z^2}{j\omega\mu_2}\left(Be^{-jk_{x2}x} + Ce^{jk_{x2}x}\right)e^{-jk_z z} \tag{5.183}$$

$$E_{x2} = 0 \tag{5.184}$$

$$E_{y2} = jk_{x2}\left(Ce^{jk_{x2}x} - Be^{-jk_{x2}x}\right)e^{-jk_z z} \tag{5.185}$$

$$E_{z2} = 0. \tag{5.186}$$

For the third region, the ansatz is

$$\psi_{H3} = D\cos\left(k_{x3}(x - h)\right)e^{-jk_z z} \tag{5.187}$$

and the field components are

$$H_{x3} = \frac{Dk_{x3}k_z}{\omega\mu_3}\sin\left(k_{x3}(x - h)\right)e^{-jk_z z} \tag{5.188}$$

$$H_{y3} = 0 \tag{5.189}$$

$$H_{z3} = \frac{D}{j\omega\mu_3}\left(k_3^2 - k_z^2\right)\cos\left(k_{x3}(x - h)\right)e^{-jk_z z} \tag{5.190}$$

$$E_{x3} = 0 \tag{5.191}$$

$$E_{y3} = -Dk_{x3}\sin\left(k_{x3}(x - h)\right)e^{-jk_z z} \tag{5.192}$$

$$E_{z3} = 0. \tag{5.193}$$

The separation parameter equations in each region ensue with

$$k_{x1}^2 + k_z^2 = k_1^2 = \omega^2 \varepsilon_1 \mu_1 \tag{5.194}$$

$$k_{x2}^2 + k_z^2 = k_2^2 = \omega^2 \varepsilon_2 \mu_2 \tag{5.195}$$

$$k_{x3}^2 + k_z^2 = k_3^2 = \omega^2 \varepsilon_3 \mu_3. \tag{5.196}$$

The matching of the tangential E- and H-components at the dielectric-air interface $x = a$ gives

$$-k_{x1} A \sin(k_{x1} x) = \mathrm{j} k_{x2} \left(C \mathrm{e}^{\mathrm{j} k_{x2} x} - B \mathrm{e}^{-\mathrm{j} k_{x2} x} \right) \tag{5.197}$$

$$\frac{A}{\mu_1} k_{x1}^2 \cos(k_{x1} x) = \frac{k_{x2}}{\mu_2} \left(B \mathrm{e}^{-\mathrm{j} k_{x2} x} + C \mathrm{e}^{\mathrm{j} k_{x2} x} \right). \tag{5.198}$$

The ratio of the second equation to the first and solving for the ratio of the unknown constants yields

$$\frac{C}{B} = \frac{\left(\mathrm{j} \frac{k_{x1}}{k_{x2}} \frac{\mu_2}{\mu_1} \cot(k_{x1} a) - 1 \right) \mathrm{e}^{-\mathrm{j} 2 k_{x2} a}}{\mathrm{j} \frac{k_{x1}}{k_{x2}} \frac{\mu_2}{\mu_1} \cot(k_{x1} a) + 1}. \tag{5.199}$$

Continuity of E_y and H_z at $x = h - d$ requires that

$$\mathrm{j} k_{x2} \left(C \mathrm{e}^{\mathrm{j} k_{x2}(h-d)} - B \mathrm{e}^{-\mathrm{j} k_{x2}(h-d)} \right) = -D k_{x3} \sin(-k_{x3} d) \tag{5.200}$$

$$\frac{k_{x2}^2}{\mu_2} \left(B \mathrm{e}^{-\mathrm{j} k_{x2}(h-d)} + C \mathrm{e}^{\mathrm{j} k_{x2}(h-d)} \right) = \frac{k_{x3}^2}{\mu_3} D \cos(-d k_{x3}). \tag{5.201}$$

From the ratio of the second to the first expression and determination of the ratio of $\frac{C}{B}$ gives the second condition for the unknown constants B and C

$$\frac{C}{B} = \frac{\left(\mathrm{j} \frac{k_{x3} \mu_2}{k_{x2} \mu_3} \cot(-d k_{x3}) - 1 \right) \mathrm{e}^{-\mathrm{j} 2 k_{x2}(h-d)}}{\mathrm{j} \frac{k_{x3} \mu_2}{k_{x2} \mu_3} \cot(-d k_{x3}) + 1}. \tag{5.202}$$

By equating 5.199 and 5.202, the following condition follows

$$\frac{\left(\mathrm{j} \frac{k_{x3} \mu_2}{k_{x2} \mu_3} \cot(-d k_{x3}) - 1 \right) \mathrm{e}^{-\mathrm{j} 2 k_{x2}(h-d)}}{\mathrm{j} \frac{k_{x3} \mu_2}{k_{x2} \mu_3} \cot(-d k_{x3}) + 1} - \frac{\left(\mathrm{j} \frac{k_{x1}}{k_{x2}} \frac{\mu_2}{\mu_1} \cot(k_{x1} a) - 1 \right) \mathrm{e}^{-\mathrm{j} 2 k_{x2} a}}{\mathrm{j} \frac{k_{x1}}{k_{x2}} \frac{\mu_2}{\mu_1} \cot(k_{x1} a) + 1} = 0. \tag{5.203}$$

The roots of Eq. (5.203) deliver the propagation constant and offer an alternative to the more costly graphical procedure presented in section 5.9. The roots can be found numerically for instance by a Newton-Raphson algorithm, which can be moreover easily applied to the case where the root is complex i.e. in the presence of losses.

6 Treatment of Open Region Problems

6.1 Integral Representation and Modal Expansion

The topic of wave representations in open regions is partly following [TO63], which gives a good introduction into the subject. Closed waveguides furnish discrete modes which may propagate without or with attenuation, in the latter case the propagation constants are complex. Most discrete modes are however completely evanescent. Regarding open waveguiding structures, the boundaries are extended to infinity in some directions causing the discrete modes falling closer and closer together until they coalesce in the limit into a continuous spectrum of modes. A discrete set of modes can be interpreted as kind of a generalised Fourier series whereas a continuous spectrum of modes relates to a corresponding Fourier integral. Besides the continuous spectrum of modes, which describes the radiation behaviour, a discrete set of modes may exist which constitutes any kind of surface waves.

In the sequel, wave representations are investigated in a geometry as depicted in Fig. 6.1 which is composed of a semi-infinite free-space region limited by a plane boundary which may either be a distinct surface such as an ideal conductor or a transition boundary between free space and other defined media e.g. layered dielectric media. The boundary condition at the interface is assumed to be invariant in y- and z-direction and hence, it may be expressed by an impedance function being specified at the interface for every single mode i in the transverse x-direction and being independent of y and z. k_x is the transverse wavenumber and characteristic for the corresponding modes. In accordance with the y-invariance, the corresponding unit source of either electric or magnetic type is a line source parallel to the y-axis and it is located at $z = 0$. The Green's function describing the problem at and above the interface $x \geq 0$ reads

$$G(x, z) = \frac{1}{2\pi} \int\limits_{-\infty}^{\infty} f(k_z) \mathrm{e}^{-\mathrm{j}k_x x} \mathrm{e}^{-\mathrm{j}k_z z} dk_z, \tag{6.1}$$

which refers to a longitudinal representation of modes. The field in Eq. (6.1) consists of a continuous spectrum with purely real eigenvalues ranging from negative to positive infinity. The time dependence $\mathrm{e}^{\mathrm{j}\omega t}$ is self-evident. Electric or magnetic line currents excite TM modes or TE modes, respectively, and $G(x, z)$ is proportional to the y-component of these modes. The term $f(k_z)$ is the specified amplitude function which contains the primary excitation of the line source and the reflection coefficient at the interface, which depends on the impedance function as well as on the location of the source. The Green's function in Eq. (6.1) represents a Fourier transform with respect to k_z expressing the field by plane waves, where the 1D integration is performed along the real axis in the complex k_z-plane according to [Som09] to maintain a field expansion in homogeneous media. The wavenumbers k_x and k_z are related via the separation equation with $k = \omega\sqrt{\mu\varepsilon}$

corresponding to plane waves in free space and it is

$$k_x = \pm\sqrt{k^2 - k_z^2}.$$ (6.2)

For a unique interpretation of the square root function, a two-sheeted Riemann surface is
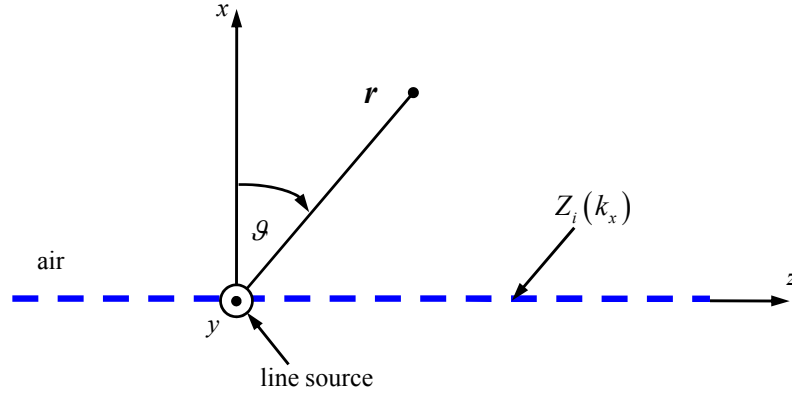
Figure 6.1: Configuration of the interface

defined such that one value or branch is assigned to one Riemann sheet and the other one to a second Riemann sheet. The two Riemann sheets are connected at arbitrary branch cuts linking the branch points. One pair of branch points results from Eq. (6.2) as $k_z = \pm k$ and another one can be assumed at ∞. In the complex k_z-plane, branch cuts are extended from the branch points $\pm k$ to infinity. The obtained Riemann sheets are categorised as proper and improper to distinguish between physically reasonable and unreasonable modal field solutions. The original Sommerfeld integration path [Som09] along the real k_z-axis gives a converging integral in Eq. (6.1). By extending k_z into the complex plane, the integration path can be deformed according to Cauchy's integral formula. However, the path must be deformed with care in order to maintain the convergence of the integral and singularities must not be crossed. However, poles can be considered separately according to Cauchy's residue theorem.

A proper solution of the problem also includes that the integral in Eq. (6.1) vanishes at infinity. The considered configuration in Fig. 6.1 requires the boundary condition as

$$\mathrm{Im}\,\{k_x\} < 0,$$ (6.3)

in order that the waves decay properly with $x \to \infty$. This boundary condition must be taken into account for a proper definition of the square root function and thus the branch cut in the complex k_z-plane. The branch cuts are chosen in the way that proper and improper sheets are clearly separated. Consequently, the upper half of the k_x-plane plots on the top sheet of the two-sheeted Riemann k_z-plane. This sheet is proper and depicted in Fig. 6.2. Also the chosen branch cuts are drawn, which are obtained from Eq. (6.2), linking the branch points $\pm k$ according to (6.2) with infinity in a way that the top Riemann sheet for k_z is mapped on $\mathrm{Im}\,\{k_x\} < 0$. For the branch cuts, $\mathrm{Im}\,\{k_x\} = -k_x'' = 0$ and infinitesimal losses for the free-space wavenumber, that is

$$0 < |\,\mathrm{Im}\,\{k\}^2\,| << |k|^2,$$ (6.4)

are assumed. The advantage of the chosen branch cuts is that the transverse integral representation that will be obtained by a contour deformation as considered below is a spectral one and the integration along the entire real k_z-axis (Sommerfeld integration path) is properly performed in the top sheet agreeing with the boundary condition.

In contrast to the integration in the complex k_z-plane corresponding to a longitudinal spectral representation, Eq. (6.1) can be evaluated in the complex k_x-plane which refers to a transverse representation of modes. Then, the former integration path P is transformed towards the path P' along a semicircle at $-\infty$ as demonstrated in Fig. 6.2 for positive z. For negative z, the semicircle would be in the upper half of the top sheet of the k_z-plane.
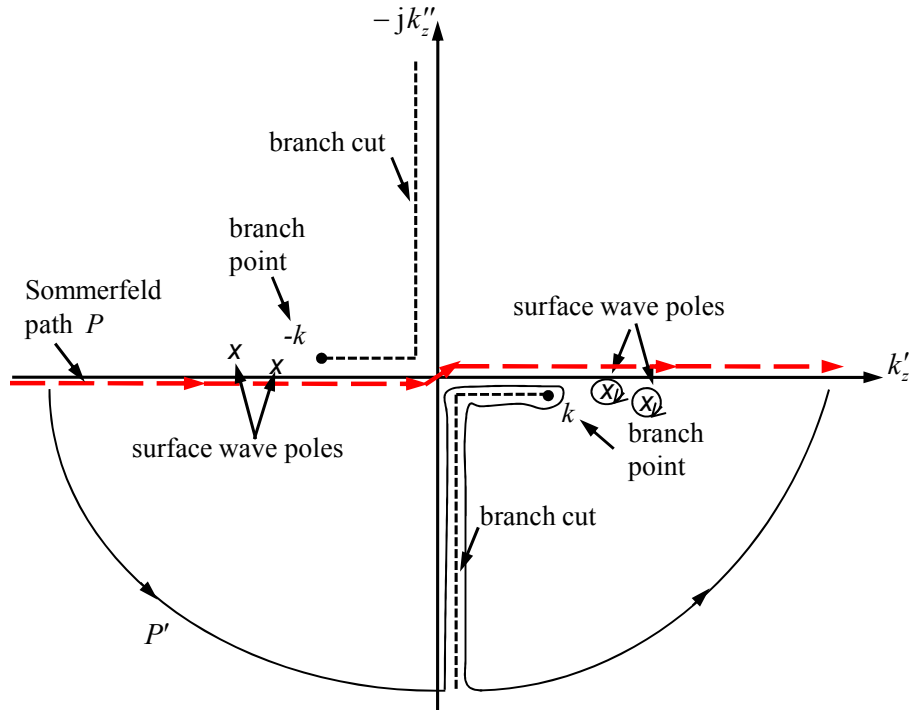
Figure 6.2: The complex k_z-plane (top sheet)

By Cauchy's theorem for complex integration [Col91], Eq. (6.1) may be expressed as

$$G(x, z) = \frac{1}{2\pi} \left[\int_{-\infty}^{\infty} \left(f(k_z(k_x)) e^{-jk_x x} e^{-jk_z z} \frac{dk_z}{dk_x} \right) dk_x + 2\pi j \sum \text{residues} \right], \qquad (6.5)$$

since the semicircle at infinity does not contribute to the integral. The integration is hence performed along the entire real k_x-axis, thus a path around the branch cuts in Fig. 6.2 as defined before. The residues account for potential pole singularities which are proper because they only occur in the top sheet of the k_z-plane and their fields are identified as surface waves *cf.* section 5.9. Improper poles never occur since they are in the lower half of the k_x-plane, which the path P' does not include. Contrary to the longitudinal representation of Eq. (6.1) yielding a continuous spectrum of modes, the transverse representation additionally spawns a discrete spectrum, which however exhibits directly the discrete waves associated with a waveguide. The continuous spectrum whereas

is not bound at the interface and may account for radiation. The poles of the field appear from the poles of $f(k_z(k_x))$ and more explicitly from the poles in the reflection coefficient $R(k_x)$ contained in $f(k_z(k_x))$ meaning that

$$Z_i(k_x) + Z_0(k_x) = 0, \qquad\qquad\qquad (6.6)$$

which is defined at the interface. $Z_i(k_x)$ is the specified impedance at the interface and $Z_0(k_x)$ the characteristic impedance of the semi-infinite transmission line in the transverse resonance method [FM94] representative for the free space. All poles of $R(k_x)$ correspond to proper eigenvalues of the spectral transverse representation if Eq. (6.3) is also fulfilled. Whenever the amplitude $|R(k_x)| \to \infty$ waves propagating in $\pm z$-direction are found which are the surface waves.

The disadvantage of the form of Eq. (6.5) is that it has only brought little progress in solving it compared to Eq. (6.1). For an explicit and complete but asymptotically approximate solution for the field at the interface and in the free space region above it, the steepest-descent representation is usually employed and treated extensively in literature, e.g. [TO63, FM94]. The great advantage of (6.5) for the present work is that it is closely related to the discrete modal expansion as used before for the treatment of closed problems. The branch cut integral can be considered as a correction to the guided mode series necessary due to the open problem. In order to utilise this representation, a procedure for the efficient evaluation of the branch cut integral is to find.

The deformation of the path of integration and the treatment of open region problems has been investigated comprehensively, e.g. [FM94],[MB87]. To circumvent the difficulties, the idea is to restore the open field problem to a closed computation domain. For this work, arbitrary open waveguiding structures are relevant. According to the strategy, they are shielded by perfectly electric conducting boundaries. To preserve the characteristics of an open problem a perfectly matched layer (PML) can be placed in front of the PEC to absorb the reflections and to pretend as if the PEC would not be present. With view to Fig. 6.3, the branch points $\pm k$ do then not exist anymore, since the wavenumber k_x only appears squared as k_x^2 in the integrand [FM94]. By deforming the integration path to $-\mathrm{j}\infty$ the original continuous path collapses into discrete residue pole contributions. The pole contributions can be handled in exactly the same way as the guided modes in the series representation. This result can be seen as a numerical integration of the integral in Eq. (6.5), which is exact. This concept has been proposed in [DdZO98], [DOdZvdB01], [RdZ02]. The corresponding discrete modes in the PML covered waveguide have been used for a mode-matching solution of step transitions in finite layered substrates. However, [DOdZvdB01] was restricted to homogeneous layered structures, where the discrete modes can be derived analytically. Possible courses of the loci of the poles for the resulting waveguide in [DOdZvdB01] are exemplarily indicated in Fig. 6.3. So-called PML modes appear of which the field mainly resides in the PML. Additionally, evanescent modes occur similar to leaky modes in the open waveguide which also contribute to the complete spectrum in the closed configuration [DOdZvdB01]. Notwithstanding, the procedure in [DOdZvdB01] is restricted to problems where an analytical eigensolution is derivable. By including numerical tools for evaluating 2D eigensolutions, the modal expansion technique will be more universal. In summary, a complicated integration technique is avoided and
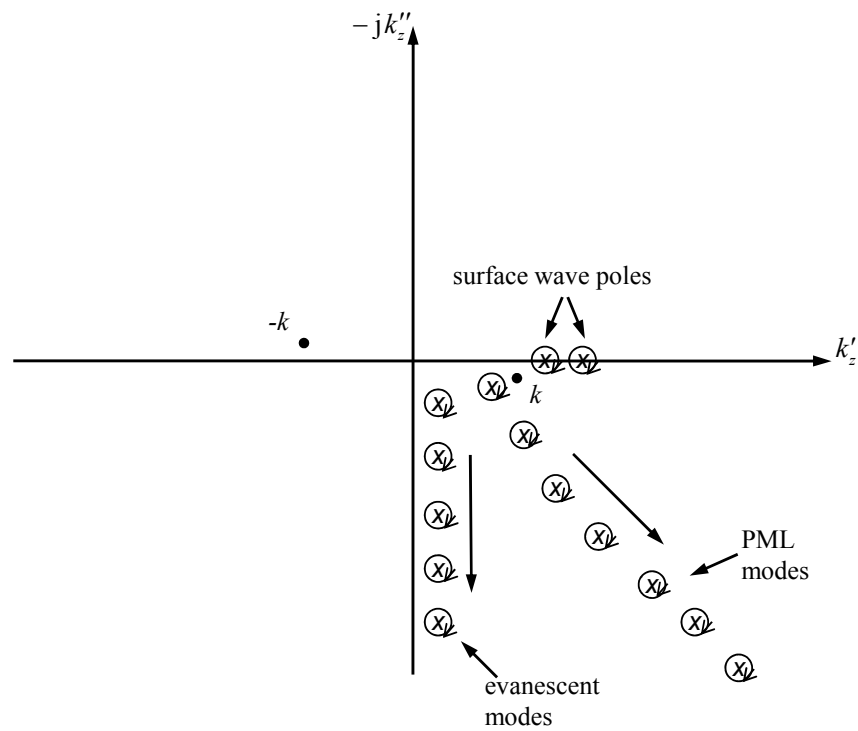
Figure 6.3: Discrete modes for the dielectric-air-PML-PEC configuration in [DOdZvdB01].

the solution to the open-region eigenproblem can be conveniently captured by a series expansion as formulated in chapter 4. The numerical implementation of such a procedure is yet not straightforward, since the determination of the discrete PML modes is hampered by the strange material properties of PML.

6.2 Transformation of Open Region Problem to Equivalent Closed Region Problem

The modal series expansion as formulated in chapter 4 does not represent a complete modal field solution for problems of the open type. To circumvent complicated integration procedures required to evaluate arising improper integrals for open regions, the idea is adopted to convert the open problem into a closed configuration as already suggested in [SW77],[MHJ80] for non-radiating structures. By introducing a PML in front of the PEC boundary [DOdZvdB01], the reflections of the PEC shall be minimised to that grade that they do not disturb the field solutions of the problem. The PML preserves the information of the open configuration while the resulting closed problem can efficiently be described by a discrete set of substrate, evanescent and so-called PML modes of the equivalent closed anisotropic waveguide. The PML modes are mainly located in the PML. In order to expand the restricted application range of [DOdZvdB01], the eigensolutions of the subregions are not deduced analytically for the method in this work. A purely numerical approach would however be plagued by the strange material properties of the PML, being active and anisotropic. Thus, to avoid an inclusion of a PML in the simulation, an isotropic absorbing layer is conceived which is simple and lossy fulfilling the task of a PML. CST MWS is then used to deliver the 2D eigensolutions for the port regions transversally placed with regard to the longitudinal axis of the waveguide. The ports cover the complete cross section including the absorption layer. Conversely to other solution processes, where modes with the field concentrated in the absorption layer are identified as unphysical and undesired, these modes provide here necessary information in the series expansion. Surface modes below the cut-off frequency mainly appear in the air layer or at lower frequencies even in the absorbing layer since they were originally leaky.

6.2.1 Perfectly Matched Layer

In 1994, J. P. Bérenger succeeded in presenting a perfectly matched layer (PML) boundary condition [Ber94] as effective means to truncate finite-difference time-domain (FDTD) lattices enabling to treat open problems with the FDTD technique. Compared to other matched layers at that time, the PML perfectly absorbs plane waves which may strike a vacuum-layer interface at any frequency and observation angle. Later, the PML was adapted to function in finite-element methods (FEM) [WKLL02]. Originally, the PML was derived by 2D considerations. Later, the analysis of PML was extended to full 3D dimensions [KTT94] and moreover to nonorthogonal grids [NWCL94],[RG97]. In 1997, a PML working in cylindrical and spherical grids has been derived by Teixeira et al. [TC97] using a complex stretching approach already introduced in [CW94]. The advantage is that the PML behaves as an isotropic layer due to its complex thickness. As such, the closed-form solutions of Maxwell's equations can be mapped onto the PML media by analytical continuation of the spatial variables in the complex domain. Gedney [Ged96] further developed the concept of an uniaxial anisotropic PML, introduced by Sacks et al. [SKLL95], working in lossy and dispersive media amending Bérenger's PML to better attenuate not only propagating but also evanescent waves.

The key elements for understanding the uniaxial anisotropic PML are outlined in the

following as to find concisely in [DOdZvdB01]. With view to Fig. 6.4, the PML is here limited by PEC at $x = h$ and by the air layer at $x = h - d_{PML}$. Its formative relations
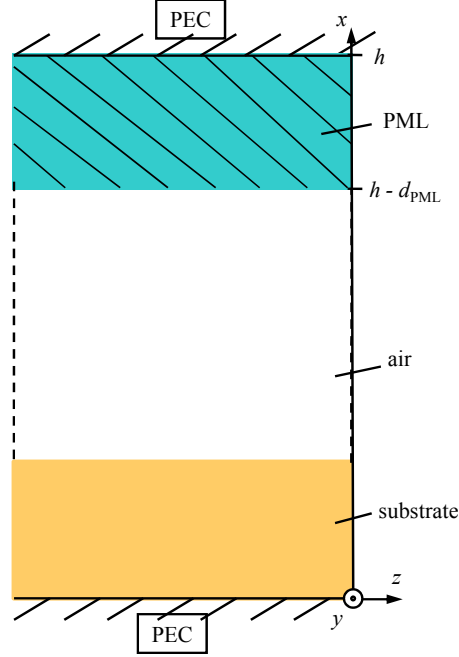
Figure 6.4: The 3-layer structure substrate, air, PML

are

$$\boldsymbol{D} = \varepsilon\bar{\boldsymbol{\alpha}} \cdot \boldsymbol{E} \tag{6.7}$$

$$\boldsymbol{B} = \mu\bar{\boldsymbol{\alpha}} \cdot \boldsymbol{H} \tag{6.8}$$

where $\bar{\boldsymbol{\alpha}}$ is in particular

$$\bar{\boldsymbol{\alpha}} = \begin{pmatrix} \frac{1}{\alpha(x)} & 0 & 0 \\ 0 & \alpha(x) & 0 \\ 0 & 0 & \alpha(x) \end{pmatrix} \tag{6.9}$$

and

$$\alpha(x) = 1 + (\kappa_0 - 1)f(x) - \mathrm{j}\frac{\sigma_0}{\omega\varepsilon_0}f(x) \tag{6.10}$$

with κ_0, σ_0 and $f(x)$ that describe the type of the PML. In especially the parameter $\kappa_0 \neq 0$ was introduced by Gedney in [Ged96] to better attenuate evanescent waves. The conductivity here is denoted with σ_0. Exemplarily, the eigenmodes are deduced [DOdZvdB01] for z as propagation direction having consequently a field dependence of $\mathrm{e}^{-\mathrm{j}k_z z}$ under the assumption to have an invariance in y-direction. Maxwell's curl equations within the PML yield two independent sets of which one refers to TE-polarised waves and the other one to TM-polarised waves related to the propagation direction. Solving both sets for E_y and

H_y, respectively, one obtains

$$\frac{1}{\alpha}\frac{\partial}{\partial x}\left(\frac{1}{\alpha}\frac{\partial E_y}{\partial x}\right) + \gamma^2 E_y = 0 \tag{6.11}$$

$$\frac{1}{\alpha}\frac{\partial}{\partial x}\left(\frac{1}{\alpha}\frac{\partial H_y}{\partial x}\right) + \gamma^2 H_y = 0 \tag{6.12}$$

with $\gamma^2 = \omega^2 \varepsilon \mu - k_z^2$. E_z and H_z yield the same equations. With the complex coordinate transformation presented in [CW94],[TC97]

$$\alpha \partial x = \partial \widetilde{x} \rightarrow \widetilde{x} = \int\limits^{x} \alpha(x') dx', \tag{6.13}$$

these equations become

$$\frac{\partial^2 E_y}{\partial \widetilde{x}^2} + \gamma^2 E_y = 0 \tag{6.14}$$

$$\frac{\partial^2 H_y}{\partial \widetilde{x}^2} + \gamma^2 H_y = 0. \tag{6.15}$$

Eqs. (6.14) and (6.15) are Helmholtz equations for homogeneous isotropic materials in the new coordinate $\widetilde{x}$. Hence, the PML behaves as an isotropic material but with a complex thickness $\widetilde{d}_{\mathrm{PML}}$ given as

$$\widetilde{d}_{\mathrm{PML}} = \int\limits_{(h-d_{\mathrm{PML}})}^{h} \alpha(x') dx'. \tag{6.16}$$

The true thickness of the PML is yet d_{PML}. This analytical continuation of space coordinates to the complex space has already been proven in [TC97], which can be used to derive PMLs for more general linear media [DOdZvdB01].

In a numerical implementation, a PML is usually modelled as a layer with finite thickness and with anisotropic material properties as given in Eqs. (6.7)-(6.10). From (6.9), it is clear that such a material is anisotropic and the α_{xx}-component is even active. The numerical handling of such a material is not easy.

6.2.2 Design of an Isotropic Absorbing Layer

In order to avoid the numerical difficulties with a PML, a conventional isotropic absorbing layer is designed consisting of six layers with tapered attenuation to achieve the necessary overall attenuation rate. These layers reach comparable performance of a single PML and their functionality definitely suffices to demonstrate the computation method in principal. Each of the six layers features $\varepsilon_r' = 1$ and $\mu_r' = 1$ but with electric and magnetic losses gradually and simultaneously increasing. The more the waves penetrate into the six layers the more the waves are attenuated. At the first layer, they only face slight attenuation in order to keep reflections especially low. While the reflected waves move back in direction of arrival they are again attenuated so that only little reflections influence the model under test. The negative imaginary part of the material parameters

marked with double primes describes the losses, i.e. ε_r'' and μ_r'', respectively. $\tan\delta$ is equal because e.g. $\tan\delta_\mu = \frac{\mu_r''}{\mu_r'}$ but chosen not to vary with frequency. The first sub layer shows $\tan\delta_{\varepsilon/\mu} = 0.01$ and is followed by layers with $\tan\delta_{\varepsilon/\mu} = 0.02$, $\tan\delta_{\varepsilon/\mu} = 0.07$, $\tan\delta_{\varepsilon/\mu} = 0.15$, $\tan\delta_{\varepsilon/\mu} = 0.3$ and $\tan\delta_{\varepsilon/\mu} = 0.8$. The last layer is covered by PEC. The losses roughly double with the intention to smoothly attenuate incident waves. The thicknesses measure $6\text{ mm}, 6\text{ mm}, 6\text{ mm}, 9\text{ mm}, 12\text{ mm}$ and 10 mm from the bottom to the top, thus slowly increasing towards the top where the losses rise. For the desired application, the absorbing layers are aimed to work from $9-14$ GHz, so the thicknesses are less than half of the wavelength for the maximum frequency 14 GHz. The idea is that the waves impinging on the layers do not have to face a jump in the material parameters experiencing little reflection. The values for permittivity and permeability are identical. Hence, the impedance of the layers, which is

$$Z_{F0} = \sqrt{\frac{\mu_0}{\varepsilon_0}}\sqrt{\frac{\mu_r' - j\mu_r''}{\varepsilon_r' - j\varepsilon_r''}}, \tag{6.17}$$

always maintains the same value of the free space impedance. In the following, it is spoken of one overall layer instead of six layers. In summary, two key aspects of Bérenger's PML are adopted but the designed absorbing layer is neither frequency nor incident angle independent. In especially waves impinging under grazing angle at the absorption layer cannot be absorbed properly. This layer however satisfies the object to evaluate the computation procedure. It is less sophisticated than its scientific peers, which however fail as well in completely absorbing incident waves under grazing angle.

The absorption capacity of the attenuation layer is tested and confirmed by the S-parameter results for a quadratic hollow waveguide set-up, as illustrated in Fig. 6.5, where the absorbing layers are placed in front of a short-circuit. In Fig. 6.6, the S-parameters of the absorption layer are directly compared to the S-paramters obtained for the weaker attenuating layer with the same material parameters ε_r' and μ_r', respectively, but with only a fourth of the loss values. Since the overall behaviour is only of interest it is not distinguished between the specific modes. For both absorbing layers, the mutual coupling between different modes $i \neq k$ is so low namely below -120 dB that it is negligible proving that the waves weakly depend on each other and can hence be considered as orthogonal. The reflection coefficients of the first to the fifth mode for the good absorption layer are very low on the order of -36 dB or better testifying broadband working. The worse absorbing layer exhibits reflection coefficients which are larger than -28 dB. The good as well as the worse absorbing layer disclose peaks next to cut-off of the individual modes as expected. One peak is off the frequency range of focus.

6.2.3 Influence of the Isotropic Absorbing Layer

The analytical eigensolutions derived in section 5.9 for the dielectric-vacuum interface pictured in Fig. 5.10 are contrasted with the solutions found by the software CST MWS [CST11]. The geometry together with the absorption layer is shown in Fig. 6.7. The dielectric slab exhibits $\varepsilon_r = 4.5$, $\tan\delta = 0.002$ and a thickness of 7 mm. The simulation model additionally includes the absorbing layer described in section 6.2.2, of which the influence is to test. In Fig. 6.8 and Fig. 6.9, it is to observe that the leaky modes are not
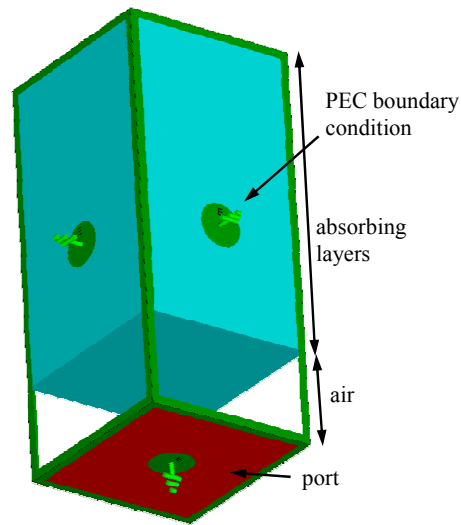
Figure 6.5: Simulation model in CST MWS to study the absorption capability.
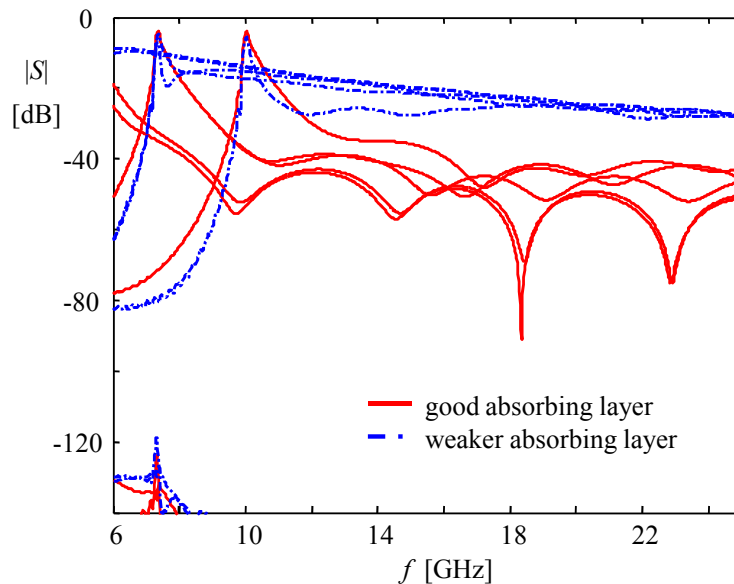
Figure 6.6: The *S*-parameters of a good and a weaker absorption layer in contrast, without specification of the individual modes.

revealed in the numerical computation. Leaky modes are however found analytically and displayed by crosses. Higher order modes below the cut-off frequency are close to the light line before they appear as guided surface modes in CST MWS. Concerning the absorbing quality of both layers, it is to observe that the results of the less absorbing layer deviate from the analytical solutions especially at the transition from the leaky into the guided state. The cut-off frequencies are plotted by diamond-symbols. The better absorption layer results approach quite exactly the analytical solutions. The fields of the port modes for the simulation model concentrate in the air or in the absorbing layer below cut-off as to see at 3.6 GHz in Fig. 6.10 for the lowest mode with cut-off at 5.72 GHz. Above cut-off

(e.g. at 16 GHz), the field is located in the substrate (Fig. 6.11). Further performance results are to find in chapter 8.3 where the absorbing layers are directly evaluated together with a periodically corrugated dielectric slab.
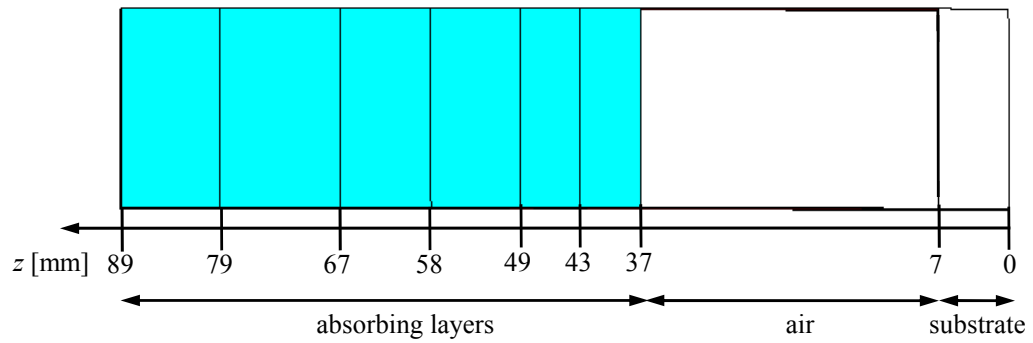
Figure 6.7: Geometry of the simulation model.
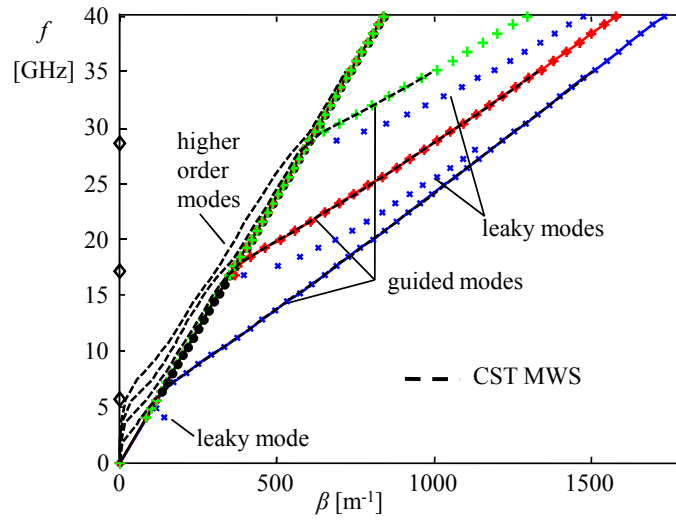
Figure 6.8: Analytical solution compared to simulation results of well performing absorber.
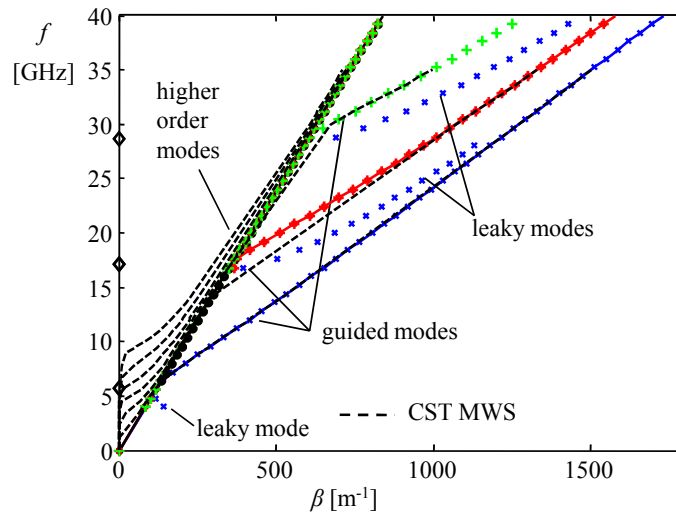
Figure 6.9: Analytical solution vs. simulation results of weaker absorption layer.
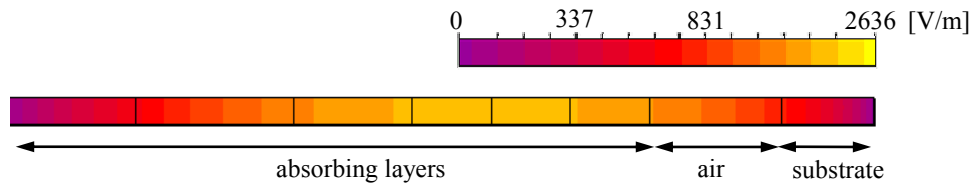
Figure 6.10: $|E|$-field distribution below cut-off for the fundamental mode at 3.6 GHz.
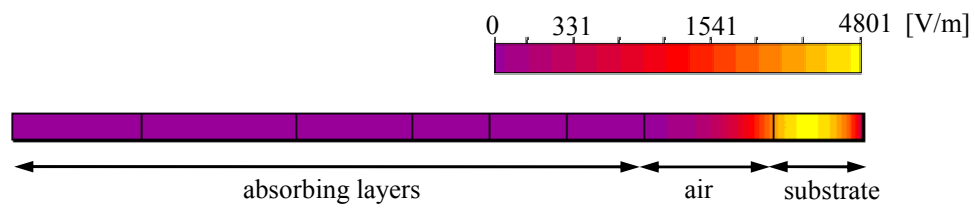
Figure 6.11: $|E|$-field distribution above cut-off for the fundamental mode at 16 GHz.

7 Closed Waveguide Realisations

7.1 Corrugated Rectangular Hollow Waveguide

The modal field solution of a dielectric-filled corrugated waveguide as pictured in Fig. 7.1 is computed by the modal series expansion method. Reference data deliver the models computed by Eshrah et al. in [EK06] and [EKYG05]. The configuration of the corrugated waveguide is closed and a discrete set of eigenvalues is to expect. In the reference literature,

(a) Hollow waveguide [EK06]

(b) Simulation model in CST MWS
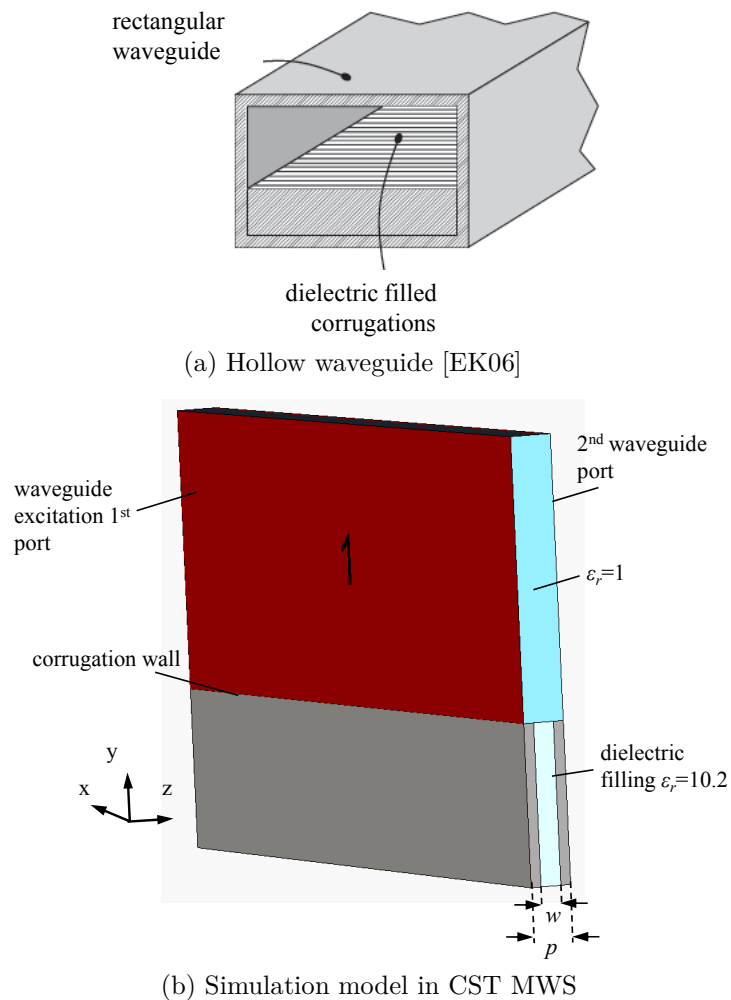
Figure 7.1: Rectangular hollow waveguide with dielectric filled corrugations.

the dispersion curves for the imaginary part of γ are derived by means of asymptotic corrugation boundary conditions [EK06] for a width-to-period ratio of $\frac{w}{p} = 0.5$ and by spectral analysis for a width-to-period ratio of $\frac{w}{p} = 0.85$ [EKYG05]. The corrugated

waveguide fulfills the EQC of a CRLH TL since the missing series capacitance is realised in form of the corrugations. LH wave propagation is enabled for frequencies $f \leq 7.6$ GHz below the bandgap for $\frac{w}{p} = 0.5$ whereas the fundamental H_{10} mode features a cut-off frequency of $f_c = 8.8$ GHz. One corrugation constitutes a periodic unit cell and is driven in a full-wave analysis (Fig. 7.1b). The waveguide ports are directly imposed on the cell and are placed on a rim of a wall. In this way, it is easier for the series of M modes to converge. The resulting S-parameters are transformed into the transfer parameters of the $\boldsymbol{T}$-matrix. Since only few modes are chosen as excitation the $\boldsymbol{T}$-matrix is of small dimension and so is the equivalent eigenproblem solvable with acceptable effort. By increasing the number of included modes the values of the start and stop frequencies of the bandgap vary. The dispersion graphs are depicted in Figs. 7.2a and 7.2b. It is found that three modes are sufficient to yield very good agreement with the solution derived by Esrah et al. in [EK06] and [EKYG05], respectively, in both cases as shown in [WE09b]. The excitation with fewer modes causes a lack of information. In Fig. 7.2b, the scattering matrix approach (SMA) also proves good coincidence with the analytical solution in the RH range. As additional feature, the modal expansion method also provides the attenuation constant, which is the real part of γ, not revealed by the reference techniques.

Once having obtained the eigenvalues and eigenvectors of a periodic unit cell, the modal field solution in the terminal plane can be deduced with Eqs. (4.1) and (4.2) and consequently in the terminal planes of the entire periodic waveguide by the Bloch-Floquet theorem. To obtain the eigensolutions for a homogeneous cross section in the waveguide serving as basis functions, a 2D eigenproblem is solved at a fixed frequency which is the reference frequency f_{ref}. It is essential to know whether the reference frequency is above or below the cut-off frequency f_c of the modal solution for a homogeneous cross section since the E and the H fields are interrelated via the wave impedance, which is imaginary below cut-off and real above cut-off. The wave impedance of the modes can be calculated analytically according to Eq. (5.118) and Eq. (5.130) for H modes and for E modes, respectively. For propagating modes, the wave impedance for TE or H waves is

$$Z_{FH} = \frac{\omega\mu}{\beta_H} = Z_F \frac{\lambda_g}{\lambda} \qquad \text{or} \qquad Z_{FH} = \frac{Z_F}{\sqrt{1 - \left(\frac{\lambda}{\lambda_c}\right)^2}}, \qquad (7.1)$$

and for TM or E waves, the wave impedance is

$$Z_{FE} = \frac{\beta_E}{\omega\varepsilon} = Z_F \frac{\lambda}{\lambda_g} \qquad \text{or} \qquad Z_{FE} = Z_F \sqrt{1 - \left(\frac{\lambda}{\lambda_c}\right)^2}. \qquad (7.2)$$

The wavelength λ_g in the waveguide is given by Eq. (5.119) whereas λ refers here to the free space wavelength or wavelength of the homogeneous plane wave λ_{HPW}. According to (7.1), Z_{FH} must become imaginary for $f < f_c$ resulting in

$$Z_{FH} = \frac{j\omega\mu}{\alpha} = j\frac{Z_F}{\sqrt{\left(\frac{f_c}{f}\right)^2 - 1}} \qquad (7.3)$$

and accordingly, the field impedance of the E modes reads below cut-off

$$Z_{FE} = \frac{\alpha}{j\omega\epsilon} = -jZ_F \sqrt{\left(\frac{f_c}{f}\right)^2 - 1}. \qquad (7.4)$$
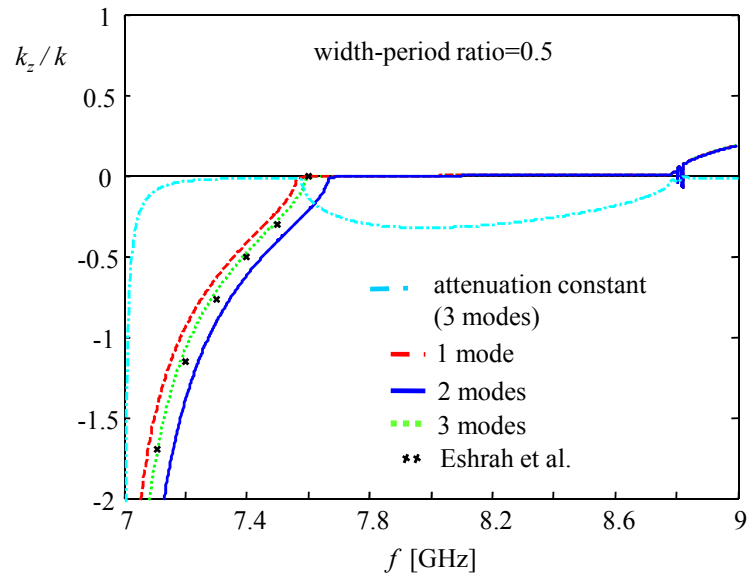
(a) Dispersion curve compared to [EK06]
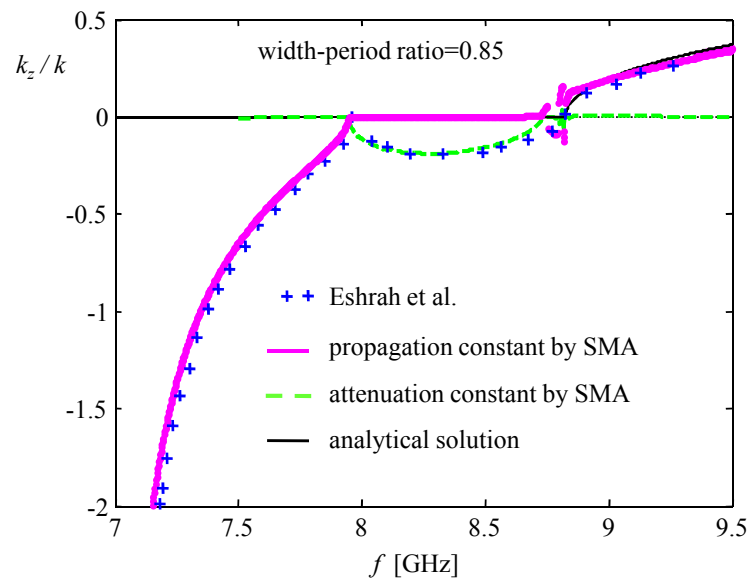
(b) Dispersion curve compared to [EKYG05]

Figure 7.2: Disperions results by SMA, analytical solution and reference literature in comparison.

The appropriate choice of the sign and the imaginary or real nature of the square root is to adapt to the frequency for which the modal field solution is intended to solve. Hence, an adequate factor is to introduce for creating the modal field solution of the periodically loaded waveguide for any other frequency f below or above f_{ref}. CST MWS determines the magnetic modal solution from the electric modal solution and the wave impedance for

f_{ref}. Thus, the magnetic modal solution results as

$$f_{ref} > f_c: \qquad H = \frac{E}{|Z_{FH}|} \qquad\qquad f_{ref} > f_c: \qquad H = \frac{E}{|Z_{FE}|}, \qquad (7.5)$$

$$f_{ref} < f_c: \qquad H = -\frac{jE}{|Z_{FH}|} \qquad\qquad f_{ref} < f_c: \qquad H = \frac{jE}{|Z_{FE}|}, \qquad (7.6)$$

where H and E waves are distinguished. Hence, the corresponding correcting factor $-j$ or j is to introduce according to whether $f_{ref} > f_c$ and $f < f_c$ or $f_{ref} < f_c$ and $f > f_c$ in order to gain the correct modal field solution for H and E modes. The correcting factors in both cases $-j$ or j for H or E modes, respectively, are derived from the fact that the Poynting vector must be identical in any case

$$\frac{E^2}{Z_{FH}} = \frac{E_{ref}^2}{Z_{FH,ref}} \qquad\qquad \rightarrow E = E_{ref}\sqrt{\frac{Z_{FH}}{Z_{FH,ref}}} \qquad (7.7)$$

and for the magnetic field

$$H^2 Z_{FH} = H_{ref}^2 Z_{FH,ref} \qquad\qquad \rightarrow H = H_{ref}\sqrt{\frac{Z_{FH,ref}}{Z_{FH}}}. \qquad (7.8)$$

For E waves Z_{FH} is to replace by Z_{FE}.

The modal field solution of the periodically loaded waveguide is displayed for the frequency $f = 7.5$ GHz in the LH range in Figs. 7.3a to 7.3c on a rim of a wall. The field distribution cannot be compared to the one shown in [EKYG05] since they derived the field solution in the aperture between two corrugations. The original cylindrical host waveguide would have exhibited only wave attenuation and no wave propagation at this frequency. The magnitude of the E_y-component is reasonably the strongest value with the highest magnitude close to the rim. In contrast to the H_{10} mode of the host waveguide a longitudinal component E_z is also present [WE09b].

From the generated field solution, the Bloch impedance Z_B is derived by the definition of an equivalent current derived from the magnetic field on the rim and by the transferred power in the cross section according to Eq. (5.140) for the model with $\frac{w}{p} = 0.85$. The integration paths are illustrated in Fig. 7.4. The real and the imaginary part of Z_B are pictured in Fig. 7.5, where an imaginary Z_B is to observe in the bandgap and a dominant real Z_B in the propagation domain. In [EKYG05], the waveguide impedance was calculated instead.

(a) E_x-component

(b) E_y-component

(c) E_z-component
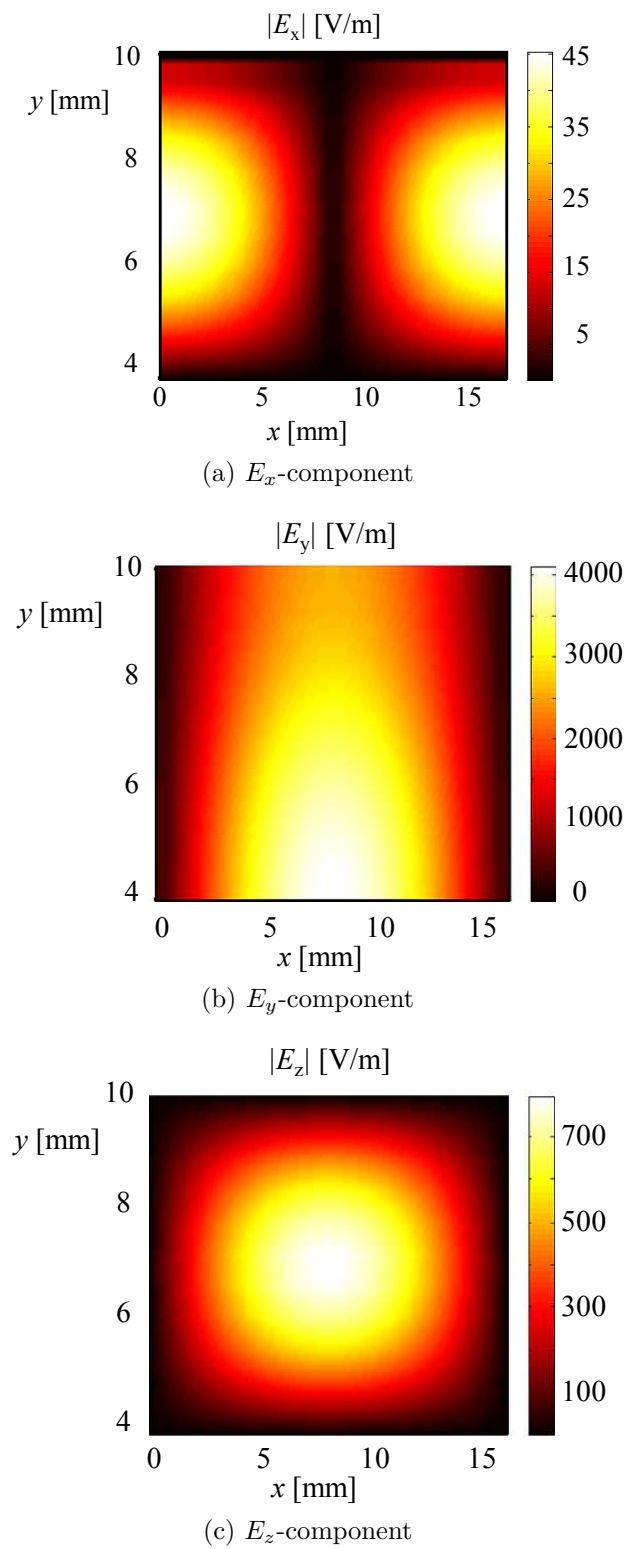
Figure 7.3: Modal field distribution in the port plane of a corrugation wall.
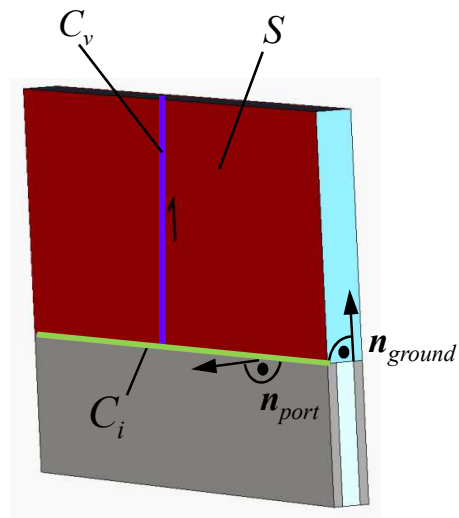
Figure 7.4: Integration paths in the port plane for equivalent current and voltage.
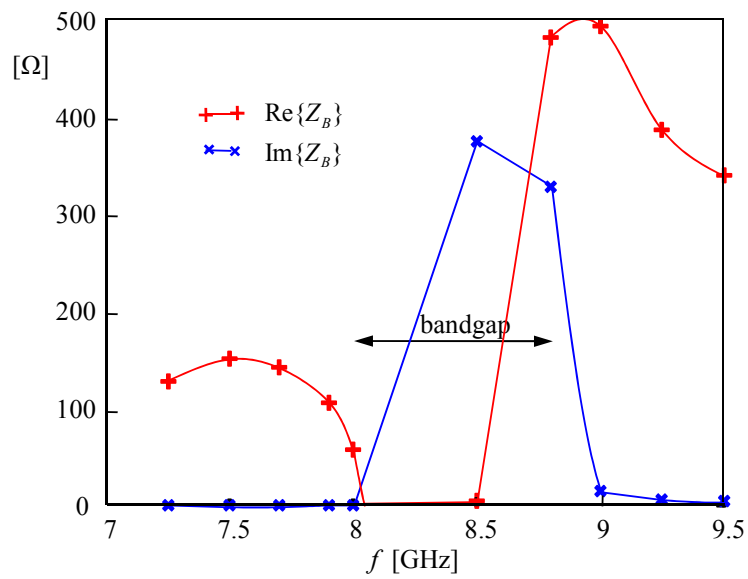
Figure 7.5: Bloch impedance versus frequency.

7.2 CRLH Waveguide in SIW Technology

In this section, the peculiarities of a composite right/left-handed transmission line are realised in a closed waveguiding structure with the purpose to transport energy with low attenuation and to exploit the special phase behaviour in the LH frequency range [WE08b]. A start from a hollow waveguide design is advantageous with respect to optimal energy transfer in comparison to an implementation in microstrip technology as many other realisations to be found in literature e.g. in [CI06]. In contrast to the design as a corrugated hollow waveguide in section 7.1, the idea is to implement the H_{10} hollow waveguide mode as an SIW. The EQC of the rectangular hollow waveguide mode H_{10} in Fig. 7.6a strongly resembles the EQC of the CRLH TL by nature with view to Fig. 7.6b, except for the series capacitance. In anticipation of sections 8.1 and 8.2, two open realisations based on the same configuration concept act as antennas. In section 8.1, an additional layer provides for the enhanced series capacitance. In order to arrive at a closed configuration, details are shown in Fig. 7.7, the open implementation is extended by the use of image principle. However, the second resulting level of metal tongues is omitted with the purpose to simplify manufacturing. Kapton foil acts as separation layer between the upper metallic pattern and the lower layer of metal tongues. In this manner, a high series capacitance can be reached and the unit sections can be kept short in length with $\Delta l \approx \lambda_0/20$. The tongues are shaped according to the distribution of the transverse current density which is higher in the center and fades towards both sides. The currents flow along the lateral vias and create the shunt inductance. The shunt capacitance can roughly be regarded as two capacitances in parallel from the top and bottom metallic layers, respectively, to the middle metallic layer. The series inductance stems from the current flowing in longitudinal direction. The shunt resonant frequency is determined by the transverse geometry of the SIW, limited by the lateral rows of vias. Once having established the shunt resonance frequency, the series resonant frequency is left to be adjusted by the longitudinal length of the unit cell in propagation direction. As such, the decisive design parameters to reach the balanced state are decoupled and a handy balancing procedure results *cf.* sections 8.1 and 8.2 [WE09a].

(a) EQC of the H_{10} mode.   (b) EQC of the CRLH transmission line
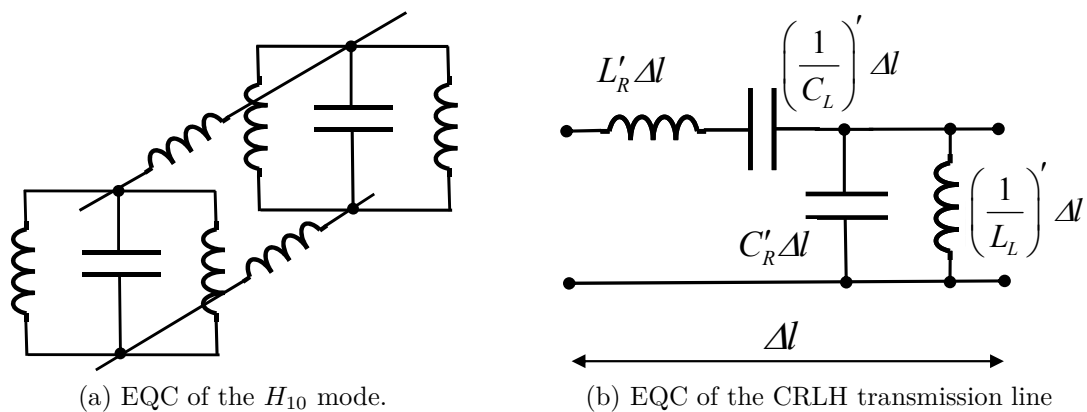
Figure 7.6: Equivalent circuit diagrams of the H_{10} mode and the CRLH TL.

A tapered feeding section provides the transition from the periodical structure to the feeding microstrip line of 50 Ω as depicted in Fig. 7.7a. The smooth transition reduces
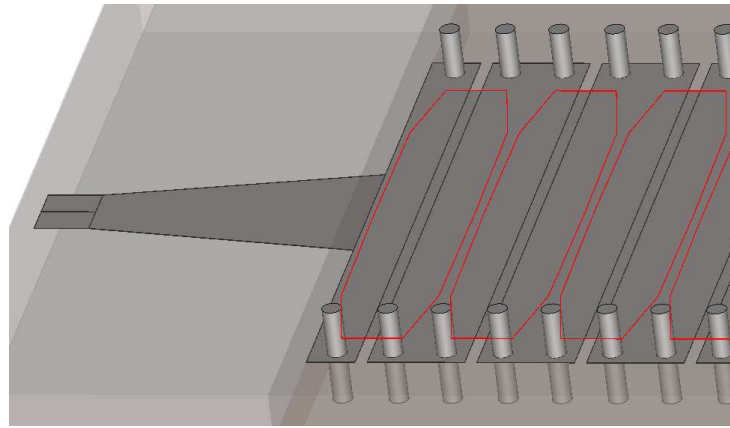
(a) Internal SIW structure revealing the tapered transition to the input
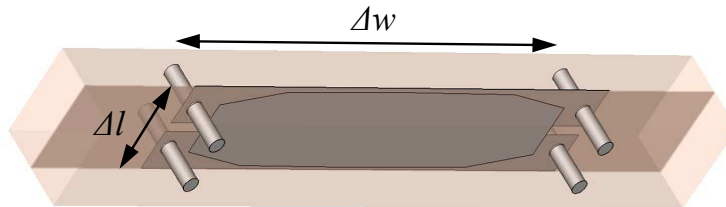
(b) Periodic unit cell

Figure 7.7: SIW configuration as CST MWS model.

reflections and promotes matching.

7.2.1 Simulation, Prototype and Measurement Results

Starting point is the transition frequency from the LH into the RH state, which is intended to be 4.35 GHz. Coincidence of the series and the shunt resonance is achieved with $\Delta w = 18.5$ mm and $\Delta l = 3.625$ mm. 40 cells add up to a total length of 184.62 mm, which are built on the dielectric Arlon 25FR with $\varepsilon_r = 3.58$, which is economically priced. In CST MWS the loss factor of the substrate is set to $\tan \delta = 0.0035$ and the material data of the Kapton foil read $\varepsilon_r = 2.8$ with $\tan \delta = 0.003$ as loss factor. However, the real effective material values cannot be exactly ascertained in the frequency range of interest. Therefore, two models with differently long tapered feeding sections are simulated. Regarding the reflection coefficient, the second designed simulation model unveils better matching at lower frequencies, where the transition section is made longer. The first design whereas delivered better matching in the higher frequency range. In order to demonstrate the functionality of the described principle a prototype has been fabricated and the measures of the second tapering have been chosen. The prototype is displayed in Fig. 7.8 even though everything is closed. In Fig. 7.9, the reflection coefficient of the prototype shows a peak at around 4.2 GHz but the reflections are nonetheless mainly below -9 dB. The first simulation model reveals an input reflection coefficient of $|S_{11}| < -13$ dB from 4 GHz to 7 GHz but the second model shows slightly better matching performance with $|S_{11}| < -15$ dB from 3.4 GHz to 4.8 GHz, which are the frequencies in focus. The

discrepancies between measurement and simulation can be explained by fabrication toler-
ances, uncertainties of the material parameters and by the simulation mesh.

The transmission parameters of the simulation and the measurement are in good agree-
ment, as shown in Fig. 7.10. The $|S_{21}|$ of the simulation model with taper 2 clearly
confirms the balanced condition by a smooth course whereas the course of the $|S_{21}|$ of the
measured prototype deviates from being perfectly balanced, that is in accordance with
the result of $|S_{11}|$. From the transmission factor, the propagation constant can be derived
by unwrapping its phase. The graphs from measurement and simulation coincide well
and are displayed in Fig 7.11. Nevertheless, a phase offset cannot be ascertained without
de-embedding.

Figure 7.8: Realised prototype.
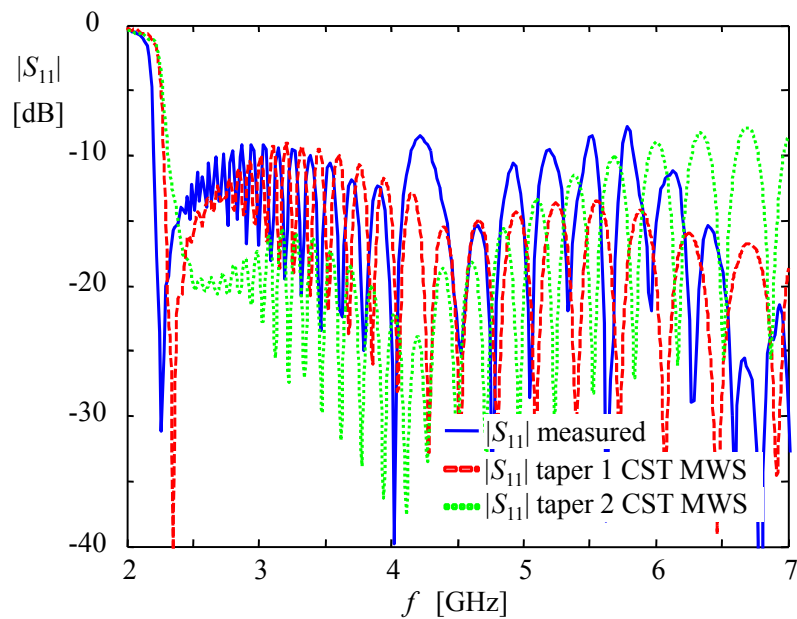
Figure 7.9: Reflection coefficient of simulation model and prototype in comparison.

7.2.2 Dispersion Diagram

The physical meaning of the mathematically complex nature of the propagation constant
γ or rather of the phase constant β versus frequency can be visualised in the dispersion
diagram. It hints to the performance of the structure. On this behalf, γ is computed on
two ways to compare the results. First, a unit section with imposed periodic boundary
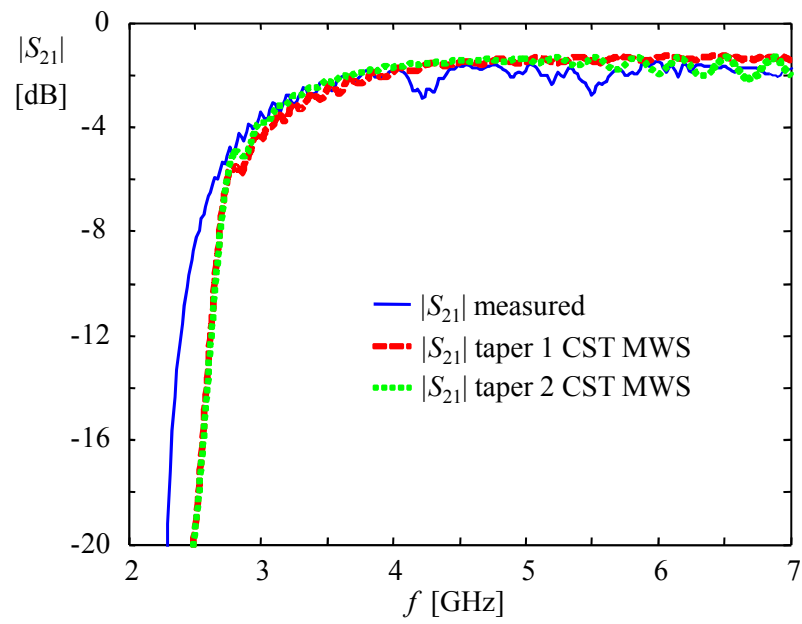
Figure 7.10: Transmission coefficient from simulation and measurement.
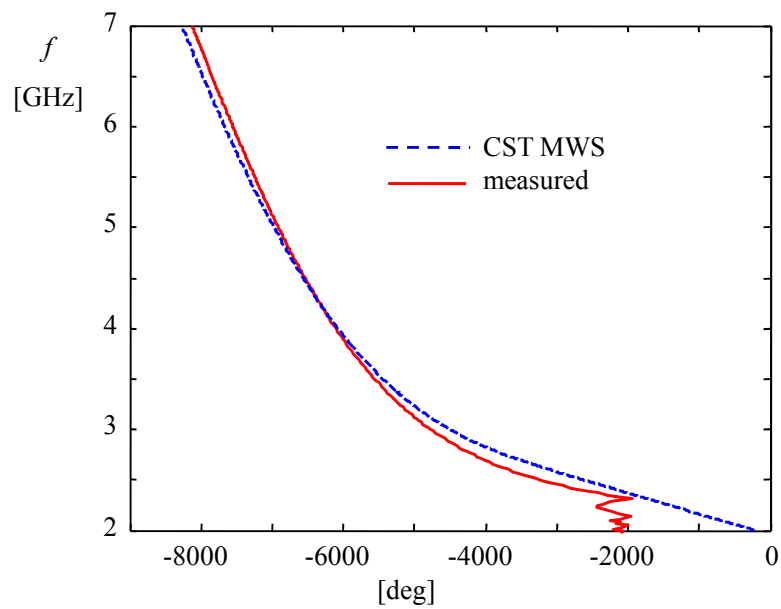
Figure 7.11: Unwrapped phase of S_{21} from simulation and measurement.

conditions is modeled in the finite element (FE) based eigenmode solver of Ansoft HFSS [Ans11]. Second, the estimation algorithm matrix pencil (MP) *cf.* appendix 9.4 processes the field solution data obtained by the driven transient simulation of the periodically loaded waveguide. Fig. 7.12 reveals the outcome of both computations and verifies almost identical dispersion behaviour. The LH trait is clearly attained to observe by the negative slope in the lower frequency domain. The balanced state with $\beta = 0$ is established at 4.35 GHz where the LH mode smoothly converts into the RH mode prevailing in the upper frequency range. A vanishing β signifies infinite wavelength as is pictured in Fig. 7.13 in the simulation plot. For comparison, the same cut in the field plot of the transverse E-component in the horizontal plane at a height of 0.5 mm is depicted for the LH frequency 3.6 GHz in Fig. 7.14 and for the RH frequency 5 GHz in Fig. 7.15. Unfortunately, the pictures cannot be animated here. That would testify the backward wave propagation in the LH case and the forward travel direction in the RH case.

As additional information, the MP method features the attenuation behaviour. The attenuation constant from the MP method and the one yielded by the not-deembedded CST MWS simulation results according to

$$\alpha \left[\mathrm{m}^{-1} \right] = -\frac{|S_{21}| \, [\mathrm{dB}]}{l \; 8.686 \, [\mathrm{dB}]} \tag{7.9}$$

are added to the dispersion graph (Fig. 7.12). The curves nicely agree except around the transition frequency where a comparable attenuation does not arise by the MP algorithm. The losses account for $\alpha = 1.026 \; \mathrm{m}^{-1}$ at 4.35 GHz and at 4.7 GHz they bring about $\alpha = 0.89 \; \mathrm{m}^{-1}$, which is in the range of the losses in [YCN$^+$07] if not better. The loss factor of the Arlon 25FR with $\tan \delta = 0.0035$ is higher than the one of Rogers 6002 used
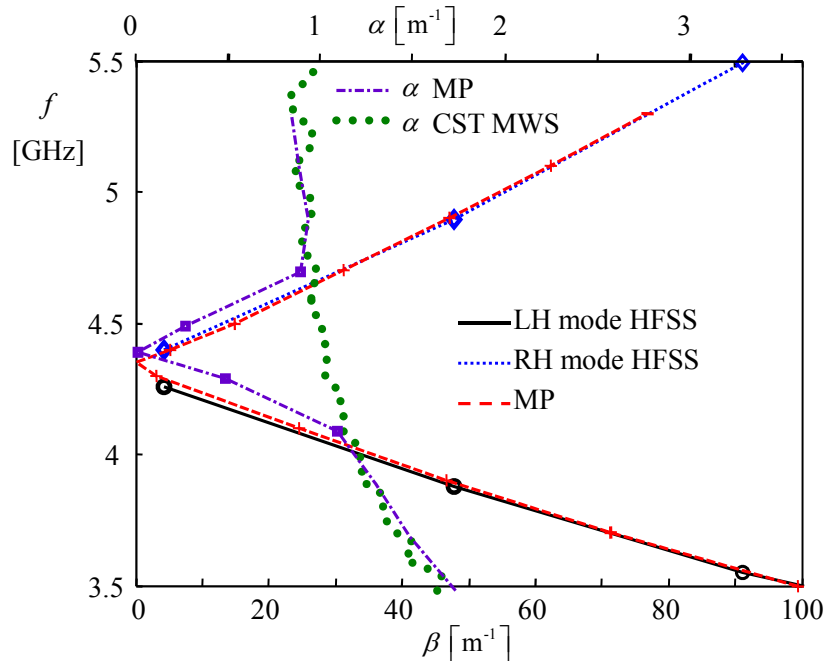
Figure 7.12: Dispersion diagram comparing results from the matrix pencil method (MP) and the eigenmode solver in HFSS.
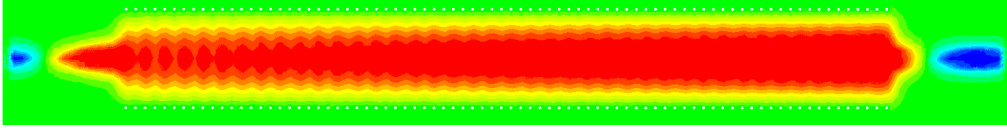
Figure 7.13: Transverse E-component for 4.3 GHz, near transition frequency.
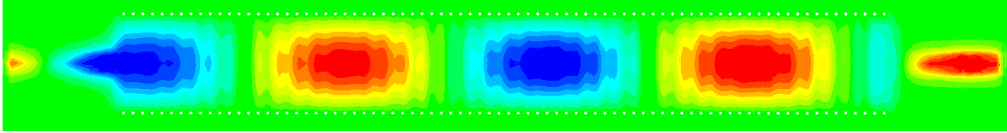
Figure 7.14: Transverse E-component for 3.6 GHz, LH region.
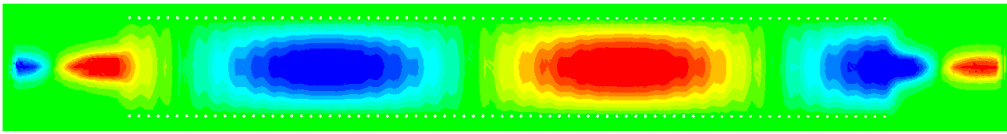
Figure 7.15: Transverse E-component for 5 GHz, RH region.

in [YCN$^+$07] with $\tan\delta = 0.002$. Additionally in [YCN$^+$07], the operation frequencies are lower and the structure exhibits only nine cells. Losses of $\alpha = 0.77$ m^{-1} are reported for 2.8 GHz.

7.2.3 Bloch Impedance

For periodic architectures, the Bloch impedance Z_B signifies the matching characteristic of the waves travelling in the periodic arrays. Z_B varies within one cell but is periodically identical at each periodic cross sectional plane. Only a forward advancing wave is assumed in the periodically modulated waveguide because of the good matching performance revealed in Fig. 7.9. As for the other CRLH structures *cf.* sections 8.1, 8.2, Z_B has been computed from the driven field solution obtained with CST MWS. The input interface of a unit cell exhibits a Bloch impedance of which the real and the imaginary parts are displayed in Fig. 7.16 over frequency. It is computed via the definition of power and current in Eq. (5.140). Compared to the open similarly designed structure in section 8.1, the value of the applied voltage remains the same. One reference potential is on the inner layer in the middle of the SIW and the other reference potential is on the outer shell, i.e. on the top and on the bottom layer. As the set-up is not perfectly symmetric the upper part supports slightly more energy. The current partly flows in the upper section and partly in the lower section. For one half of the cross section Z_B mainly remains the same compared with Z_B of the open composition. For the entire structure, the Bloch impedance is only half of it since the lower and the upper part can be regarded as in parallel. The imaginary part is $|\operatorname{Im}(Z_B)| \leq 4\ \Omega$ and fluctuates around the zero line. The real part is between 8 Ω and 14 Ω.

The lowest possible reflection coefficient is attained with a reference impedance of the waveguide of $Z_L = 10.75\ \Omega$ depicted in Fig. 7.17. In conclusion, the CRLH waveguide
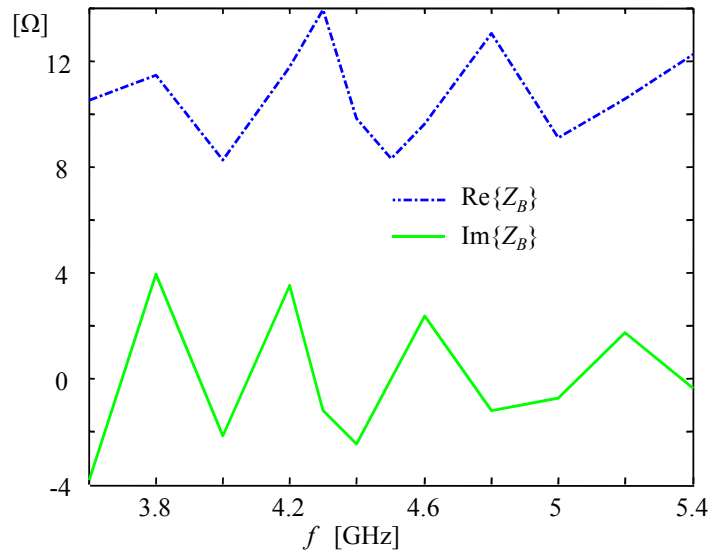
Figure 7.16: Bloch impedance by real and imaginary part.

promises broadband operation with the balanced frequency as center frequency. Additionally, it can be easily included in conventional RH TL circuits by relatively simple matching networks.
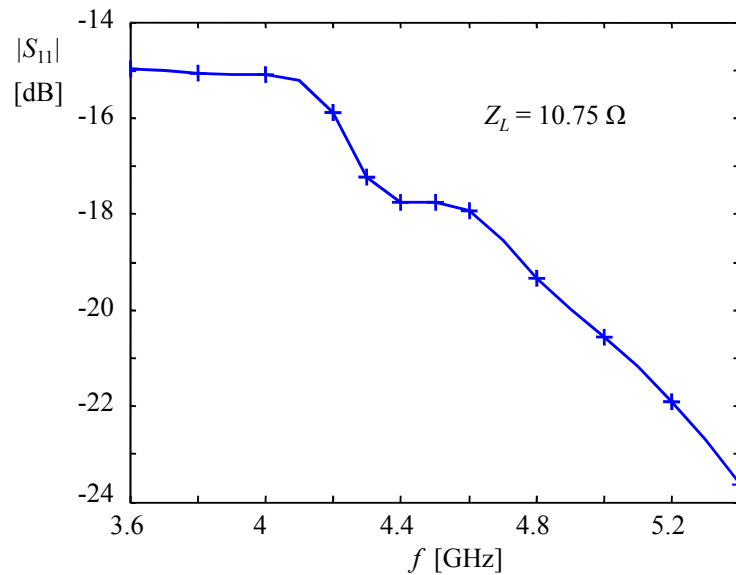
Figure 7.17: Reflection coefficient due to the Bloch impedance and a reference impedance $Z_L = 10.75 \, \Omega$.

8 Leaky-Wave Antenna Realisations

8.1 CRLH Leaky-Wave Antenna: Slotted Substrate Integrated Waveguide

Conventionally, slots introduced in the metallic enclosure of hollow waveguides typically serve for alternating sign sampling to realise broadside radiation for rectangular hollow waveguides [EE10]. An attractive alternative to trigger broadside radiation offer composite right-/left-handed transmission lines since they enable broadside radiation directly in the fundamental mode. For this goal, slots are introduced in the top metallic plate perpendicular to the direction of propagation and in distance much smaller than in the traditional way and than the operating wavelength. One periodic unit cell is shown in Fig. 8.1a. One cut is thereby very narrow in order to attain a considerable capacitance value. On a second level just below the top level, metallic strips or metal tongues are to bridge the gaps and are to enhance the capacitance to keep the periodic sections particularly short. The form of the metal tongues accounts for the transverse currents and the corresponding field distribution within the waveguide by having a tapered shape toward the ends. As such, the nature of the field is preserved and no additional parasitic effects are created besides the desired series capacitance to the original EQC of the H_{10} rectangular hollow waveguide mode displayed in Fig. 8.1b. The functional field dependence within the rectangular SIW is similar to the known sine-functional course of the H_{10} mode promoted by the host waveguide. To separate the metallisations, Kapton foil serves as separation layer. The resulting upper metallic strips are short-circuited with the metallic ground plane by lateral via holes, which define the transverse dimension of the modified waveguide and replace metallic side walls of the rectangular hollow waveguide equivalent. The currents flow along the lateral vias and induce shunt inductances as represented in the EQC in Fig. 8.2. The horizontal geometry not only specifies the cut-off frequency of the H_{10} mode of the host waveguide but also assigns the frequency of the shunt resonance of the EQC. The longitudinal dimensions determine the series resonance. The equivalences are depicted in Fig. 8.2. For this reason, establishing the balanced condition [CI06] is very convenient since the decisive parameters are decoupled from each other. Once, having fixed the transverse geometry, balancing remains the task of adjusting the length Δl of a cell and the overlapping area covered by the bars on the top and the metal tongue below. Fig. 8.1a pictures the unit cell. In the balanced state, the series and the shunt resonant frequencies are identical.

8.1.1 Simulation Results

The antenna configuration [WE08a] is simulated with CST MWS [CST11] in time domain with the transient solver for $2 - 7$ GHz. A magnetic symmetry plane along the propagation axis is set in accordance to the electric field distribution within the SIW

(a) Elementary cell

(b) EQC of the original RH H_{10} mode.
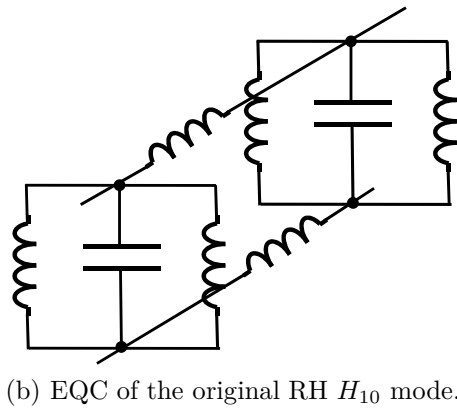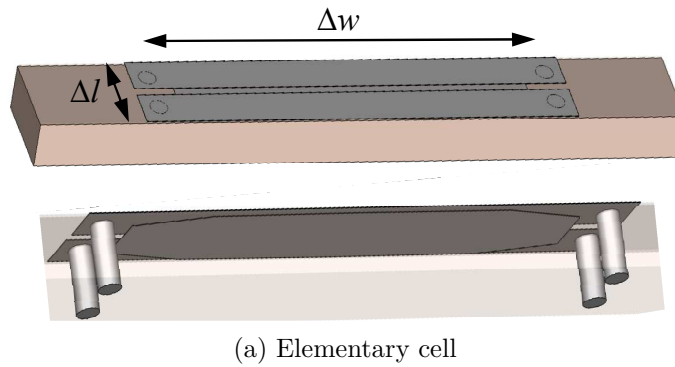
Figure 8.1: Open CRLH waveguide in SIW technology.

known from the regular rectangular waveguide equivalence. It promotes the modes which are interesting for the very application. The simulation model follows in Fig. 8.3. With respect to economic fabrication, the low-cost substrate FR-4 is used known for common planar printed circuit board (PCB) production. Its permittivity is $\varepsilon_r = 4.5$ and generates with $\tan \delta = 0.025$ relatively high losses. The Kapton foil as separation layer features an $\varepsilon_r = 2.8$ with $\tan \delta = 0.003$. The thicknesses are 1.7 mm and 70 μm, respectively. Especially the physical values of the latter are not reliable due to its fineness and its frequency-dependency. The total composition is accomplished by 50 unit cells in repetition. The fabricated prototype can be inspected in Fig. 8.4. It has been produced by
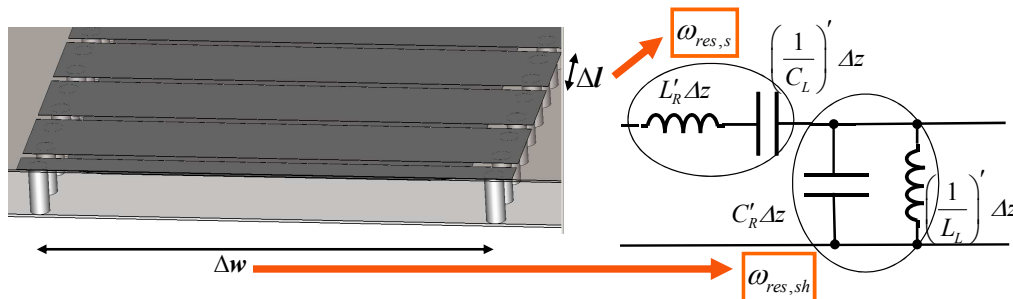
Figure 8.2: Correspondence of dimensions of the SIW LWA and circuit model equivalences.

common planar printed technology.
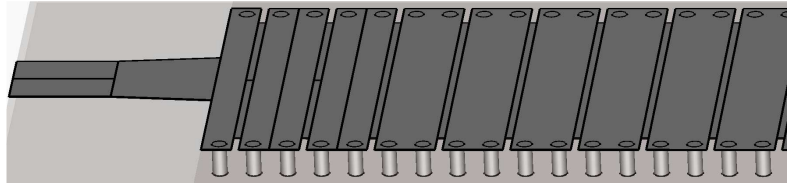
Figure 8.3: Simulation model: Metallic structure.
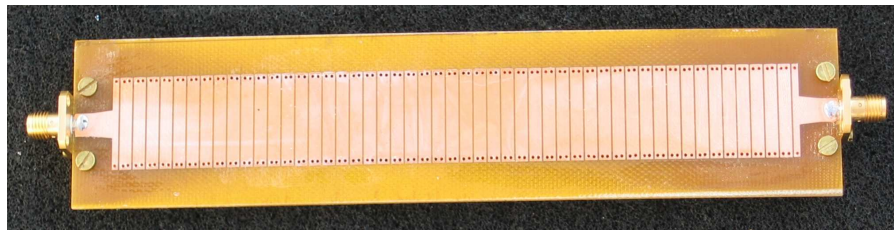
Figure 8.4: Fabricated prototype.

Since the waveguide width has already been fixed it remains to tune the series resonance by modifying the length of a unit cell. With it, the distance the current has to flow varies affecting the value of the serial inductance. The gap between the rectangular strips makes up the serial capacitance. The capacitor area is increased by the metal tongue below. The arrangement can be understood as two capacitances in series resulting in half of the value of one capacitance. The effect of varying Δl becomes visible in the Smith chart as Fig. 8.5 shows. The dotted red curve of the reflection coefficient belongs to a unit cell length of 3.6 mm and encircles the matching point, thus broadband matching is confirmed. Referring to transmission line theory, the relevant characteristic impedance ideally becomes independent of frequency for a balanced structure as stated in [CI06]. As additional verification, the magnitude of the reflection coefficient is presented in Fig. 8.6. The periodic cell continuation is matched to a 50 Ω microstrip line by a tapered transition section (see Fig. 8.3).

8.1.2 Bloch Impedance

For matching and integration reasons, it is important to know the Bloch impedance of a periodic structure in any arbitrary cross sectional plane. The value of the Bloch impedance varies only within the periodic unit cell *cf.* section 3.3. It is retrieved from the field solution obtained by the simulation. The field data is extracted from a unit cell in the middle of the antenna, where reflections from the transitions at both ends are faded away and the field can be considered as steady-state. As explained in section 3.2, the Bloch impedance differs within a unit cell and for the three definitions (5.139) to (5.141) as can be seen in Fig. 8.7, which is plotted along the unit cell. In Fig. 8.8, Z_B is calculated depending on frequency at the input interface. Notable is that the imaginary part changes from positive to negative values at about 4 GHz, which is designed as the balanced frequency, and the imaginary part is about $|\mathrm{Im}| \lesssim 5$ Ω.
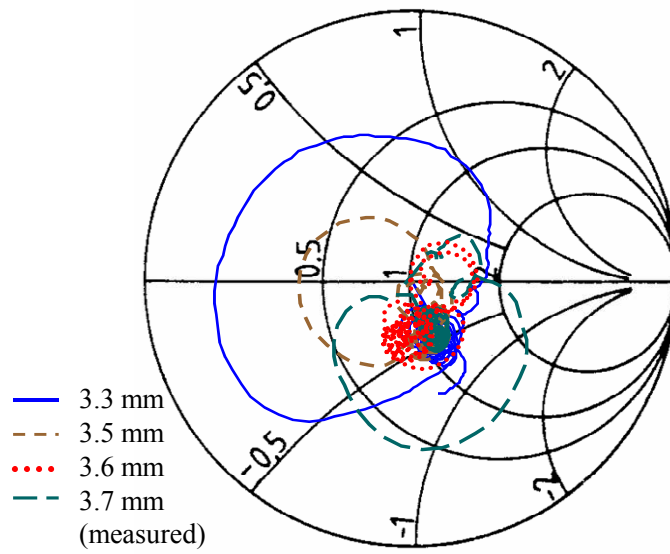
Figure 8.5: S_{11} of structures with different unit cell size lengths.
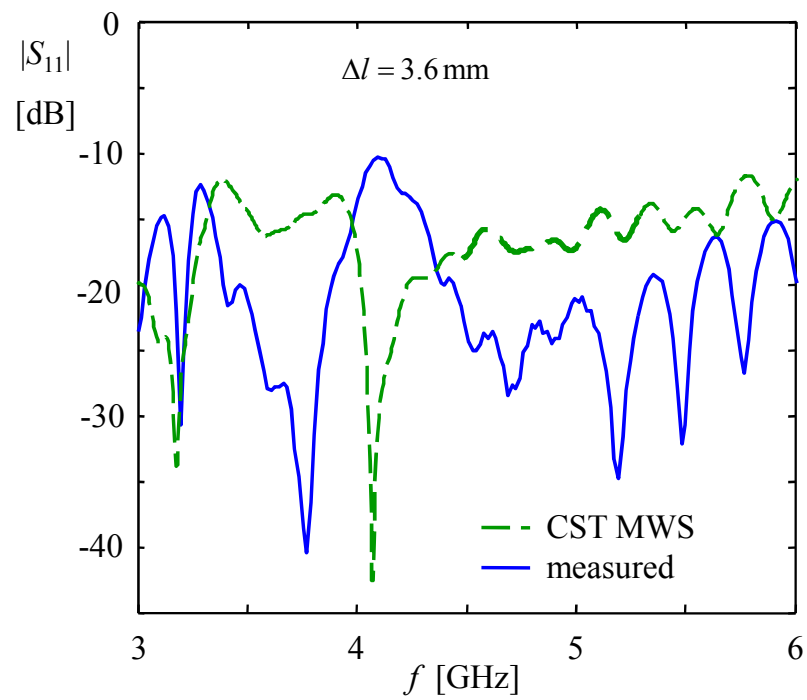
Figure 8.6: S_{11} of the antenna structure with unit-cell length 3.6 mm.
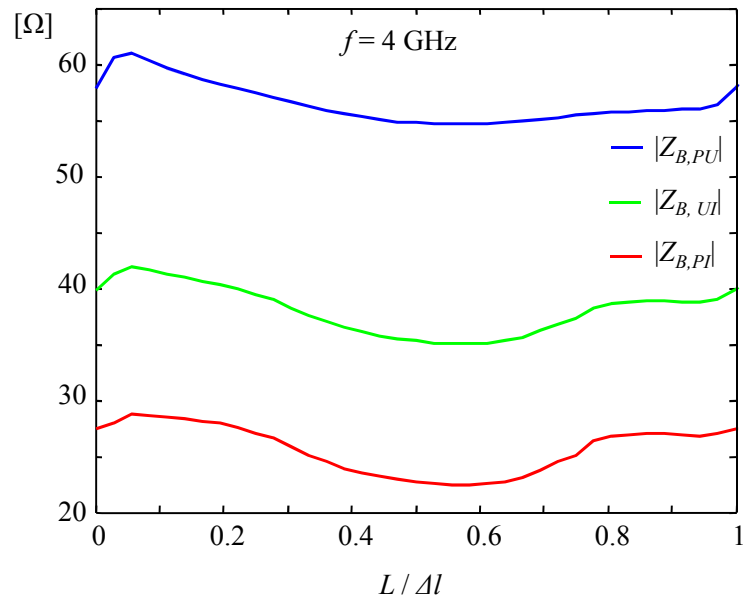
Figure 8.7: Z_B computed by Eqs. (5.139) to (5.141) for 4 GHz.
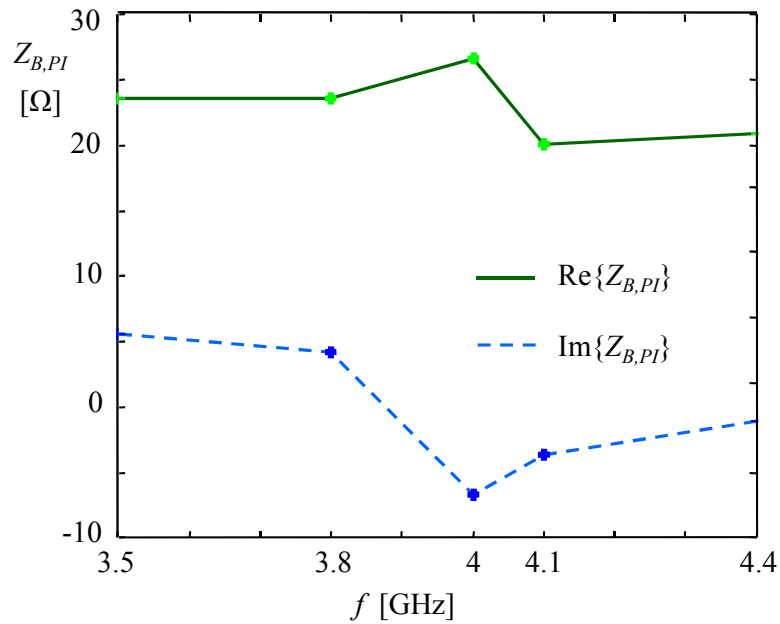
Figure 8.8: Z_B computed by Eq. (5.140) over frequency at the input interface.

8.1.3 Dispersion Diagram

The diagram discloses the fast and the slow wave regions of this antenna, in which radiation and bound waves occur, respectively, *cf.* section 3.4.2. The dispersion behaviour is computed by various methods, as demonstrated in Fig. 8.9. The border between fast and slow waves is given by the light line representing the wavenumber of free space. In the slow wave part, a mode is to notice which first approaches the light line. This mode is a perturbed plane wave above the antenna structure, which eventually inclines to a bound LH mode around 3 GHz with anti-parallel group and phase velocities. Since the wavelength is relatively long at low frequencies the mode just perceives a metallic plate. While the wavelength reduces with increasing frequency the mode begins to interact with the configuration of the LWA and converts into a LH mode. Nevertheless, the wave is purely bound through its entire pathway because its propagation constant is bigger than the constant of free space. The values are calculated with the eigenmode solver of the commercial software tool Ansoft HFSS [Ans11] working in the frequency domain. As long as the wave is not bound, i.e. outside the structure, it is not found by the matrix pencil algorithm, which processes the field data of the driven entire antenna configuration. The unit cell modeled as periodic unit in the eigenmode solver of HFSS is shown in Fig. 8.10. As upper boundary condition, a perfectly matched layer (PML) is placed while the lateral boundaries are defined as periodic with a phase shift between them. Despite the name the PML does not operate perfectly and physically reasonable modes have to be selected from unphysical modes.

The transition frequency 4 GHz is clearly confirmed by both methods, by simulation and by the numerical estimation technique, where ideally $\beta = 0$ and with it $\lambda \to \infty$. Infinite wavelength entails a homogeneous phase so the field is evenly distributed along the antenna, and moreover broadside radiation occurs. Similarly, the graphs of the LH mode and the RH mode are well consistent in both computational methods. The light line intersects both modes. Up to a phase of $\beta \Delta l \approx 0.22$, the LH mode leaks energy while propagating along the antenna. The RH mode radiates up to a phase of $\beta \Delta l \approx 0.31$. In contrast to HFSS, the matrix pencil method also delivers the attenuation constant α, which is $\alpha \Delta l < 0.05$ and includes dielectric and metal losses but also radiated energy. The three attenuation shares are non-separable within the matrix pencil computations. To emphasise is that the antenna is operated only in its fundamental mode and not in higher space harmonics ensuring reliable and predictable operation.

8.1.4 Measurement Results

Fig. 8.11 reveals that the simulation results and the measurement results agree well for the transmission parameter S_{21}, which is below -10 dB up to 5 GHz, promising good radiation performance. The amount of the accepted energy at the input is consumed sufficiently by radiation but also by losses. At the same time, gradual energy consumption is to establish while the wave travels along the antenna. This leads to a large aperture and thus to a high gain. Fig. 8.12a illustrates the measured gain over the elevation angle in accordance to the IEEE definition for $\varphi = 0°$ corresponding to the *E*-plane. For the depicted frequencies, the maximum is reached at 4.4 GHz with 9.15 dBi. At radiation perpendicular to the aperture at 4 GHz, a gain of 8.64 dBi is accomplished. With in-
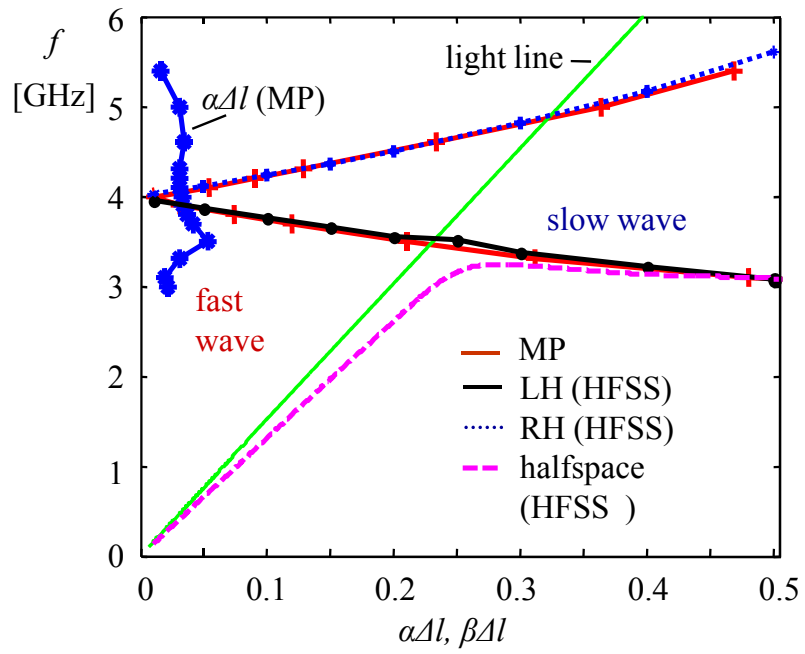
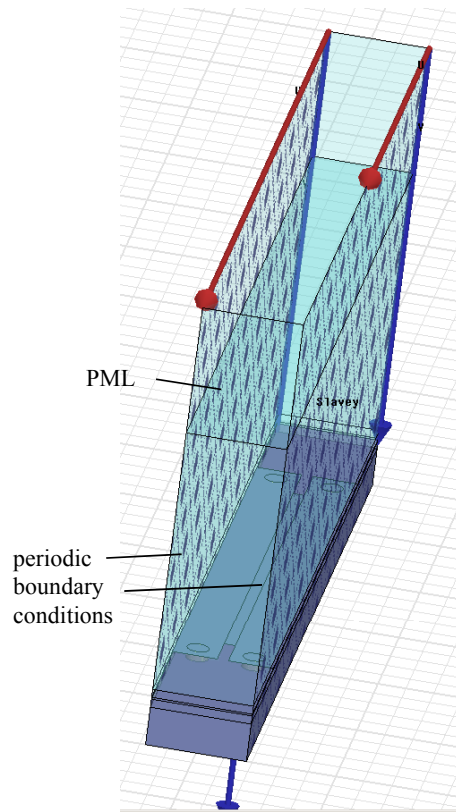**Figure 8.9:** α and β for the LWA.


Figure 8.10: Simulation model in Ansoft HFSS.

creasing propagation constant and increasing frequency the radiation angle turns toward endfire while the antenna is operated in the RH mode. Scanning the radiation angle only by a change in frequency is therefore possible from backfire to endfire including broadside direction. The side lobe level is thereby satisfactory. In Fig. 8.12b, the radiation patterns by simulation and measurement are compared for 4.0 GHz, 4.4 GHz and 5 GHz. The main beam directions are in good agreement as are their shapes.

For the same plane at $\varphi = 0°$, the maximum gain is reported over frequency in Fig. 8.13. Measured and simulated data accord in a pleasant manner with each other. The tendency is the same, the gain increases slightly with increasing frequency. Measurements [1] figure out the maximum gain to be at 5.3 GHz with 10.15 dBi, which is a good value but the shape of the beam becomes rather broad. The efficiency over frequency obtained from the 3D measurement and gain calculation is given in Fig. 8.14. It shows a maximum efficiency η of 69% at 3.8 GHz. The efficiency from the simulation is compared with the measurements. If a less lossy substrate was employed the efficiency could be enhanced. The 3D radiation pattern at broadside for $\vartheta = 0°$ is visualised in Fig. 8.15, which stems from the farfield calculation in CST MWS. In Fig. 8.16, the contiguous radiation pattern is remarkable over frequency and scanning range as presented in [WE08a].
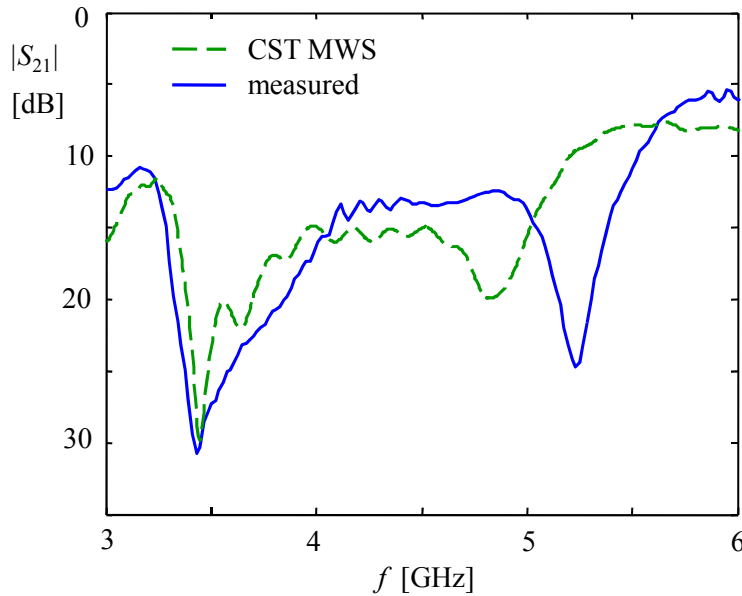
Figure 8.11: Transmittance of the LWA for $\Delta l = 3.6$ mm.
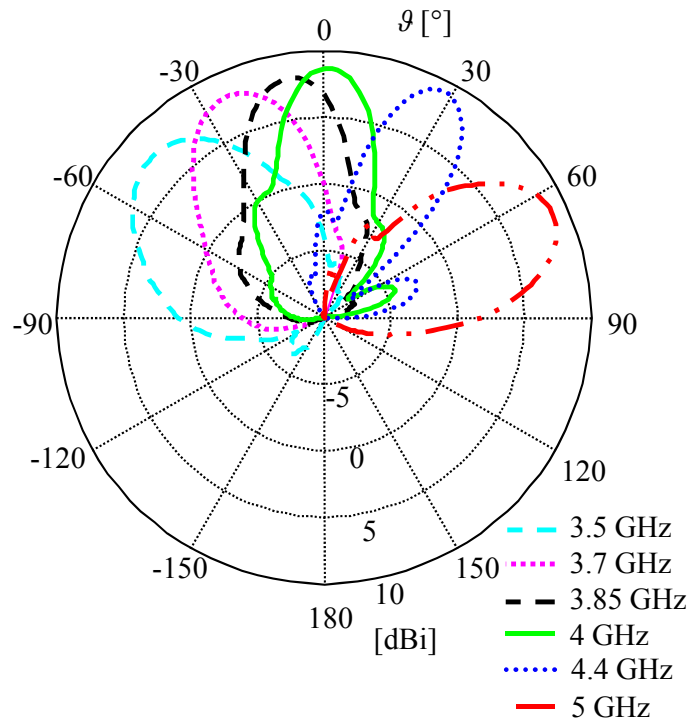
(a) The gain from measurements in the E-plane.
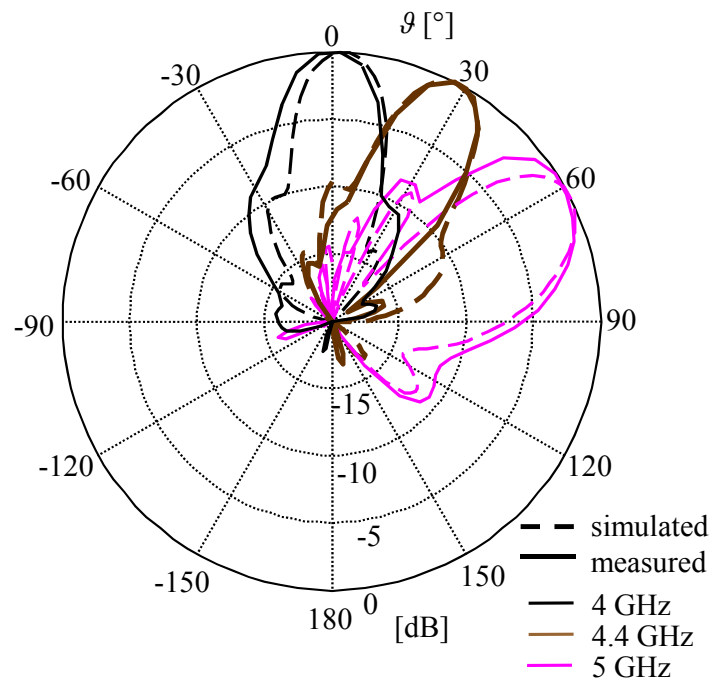
(b) Comparison of measured and simulated radiation patterns in the E-plane.
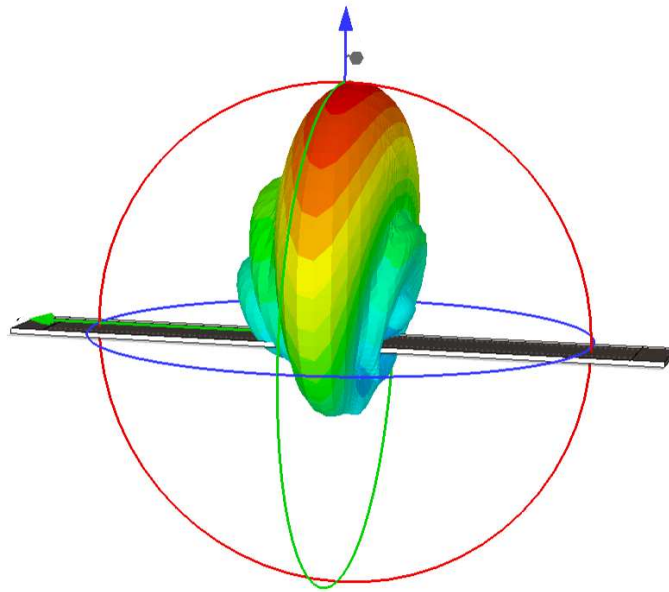
Figure 8.12: Radiation patterns.
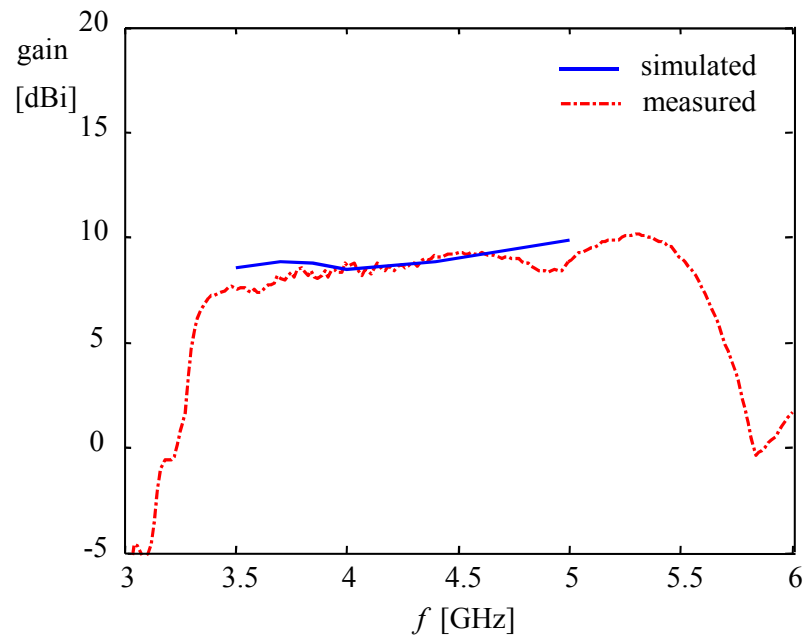
Figure 8.13: Maximum gain from simulation and measurements versus frequency.
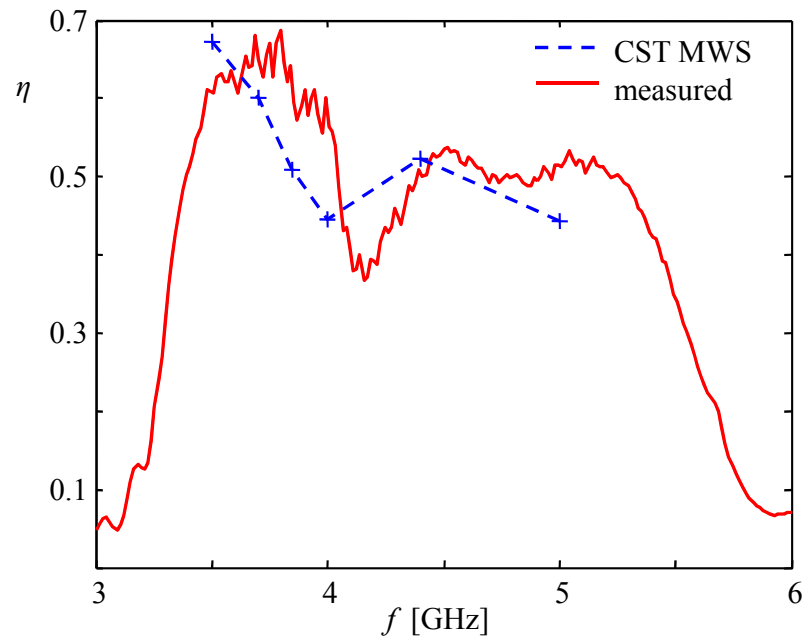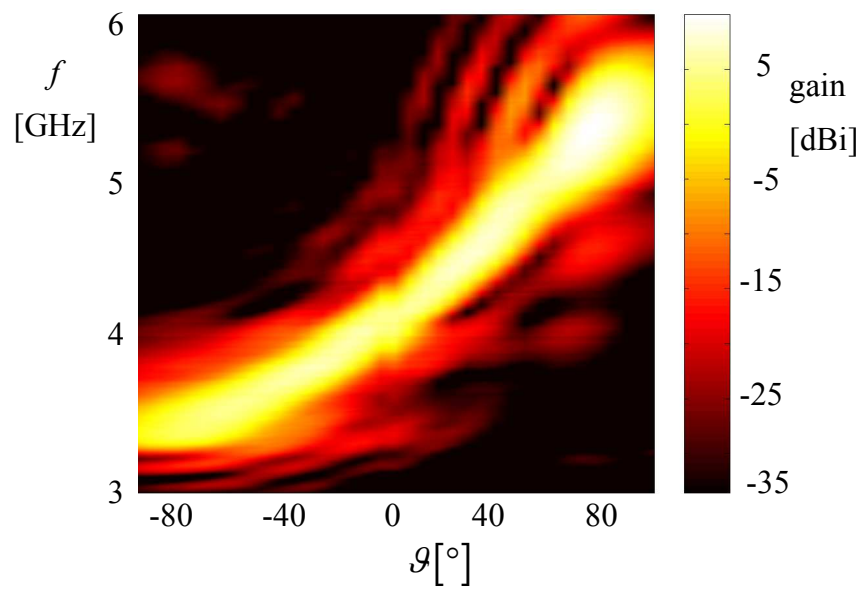
Figure 8.14: Radiation efficiency obtained by measurement and simulation.

Figure 8.15: The 3-dimensional pattern in the farfield while radiating at broadside.

Figure 8.16: Frequency-dependent scan behaviour from $-90°$ to $90°$.

8.2 CRLH Leaky-Wave Antenna: Interdigital Design

The concept to realise the CRLH TL by a periodically modified dielectric-filled rectangular hollow waveguide has already been proven to work successfully by the prototypes presented in [WE07b],[WE07a]. The antennas exhibit a considerable gain while having a low conformal profile. Fabrication remains economic and easy to handle. By substrate integrated waveguide technology the design of a rectangular hollow waveguide is relieved and the final product is of compact size and light weight.

The second open configuration further simplifies manufacturing substantially since this time single-layer printed technology has been used. The required series capacitance is yet still attained while a unit cell can be maintained relatively short in relation to the operating wavelength. This time however, a slightly longer unit cell is the goal with the aim to reach a longer aperture, a more gradual radiation process and thus a higher gain. The dielectric substrate Rogers RO4003 with $\varepsilon_r = 3.38$ and $\tan\delta = 0.0027$ is sandwiched between the ground plane and the top plate. The upper metallic is slotted in interdigital form. It appears as if two metallic rows of "teeth" interdigitate with each other leaving a gap between them. In this manner, a longer capacitive slot is accomodated within little area and a substantial capacitance is reached. The interdigital slot is repeated periodically as can be seen in Fig. 8.17a showing one periodic cell and Fig. 8.17b is an extract of the periodical composition, which also displays the tapered input section. Observable is that the teeth are narrower in the middle of the structure and become broader towards the sides. The field strength of the fundamental mode of the host waveguide is more concentrated in the center and more slits can incorporate more field. Otherwise, the surface currents would be forced to flow laterally which would distort their natural flowing form and thus, the EQC would deviate from the original one. For the same argumentation, the slots continue until the very edges unlike in Fig. 8.18a from [DI09]. In [DI09], the slots end in front of the lateral rows of vias and are thus not adapted to the corresponding field distribution. Thus, extra longitudinal currents are created and an additional shunt inductance L_p to the series capacitance is generated as depicted in Fig. 8.18b. By respecting the introduced parasitic inductance in the perfect CRLH TL EQC, the opening between the LH and the RH mode in the dispersion diagram becomes closer and the frequency range above the light line, where radiation is possible, becomes smaller. A smaller bandwidth of the radiation operation ensues. In [DI09], less periodic cells achieve a comparable gain but the working frequency range is higher with the balanced frequency at 10 GHz and the unit cells are also longer leading to a larger aperture and theoretically to a higher gain.

Eventually, a prototype (Fig. 8.19) based on the cell concept in Fig. 8.17a has been manufactured with 30 cells. A tapered transition section again serves as connection to a common 50 Ω microstrip line.

8.2.1 Comparison of Measurement and Simulation Results

In Fig. 8.20 and 8.21, the reflection and the transmission parameters are shown obtained by simulation and measurement. The $|S_{11}|$ of the prototype even reveals slightly better input matching with $|S_{11}| \leq 15$ dB at some frequencies in the interval of $2.5-5$ GHz than in the simulation. The outcome from simulation and measurement is overall in good agreement

(a) Unit section with a slot in interdigital design.

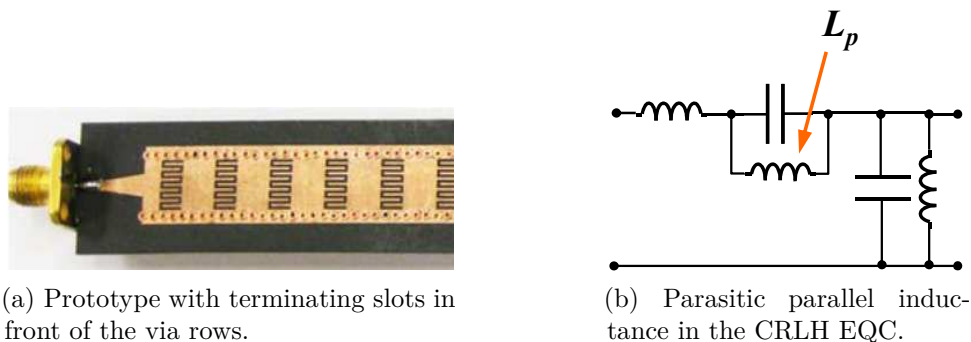(b) Detail from the LWA showing the tapered transition from the feed to the structure.
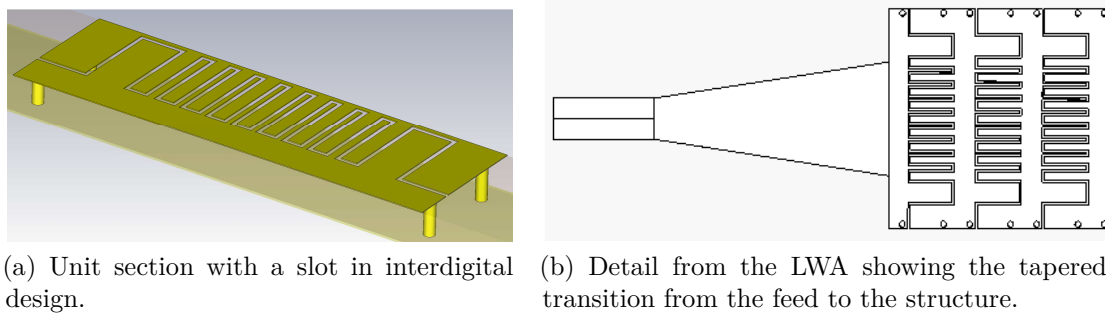
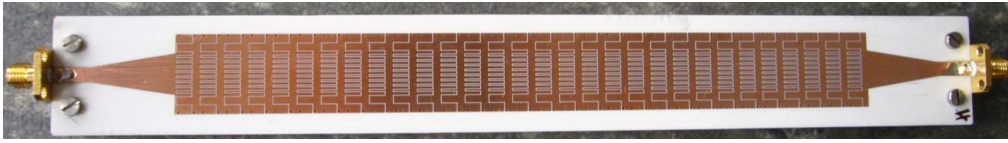**Figure 8.17:** Antenna structure with interdigitally slotted metallic top layer.

and deviations are in the range of under-etching effects and material inaccuracies. The plot of the measured transmission is shifted by 0.5 GHz to lower frequencies but both graphs follow the same course. Compared to the realisations in sections 7.2 and 8.1, which are based on the same idea, one periodic cell is longer with 5.9 mm compared to 3.6 mm in order to obtain a more gradual radiation. A larger aperture arises with the potential to achieve a higher gain. The resulting transmission alludes to a low leakage constant along the LWA being prerequisite for a large effective aperture.

8.2.2 Numerical Computation Results by Modal Series Expansion Approach

To apply the modal series expansion approach, the simulation results of one unit cell are required. The magnitude of some S-parameters at some frequencies seem to be physically not reasonable. With view to Fig. 8.22, illustrating a typical data set for the unit cell of the interdigitally slotted LWA, values above 0 dB attract attention although no active elements are included in the cell. The contributions of the first two modes are visualised as indicated in the parentheses next to the port numbers in the legend. Higher order modes are not indicated because they are hardly excited due to the low port size. The first and second mode do not propagate below their cut-off frequencies 4.3 GHz and 13 GHz, respectively. Modes below cut-off only contribute real energy if by superposition a phase difference exists and if the modes have not decayed to zero. In addition, the S-parameters of evanescent modes are defined with respect to complex power. Consequently, energy

(a) Prototype with terminating slots in front of the via rows.
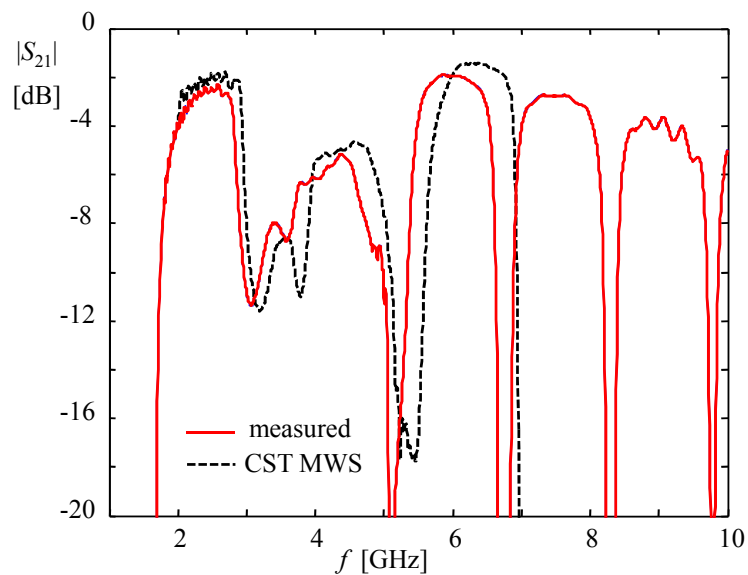
(b) Parasitic parallel inductance in the CRLH EQC.

Figure 8.18: Leaky-wave antenna from [DI09].

Figure 8.19: Prototype fabricated by single-layer printed circuit board design.
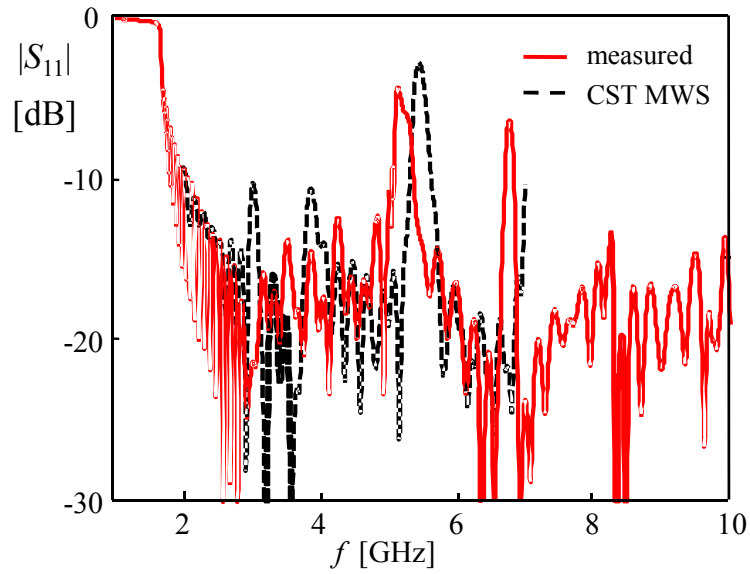
Figure 8.20: The reflection coefficient of the simulation model and the measured prototype.

Figure 8.21: The transmission coefficient simulated and measured.

conservation is not necessarily violated for $|S|$ above 0 dB. By this reasoning, the peak at 5.3 GHz can be explained. However, another peak occurs at the cut-off frequency of the first mode of the homogeneous waveguide. At the cut-off frequency, the propagation constant is zero. When an ansatz to the eigenproblem is posed the forward directed wave is not to distinguish from the backward directed wave, which can be considered as degeneracy *cf.* section 4.1. The *S*-parameters however are defined as relation from the backward to the forward oriented waves and are therefore not exactly declared. Therefore, physical events may occur which seem weird at first sight. In the vicinity of cut-off, the $\boldsymbol{S}$-matrix is ill-conditioned causing numerical problems.
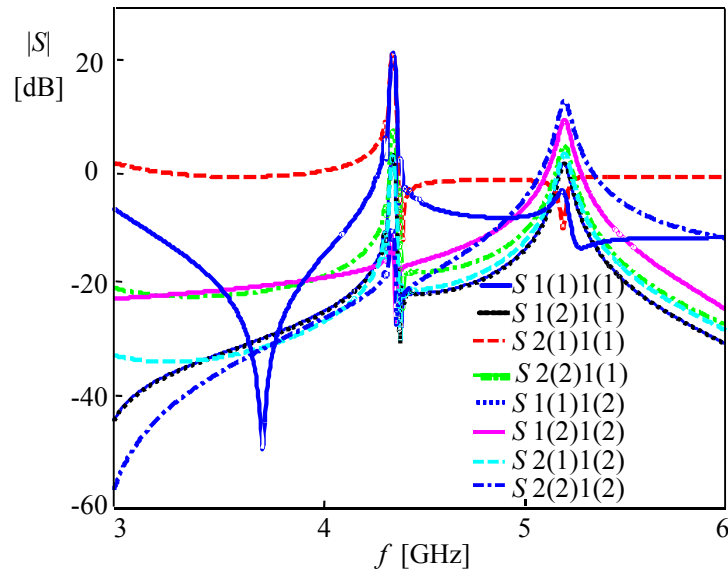
**Figure 8.22:** *S*-parameters showing values above 0 dB.

8.2.3 Dispersion Diagram and Radiation Performance

The open configuration leads to a continuous spectrum of eigenvalues. By evaluating the problem with a series expansion, only an approximation is to expect. The waveguide ports only cover the waveguiding structure. Hence, the eigensolutions serving as basis functions in the modal series expansion merely refer to the structure and do not incorporate the adjacent free space. In the following the modal series expansion is abbreviated as SMA. The simulation model in CST MWS is pictured in Fig. 8.23. Again, the decisive advantage of the reformulation of the eigenvalue problem with the $\boldsymbol{T}$-matrix in Eq. (4.11) is that it can be conveniently solved in a driven simulation by CST MWS. For this model, the frequency solver is employed delivering fast results for certain frequency points. The unit cell as simulation model is meshed with tetrahedra. To account for the non-symmetry of the model, the excitation at both ports is required. The simulation model has been excited by five modes. The outcome where the $\boldsymbol{S}$- or $\boldsymbol{T}$-matrix, respectively, is composed of just one mode agrees best with the reference data generated by the matrix pencil method *cf.* section 9.4, which evolves the eigensolution from the field data of the complete periodic antenna obtained by the time domain solver. This is to observe in Fig. 8.24. The balanced frequency is about at 3.75 GHz. The matrix pencil method only reveals
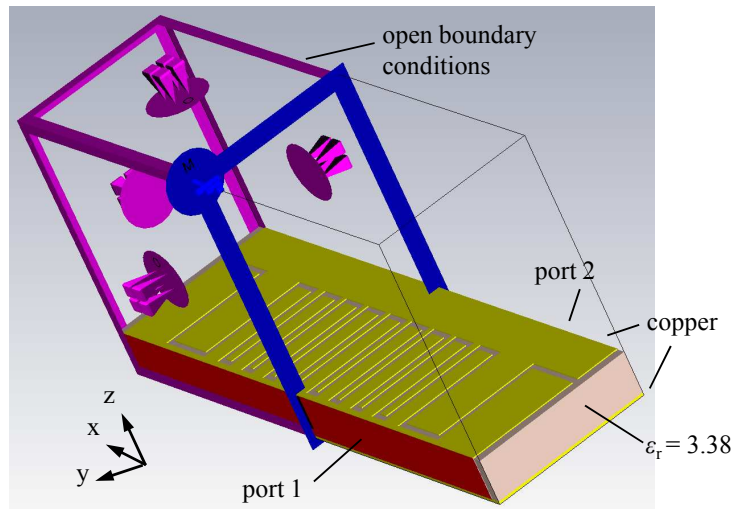
Figure 8.23: The unit cell of the interdigitally slotted LWA.

approximate balancing. Below 3.75 GHz, LH wave propagation is to note characterised by anti-parallel phase and group velocity. By constituting the matrix by two modes, the graph is perturbed around 4.5 GHz, what corresponds with the cut-off frequency of the first mode in this particular simulation. Compared to the other LWA realisation with a periodic length of 3.6 mm, the unit cell length of this model is 5.9 mm. The vertical vias indeed function as metallic side walls of a conventional waveguide but the field can penetrate between the vias in particular for the longer cell length. The balanced frequency 3.75 GHz approximately corresponds to an equivalent waveguide width of 22.05 mm with solid side walls, which is larger than the opening width of 18 mm between the vias.
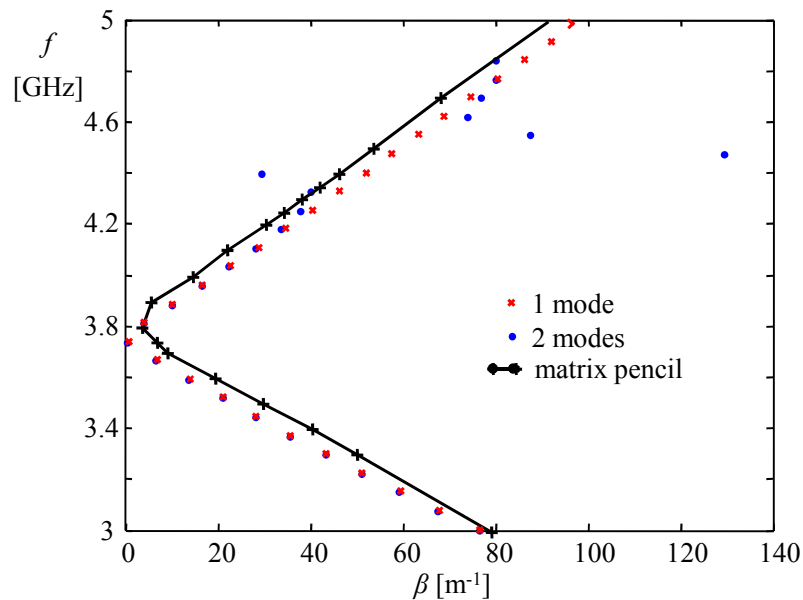
Figure 8.24: The dispersion behaviour computed by matrix pencil and SMA technique.

MP and SMA deliver the attenuation as plotted in Fig. 8.25, which the eigenmode solver of CST MWS or Ansoft HFSS do not provide. Nevertheless, the value of α is composed of losses and radiation. Both diminish the energy of the wave that travels from the input to the end of the LWA. The SMA reveals high attenuation around 3.75 GHz due to a little bandgap, which appears in the infinite structure but it is not that obvious for the finite antenna. Even though the modal series expansion only provides an approximation
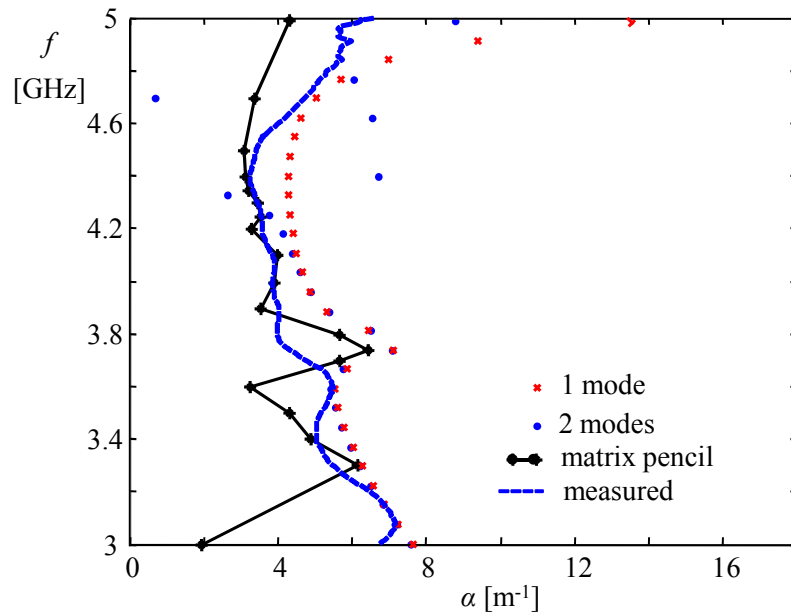

**Figure 8.25:** The attenuation.

for the open periodic SIW the dispersion graph agrees well with the results of the matrix pencil method. The fact that the modal series expansion method functions well for this antenna can be explained by the configuration of the antenna. Despite the slots, the upper metallisation can be treated as a compact metal layer which clearly separates the waveguiding structure from the surrounding free space. Therefore, the eigensolutions of the waveguiding structure together with the information contained in the S-parameter results of the unit cell, as illustrated in Fig. 8.23, reveal a dispersion behaviour which also predicts the radiation performance. It is to observe that, if more modes than one constitute the $\boldsymbol{S}$-matrix, the results are distorted. The cause is that the vertical dimension of the port is low and higher order modes are far below cut-off in the frequency interval $3-5$ GHz of interest, in which the fundamental mode operates, and are thus insignificant. Therefore, few modes deliver better results than more modes.

It can be summarised that an LH mode is established leading to backfire radiation as well as an RH wave turning the radiation angle towards endfire. Broadside radiation meaning radiation perpendicular to the antenna is achieved. That is testified and visualised in the diagrams Fig. 8.26 to Fig. 8.28. Fig. 8.28 shows very well the scanning capability of the antenna ranging from backfire to endfire. The measured prototype verifies the scanning capability in Fig. 8.26. At the lower frequencies belonging to the LH

frequency domain, the radiation beam points towards backfire, which is the feeding side and equivalent with 0°. The measurements reveal broadside radiation at 3.65 GHz differing from the simulation result by 0.1 GHz. There, the beam points towards broadside at 3.75 GHz. In Fig. 8.27, the forms of the radiation patterns are compared. The patterns from simulation are shifted by 15° because the measurements let assume an offset since the radiation angle was not calibrated in the measurement set-up. The shapes of the radiation patterns are in good agreement. In Fig. 8.29, the cross- and co-polarisation of the simulation is to observe. They are pictured for broadside radiation (3.75 GHz) in the H-plane. To highlight is the very low cross-polarisation and the smooth and symmetric co-polarisation. In addition, the cross-polarisation is negligible in the E-plane.
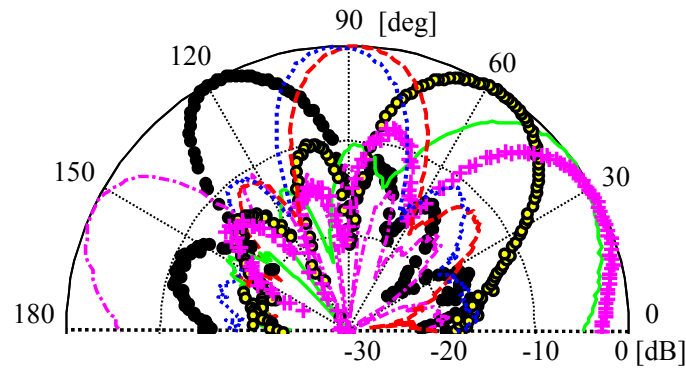
Figure 8.26: Scan for 3 GHz, 3.1 GHz, 3.3 GHz, 3.6 GHz, 3.7 GHz, 4.1 GHz and 4.8 GHz (from right to left) in the E-plane.
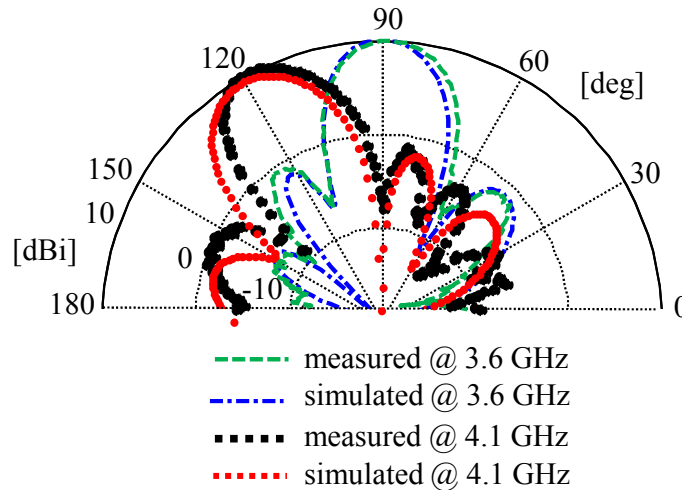

**Figure 8.27:** Measured and simulated radiation patterns in the E-plane.

The gain over frequency measured as well as simulated is depicted in Fig. 8.30, where both data are comparable for a 30-cell antenna. The gain in the simulation attains more than 10 dB at 4 GHz and can maintain the value for higher frequencies whereas the gain of the prototype begins to fluctuate. For comparison, the gain of a 40-cell antenna is
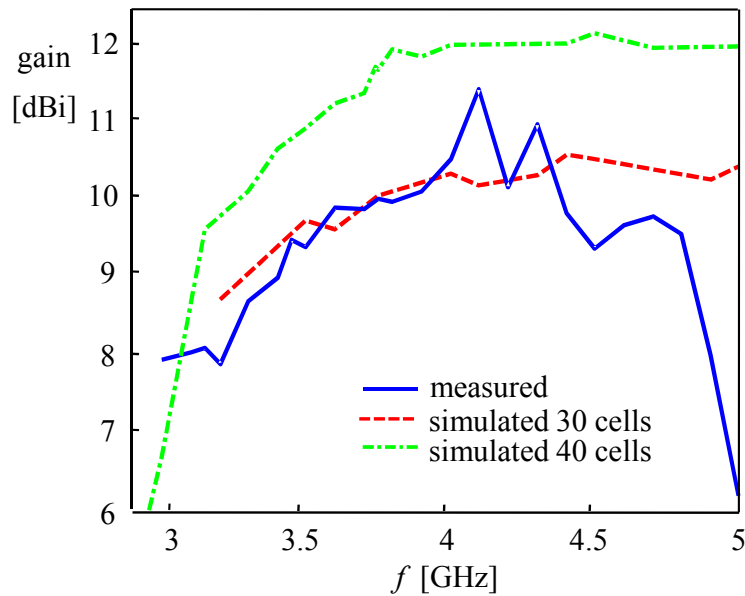
simulated, which proves an extendable gain up to 12 dB. The overall measured gain over frequency and over elevation angle ϑ is shown in Fig. 8.28. The diagram verifies contiguous radiation performance and a gain up to 11 dB.
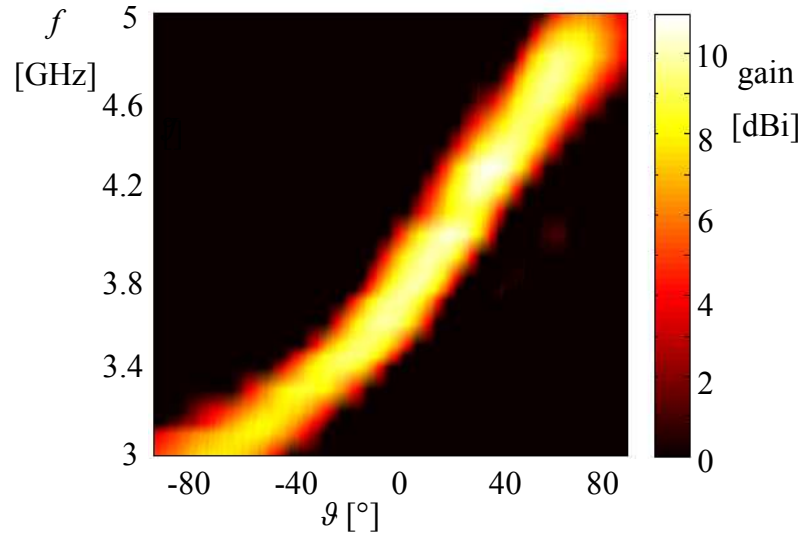
Figure 8.28: The measured gain over elevation angle and frequency.
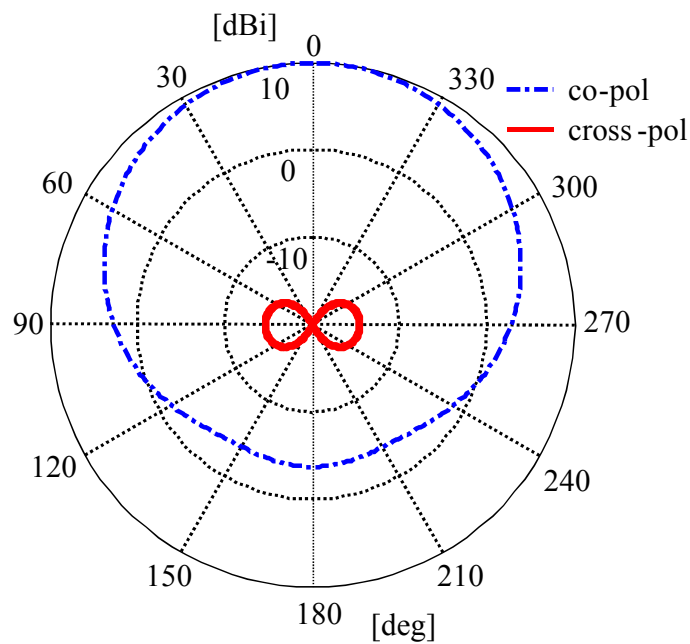
**Figure 8.29:** Cross- and co-polarisation in the H-plane.

Figure 8.30: The measured and the simulated gain in comparison.

### 8.2.4 Bloch Impedance and Modal Field Distribution

For matching and for validation reasons, the Bloch impedance is computed for the input interface of a unit cell. An equivalent current and power is computed from the field solution of the driven entire antenna structure as described for the other structures. It is to observe in Fig. 8.31a that the real part is in the range of 20 Ω. The imaginary part tends to be $|\operatorname{Im}\{Z_B\}| \lesssim 5$ except for the jump discontinuities at 3.75 GHz and 4.3 GHz. The first jump is at the transition where the LH mode converts to the RH mode. The second one is the cut-off of the H_{10} mode in the homogeneous background waveguide of the underlying simulation. The imaginary part as well shows peaks in the graph at the same positions. Except for the irregularities, $|\operatorname{Im}\{Z_B\}| \lesssim 5 \Omega$. A real wave impedance signifies wave propagation whereas an imaginary impedance is an indication of purely evanescent waves. Fig. 8.31b confirms Z_B to vary within a periodic unit cell showing the magnitude of it.

The field distributions for the dominant mode are shown in Figs. 8.32a-8.32c at the LH frequency 3.4 GHz. The components do not deviate much from the field solution of the TE_{10} mode of the background waveguide except that they are present below the former cut-off. The similarity is no surprise since the profile is low and any higher order modes are unlikely to propagate.

Next, the Z_B gained from the simulated unit cell is compared with the one computed with the field solutions of the total LWA for the same cross sectional plane. The unit cell simulation yields modal solutions of two dominant waves. They travel in forward and in backward direction. Z_B is defined according to power flow in positive direction and computed by taking the mean value of both waves. The Bloch impedance from the complete antenna is computed for the transversal plane identical to the port plane of the
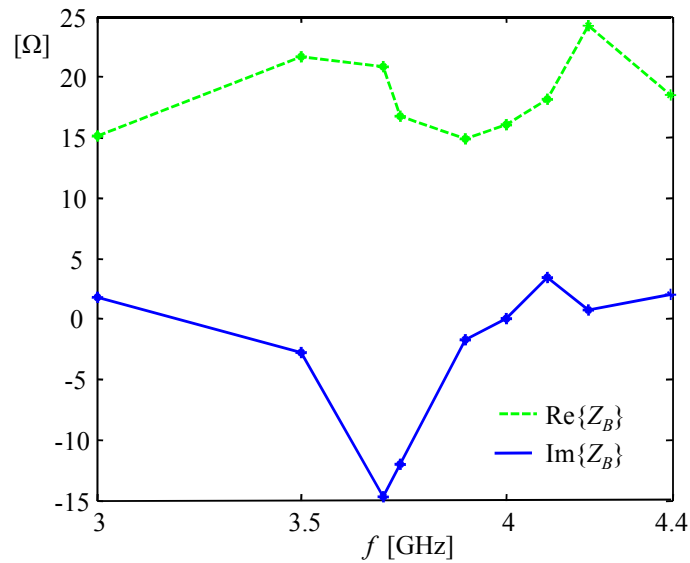
(a) Bloch impedance for the input interface in the unit cell
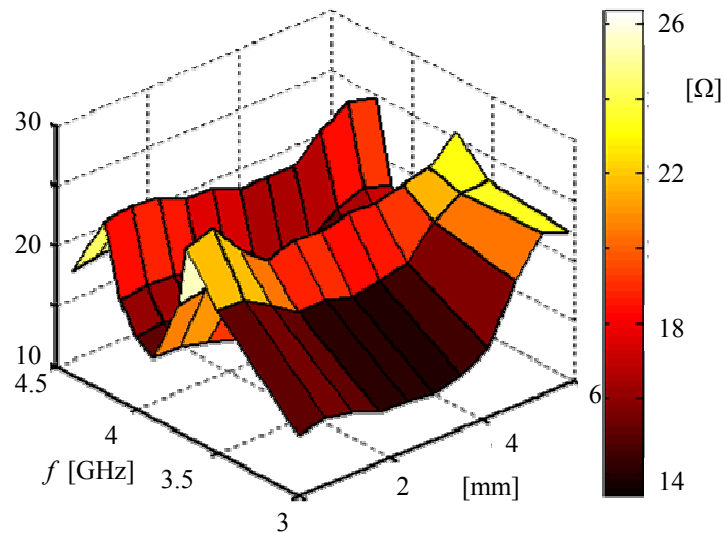
(b) $|Z_B|$ depending on frequency and position within the single cell

Figure 8.31: The Bloch impedance of a unit cell in the entire antenna structure.

unit cell. The field is extracted in the middle of the periodic structure where reflections from the transitions at both ends are assumed to have mainly faded away. The reflection coefficient gained by the MP method has also been taken into account but has not altered the result significantly. The results for Z_B for the unit cell simulation as well as for the antenna are contrasted in Figs. 8.33 and 8.34. Equivalences can be observed.

$|H_x|$ [A/m]

(a) H_x-component

$|H_y|$ [A/m]

(b) H_y-component

$|E_z|$ [V/m]

(c) E_z-component
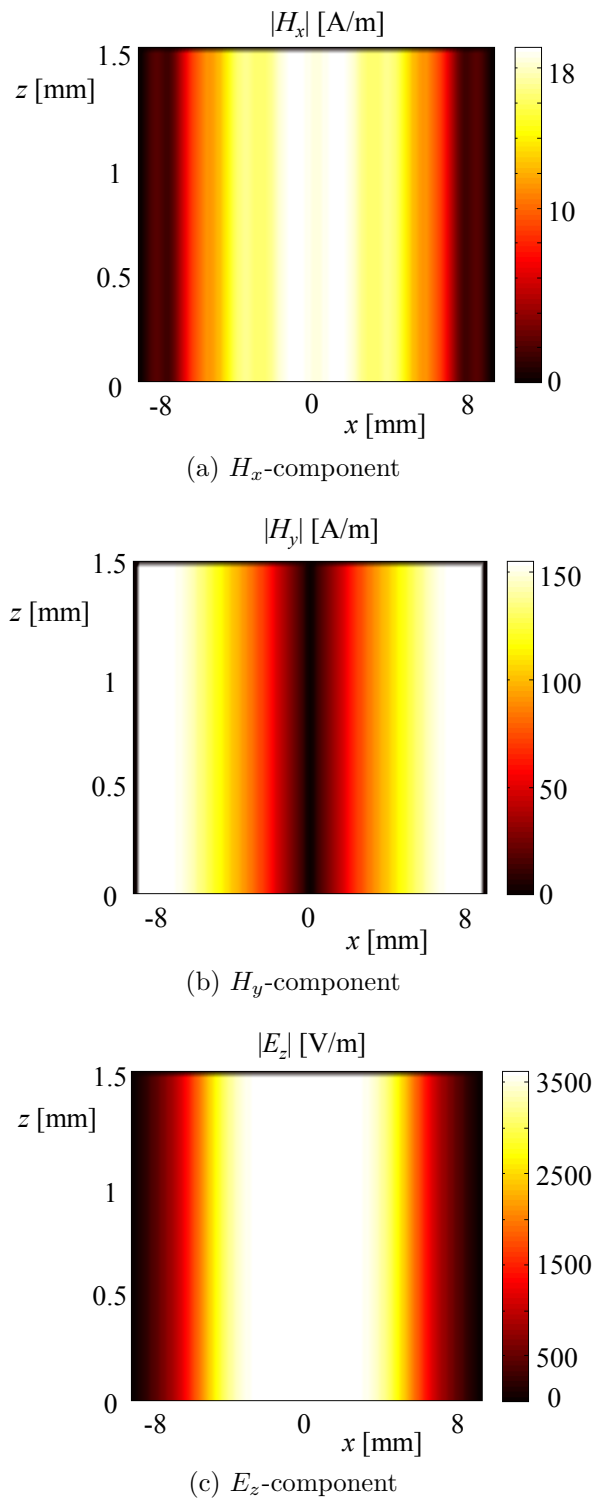
Figure 8.32: Modal field distributions in the port plane.
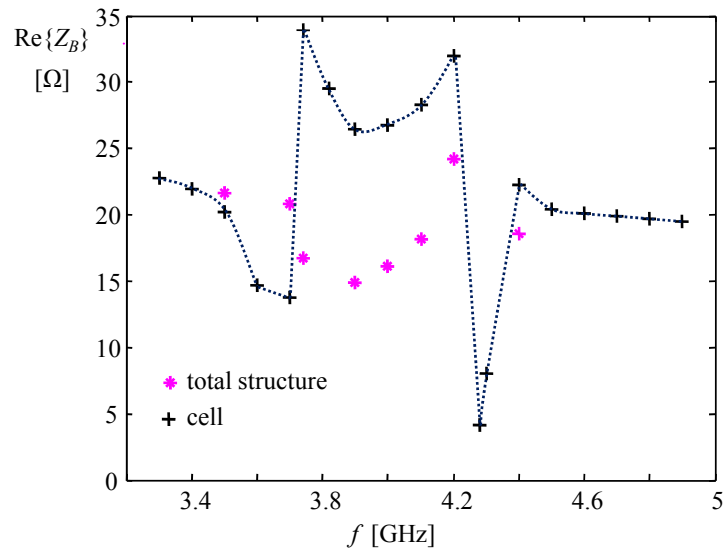
Figure 8.33: Real part of Z_B by simulation of a unit cell and of the complete structure in comparison.
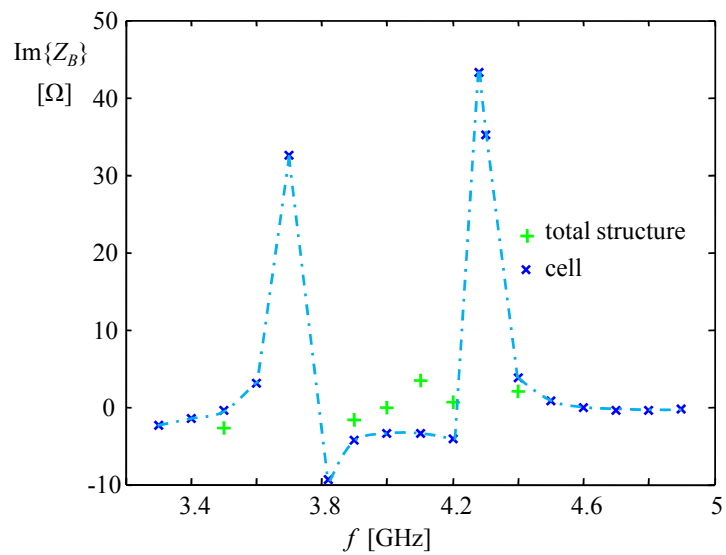
Figure 8.34: Imaginary part of Z_B by simulation of a unit cell and of the complete structure in comparison.

8.3 Periodically Modulated Grounded Dielectric Slab

The considered periodically modulated grounded dielectric slab is an open configuration, whose full-wave dispersion analysis is a challenging problem. In this work, it serves in particular to demonstrate the capabilities of the extended scattering matrix approach as proposed in chapter 6. The periodically modulated grounded dielectric slab is a conventional waveguide functioning as a leaky-wave antenna. However, as a leaky-wave antenna it is operated in higher order space harmonics which exhibit metamaterial-like behaviour.

8.3.1 Design Data

One way to periodically modulate the grounded dielectric slab is to form corrugations. According to the design rules given in [SP83], the following antenna has been developed. The frequency range of operation is aimed at $9.4 - 14$ GHz. In [SP83], the frequencies are higher by a factor of 10, where they commonly use substrates with a higher dielectric constant e.g. $\varepsilon_r = 12$ exhibited by silicon mostly employed in integrated optical circuits. For the frequency range $9.4 - 14$ GHz, the dielectric substrate Rogers TMM4 with $\varepsilon_r = 4.5$ and $\tan \delta_\varepsilon = 0.002$ is adequate. In [SP83], a height of the homogeneous dielectric slab $h/\lambda = 0.2$ is recommended whereas here, the thickness $h/\lambda = 0.35$ is chosen which is slightly increased to compensate the lower permittivity in order to attract the waves more to the dielectric layer. The reference wavelength $\lambda = 20$ mm corresponds to an effective $\beta = 315$ m^{-1} at 10 GHz, which is obtained from the 2D eigensolution of the uniform port cross section from CST MWS. The periodical length p should equal $p = \lambda$ since radiation is achieved by the periodic perturbation of the waves guided by the uniform waveguiding structure. A suitable periodic length can be obtained from Eq. (6) in [SP83]

$$\frac{\lambda}{\sqrt{\beta/k_0} + 1} \leq p \leq \frac{2\lambda}{\sqrt{\beta/k_0} + 1}. \tag{8.1}$$

The expression follows from the requirement of single-beam operation such that only the $n = -1$ harmonic wave radiates. Hence, the transverse propagation constant in z-direction must be real for $n = -1$ and simultaneously, the transverse wavenumbers of the other space harmonics with $n \neq -1$ must result as imaginary according to the expression

$$k_{zn} = k_0 \left[1 - \left(\frac{\beta}{k_0} + \frac{n\lambda}{d} \right)^2 \right]^{1/2} \tag{8.2}$$

cf. section 3.4. For a good and and preferably gradual radiation performance, the length of the corrugation is determined as $d = 0.5p$ and the depth of the corrugation is ascertained as $t = 0.0035$ m $= 0.175\lambda$ with view to the scattering parameters. The measures of the unit cell are depicted in Fig. 8.35, which is also the cell model in the simulation. The reached transmission coefficient and the reflection coefficient of a 25-cell continuation are depicted in Fig. 8.36.

8.3.2 Modal Solutions and Radiation Behaviour

The dispersion behaviour obtained by the extended scattering matrix approach (SMA), according to section 6.2, is plotted in Fig. 8.37 for the frequency range of interest. The
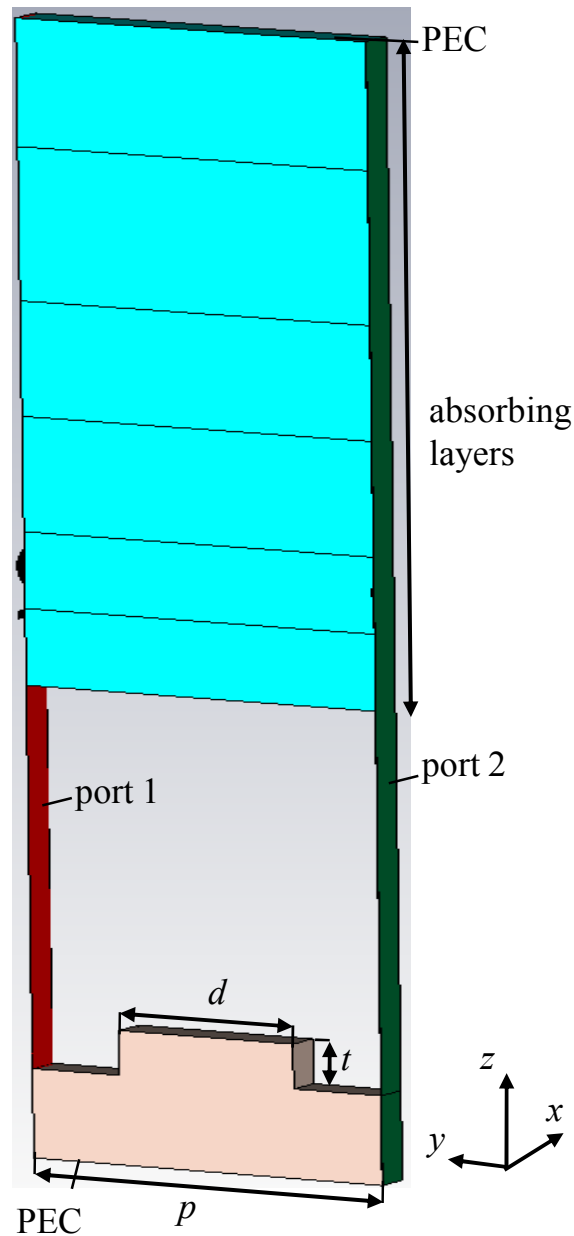
Figure 8.35: A periodic unit cell of the grounded dielectric corrugated slab antenna with an absorber-covered PEC shield at the top according to section 6.2.

phase constant does hardly not differ if one or four modes constitute the S-matrix. It is clearly smaller than the wavenumber of free space meaning radiation occurs. Although it is stated in [SP83] that dielectric grating antennas do not feature radiation at broadside direction β vanishes at 9.4 GHz, promising radiation perpendicular to the aperture. According to [SP83] an internal resonance shall cause a stopband. The reflection coefficient rises at 9.4 GHz but is still ≤ -10 dB in Fig. 8.36. The conventional operation in the right-handed sense turns into left-handed wave behaviour at 12.7 GHz according to the graph in Fig. 8.37. At the transition, the matching behaviour reaches the maximum value
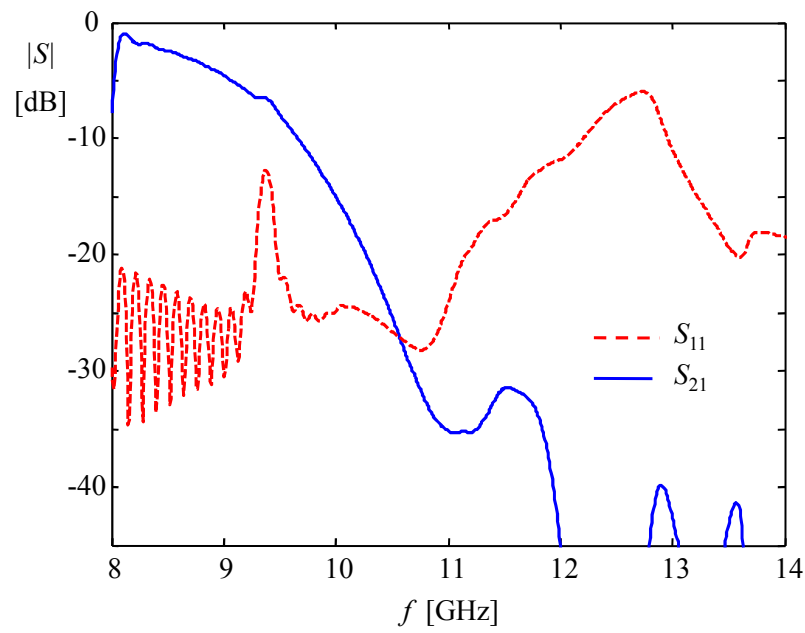
Figure 8.36: Reflection and transmission coefficient for the corrugated dielectric slab antenna.
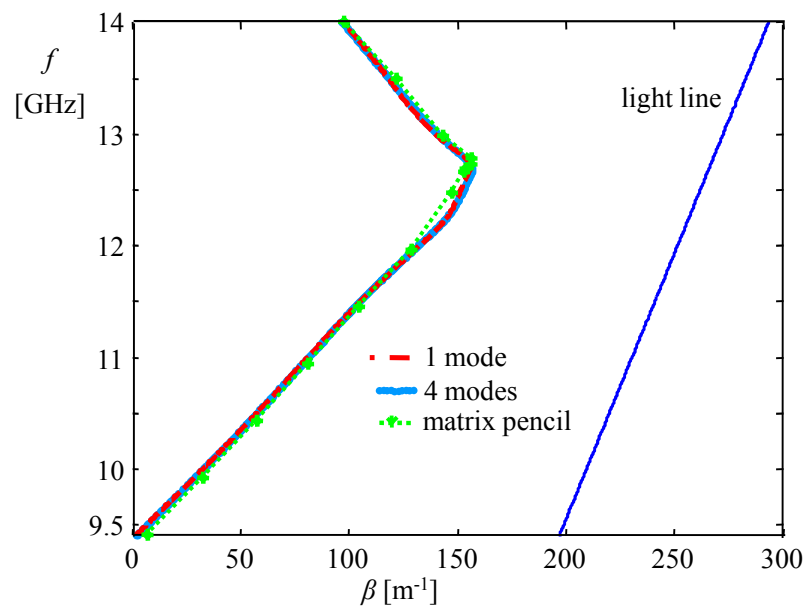

**Figure 8.37:** Confirmed dispersion characteristic.

-6 dB (Fig. 8.36). The slope of the dispersion curve above 12.7 GHz is negative indicating anti-parallel group and phase velocities. The matrix pencil method [HS88] additionally agrees well with the results. The matrix pencil algorithm processes the field data of a 25-unit-cell structure. Attenuation is pictured in Fig. 8.38, where the number of modes building the $\boldsymbol{S}$-matrix clearly makes a difference. By considering just one mode the attenuation is the highest with 18.1 m^{-1} at 12.5 GHz. If the results of the matrix pencil method are taken as reference data four modes appear as converged because the result by five modes is almost identical. The maximum of attenuation is reached with 15.19 m^{-1} at 12.53 GHz.
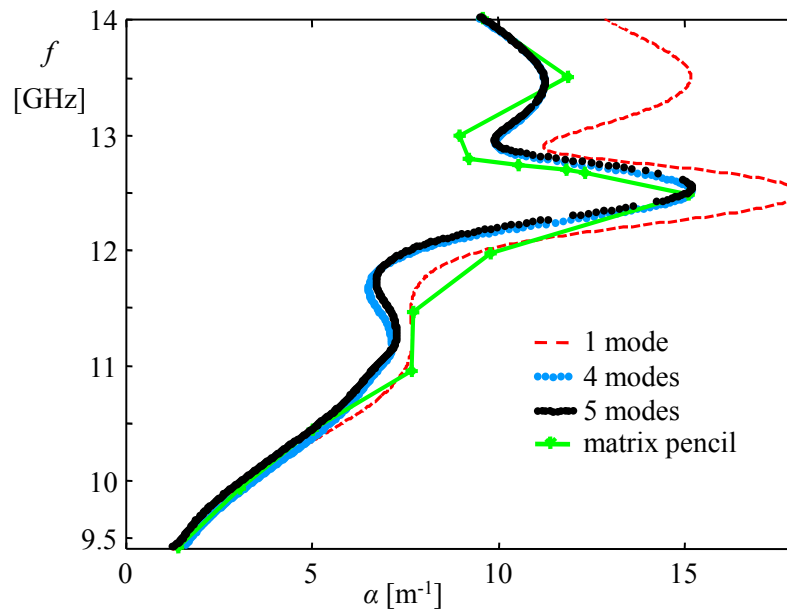

Figure 8.38: The attenuation behaviour can be considered as converged with four modes.

The results are obtained by employing the good absorbing layer as designed in section 6.2, comprised by six sublayers (Fig. 8.35), which are placed in front of the PEC top boundary. In Fig. 8.39 and Fig. 8.40, the outcome with the good absorption layer is compared with the results obtained by employing the worse absorption layer (*cf.* section 6.2), which is also constituted by six sublayers but with only a fourth of the absorbing capacity. The phase constant is hardly influenced (Fig. 8.39) while the attenuation constant is affected with view to Fig. 8.40, for which the weaker absorbing layer leads to a higher attenuation.

To visualise the 2π-periodic behaviour of the phase constant with respect to relation (3.34), the frequency range $0-25$ GHz is depicted in Fig. 8.41. The values of the phase constants of higher order modes or of the fundamental mode at higher frequencies can always be reduced to the Brillouin zone with $|\beta| \leq 157$ m^{-1}. The 2D eigensolutions of the port cross section from CST MWS (unperturbed waveguide) are compared to the SMA results of the perturbed structure with four modes. In CST MWS, higher order modes below cut-off are close to the light line as to see in Fig. 8.41. These modes mainly reside in the absorbing layers *cf.* Fig. 6.10 in section 6.2.3. In the analytical solution where no absorbing layer is present these modes appear as leaky modes, which is to observe in Fig. 8.42. The cut-off frequency of the lowest mode of the unperturbed structure is
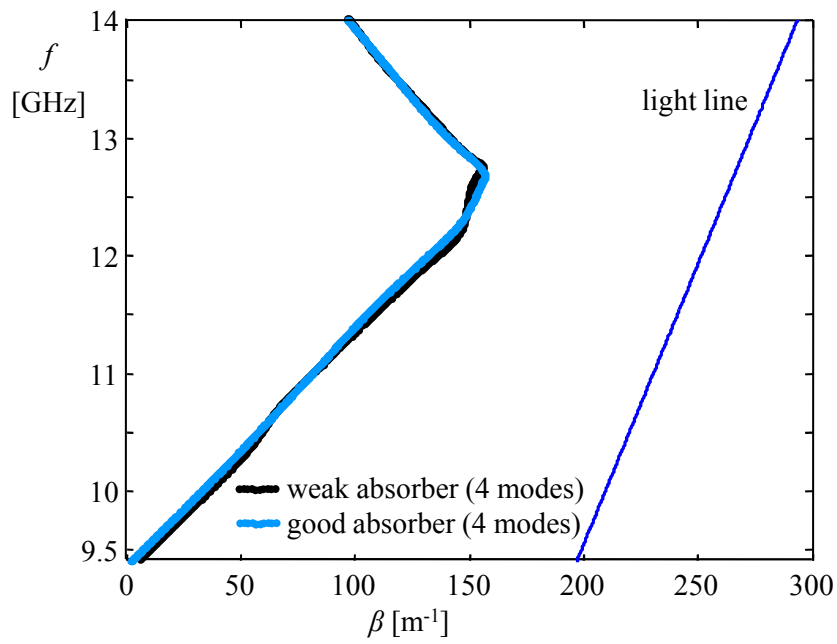
Figure 8.39: The dispersion behaviour with four modes.
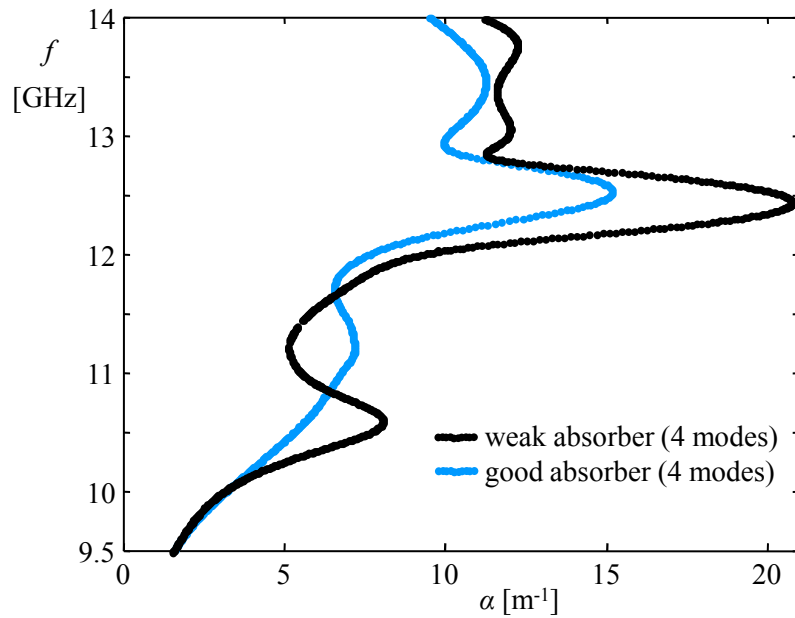
Figure 8.40: The weakly absorbing layer causes a higher attenuation with four modes included.
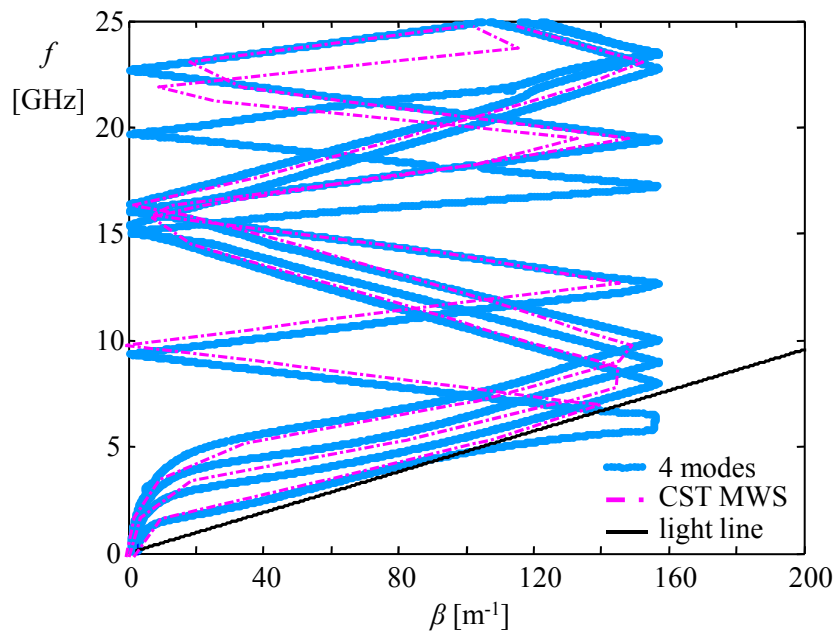
Figure 8.41: The dispersion behaviour found by using CST MWS for the unperturbed waveguide and by the SMA for the perturbed waveguide.
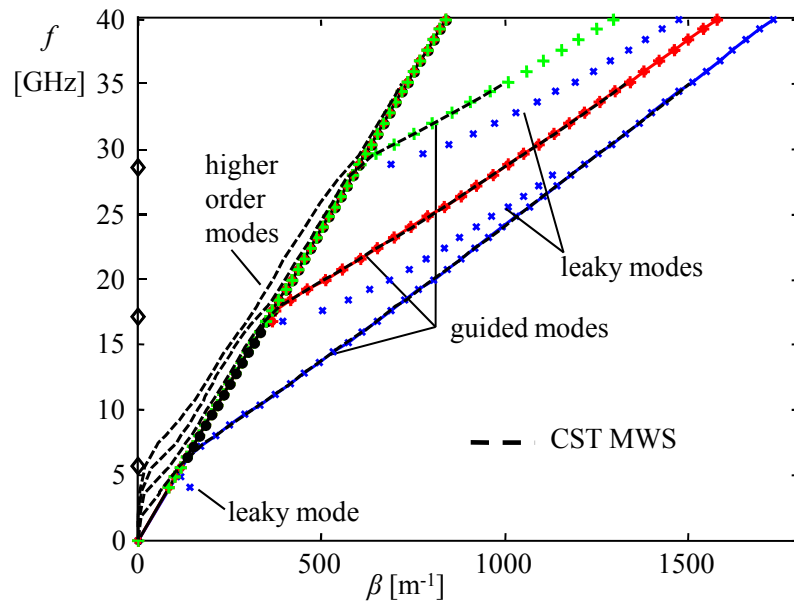
Figure 8.42: Dispersion diagram for unperturbed dielectric slab, analytical vs. numerical results with good absorber (identical with Fig. 6.8).

5.72 GHz, where one mode (dash-dotted) in Fig. 8.41 converts from the leaky state into a guided surface mode and turns away from the light line. In Figs. 8.43 and 8.44, the amplitude of the transverse E_x component is plotted over the configuration perpendicular to the aperture of the dielectric slab at 10.5 GHz. The figures depict the field distribution for the perturbed dielectric waveguide in the plane of the port cross section. In Fig. 8.43, one mode can be observed which is located in the substrate, so it is a guided surface wave, whereas the others are mainly in the air or in the absorbing layers. At the position of the PEC shield, the tangential E component vanishes and the performance of the absorption layer is satisfactory. In Fig. 8.44, corresponding modes can be noted but the influence of the weaker absorption capacity is also to observe because reflections at the PEC boundary result in standing waves. In [DOdZvdB01], a similar mode characterisation is pictured but the modes are valid for the homogeneous waveguide configuration treated there. In
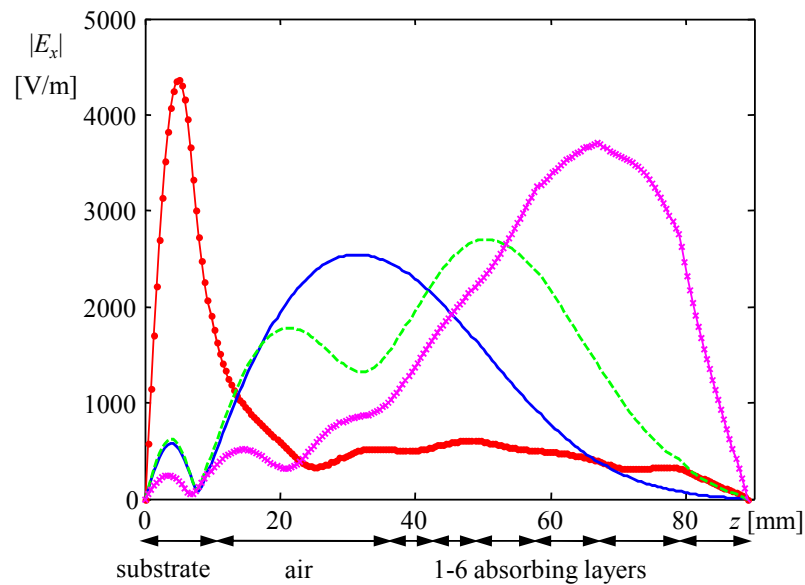
Figure 8.43: Guided, evanescent and absorber modes with good absorbing layer.

Figs. 8.45a-8.45c, the modal field distribution of the fundamental mode above cut-off is visualised in the port plane for the periodically corrugated dielectric slab. In Figs. 8.46a-8.46c, the modal field is shown at the same conditions for a higher order mode in the perturbed structure at the same frequency 10.5 GHz. Figs. 8.47a and 8.47b confirm the radiation performance at broadside direction. The frequency agrees with 9.4 GHz where β vanishes in the dispersion diagram. Although periodic antennas are not supposed to radiate at broadside direction according to [SP83], the corrugated dielectric slab featuring 25 cells exhibits 8.9 dBi at $\vartheta = 0°$. It is to note that the radiation characteristic is remarkably symmetric with respect to the longitudinal axis.
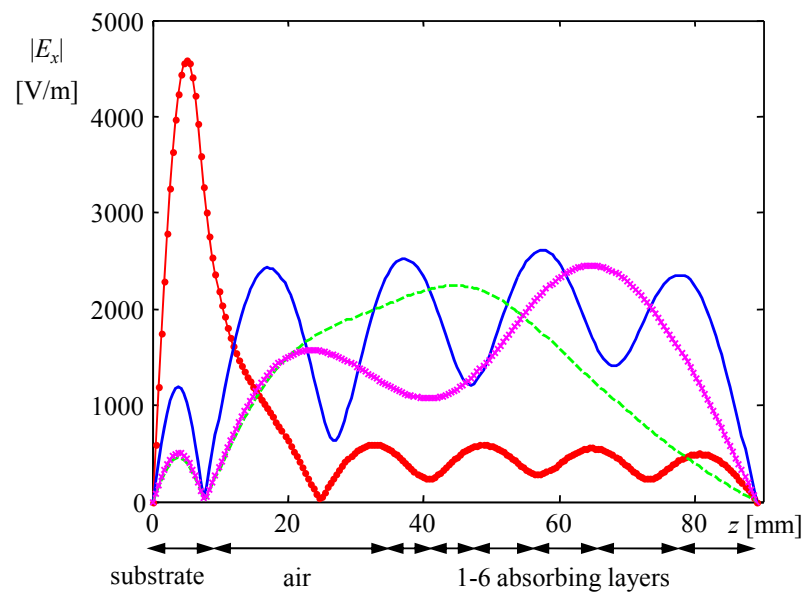
Figure 8.44: Guided, evanescent and absorber modes with weaker absorbing layer.
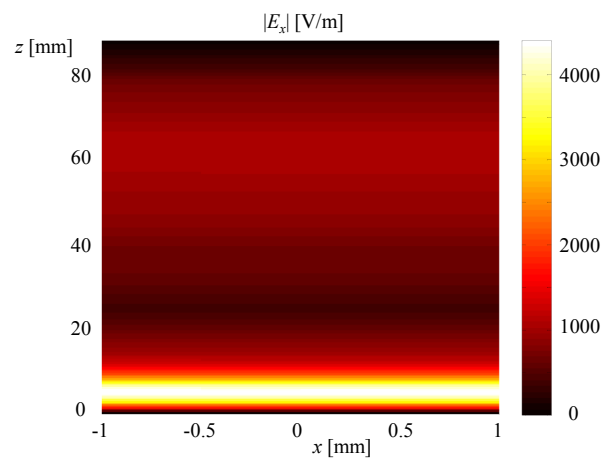
(a) E_x-component
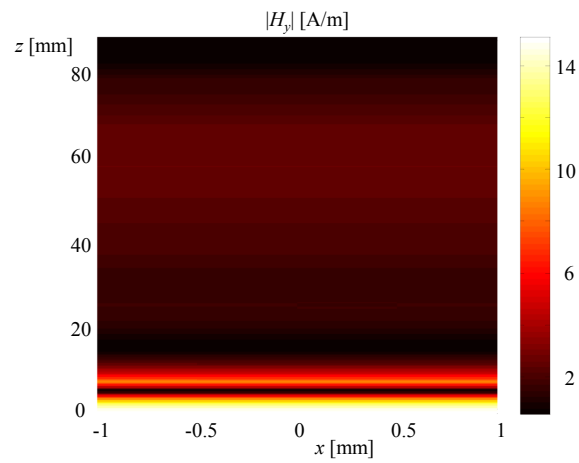
(b) H_y-component
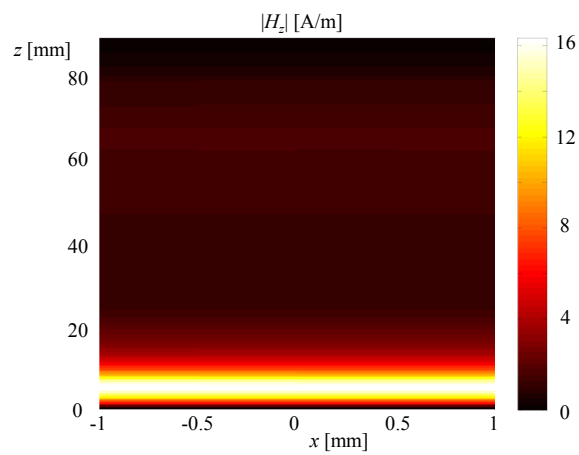
(c) H_z-component

Figure 8.45: Modal field distribution of the fundamental mode at 10.5 GHz.

(a) E_x-component

(b) H_y-component

(c) H_z-component
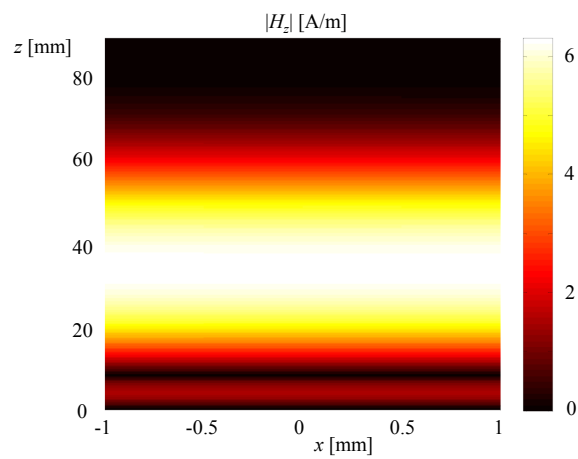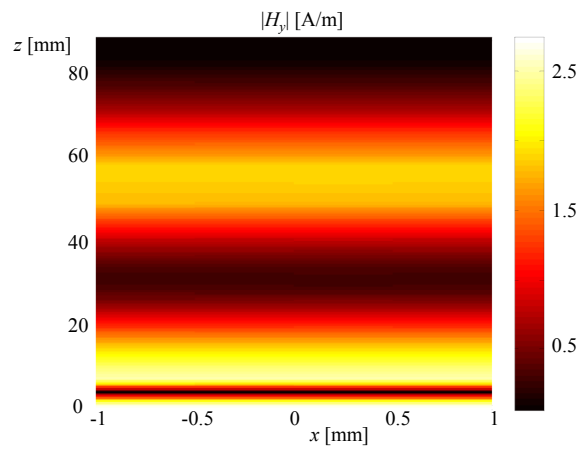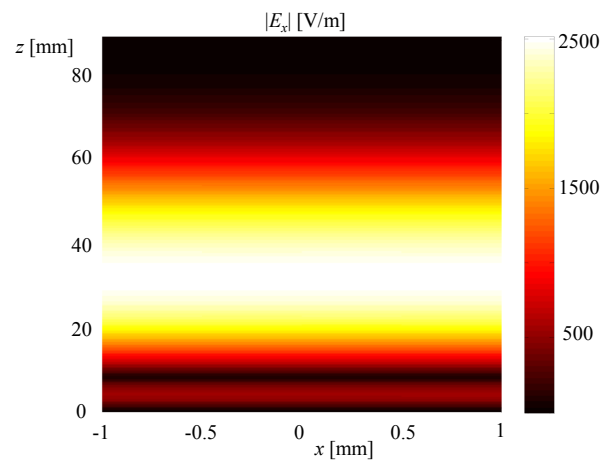
Figure 8.46: Modal field distribution of a higher order mode at 10.5 GHz.
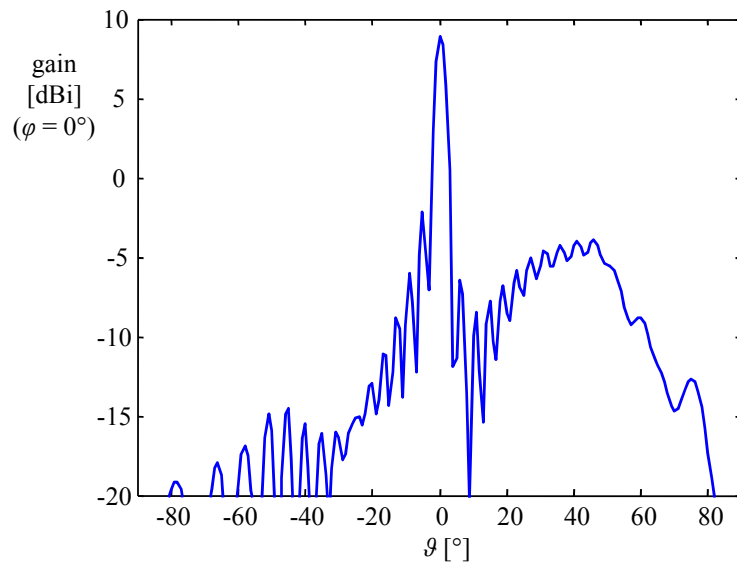
(a) *E*-plane
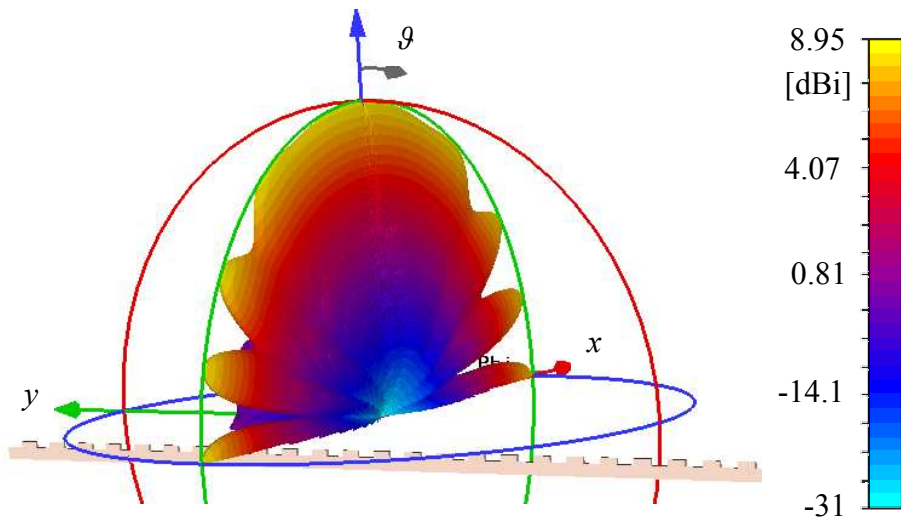
(b) 3D radiation pattern

Figure 8.47: Radiation performance for 25 cells at 9.4 GHz (broadside radiation).

9 Appendix

9.1 Singular Value Decomposition

For every matrix $\boldsymbol{A}$, a scalar τ as singular value and corresponding singular vectors $\boldsymbol{u}$ and $\boldsymbol{v}$ fulfill the following expression

$$\boldsymbol{A}\boldsymbol{v} = \tau\boldsymbol{u}. \tag{9.1}$$

In form of matrices, the singular values are to find on the diagonal of the matrix $\boldsymbol{D}$. The corresponding singular vectors constitutes the columns of $\boldsymbol{V}$ and $\boldsymbol{U}$, and it is

$$\boldsymbol{A}\boldsymbol{V} = \boldsymbol{U}\boldsymbol{D}. \tag{9.2}$$

The singular value decomposition (SVD) of $\boldsymbol{A}$ is

$$\boldsymbol{A} = \boldsymbol{U}\boldsymbol{D}\boldsymbol{V}^T \tag{9.3}$$

with the orthogonal matrices $\boldsymbol{U}$ and $\boldsymbol{V}$. $\boldsymbol{D}$ has the form

$$D = \begin{pmatrix} \tau_1 & 0 & \cdots & \cdots & 0 \\ 0 & 0 & \cdots & \cdots & 0 \\ 0 & \ddots & \ddots & 0 & \vdots \\ \vdots & 0 & \tau_r & \ddots & 0 \\ \vdots & \vdots & 0 & 0 & \vdots \\ \vdots & \vdots & \vdots & \vdots & \vdots \\ 0 & 0 & 0 & 0 & 0 \end{pmatrix}. \tag{9.4}$$

The rank r of $\boldsymbol{D}$ gives the number of linearly independent rows or columns of a full matrix coming along with r nonequivalent to zero different singular values. They are the square roots of the eigenvalues $\tau_i = \sqrt{\Gamma_i}$ in ascending order with $i = 1, 2, \ldots, r$. The Γ_i are the eigenvalues of $\boldsymbol{A}^T\boldsymbol{A}$. Normally neither the eigenvectors of $\boldsymbol{A}^T\boldsymbol{A}$ to the eigenvalue $\Gamma = 0$ nor the corresponding vectors from the matrix $\boldsymbol{U}$ are needed.

9.2 Eigenvalue Decomposition

Considering the eigenvalue decomposition, $\boldsymbol{A}$ describes a mapping of a vector $\boldsymbol{v}$ being equal to the mapping of its eigenvalue Γ with the eigenvector $\boldsymbol{v}$

$$\boldsymbol{A}\boldsymbol{v} = \Gamma\boldsymbol{v} \tag{9.5}$$

but $\boldsymbol{A}$ needs to be square in contrast to the SVD. The eigenvalue decomposition (EVD) is similar to (9.3) and can be written as

$$\boldsymbol{A} = \boldsymbol{V}\boldsymbol{D}\boldsymbol{V}^{-1} \tag{9.6}$$

if $\boldsymbol{V}$ is nonsingular. In contrast to the SVD, $\boldsymbol{A}$ in the EVD describes a mapping from a vector space into itself like in an ordinary differential equation. In an SVD, the mapping from one vector space into another one is regarded, also with different possible dimensions. That is mostly the case for systems of simultaneous linear equations. The EVD and SVD of $\boldsymbol{A}$ are identical if the matrix is square, symmetric and positive definite.

9.3 Pseudoinverse

The condition number is the relation from the minimum to the maximum singular value. For matrices with large condition numbers meaning they are ill-conditioned, the pseudoinverse is to prefer which treats SVs less than a tolerance as zero. For the SV-decomposed matrix $\boldsymbol{A}$ the pseudoinverse $\boldsymbol{A}^+$ is

$$\boldsymbol{A}^+ = \boldsymbol{V}\boldsymbol{D}^+\boldsymbol{U}^T \tag{9.7}$$

with

$$\boldsymbol{D}^+: \quad D'_{ij} = \begin{cases} \frac{1}{\sqrt{T_i}} & \text{for } i = j \text{ and } i = 1, ..., \text{rang}(\boldsymbol{A}) \\ 0 & \text{else} \end{cases} \tag{9.8}$$

Thus, for an appropriate threshold ε, an SVD is to compute first to get the maximum SV. It follows a definition of $\varepsilon > 0$ such that $D'_{ii} = 0$ for $\frac{1}{\sqrt{T_i}} < \varepsilon$.

9.4 Matrix Pencil Algorithm

The matrix pencil method is a particular case of a matrix prediction approach for the estimation of signal parameters like frequencies and attenuation factors, of exponentially damped and/or undamped sine waves in noise. It has been mainly developed by Sarkar et al. [HS88] and [HS89]. In the latter reference, it has been generalised for electromagnetic systems but its origin dates back to 1974, where Jain [Jai74] employs it in the area of filters and signal processing. Furthermore, it has been applied in [Rul99], to decompose a one-dimensional complex signal with time-harmonic time dependence in forward and backward propagating wave terms. The main principle is the following. A set of "information" vectors is grouped into L overlapping intervals or pencils, where L is also referred to as free-moving window length. The intervals are assembled in two matrices, which are arranged in a form of an eigenvalue problem. Each time an eigenvalue is found the characteristic value also serves as rank-reducing number or in other words, every eigenvalue helps to decrease the dimension of the space the set of pencils span.

9.4.1 Determination of the Propagation Constants

The matrix pencil method is used to identify a system's properties with the purpose in this case to extract the propagation constants and the amplitudes of waves contained in the one-dimensional complex field solution with harmonic time dependence. The propagation constants or poles are estimated via the matrix pencil method. After these values are known the corresponding amplitudes are determined according to the principle of least mean squares.

The goal is to obtain the eigenvalues corresponding to the complex structure under investigation, which is simulated within a full-wave simulation. Therefore, the field values are equidistantly sampled in propagation direction along the architecture with sample distance κ. To keep the numerical noise low, it is advantageous if the discretisation on which the field is computed corresponds to an integer multiple of κ.

As a first step the sampled signal is represented by

$$y_k = x_k + n_k \tag{9.9}$$

$$= \sum_{t=1}^{M} |A_t| e^{(\alpha_t + \mathrm{j}\beta_t)\kappa k + \mathrm{j}\varphi_t} + n_k. \tag{9.10}$$

The index k runs from 0 to $N-1$, with N as number of samples and M the number of exponentials. Further

$$A_t = |A_t| e^{\mathrm{j}\varphi_t} \tag{9.11}$$

$$z_t = e^{\gamma_t \kappa}, \tag{9.12}$$

where A_t is the tth complex amplitude and z_t the tth complex pole with the complex propagation constant $\gamma = \alpha + \mathrm{j}\beta$. The overlying noise is n_k. The matrix pencil method is based on the peculiar traits of undisturbed exponentials, which can be represented by means of special matrices. First, a set of the first and the last sampled values are cut to eliminate reflections nearby the in- and output feed-ins. Column vectors are formulated

$$\boldsymbol{y}_0, \boldsymbol{y}_1, \ldots, \boldsymbol{y}_L, \tag{9.13}$$

where

$$\boldsymbol{y}_t = (y_t, \ldots, y_{N-L+t-1})^T \tag{9.14}$$

with which the $(N-L) \times L$ matrices $\boldsymbol{Y}_1$ and $\boldsymbol{Y}_2$

$$\boldsymbol{Y}_1 = (\boldsymbol{y}_0, \boldsymbol{y}_1, \ldots \boldsymbol{y}_{L-1}) \tag{9.15}$$

$$\boldsymbol{Y}_2 = (\boldsymbol{y}_1, \boldsymbol{y}_2, \ldots \boldsymbol{y}_L) \tag{9.16}$$

are created. To note is that one matrix is built up by the sample values shifted by one pencil compared to the second one. The parameter L denotes the pencil parameter, giving the number of pencils. A beneficial choice is found in [HS90] to be $2L = N$. The distinctive feature of the two matrices becomes obvious by the subsequent decomposition

$$\boldsymbol{Y}_1 = \boldsymbol{Z}_1 \boldsymbol{B} \boldsymbol{Z}_2 \tag{9.17}$$

$$\boldsymbol{Y}_2 = \boldsymbol{Z}_1 \boldsymbol{B} \boldsymbol{Z}_0 \boldsymbol{Z}_2, \tag{9.18}$$

where

$$
\boldsymbol{Z}_1 = \begin{pmatrix} 1 & 1 & \cdots & 1 \\ z_1 & z_2 & \cdots & z_M \\ \vdots & \vdots & \cdots & \vdots \\ z_1^{N-L-1} & z_2^{N-L-1} & \cdots & z_M^{N-L-1} \end{pmatrix}, \tag{9.19}
$$

$$
\boldsymbol{Z}_2 = \begin{pmatrix} 1 & z_1 & \cdots & z_1^{L-1} \\ & & \cdots & \\ 1 & z_M & \cdots & z_M^{L-1} \end{pmatrix}, \tag{9.20}
$$

$$
\boldsymbol{Z}_0 = \mathrm{diag}(z_1, z_2, \ldots, z_M), \tag{9.21}
$$
$$
\boldsymbol{B} = \mathrm{diag}(b_1, b_2, \ldots, b_M). \tag{9.22}
$$

For verifying the capability of z_t to reduce the matrix pencil $\boldsymbol{Y}_2 - z\boldsymbol{Y}_1$, note

$$
\boldsymbol{Y}_2 - z\boldsymbol{Y}_1 = \boldsymbol{Z}_1\boldsymbol{B}\boldsymbol{Z}_0\boldsymbol{Z}_2 - z\boldsymbol{Z}_1\boldsymbol{B}\boldsymbol{Z}_2 = \boldsymbol{Z}_1\boldsymbol{B}(\boldsymbol{Z}_0 - z\boldsymbol{I})\boldsymbol{Z}_2 \tag{9.23}
$$

as in [Rul99]. It is shown in [GvL96] that if $M \le L \le N - M$ the poles $\{z_t; t = 1, \ldots, M\}$ are the generalised eigenvalues of the matrix pencil $\boldsymbol{Y}_2 - z\boldsymbol{Y}_1$. Videlicet, if $M \le L \le N - M$, $z = z_t$ is a rank-reducing number of $\boldsymbol{Y}_2 - z\boldsymbol{Y}_1$ by one since the tt^{th}-element of the matrix $\boldsymbol{Z}_0 - z\boldsymbol{I}$ is zero. With it, the effects of the tth column of $\boldsymbol{Z}_1$ and the tth row of $\boldsymbol{Z}_2$ are eliminated. For noisy data, it is important to formulate the truncated pseudo-inverse $\boldsymbol{Y}_1^+$ of $\boldsymbol{Y}_1$ with $\tau_1, \ldots, \tau_M$ the M largest singular values of $\boldsymbol{Y}_1$. M is chosen such that τ/τ_M is larger than a defined threshold. So, the singular value decomposition of $\boldsymbol{Y}_1$ is used

$$
\boldsymbol{Y}_1 = \sum_{t=1}^{M} \tau_t \boldsymbol{u}_i \boldsymbol{v}_i^H \tag{9.24}
$$
$$
= \boldsymbol{U}\boldsymbol{D}\boldsymbol{V}^H \tag{9.25}
$$
$$
\boldsymbol{Y}_1^+ = \boldsymbol{V}\boldsymbol{D}^{-1}\boldsymbol{U}^H \tag{9.26}
$$

with $\boldsymbol{U} = (\boldsymbol{u}_1, \ldots, \boldsymbol{u}_M)$, $\boldsymbol{V} = (\boldsymbol{v}_1, \ldots, \boldsymbol{v}_M)$, and $\boldsymbol{D} = \mathrm{diag}(\boldsymbol{\tau}_1, \ldots \boldsymbol{\tau}_M)$. The superscript H denotes the conjugate transpose of a matrix, also referred to as Hermitian, and $^{-1}$ the (regular) inverse of a matrix. $\boldsymbol{U}$ and $\boldsymbol{V}$ are left and right singular vectors, respectively. For explanation of the algorithm yielding the generalised eigenvalues of the matrix pencil, it is useful to consider

$$
\boldsymbol{Y}_1^+\boldsymbol{Y}_2 = \boldsymbol{Z}_2^+\boldsymbol{B}^{-1}\boldsymbol{Z}_1^+\boldsymbol{Z}_1\boldsymbol{B}\boldsymbol{Z}_0\boldsymbol{Z}_2 \tag{9.27}
$$
$$
= \boldsymbol{Z}_2^+\boldsymbol{Z}_0\boldsymbol{Z}_2. \tag{9.28}
$$

From Eq. (9.28), it can be seen that vectors $\{\boldsymbol{p}_t; t = 1, \ldots, M\}$ exist such that

$$
\boldsymbol{Y}_1^+\boldsymbol{Y}_1\boldsymbol{p}_t = \boldsymbol{p}_t, \quad \text{and} \tag{9.29}
$$
$$
\boldsymbol{Y}_1^+\boldsymbol{Y}_2\boldsymbol{p}_t = z_t\boldsymbol{p}_t. \tag{9.30}
$$

The latter originates from the generalised eigenvalue problem

$$
(\boldsymbol{Y}_2 - z\boldsymbol{Y}_1)\boldsymbol{p} = 0 \tag{9.31}
$$

where $\boldsymbol{p}$ are the generalised eigenvectors and which is left multiplied by $\boldsymbol{Y}_1^+$. Employing $\boldsymbol{Y}_1^+\boldsymbol{Y}_1 = \boldsymbol{V}\boldsymbol{V}^H$ and $\boldsymbol{V}^H\boldsymbol{V} = \boldsymbol{I}$ and substituting Eq. (9.26) into Eq. (9.30), further left multiplying Eq. (9.30) by $\boldsymbol{V}^H$ gives

$$(\boldsymbol{Z} - z_t\boldsymbol{I})\boldsymbol{z}_t = 0 \tag{9.32}$$

with $t = 1, \ldots, M$ and

$$\boldsymbol{Z} = \boldsymbol{D}^{-1}\boldsymbol{U}^H\boldsymbol{Y}_2\boldsymbol{V} \tag{9.33}$$

and

$$\boldsymbol{z}_t = \boldsymbol{V}^H\boldsymbol{p}_t. \tag{9.34}$$

$\boldsymbol{Z}$ is an $M \times M$ matrix and z_t and $\boldsymbol{z}_t$ are respectively eigenvalues and eigenvectors of $\boldsymbol{Z}$. Solving for the M complex eigenvalues, the attenuation and propagation constants are obtained from Eq. (9.12) with

$$\alpha = -\ln(|z_t|) \quad \text{and} \tag{9.35}$$
$$\beta = \angle(z_t) \tag{9.36}$$

after having divided the exponent by the sample distance κ. The corresponding amplitudes Eq. (9.11) are computed according to the least mean square.

9.4.2 Determination of the Amplitudes

After having established the propagation constants the corresponding amplitudes A_t are to ascertain, which fulfill the expression

$$x(\kappa k) = \sum_{t=1}^{M} A_t e^{\gamma\kappa k} \tag{9.37}$$

as close as possible to the given N samples $y(\kappa k)$ within the least mean square. First, under the assumption of the equality of wave representation and sample values on the sample locations, it is

$$\boldsymbol{F}\boldsymbol{a} = \boldsymbol{y} \tag{9.38}$$

a system of equations. The vector composed of the amplitudes is

$$\boldsymbol{a} = (A_1, \ldots, A_M)^T \tag{9.39}$$

and the vector of the data is

$$\boldsymbol{y} = (y_1, \ldots, y_N)^T \tag{9.40}$$

and the drafted matrix

$$\boldsymbol{F} = \begin{pmatrix} 1 & \cdots & 1 \\ z_1 & \cdots & z_M \\ \vdots & \vdots & \vdots \\ z_1^M & \cdots & z_M^N \end{pmatrix} \tag{9.41}$$

with Eq. (9.12) included. Since $N > M$ the system of equation is over-determined and inconsistent. Now, the quantity

$$\chi^2 = ||\boldsymbol{F}\boldsymbol{a} - \boldsymbol{y}||^2 \tag{9.42}$$

is to minimise. The singular value decomposition of $\boldsymbol{F}$

$$\boldsymbol{F} = \boldsymbol{U}\,\mathrm{diag}(\omega_1, \ldots, \omega_{M-\nu}; 0_{M-\nu+1}, \ldots, 0_M)\boldsymbol{V}^H \tag{9.43}$$

is helpful thereby. Is is presumed that ν of the ordered by sized singular values is zero. Numerically small singular values are set to zero as well. The solution of the system of equations arises as

$$\boldsymbol{a} = \boldsymbol{V}\,\mathrm{diag}(1/\omega_1, \ldots, 1/\omega_{M-\nu}; 0_{M-\nu+1}, \ldots, 0_M)\boldsymbol{U}^H\boldsymbol{y}. \tag{9.44}$$

The proof is to find in [Rul99]. The determination of the maximum coefficients of $\boldsymbol{a}$ yields the number M. With the known number the corresponding propagation constants are to choose and the least mean square computation of amplitudes are proceeded again but now with the knowledge of M. To prove the solution, a small variation with $\boldsymbol{a}'$ of the solution $\boldsymbol{a}$ is assumed. Due to orthonormality of the column vectors which span the co-domain, it can be demonstrated that no better solution than the solution $\boldsymbol{a}$ is yet found.

Bibliography

[Ans11]   Ansoft.   Ansoft   HFSS - High-Frequency Structure Simulator.
             http://www.ansoft.com/products/hf/hfss/, 2011.

[Bal05]   C. A. Balanis. *Antenna Theory: Analysis and Design*. Wiley, Hoboken,
             3rd edition, 2005.

[Ber94]   J.-P. Berenger. A perfectly matched layer for the absorption of electromag-
             netic waves. *Journal of Computational Physics*, 114(2):185–200, October
             1994.

[BSS10]   B. Bandlow, D. Sievers, and R. Schuhmann. An improved Jacobi-Davidson
             method for the computation of selected eigenmodes in waveguide cross
             sections. *IEEE Transactions on Magnetics*, 46(8):3461–3464, 2010.

[CH53]   R. Courant and D. Hilbert. *Methods of Mathematical Physics*. Wiley, New
             York, 1953.

[CI02]   C. Caloz and T. Itoh. Application of the transmission line theory of left-
             handed (LH) materials to the realization of a microstrip LH line. In *IEEE
             Antennas and Propagation Society International Symposium*, volume 2,
             pages 412–418, 2002.

[CI06]   C. Caloz and T. Itoh. *Electromagnetic Metamaterials*. Wiley, Hoboken,
             2006.

[COII02]   C. Caloz, H. Okabe, T. Iwai, and T. Itoh. Anisotropic PBG surface and its
             transmission line model. In *USNC/URSI National Radio Science Meeting*,
             San Antonio, TX, 2002.

[Col91]   R. E. Collin. *Field Theory of Guided Waves*. IEEE Press, New York, 1991.

[Col00]   R. E. Collin. *Foundations for Microwave Engineering*. Wiley, Hoboken,
             2nd edition, 2000.

[CST11]   CST. 3D EM field simulation MWS Microwave Studio - CST Computer
             Simulation Technology. http://www.cst.com/, 2011.

[CW94]   W. C. Chew and W. H. Weedon. A 3-D perfectly matched medium from
             modified Maxwell's equations with stretched coordinates. *Microwave Opt.
             Tech. Lett.*, 7:599–604, 1994.

[DdZO98]   H. Derudder, D. de Zutter, and F. Olyslager. Analysis of waveguide discon-
             tinuities using perfectly matched layers. *Electronics Letters*, 34(22):2138–
             2140, 1998.

[DI09]   Y. D. Dong and T. Itoh. Composite right/left-handed substrate integrated waveguide leaky-wave antennas. In *European Microwave Conference*, pages 276–279, October 2009.

[DOdZvdB01]   H. Derudder, F. Olyslager, D. de Zutter, and S. van den Berghe. Efficient mode-matching analysis of discontinuities in finite planar substrates using perfectly matched layers. *IEEE Transactions on Antennas and Propagation*, 49(2):185–195, February 2001.

[DP02]   N. K. Das and D. M. Pozar. Full-wave spectral-domain computation of material, radiation, and guided wave losses in infinite multilayered printed transmission lines. *IEEE Transactions on Microwave Theory and Techniques*, 39(1):54–63, 2002.

[Dru00]   P. Drude. Zur Elektronentheorie der Metalle. *Annalen der Physik*, 306(3):566–613, 1900.

[DW05]   D. Deslandes and K. Wu. Analysis and design of current probe transition from grounded coplanar to substrate integrated rectangular waveguides. *IEEE Transactions on Microwave Theory and Techniques*, 53(8):2487–2494, 2005.

[EE10]   T. F. Eibert and M. A. Eberspächer. Treating linear antenna arrays as sampled continuous source distributions. In *URSI International Symposium on Electromagnetic Theory (EMTS)*, pages 707–710, 2010.

[EIK02]   G. V. Eleftheriades, A. K. Iyer, and P. C. Kremer. Planar negative refractive index media using periodically L-C loaded transmission lines. *IEEE Transactions on Microwave Theory and Techniques*, 50(12):2702–2712, 2002.

[EK06]   I. A. Eshrah and A. A. Kishk. Analysis of left-handed rectangular waveguides with dielectric-filled corrugations using the asymptotic corrugation boundary conditions. *IEE Proceedings - Microwaves, Antennas and Propagation*, 153(3):221–225, 2006.

[EKYG05]   I. A. Eshrah, A. A. Kishk, A. B. Yakovlev, and A. W. Glisson. Spectral analysis of left-handed rectangular waveguides with dielectric-filled corrugations. *IEEE Transactions on Antennas and Propagation*, 53(11):3673–3683, 2005.

[Erm78]   H. Ermert. Guiding characteristics and radiation characteristics of planar waveguides. In *8th European Microwave Conference*, pages 94–98, Paris, France, 1978.

[EW06]   T. F. Eibert and Y. Weitsch. Periodic array modelling by the hybrid finite element - boundary integral technique accelerated by a multilevel fast spectral domain algorithm. In *International Workshop on Finite Elements for Microwave Engineering*, Stellenbosch, May 2006.

[EW10]   T. F. Eibert and Y. Weitsch. Physics based computation of eigenvalue prob-
             lems and dispersion characteristics. In *The 10th International Workshop
             on Finite Elements for Microwave Engineering*, Meredith, NH, October
             2010.

[EWC11]   T. F. Eibert, Y. Weitsch, and H. Chen. Dispersion analysis of periodic
             structures by solving corresponding excitation problems. In *German Mi-
             crowave Conference (GeMIC)*, Darmstadt, Germany, March 2011.

[EZ06]   N. Engheta and R. W Ziolkowski. *Metamaterials: Physics and Engineering
             Explorations*. Wiley, Hoboken, 2006.

[FM94]   L. B. Felsen and N. Marcuvitz. *Radiation and Scattering of Waves*. IEEE
             Press, Piscataway, 1994.

[FYC09]   C. M. Fan, D. L. Young, and C. L. Chiu. Method of fundamental solutions
             with external source for the eigenfrequencies of waveguides. *Journal of
             Marine Science and Technology*, 17(3):164–172, 2009.

[GAA$^+$04] K. Guven, K. Aydin, K. Alici, C. Soukoulis, and E. Ozbay. Spectral nega-
             tive refraction and focusing analysis of a two-dimensional left-handed pho-
             tonic crystal lens. *Physical Review B*, 70(20), 2004.

[GE02]   A. Grbic and G. V. Eleftheriades. A backward-wave antenna based on
             negative refractive index LC networks. In *IEEE Antennas and Propagation
             Society International Symposium*, volume 4, 2002.

[Ged96]   S. D. Gedney. An anisotropic PML - absorbing media for the FDTD - sim-
             ulation of fields in lossy and dispersive media. *Electromagnetics*, 16(4):399,
             1996.

[GRB00]   H. W. Glock, K. Rothemund, and M. Borecky. Calculation of RF eigen-
             modes using S-parameters of resonator parts. In *April Meeting of the
             American Physical Society, Long Beach, CA*, 2000.

[GTRQP$^+$06] J. L. Gomez-Tornero, D. C. Rebenaque, F. Quesada-Pereira, J. P. Martinez,
             and A. Alvarez-Melcon. PAMELA: a useful tool for the study of leaky-
             wave modes in strip-loaded open dielectric waveguides. *IEEE Antennas
             and Propagation Magazine*, 48(4):54–72, August 2006.

[GvL96]   G. H. Golub and C. F. van Loan. *Matrix Computations*. JHU Press,
             Baltimore, 1996.

[Haf90]   C. Hafner. *Generalized Multipole Technique for Computational Electro-
             magnetics*. Artech House, Boston, 1990.

[Har01]   R. F. Harrington. *Time-Harmonic Electromagnetic Fields*. Wiley, New
             York, 2001.

[HHMS91]   C. I. G. Hsu, R. F. Harrington, J. R. Mautz, and T. K. Sarkar. On
             the location of leaky wave poles for a grounded dielectric slab. *IEEE
             Transactions on Microwave Theory and Techniques*, 39(2):346–349, 1991.

[HS88]   Y. Hua and T. K. Sarkar. Matrix pencil method and its performance. In *International Conference on Acoustics, Speech, and Signal Processing*, pages 2476–2479, April 1988.

[HS89]   Y. Hua and T. K. Sarkar. Generalized pencil-of-function method for extracting poles of an EM system from its transient response. *IEEE Transactions on Antennas and Propagation*, 37(2):229–234, February 1989.

[HS90]   Y. Hua and T. K. Sarkar. Matrix pencil method for estimating parameters of exponentially damped/undamped sinusoids in noise. *IEEE Transactions on Acoustics, Speech, and Signal Processing*, 38(5):814–824, 1990.

[IE02]   A. K. Iyer and G. V. Eleftheriades. Negative refractive index metamaterials supporting 2-D waves. In *IEEE MTT-S International Microwave Symposium*, pages 1067–1070, Seattle, WA, USA, 2002.

[Ish90]   A. Ishimaru. *Electromagnetic Wave Propagation, Radiation, and Scattering.* Prentice Hall, 1990.

[Jai74]   V. Jain. Filter analysis by use of pencil of functions: Part I. *IEEE Transactions on Circuits and Systems*, 21(5):574–579, 1974.

[Jin02]   J. Jin. *The Finite Element Method in Electromagnetics.* Wiley, New York, 2002.

[Kar01]   A. Karageorghis. The method of fundamental solutions for the calculation of the eigenvalues of the Helmholtz equation. *Applied Mathematics Letters*, 14(7):837–842, 2001.

[KTT94]   D. S. Katz, E. T. Thiele, and A. Taflove. Validation and extension to three dimensions of the Berenger PML absorbing boundary condition for FD-TD meshes. *IEEE Microwave and Guided Wave Letters*, 4(8):268–270, 1994.

[KW93]   N. Kamiya and S. T. Wu. Generalized eigenvalue formulation of the Helmholtz equation by the Trefftz method. *Engineering Computations*, 11(2):177–186, 1993.

[LBSW09]   G. Lubkowski, B. Bandlow, R. Schuhmann, and T. Weiland. Effective modeling of double negative metamaterial macrostructures. *IEEE Transactions on Microwave Theory and Techniques*, 57(5):1136–1146, 2009.

[Li07]   Z. C. Li. Error analysis of the Trefftz method for solving Laplace's eigenvalue problems. *Journal of Computational and Applied Mathematics*, 200(1):231–254, 2007.

[LM07]   C. Liu and W. Menzel. On the relation between a negative refractive index transmission line and Chebyshev filters. In *European Microwave Conference*, pages 704–707, Munich, Germany, 2007.

[Lor16]   H. A. Lorentz. *The Theory of Electrons and its Applications to the Phenomena of Light and Radiant Heat.* Teubner, Leipzig, 1916.

[LSY98]   R. B. Lehoucq, D. C. Sorensen, and C. Yang. *ARPACK Users' Guide: Solution of Large-Scale Eigenvalue Problems with Implicitly Restarted Arnoldi Methods.* SIAM, 1998.

[Mar51]   N. Marcuvitz. *Waveguide Handbook.* McGraw-Hill, New York, 1951.

[Mar69]   E. A. J. Marcatili. Dielectric rectangular waveguide and directional coupler for integrated optics. *Bell Systems Technical Journal*, 48(21):2071–2102, September 1969.

[Max92]   J. C. Maxwell. *Treatise on Electricity and Magnetism.* Clarendon, Oxford, 3rd edition, 1892.

[MB87]   K. A. Michalski and C. M. Butler. Evaluation of Sommerfeld integrals arising in the ground stake antenna problem. *IEE Proceedings H Microwaves, Antennas and Propagation*, 134(1):93–97, February 1987.

[Men78]   W. Menzel. A new travelling wave antenna in microstrip. In *8th European Microwave Conference*, pages 302–306, Paris, France, 1978.

[MG92]   H. H. Meinke and F. W. Gundlach. *Taschenbuch der Hochfrequenztechnik.* Springer, Berlin, 1992.

[MHJ80]   R. Mittra, Y.-L. Hou, and V. Jamnejad. Analysis of open dielectric waveguides using mode-matching technique and variational methods. *IEEE Transactions on Microwave Theory and Techniques*, 28(1):36–43, January 1980.

[MIM75]   W. V. McLevige, T. Itoh, and R. Mittra. New waveguide structures for millimeter-wave and optical integrated circuits. *IEEE Transactions on Microwave Theory and Techniques*, 23(10):788–794, October 1975.

[MZ89]   K. A. Michalski and D. Zheng. Rigorous analysis of open microstrip lines, of arbitrary cross section in bound and leaky regimes. *IEEE Transactions on Microwave Theory and Techniques*, 37(12):2005–2010, December 1989.

[Not00]   M. Notomi. Theory of light propagation in strongly modulated photonic crystals: Refractionlike behavior in the vicinity of the photonic band gap. *Physical Review B*, 62(16):10696–10705, 2000.

[NWCL94]   E. A. Navarro, C. Wu, Y. Chung, and J. Litva. Application of PML superabsorbing boundary condition to nonorthogonal FDTD method. *Electronics Letters*, 30(20):1654–1655, 1994.

[OJ07]   A. A. Oliner and D. R. Jackson. Leaky-wave antennas. In J. L. Volakis, editor, *Antenna Engineering Handbook*, chapter 11. McGraw-Hill, New York, 2007.

[Oli02]   A. A. Oliner. A periodic-structure negative-refractive-index medium without resonant elements. In *USNC/URSI Natinonal US Radio Science Meeting*, pages 16–21, 2002.

[Pen00]   J. B. Pendry. Negative refraction makes a perfect lens. *Physical Review Letters*, 85(18):3966, October 2000.

[Poz04]   D. M. Pozar. *Microwave Engineering*. Wiley, Hoboken, 3rd edition, 2004.

[QCI+99]   Y. Qian, B. C. C. Chang, T. Itoh, K. C. Chen, and C. K. C. Tzuang. High efficiency and broadband excitation of leaky mode in microstrip structures. In *IEEE MTT-S International Microwave Symposium*, pages 1419–1422, Anaheim, CA, USA, 1999.

[RdZ02]   H. Rogier and D. de Zutter. Berenger and leaky modes in optical fibers terminated with a perfectly matched layer. *Journal of Lightwave Technology*, 20(7):1141–1148, 2002.

[Reu07]   S. Y. Reutskiy. The methods of external and internal excitation for problems of free vibrations of non-homogeneous membranes. *Engineering Analysis with Boundary Elements*, 31(11):906–918, 2007.

[Reu08]   S. Y. Reutskiy. The methods of external excitation for analysis of arbitrarily-shaped hollow conducting waveguides. *Progress In Electromagnetics Research*, 82:203–226, 2008.

[Reu09]   S. Y. Reutskiy. The method of external excitation for solving Laplace singular eigenvalue problems. *Engineering Analysis with Boundary Elements*, 33(2):209–214, 2009.

[Reu10]   S. Y. Reutskiy. The method of external excitation for solving generalized Sturm–Liouville problems. *Journal of Computational and Applied Mathematics*, 233(9):2374–2386, 2010.

[RG97]   J. A. Roden and S. D. Gedney. Efficient implementation of the uniaxial-based PML media in three-dimensional nonorthogonal coordinates with the use of the FDTD technique. *Microwave Opt. Tech. Lett.*, 14(2):71–75, 1997.

[Rul99]   I. D. Rullhusen. *Hybride Finite-Elemente-Integralgleichungsmethode im Ortsbereich zur flexiblen Berechnung dreidimensionaler Strukturen der Antennen- und MMIC-Technik sowie von Wellenleitern der integrierten Optik*. PhD thesis, Universität Bremen, Bremen, 1999.

[Saa92]   Y. Saad. *Numerical Methods for Large Eigenvalue Problems*. Manchester University Press ND, 2nd edition, 1992.

[SGG02]   P. Savi, I.-L. Gheorma, and R. D. Graglia. Full-wave high-order FEM model for lossy anisotropic waveguides. *IEEE Transactions on Microwave Theory and Techniques*, 50(2):495–500, February 2002.

[SKLL95]   Z. S. Sacks, D. M. Kingsland, R. Lee, and J.-F. Lee. A perfectly matched anisotropic absorber for use as an absorbing boundary condition. *IEEE Transactions on Antennas and Propagation*, 43(12):1460–1463, 1995.

[SLW05]   R. Schuhmann, G. Lubkowski, and T. Weiland. Full-wave simulations and extraction of effective material parameters for left-handed metamaterials. In *German Microwave Conference (GeMIC)*, Ulm, April 2005.

[SMIN06]   K. Sato, S. Matsuzawa, Y. Inoue, and T. Nomura. Electronically scanned left-handed leaky wave antenna for millimeter-wave automotive applications. In *IEEE International Workshop on Antenna Technology Small Antennas and Novel Metamaterials*, pages 420–423, 2006.

[Som09]   A. Sommerfeld. Über die Ausbreitung der Wellen in der drahtlosen Telegraphie. *Annalen der Physik*, 333(4):665–736, 1909.

[SP83]   F. K. Schwering and S.-T. Peng. Design of dielectric grating antennas for millimeter-wave applications. *IEEE Transactions on Microwave Theory and Techniques*, 31(2):199–209, February 1983.

[SPV$^+$00]   D. R. Smith, W. J. Padilla, D. C. Vier, S. C. Nemat-Nasser, and S. Schultz. Composite medium with simultaneously negative permeability and permittivity. *Physical Review Letters*, 84(18):4184, May 2000.

[SW77]   K. Solbach and I. Wolff. The electromagnetic fields and the phase constants of dielectric image lines. In *IEEE MTT-S International Microwave Symposium*, pages 456–458, 1977.

[TC97]   F. L. Teixeira and W. C. Chew. PML-FDTD in cylindrical and spherical grids. *IEEE Microwave and Guided Wave Letters*, 7(9):285–287, September 1997.

[TO63]   T. Tamir and A. A. Oliner. Guided complex waves. part 1: Fields at an interface. *Proceedings of the Institution of Electrical Engineers*, 110(2):310–324, February 1963.

[Ves68]   V. G. Veselago. The electrodynamics of substances with simultaneously negative values of ε and μ. *Physics-Uspekhi*, 10(4):509–514, 1968.

[WE07a]   Y. Weitsch and T. F. Eibert. Continuous beam-steering leaky-wave antenna based on substrate integrated waveguide. In *European Conference on Antennas and Propgation (EuCAP)*, Edinburgh, UK, 2007.

[WE07b]   Y. Weitsch and T. F. Eibert. A left-handed/right-handed leaky-wave antenna derived from slotted rectangular hollow waveguide. In *European Microwave Conference (EuMC)*, pages 917–920, Munich, October 2007.

[WE08a]   Y. Weitsch and T. F. Eibert. Analysis and design of a composite left-/right-handed leaky wave antenna based on the H_{10} rectangular hollow waveguide mode. *Advances in Radio Sciences, www.adv-radio-sci.net/6/49/2008*, 6:49–54, 2008.

[WE08b]   Y. Weitsch and T. F. Eibert. A non-radiating composite right-/left-handed transmission line derived from substrate integrated rectangular hollow waveguide. In *XXIX U.R.S.I. General Assembly*, Chicago, USA, August 2008.

[WE09a]   Y. Weitsch and T. F. Eibert. A closed composite right-/left-handed trans-
            mission line based on substrate integrated waveguide technology. *Frequenz*,
            63(7-8):160–162, 2009.

[WE09b]   Y. Weitsch and T. F. Eibert. Periodically loaded waveguide analysis by
            propagating and evanescent mode superposition. In *European Microwave
            Conference*, pages 950–953, Rome, Italy, October 2009.

[WE10a]   Y. Weitsch and T. F. Eibert. Composite right-/left-handed interdigital
            leaky-wave antenna on a substrate integrated waveguide. In *European
            Conference on Antennas and Propagation (EuCAP)*, pages 1–5, Barcelona,
            April 2010.

[WE10b]   Y. Weitsch and T. F. Eibert. Modal expansion of periodically loaded
            waveguides extended to the evanescent frequency domain. In *Progress in
            Electromagnetics Research Symposium (PIERS)*, Xian, China, March 2010.

[WE11]   Y. Weitsch and T. F. Eibert. Eigenvalue computation of open periodi-
            cally composed waveguides by series expansion. In *IEEE Antennas and
            Propagation Society International Symposium*, Spokane, WA, July 2011.

[WKLL02]   J. Y. Wu, D. M. Kingsland, J. F. Lee, and R. Lee. A comparison of
            anisotropic PML to Berenger's PML and its application to the finite-
            element method for EM scattering. *IEEE Transactions on Antennas and
            Propagation*, 45(1):40–50, 2002.

[WTM08]   T. Weiland, M. Timm, and I. Munteanu. A practical guide to 3-D simula-
            tion. *IEEE Microwave Magazine*, 9(6):62–75, 2008.

[YCN⁺07]   N. Yang, C. Caloz, V. Nguyen, S. Abielmona, and K. Wu. Non-radiative
            CRLH boxed stripline structure with high Q performances. In *EMTS In-
            ternational URSI Commission B-Electromagnetic Theory Symposium*, Ot-
            tawa, Ca, 2007.

[ZB65]   O. Zinke and H. Brunswig. *Lehrbuch der Hochfrequenztechnik*. Springer,
            Berlin, 1965.